Machining with Nanomaterials

Machining with Nanomaterials

Mark J. Jackson
Jonathan S. Morrell
Editors

Springer

Mark J. Jackson
Center for Advanced Manufacturing
Purdue University
West Lafayette, IN 47907

Jonathan Morrell
Y-12 Security Complex
Technology Development Division
Oak Ridge, TN 37831

ISBN 978-0-387-87659-7 e-ISBN 978-0-387-87660-3

Library of Congress Control Number: 2008935101

Printed on acid-free paper

springer.com

Contents

List of Authors

Waqar Ahmed
University of Central Lancashire
Preston, PR1 4BU
United Kingdom
E-mail: *wahmed4@uclan.ac.uk*

Jeffrey J. Evans
Purdue University
College of Technology
401 North Grant Street
West Lafayette, IN 47907-2021, USA
E-mail: *jje@purdue.edu*

Rodney G. Handy
Purdue University
College of Technology
401 North Grant Street
West Lafayette, IN 47907-2021, USA
E-mail: *rhandy@purdue.edu*

Mark J. Jackson
Purdue University
Center for Advanced Manufacturing
College of Technology
401 North Grant Street
West Lafayette, IN 47907-2021, USA
E-mail: *jacksomj@purdue.edu*

Jonathan S. Morrell
Y12 National Security Complex
Oak Ridge
Tennessee, USA
E-mail: *morrelljs@y12.doe.gov*

Jun Ni
University of Michigan
Ann Arbr, Michigan, USA
E-mail: *ni@umich.edu*

Grant M. Robinson
Micro Machinists, LLC
3000 Kent Avenue
West Lafayette, IN 47906
E-mail: *grant@micromachinists.com*

Michael D. Whitfield
Micro Machinists, LLC
3000 Kent Avenue
West Lafayette, IN 47906
E-mail: *mike@micromachinists.com*

Michael D. Whitt
Purdue University
Mechanical Engineering Technology
Knoy Hall of Technology
West Lafayette, IN 47907-2021
E-mail: *mwhitt@purdue.edu*

Haiyan Zhang
Purdue University
Mechanical Engineering Technology
Knoy Hall of Technology
West Lafayette, IN 47907-2021
E-mail: *hzhang@purdue.edu*

Chengying Xu
University of Central Florida
Orlando, Florida
E-mail: *cxu@mail.ucf.edu*

Preface

Machining is a widely used process for producing intricate shapes on components and artifacts and for providing precise tolerances that are required especially for the manufacture of parts at the microscale. Modern machining requires the use of minimum quantities of lubricants, dry machining capability, high cutting speeds, and long tool lives. However, existing tool materials have proven to be sub-standard compared to newly developed nanostructured thin film coatings. There is also a growing need for specially developed cutting tools for machining nanocrystalline metals and alloys.

Recently, President William J. Clinton talked about the exciting promise of nanotechnology in January 2000, and later announced an ambitious national nanotechnology initiative (NNI) that was enacted in 2001, and re-authorized by President George W. Bush in 2006, with an initial budget of $497 million to promote nanoscale research that would benefit society. The initiative has created a new industry focused on providing nanostructured coatings and materials. The purpose of this book is to present information and knowledge on the emerging field of machining with nanomaterials. The book is written in the spirit of scientific endeavor outlined by Richard Feynman, who stated in 1960 that one of the greatest challenges to scientists in the field of miniaturization is the manufacture of objects using techniques such as turning and milling. The book presents information on machining fundamentals, machining stability and chatter, developments in tool coatings, machining common engineering materials with coated tools, dry machining, creating nanostructured metals using coated cutting tools, and machining with nanostructured diamond.

The structure of the book is based on matter provided by many colleagues and the author wishes to thank the contributors of this book for helping construct a source of knowledge and information on machining with and creating nanomaterials and for granting the editors permission to use such material. The editors also acknowledge the help and support of Inderscience Publishers for allowing the chapter contributors and editors to reproduce their work that was originally published in refereed Inderscience journals.

Mark J. Jackson
Purdue University

Jonathan S. Morrell
Y-12 National Security Complex

July 2008

Chapter 1

Fundamentals of Machining

M. J. Jackson, W. Ahmed and C. Xu

1.1 Introduction

There is a substantial increase in the specific energy required with a decrease in chip size during machining. It is believed this is due to the fact that all metals contain defects such as grain boundaries, missing and impurity atoms, etc., and when the size of the material removed decreases the probability of encountering a stress-reducing defect decreases. Since the shear stress and strain in metal cutting is unusually high, discontinuous microcracks usually form on the primary shear plane. If the material is very brittle, or the compressive stress on the shear plane is relatively low, microcracks will grow into larger cracks giving rise to discontinuous chip formation. When discontinuous microcracks form on the shear plane they will weld and reform as strain proceeds, thus joining the transport of dislocations in accounting for the total slip of the shear plane. In the presence of a contaminant, such as carbon tetrachloride vapor at a low cutting speed, the re-welding of microcracks will decrease, resulting in a decrease in the cutting force required for chip formation. A number of special experiments that support the transport of microcracks across the shear plane, and the important role compressive stress plays on the shear plane are explained. An alternative explanation for the size effect in cutting is based on the belief that shear stresses increase with increasing strain rate. When an attempt is made to apply this to metal cutting, it is assumed in the analysis that the von Mises criterion applies to the shear plane. This is inconsistent with the experimental findings by Merchant. Until this difficulty is resolved with the experimental verification of the strain rate approach, it should be assumed that the strain rate effect

may be responsible for some portion of the size effect in metal cutting.

1.2 Machining Effects

It has been known for a long time that a size effect exists in metal cutting, where the specific energy increases with decrease in deformation size. Backer et al. [1] performed a series of experiments in which the shear energy per unit volume deformed (u_S) was determined as a function of specimen size for a ductile metal (SAE 1112 steel). The deformation processes involved were as follows, listed from top to bottom with increasing size of specimen deformed:

- surface grinding;
- micromilling;
- turning; and
- tensile test.

The surface grinding experiments were performed under relatively mild conditions involving plunge type experiments in which an 8-inch (20.3 cm) diameter wheel was directed radially downward against a square specimen of length and width 0.5 in (1.27 cm). The width of the wheel was sufficient to grind the entire surface of the work at different downfeed rates (t). The vertical and horizontal forces were measured by a dynamometer supporting the workpiece. This enabled the specific energy (u_S) and the shear stress on the shear plane (τ) to be obtained for different values of undeformed chip thickness (t). The points corresponding to a constant specific energy below a value of down feed of about 28 μinch (0.7 μm) are on a horizontal line due to a constant theoretical strength of the material being reached when the value of, t, goes below approximately 28 μinch (0.7 μm). The reasoning in support of this conclusion is presented in Backer et al [1]. In the micromilling experiments, a carefully balanced 6-inch (152 cm) carbide tipped milling cutter was used with all but one of the teeth relieved so that it operated as a fly milling cutter. Horizontal and vertical forces were measured for a number of depths of cut (t) when machining the same sized surface as in grinding. The shear stress on the shear plane (τ)

was estimated by a rather detailed method presented in Backer et al [1]. Turning experiments were performed on a 2.25-inch (5.72 cm) diameter SAE 1112 steel bar pre-machined in the form of a thin-walled tube having a wall thickness of 0.2 inch (5 mm). A zero degree rake angle carbide tool was operated in a steady-state two-dimensional orthogonal cutting mode as it machined the end of the tube. Values of shear stress on the shear plane (τ) versus undeformed chip thickness were determined for experiments at a constant cutting speed and different values of axial infeed rate and for variable cutting speeds and a constant axial infeed rate. The grinding, micromilling, and turning results are shown in Fig. 1.1.

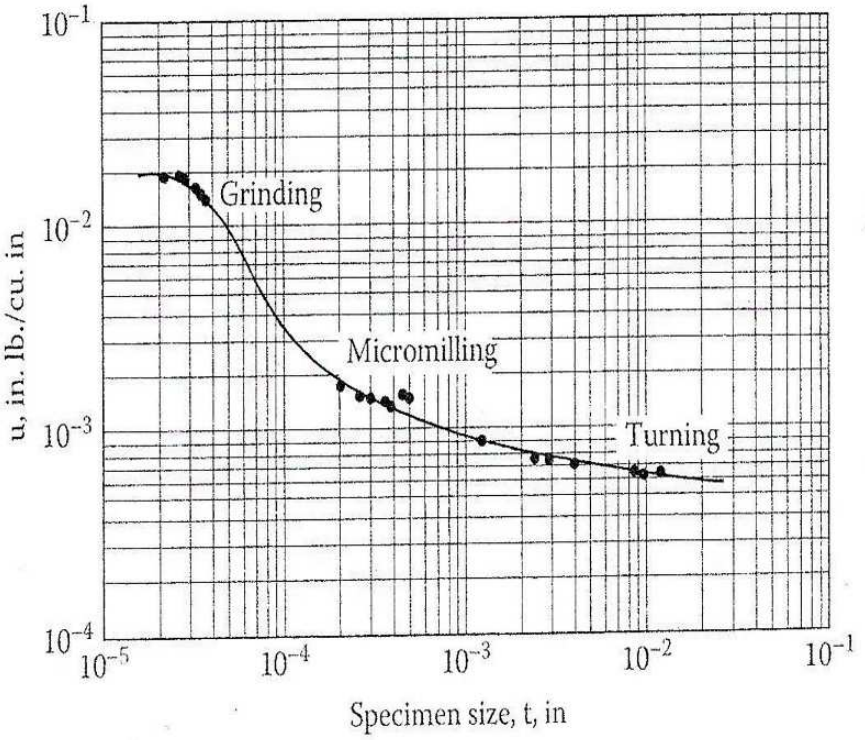

Figure 1.1. Variation of shear stress on shear plane when cutting SAE 1112 steel [1]

A true stress-strain tensile test was performed on a 0.505-inch (1.28 cm) diameter by 2-inch (5.08 cm) gage length specimen of SAE 1112 steel. The mean shear stress at fracture was 22,000 psi (151.7 MPa). This value is not shown in Fig. 1.1 since it falls too far to the right. Taniguchi discussed the size effect in cutting and forming and presented his version of Fig. 1.1 in Fig. 1.2 [2]. Shaw [3] discusses the origin of the size effect in metal cutting, which is believed to be primarily due to short-range inhomogeneities present in all engineering metals.

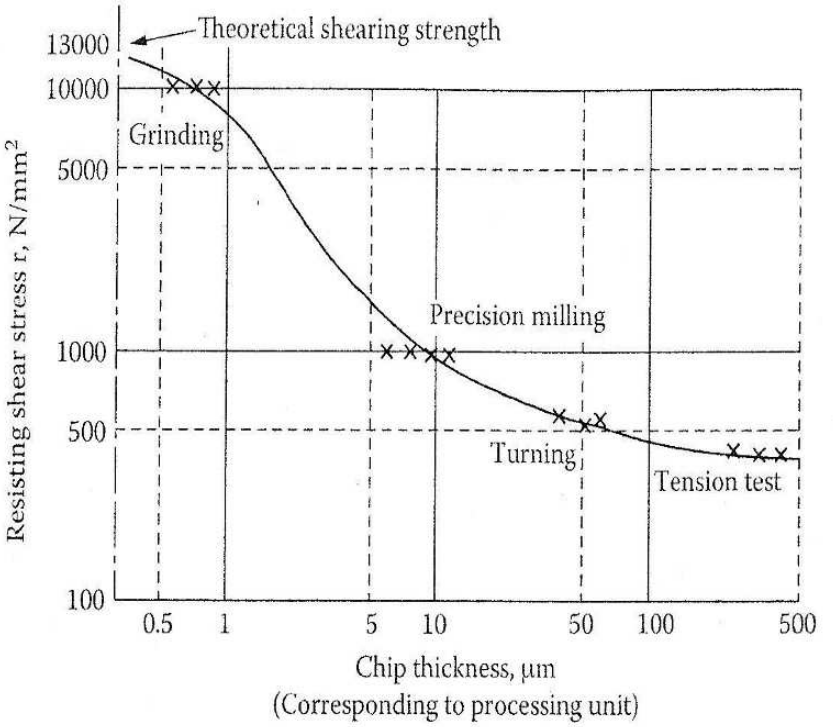

Figure 1.2. Relationship between chip thickness and resisting shear stress for Fig. 1.1 as modified by Taniguchi [2]

When the back of a metal cutting chip is examined at very high magnification by means of an electron microscope individual slip lines are evident as shown in Fig. 1.3. In deformation studies,

Heidenreich and Shockley [4] found that slip does not occur on all atomic planes but only on certain discrete planes. In experiments on deformed aluminium single crystals the minimum spacing of adjacent slip planes was found to be approximately 50 atomic spaces while the mean slip distance along the active slip planes was found to be about 500 atomic spaces. These experiments further support the observation that metals are not homogeneous and suggest that the planes along which slip occurs are associated with inhomogeneities in the metal. Strain is not uniformly distributed in many cases. For example, the size effect in a tensile test is usually observed only for specimens less than 0.1 inch (2.5 mm) in diameter. On the other hand, a size effect in a torsion test occurs for considerably larger samples due to the greater stress gradient present in a torsion test than in a tensile test. This effect and several other related ones are discussed in detail by Shaw [3].

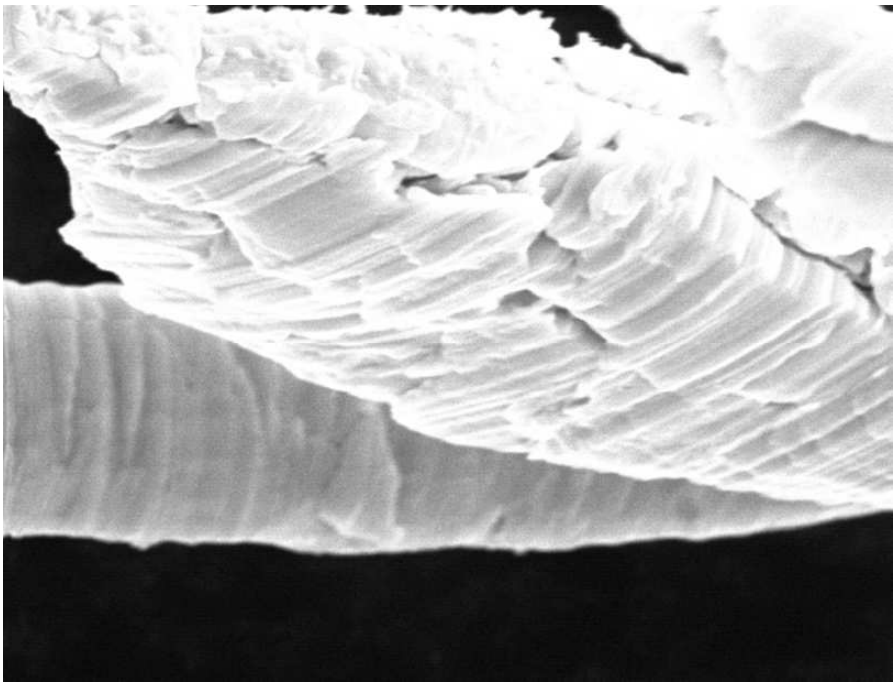

Figure 1.3. Back free surface of chip showing regions of discontinuous strain or microfracture

1.2.1 Prediction of shear angle

There have been many notable attempts to derive an equation for the shear angle (ϕ) shown in Fig. 1.4 for steady-state orthogonal cutting. Ernst and Merchant [5] presented the first quantitative analysis. Figure 10.5 shows forces acting on a chip at the tool point where: R = the resultant force on the tool face, R' = the resultant force in the shear plane, N_C and F_C are the components of R normal to and parallel to the tool face, N_S and F_S are the components of R' normal to and parallel to the cutting direction, F_Q and F_P are the components of R normal to and parallel to the cutting direction, and $\beta = \tan^{-1} F_C/N_C$ (is called the friction angle).

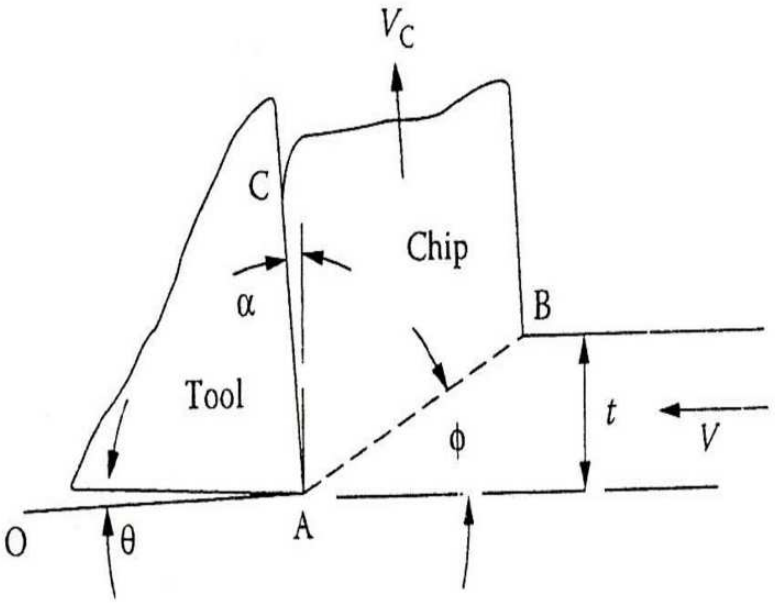

Figure 1.4. Nomenclature for two-dimensional steady-state orthogonal cutting process

Assuming the shear stress on the shear plane (τ) to be uniformly distributed it is evident that:

$$\tau = \frac{F_S}{A_S} = \frac{R'\cos(\phi + \beta - \alpha)\sin\phi}{A} \tag{1.1}$$

Where A_S and A are the areas of the shear plane and that corresponding to the width of cut (b), times the depth of cut (t). Ernst and Merchant [5] reasoned that τ should be an angle such that τ would be a maximum and a relationship for ϕ was obtained by differentiating Eq. 1.1 with respect to ϕ and equating the resulting expression to zero produces,

$$\phi = 45 - \frac{\beta}{2} + \frac{\alpha}{2} \tag{1.2}$$

However, it is to be noted that in differentiating, both R' and β were considered independent of ϕ.

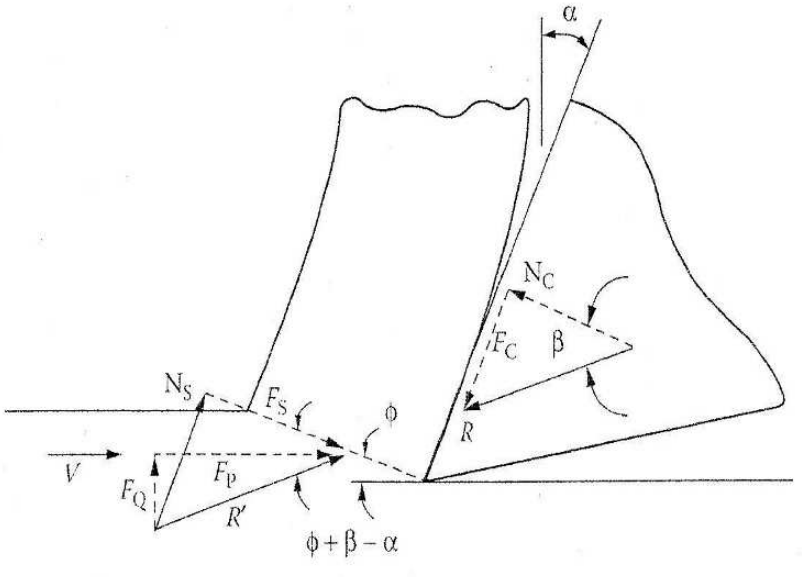

Figure 1.5. Cutting forces at the tool tip for the cutting operation shown in Fig. 1.4

Merchant [6] presented a different derivation that also led to Eq. 1.2. This time an expression for the total power consumed in the cutting process was first written as,

$$P = F_P V = (\tau A V)\frac{\cos(\beta - \alpha)}{\sin\phi\cos(\phi + \beta - \alpha)} \tag{1.3}$$

It was then reasoned that ϕ would be such that the total power would be a minimum. An expression identical to Eq. 1.2 was obtained when P was differentiated with respect to ϕ, this time considering τ and β to be independent of ϕ. Piispanen [7] had done this previously in a graphical way. However, he immediately carried his line of reasoning one step further and assumed that the shear stress τ would be influenced directly by normal stress on the shear plane as follows,

$$\tau = \tau_0 + K_\sigma \tag{1.4}$$

Where K is a material constant. Piispanen then incorporated this into his graphical solution for the shear angle. Upon finding Eq. 1.2 to be in poor agreement with experimental data Merchant also independently (without knowledge of Piispanen's work at the time) assumed that the relationship given in Eq. 1.4, and proceeded to work this into his second analysis as follows. From Fig. 1.5 it may be seen that,

$$\sigma = \tau\tan(\phi + \beta - \alpha) \tag{1.5}$$

Or, from Eq. 1.4

$$\tau_0 = \tau + K\tau\tan(\phi + \beta - \alpha) \tag{1.6}$$

Hence,

$$\tau = \frac{\tau_0}{1 - K\tan(\phi + \beta - \alpha)} \tag{1.7}$$

When this is substituted into Eq. 1.3 we have,

$$P = \frac{\tau_0 AV\cos(\beta - \alpha)}{[1 - K\tan(\phi + \beta - \alpha)]\sin\phi\cos(\phi + \beta - \alpha)} \tag{1.8}$$

Now, when P is differentiated with respect to ϕ and equated to zero (with τ_0 and p considered independent of ϕ we obtain,

$$\phi = \frac{\cot^{-1}(K)}{2} - \frac{\beta}{2} + \frac{\alpha}{2} = \frac{C - \beta + \alpha}{2} \tag{1.9}$$

Merchant called the quantity, $\cot^{-1}$ K, the machining "constant" C. The quantity C is seen to be the angle the assumed line relating τ and ϕ makes with the τ axis [6-7,9]. Merchant [8] has determined the values of C given in Table 1.1 for materials of different chemistry and structure being turned under finishing conditions with different tool materials. From this table it is evident that C is not a constant. Merchant's empirical machining "constant" C that gives rise to Eq. 1.9 with values of ϕ is in reasonably good agreement with experimentally measured values.

While it is well established that the rupture stress of both brittle and ductile materials is increased significantly by the presence of compressive stress (known as the Mohr Effect), it is generally believed that a similar relationship for flow stress does not hold. However, an explanation for this paradox with considerable supporting experimental data is presented below. The fact that this discussion is limited to steady-state chip formation rules out the possibility of periodic gross cracks being involved. However, the role of micro-cracks is a possibility consistent with steady-state chip formation and the influence of compressive stress on the flow stress in shear.

Table 1.1. Values of C in Eq. 1.9 for a variety of work and tool materials in finish turning without a cutting fluid

Work material	Tool material	C (Degrees)
SAE 1035 Steel	HSS*	70
SAE 1035 Steel	Carbide	73
SAE 1035 Steel	Diamond	86
AISI 1022 (leaded)	HSS*	77
AISI 1022 (leaded)	Carbide	75
AISI 1113 (sul.)	HSS*	76
AISI 1113 (sul.)	Carbide	75
AISI 1019 (plain)	HSS*	75
AISI 1019 (plain)	Carbide	79
Aluminum	HSS*	83
Aluminum	Carbide	84
Aluminum	Diamond	90
Copper	HSS*	49
Copper	Carbide	47
Copper	Diamond	64
Brass	Diamond	74

*HSS = High-speed steel

A discussion of the role micro-cracks can play in steady-state chip formation is presented in the next section. Hydrostatic stress plays no role in the plastic flow of metals if they have no porosity. Yielding then occurs when the von Mises criterion reaches a critical value. Merchant [9] has indicated that Barrett [10] found that for single crystal metals τ_S is independent of τ_S when plastics such as celluloid are cut. In general, if a small amount of compressibility is involved yielding will occur when the von Mises criterion reaches a certain value.

However, based on the results of Table 1.1 the role of compressive stress on shear stress on the shear plane in steady-state metal cutting is substantial. The fact there is no outward sign of voids or porosity in steady-state chip formation of a ductile metal during cutting and yet there is a substantial influence of normal stress on shear stress on the shear plane represents an interesting paradox. It is interesting to note that Piispanen [7] had assumed that shear stress on the shear plane would increase with normal stress and had incorporated this into his graphical treatment.

1.2.2 Plastic behavior at large strains

There has been little work done in the region of large plastic strains. Bridgman [11] used hollow tubular notched specimens to perform experiments under combined axial compression and torsion. The specimen was loaded axially in compression as the centre section was rotated relative to the ends. Strain was concentrated in the reduced sections and it was possible to crudely estimate and plot shear stress vs. shear strain with different amounts of compressive stress on the shear plane. From these experiments Bridgman concluded that the flow curve for a given material was the same for all values of compressive stress on the shear plane, a result consistent with other materials experiments involving much lower plastic strains. However, the strain at gross fracture was found to be influenced by compressive stress. A number of related results are considered in the following subsections.

1.2.3 Langford and Cohen's model

Langford and Cohen [12] were interested in the behaviour of dislocations at very large plastic strains and whether there was saturation relative to the strain hardening effect with strain, or whether strain hardening continued to occur with strain to the point of fracture. Their experimental approach was an interesting and fortunate one. They performed wire drawing on iron specimens using a large number of progressively smaller dies with remarkably low semi die angle (1.5º) and a relatively low (10%) reduction in area per die pass. After each die pass, a specimen was tested in

uniaxial tension and a true stress-strain curve obtained. The drawing and tensile experiments were performed at room temperature and low speeds to avoid heating and specimens were stored in liquid nitrogen between experiments to avoid strain aging effects. All tensile results were then plotted in a single diagram, the strain used being that introduced in drawing (0.13 per die pass) plus the plastic strain in the tensile test. The general overlap of the tensile stress-strain curves gives an overall strain-hardening envelope, which indicates that the wire drawing and tensile deformations are approximately equivalent relative to strain hardening [13].

Blazynski and Cole [14] were interested in strain hardening in tube drawing and tube sinking. Drawn tubes were sectioned and tested in plane strain compression. Up to a strain of about 1 the usual strain-hardening curve was obtained that is in good agreement with the generally accepted equation,

$$\sigma = \sigma_1 \varepsilon^n \tag{1.10}$$

However, beyond a strain of 1, the curve was linear corresponding to the equation,

$$\sigma = A + B\varepsilon, (\varepsilon < 1) \tag{1.11}$$

Where A and B are constants. It may be shown that,

$$A = (1 - n)\, \sigma_1 \tag{1.12}$$

$$B = n\sigma_1 \tag{1.13}$$

From transmission electron micrographs of deformed specimens, Langford and Cohen found that cell walls representing concentrations of dislocations began to form at strains below 0.2 and became ribbon shaped with decreasing mean linear intercept cell size as the strain progressed. Dynamic recovery and cell wall migration resulted in only about 7 percent of the original cells remaining after a strain of 6. The flow stress of the cold-worked

wires was found to vary linearly with the reciprocal of the mean transverse cell size [15].

1.2.4 Walker and Shaw's model

Acoustic studies were performed on specimens of the Bridgman type but fortunately, lower levels of axial compressive stress than Bridgman had used were employed in order to more closely simulate the concentrated shear process of metal cutting. The apparatus used that was capable of measuring stresses and strains as well as acoustic signals arising from plastic flow is described in the dissertation of T. J. Walker [16]. Two important results were obtained:

1. A region of rather intense acoustical activity occurred at the yield point followed by a quieter region until a shear strain of about 1.5 was reached. At this point there was a rather abrupt increase in acoustical activity that continued to the strain at fracture which was appreciably greater than 1.5; and

2. The shear stress appeared to reach a maximum at strain corresponding to the beginning of the second acoustic activity ($\gamma \approx 1.5$).

The presence of the notches in the Bridgman specimen made interpretation of stress-strain results somewhat uncertain. Therefore, a new specimen was designed which substitutes simple shear for torsion with normal stress on the shear plane. By empirically adjusting distance Δx to a value of 0.25 mm it was possible to confine all the plastic shear strain to the reduced area, thus making it possible to readily determine the shear strain ($\gamma \approx \Delta y / \Delta x$). When the width of minimum section was greater or less than 0.25 mm, the extent of plastic strain observed in a transverse micrograph at the minimum section either did not extend completely across the 0.25 mm dimension or beyond this width.

Similar results were obtained for non-resulfurised steels and other ductile metals. There is little difference in the curves for

different values of normal stress on the shear plane (σ) to a shear strain of about 1.5 [17]. This is in agreement with Bridgman. However, beyond this strain the curves differ substantially with compressive stress on the shear plane. At large strains, τ, was found to decrease with increase in (γ), a result that does not agree with Bridgman [11].

It is seen that for a low value of normal stress on the shear plane of 40 MPa strain hardening appears to be negative at a shear strain of about 1.5; that is, when the normal stress on the shear plane is about 10% of the maximum shear stress reached, negative strain hardening sets in at a shear strain of about 1.5. On the other hand, strain hardening remains positive to a normal strain of about 8 when the normal stress on the shear plane is about equal to the maximum shear stress.

1.2.5 Usui's model

In Usui et al [18] an experiment is described designed to determine why CCl_4 is such an effective cutting fluid at low cutting speeds. Since this also has a bearing on the role of microcracks in large strain deformation, it is considered here. A piece of copper was prepared [18]. The piece that extends upward and appears to be a chip is not a chip but a piece of undeformed material left there when the specimen was prepared. A vertical flat tool was then placed precisely opposite the free surface and fed horizontally. Horizontal F_P and vertical F_Q forces were recorded as the shear test proceeded. It was expected that the vertical piece would fall free from the lower material after the vertical region had been displaced a small percentage of its length. However, it went well beyond the original extent of the shear plane and was still firmly attached to the base. This represents a huge shear strain since the shear deformation was confined to a narrow band. When a single drop of CCl_4 was placed before the shear test was conducted the protrusion could be moved only a fraction of the displacement in air before gross fracture occurred on the shear plane. Figure 1.6 shows photomicrographs of experiments without and with CCl_4. It is apparent that CCl_4 is much more effective than air in preventing microcracks from re-welding.

1.2.6 Saw tooth chip formation

Saw tooth chip formation for hard steel discussed by Vyas and Shaw [19] is another example of the role microcracks play. In this case gross cracks periodically form at the free surface and run down along the shear plane until sufficient compressive stress is encountered to cause the gross crack to change to a collection of isolated microcracks.

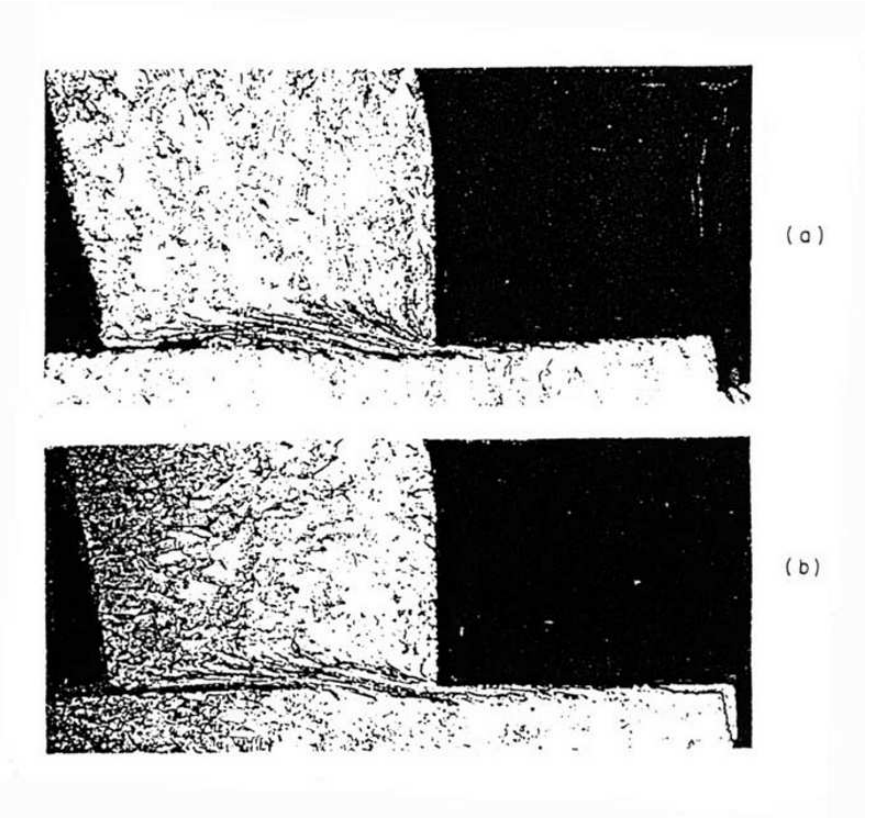

Figure 1.6. Photomicrographs of specimens that have been sheared a distance approximately equal to the shear plane length: (a) in air; and (b) with a drop of CCl_4 applied

1.2.7 Fluid-like flow in chip formation

An interesting paper was presented by Eugene [20]. Water was pumped into baffled chamber that removed eddy currents and then caused flow under gravity past a simulated tool. Powdered bakelite was introduced to make the streamlines visible as the fluid flowed passed the tool.

The photographs taken by the camera were remarkably similar to quick stop photomicrographs of actual chips. It was thought by this author at the time that any similarity between fluid flow and plastic flow of a solid was not to be expected. That was long before it was clear that the only logical explanation for the results of Bridgman and Merchant involve microfracture [21]. A more recent paper was presented that again suggests that metal cutting might be modeled by a fluid [22]. However, this paper was concerned with ultraprecision machining (depths of cut < 4 μm*)* and potential flow analysis was employed instead of the experimental approach taken by Eugene.

It is interesting to note that chemists relate the flow of liquids to the migration of vacancies (voids) just as physicists relate ordinary plastic flow of solid metals to the migration of dislocations. Henry Eyring and co-workers [24-26] have studied the marked changes in volume, entropy and fluidity that occur when a solid melts. For example, a 12% increase in volume accompanies melting of Argon, suggesting the removal of every eighth molecule as a vacancy upon melting. This is consistent with X-ray diffraction of liquid argon that showed good short-range order but poor long-range order. The relative ease of diffusion of these vacancies accounts for the increased fluidity that accompanies melting.

A random distribution of vacancies is also consistent with the increase in entropy observed on melting. Eyring's theory of fluid flow was initially termed the *"hole theory of fluid flow"* but later *"The Significant Structure Theory"* which is the title of the Eyring-Jhon book [25]. According to this theory the vacancies in a liquid move through a sea of molecules. Eyring's theory of liquid flow is mentioned here since it explains why the flow of a liquid

approximates the flow of metal passed a tool in chip formation. In this case microcracks (voids) move through a sea of crystalline solid.

1.3 Size Effects in Micromachining

It is appropriate at this point to mention that an alternative explanation for the increase in hardness that occurs when the indentation size is reduced in metals has recently been introduced [27-38]. This is based on the fact that there is an increase in the strain gradient with reduction in indentation size. This has been extended by Dinesh et al [39] to explain the size effect in machining. In the Dinesh et al [39] analysis the size effect in hardness is related to that in cutting by assuming the von Mises criterion is applicable. Based on the experiments of Merchant, it is evident that this is not applicable in steady-state chip formation.

In this strain gradient theory two types of dislocations are proposed: geometrically necessary dislocations (ρ_g) that are responsible for work hardening and statistically stored dislocations (ρ_S) that are affected by a strain gradient. When $\rho_g >> \rho_S$ conventional plasticity pertains (strain rate unimportant) but when $\rho_g << \rho_S$ a constitutive equation including strain rate should be included.

The impression one obtains in reading Dinesh et al [39] is that the strain gradient approach is uniquely responsible for the size effect in cutting. In their concluding remarks it is suggested that it should be possible to verify the validity of the strain rate formulation by experiments designed to test predictions of this approach. This has not yet been done and until it is it will not be possible to determine whether the influence of strain rate is significant in the chip formation application. In any case, it is believed the explanation presented here based on the influence of defects and normal stress on the shear plane is sufficiently well supported by the experiments described that it should not be considered insignificant.

1.4 Nanomachining

Nanomachining can be classified into four categories:

- Deterministic mechanical nanometric machining. This method utilizes fixed and controlled tools, which can specify the profiles of three-dimensional components by a well-defined tool surface and path. The method can remove materials in amounts as small as tens of nanometers. It includes typically diamond turning, micro milling and nano/micro grinding, etc.;
- Loose abrasive nanometric machining. This method uses loose abrasive grits to removal a small amount materials. It consists of polishing, lapping and honing, etc.
- Non-mechanical nanometric machining. It comprises focused ion beam machining, micro-EDM, and excimer laser machining; and
- Lithographic method. It employs masks to specify the shape of the product. Two-dimensional shapes are the main outcome; severe limitations occur when three-dimensional products are attempted. It mainly includes X-ray lithography, LIGA, electron beam lithography.

Mechanical nanometric machining has more advantages than other methods since it is capable of machining complex 3D components in a controllable way. The machining of complex surface geometry is just one of the future trends in nanometric machining, which is driven by the integration of multiple functions in one product.

For instance, the method can be used to machine micro moulds and dies with complex geometric features and high dimensional and form accuracy, and even nanometric surface features. The method is indispensable to manufacturing complex micro and miniature structures, components and products in a variety of engineering materials. This chapter focuses on nanometric cutting theory, methods and its implementation and application perspectives [40-44].

1.4.1 Nanometric machining

Single-point diamond turning and ultraprecision grinding are two major nanometric machining approaches. They are both capable of producing extremely fine cuts. Single-point diamond turning has been widely used to machine nonferrous metals such as aluminum and copper. An undeformed chip thickness about 1 nm is observed in diamond turning of electroplated copper [45]. Diamond grinding is an important process for the machining of brittle materials such as glasses and ceramics to achieve nanometer levels of tolerances and surface finish. A repeatable optical quality surface roughness (surface finish < 10 nm Ra) has been obtained in nanogrinding of hard steel by Stephenson et al. using 76 μm grit cBN wheel on the ultra-precision grinding machine tool [46]. Recently, diamond fly-cutting and diamond milling have been developed for machining non-rotational non-symmetric geometry, which has enlarged the product spectrum of nanometric machining [47]. In addition the utilization of ultra-fine grain hard metal tools and diamond coated micro tools represents a promising alternative for microcutting of even hardened steel [48].

Early applications of nanometric machining are in the mass production of some high precision parts for microproducts, or microsystems. In fact, microproducts, or Microsystems, will be the first path that enables nanoproducts to enter the marketplace since microproducts, or microsystems, have been dominating nanotechnology application markets worldwide [49]. It also anticipates that microproducts will have more and more requirements around the world. It is very interesting to see that the IT peripheral market is still the biggest market of microproducts. In 2005, the total turnover of microproducts reached US $38 billion, which is two times that of the total turnover in 2000. Nanometric machining can be applied in bulk machining of silicon, aluminum substrates for computer memory disks, etc. In other areas such as biomedical, automotive, household, and telecommunication the total turnovers of microproducts are still steadily growing. Nanometric machining is also very promising in the production of sensors,

accelerometer, actuators, micro-mirror, fiber optics connectors, and micro-displays. In fact applications of nanoproducts will enhance the performance of microproducts in the form of sensitivity, selectivity, and stability [50]. In 2006, IT was lost this predominant position owing to new MEMS-based applications in sectors such as biotechnology and communication (optical and radio frequency switching for example will become a major growth area) [51]. Nanometric machining still has priority in this application area. The microproducts are normally integrated products of some electronics, mechanical parts and optical parts while in miniature or micro dimensions. In fact only small number of microproducts solely relies on electronics. The mechanical and optical parts are of significant importance for microproducts. The indispensable advantage of nanometric machining is its applicability to manufacture 3D complex components/devices including micro moulds, dies and embossing tooling for cheap mass production of optical and mechanical parts. Therefore, it is undoubtedly one of the major enabling technologies for commercialization of nanotechnology in the future.

1.4.2 Theoretical basis of nanomachining

Scientific study of nanometric machining has been been undertaken since late 1990s. Much attention to the study has been paid especially with the advance of nanotechnology [52]. The scientific study will result in the formation of the theoretical basis of nanometric machining, which enables the better understanding of nanometric machining physics and the development of its controllable techniques to meet the advanced requirements for nanotechnology and nanoscience.

1.4.2.1 Cutting force and energy

In nanomanufacturing, the cutting force and cutting energy are important issues. They are important physical parameters for understanding cutting phenomena as they clearly reflect the chip removal process. From the aspect of atomic structures cutting forces are the superposition of the interactions forces between workpiece

atoms and cutting tool atoms. Specific energy is an intensive quantity that characterizes the cutting resistance offered by a material [53]. Ikawa et al., and Luo et al. have acquired the cutting forces and cutting energy by Molecular Dynamics simulations [52-55]. Moriwaki and Lucca have carried out experiments to measure the cutting forces in nanometric machining [52]. Figure 1.7 shows the simulation and experimental results in nanometric cutting. Figure 1.7 (a) illustrates the linear relation exists between the cutting forces per width and depth of uncut in both simulations and experiments. The cutting forces per width increase with the increment of the depth of cut.

The difference in the cutting force between the simulations and the experiments is caused by the different cutting edge radii applied in the simulations. In nanometric machining the cutting edge radius plays an important role since the depth of cut is similar in scale. Under the same depth of cut higher cutting forces are needed for a tool with a large cutting edge radius compared with a tool with a small cutting edge radius. The low cutting force per width is obviously the result of fine cutting conditions, which will decrease the vibration of the cutting system and thus improve the machining stability and will also result in better surface roughness. A linear relationship between the specific energy and the depth of cut can also be observed in Fig. 1.7 (b). The figure shows that the specific energy increases with a decreasing of depth of cut, because the effective rake angle is different under different depths of cut. In small depths of cut the effective rake angle will increase with the decreasing of depth of cut. Large rake angle results in the increasing of specific energy. This phenomenon is often called the “size effect”, which can be clearly explained by material data listed in Table 1.2. According to Table 1.2, in nanometric machining only point defects exist in the machining zone in a crystal, so it will need more energy to initiate the atomic-crack or atomic-dislocation. The decreasing of depth of cut will decrease the chance for the cutting tool to meet point defects and result in the increasing of the specific cutting energy.

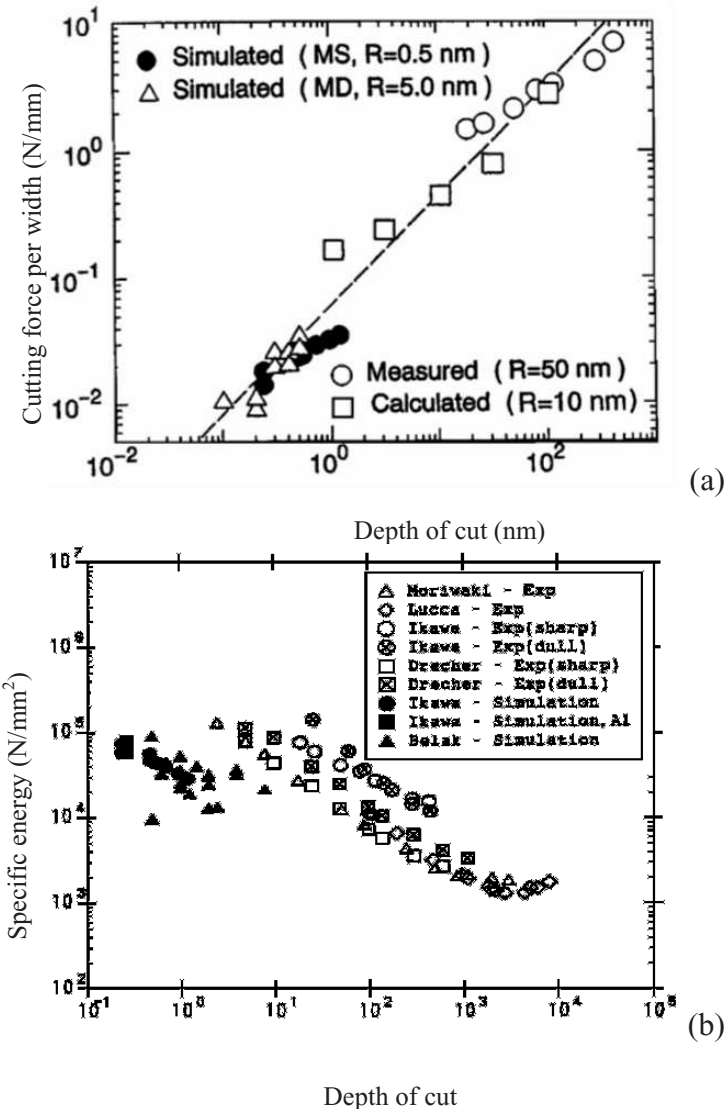

Figure 1.7. Comparison of results between simulations and experiments: (a) cutting force per width against depth of cut; (b) specific energy against depth of cut [52]

Table 1.2. Material properties under different machining units [56]

	1nm – 0.1 μm	**0.1 μm – 10 μm**	**10 μm – 1 mm**
Defects/Impurities	Point defect	Dislocation/crack	Crack/grain boundary
Chip removal unit	Atomic cluster	Sub-crystal	Multi-crystals
Brittle fracture limit	10^4 J/m^3 - 10^3 J/m^3 Atomic-crack	10^3 J/m^3 - 10^2 J/m^3 Micro-crack	10^2 J/m^3 - 10^1 J/m^3 Brittle crack
Shear failure limit	10^4 J/m^3 - 10^3 J/m^3 Atomic-dislocation	10^3 J/m^3 - 10^2 J/m^3 Dislocation slip	10^2 J/m^3 - 10^1 J/m^3 Shear deformation

If the machining unit is reduced to 1 nm, the workpiece material structure at the machining zone may approach atomic perfection, so more energy will be required to break the atomic bonds. On the other hand when machining unit is higher than 0.1 μm, the machining points will fall into the distribution distances of some defects such as dislocations, cracks, and grain boundaries. The pre-existing defects will ease the deformation of workpiece material and result in a comparatively low specific cutting energy. Nanometric cutting is also characterized by the high ratio of the normal to the tangential component in the cutting force [53, 55], as the depth of cut is very small in nanometric cutting, and the workpiece is mainly processed by the cutting edge. The compressive interactions will thus become dominant in the deformation of workpiece material, which will therefore result in the increase of friction force at the tool-chip interface and the relative high cutting ratio. Usually the cutting force in nanometric machining is very difficult to measure due to its small amplitude compared with the noise (mechanical or electronic) [52]. A pizeoelectric dynamometer or load cell is used to measure the cutting forces because of their high sensitivity and natural frequency [57].

1.4.2.2 Cutting temperatures

In molecular dynamics simulation, the cutting temperature can be calculated under the assumption that cutting energy totally transfers into cutting heat and results in the rising of cutting temperature and kinetic energy of system. The lattice vibration is the major form of thermal motion of atoms. Each atom has three degrees of freedom. According to theorem of equi-partition of energy, the average kinetic energy of the system can be expressed as:

$$\bar{E_k} = \frac{3}{2} N k_B T = \sum_i \frac{1}{2} m(V_i^2) \tag{1.14}$$

Where $\bar{E_k}$ is average kinetic energy in equilibrium state, K_B is Boltzmann's constant. T is temperature, m_i and V_i are the mass and velocity of an atom respectively, and N is the number of atoms. The cutting temperature can be deduced as:

$$T = \frac{2\bar{E_k}}{3Nk_B} \tag{1.15}$$

Figure 1.8 shows the variation of cutting temperature on the cutting tool in a molecular dynamics simulation of nanometric cutting of single crystal aluminum. The highest temperature is observed at cutting edge although the temperature at the flank face is also higher than that at the rake face. The temperature distribution suggests that a major heat source exists in the interface between cutting edge and workpiece and the heat is conducted from there to the rest of the cutting zone in workpiece and cutting tool. The reason is that because most cutting actions take place at the cutting edge of the tool, the dislocation deformations of workpiece materials will transfer potential energy into the kinetic energy and result in a rise in temperature. The comparative high temperature at the tool flank face is obviously caused by the friction between tool flank face and workpiece. The released energy due to the elastic recovery of the

machined surface also contributes to the increment of temperature at tool flank face. Although there is also friction between the tool rake face and the chip, the heat will be taken away from the tool rake face by the removal of the chip.

Therefore, the temperature at tool rake face is lower than that at the tool cutting edge and tool flank face. The temperature value shows that the cutting temperature in diamond machining is quite low in comparison with that in conventional cutting, due to low cutting energy as well as the high thermal conductivity of diamond and the workpiece material. The cutting temperature is considered to govern the wear of a diamond tool in a molecular dynamics simulation study by Cheng et al [58]. More in-depth experimental and theoretical studies are needed to find out the quantitative relationship between cutting temperature and tool wear although there is considerable evidence of chemical damage on diamond in which temperature plays a significant role [52].

1.4.2.3 Chip formation

Chip formation and surface generation can be simulated by molecular dynamics simulation. Figure 1.9 shows an MD simulation of a nanometric cutting process on single crystal aluminum. From Fig. 1.6(a) it is shown that after the initial plow of the cutting edge the workpiece atoms are compressed in the cutting zone near to the rake face and the cutting edge. The disturbed crystal lattices of the workpiece and even the initiation of dislocations can be observed in Fig. 1.9 (b). Figure 1.9 (c) shows the dislocations have piled up to form a chip. The chip is removed with the unit of an atomic cluster as shown in Fig. 1.9 (d). Lattice disturbed workpiece material is observed on the machined surface.

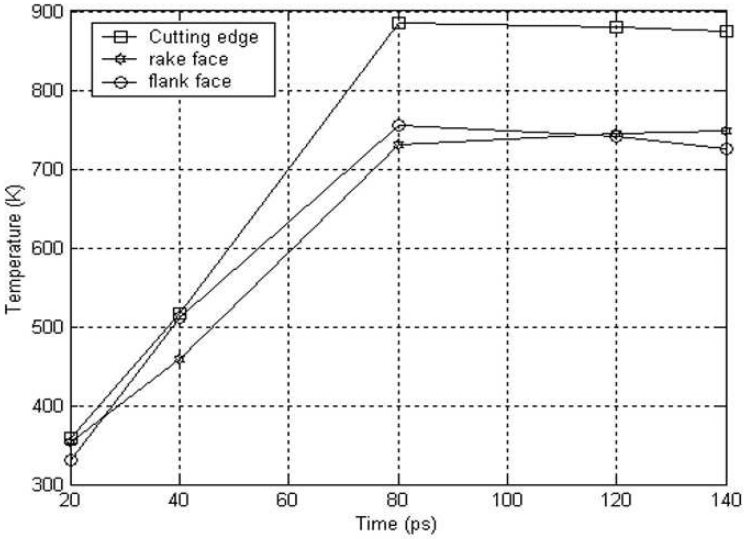

Figure 1.8. Cutting temperature distribution of cutting tool in nanometric cutting (cutting speed = 20 m/s, depth of cut = 1.5 nm, cutting edge radius = 1.57 nm) [58]

Based on the visualisation of the nanometric machining process, the mechanism of chip formation and surface generation in nanometric cutting can be explained. Owing to the plowing of the cutting edge, the attractive force between the workpiece atoms and the diamond tool atoms becomes repulsive. Because the cohesion energy of diamond atoms is much larger than that of Al atoms, the lattice of the workpiece is compressed. When the strain energy stored in the compressed lattice exceeds a specific level, the atoms begin to rearrange so as to release the strain energy. When the energy is not sufficient to perform the rearrangement, some dislocation activity is generated. Repulsive forces between compressed atoms in the upper layer and the atoms in the lower layer are increasing, so the upper atoms move along the cutting edge, and at the same time the repulsive forces from the tool atoms cause the resistance for the upward chip flow to press the atoms under the cutting line. With the movement of the cutting edge, some

dislocations move upward and disappear from the free surface as they approach the surface.

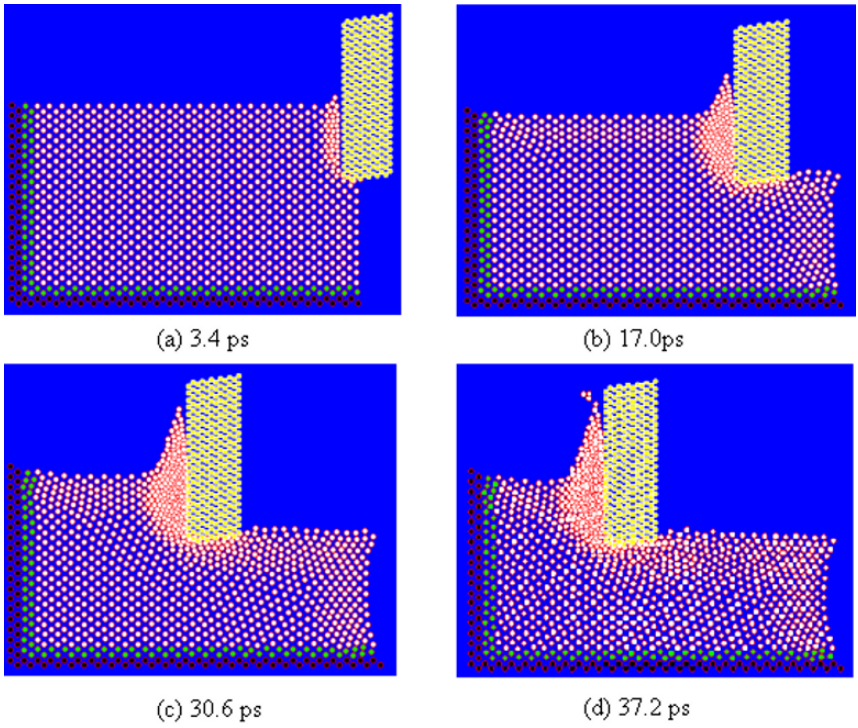

Figure 1.9. MD simulations of the nanometric machining process (Cutting speed =20 m/s, depth of cut = 1.4 nm, cutting edge radius = 0.35 nm) [58]

This phenomenon corresponds to the process of the chip formation. As a result of the successive generation and disappearance of dislocations, the chip seems to be removed steadily. After the passing of the tool, the pressure at the flank face is released. The layers of atoms move upwards and result in elastic recovery, so the machined surface is generated. The conclusion can therefore be drawn that the chip removal and machined surface generation are in nature the dislocation slip movement inside the workpiece material crystal grains. In conventional cutting the dislocations are initiated from the existing defects between the

crystal grains, which will ease the movement of dislocation and result in smaller specific cutting forces compared with that in nanometric cutting.

The height of the atoms on the surface layer of the machined surface create the surface roughness. For this, 2-D MD simulation R_a can be used to assess the machined surface roughness. The surface integrity parameters can also be calculated based on the simulation results. For example, the residual stress of the machined surface can be estimated by averaging the forces acting on the atoms in a unit area on the upper layer of the machined surface. Molecular dynamics (M.D.) simulation has been proved to be a useful tool for the theoretical study of nanometric machining [59]. At present the MD simulation studies on nanometric machining are limited by the computing memory size and speed of the computer. It is therefore difficult to enlarge the dimension of the current MD model on a personal computer. In fact, the machined surface topography is produced as a result of the copy of the tool profile on a workpiece surface that has a specific motion relative to the tool. The degree of the surface roughness is governed by both the controllability of machine tool motions (or relative motion between tool and workpiece) and the transfer characteristics (or the fidelity) of tool profile to workpiece [52]. A multi-scale analysis model, which can fully model the machine tool and cutting tool motion, environmental effects and the tool-workpiece interactions, is much needed to predict and control the nanometric machining process in a determinative manner.

1.4.2.4 Minimum undeformed chip thickness

Minimum undeformed chip thickness is an important issue in nanometric machining because it relates with the ultimate machining accuracy. In principle the minimum undeformed chip thickness will be determined by the minimum atomic distance within the workpiece. But in ultra-precision machining practices, it much depends on the sharpness of the diamond cutting tool, the capability of the ultra-precision machine tool and machining environment. The

diamond turning experiments of non-ferrous work materials carried out at LLNL show the minimum undeformed chip thickness, down to 1 nm, is attainable with a specially prepared fine diamond cutting tool on a highly reliable ultra-precision machine tool [45]. Based on the tool wear simulation, the minimum undeformed chip thickness is further studied in this chapter. Figure 1.10 illustrates chip formation of single crystal aluminum with the tool cutting edge radius of 1.57 nm. No chip formation is observed when the undeformed chip thickness is 0.25 nm. But the initial stage of chip formation is apparent when the undeformed chip thickness is at 0.26 nm. In nanometric cutting, as the depth of cut is very small, the chip formation is related to the force conditions on the cutting edge. Generally, chip formation is mainly a function of tangential cutting force.

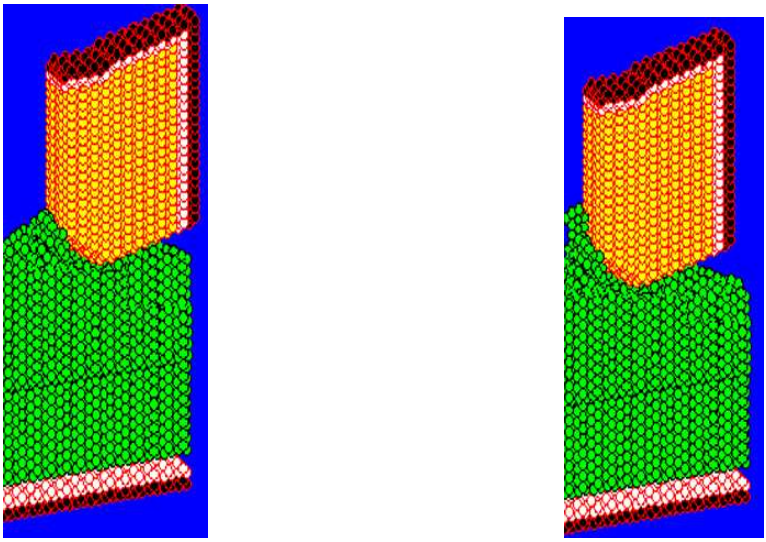

(a)Undeformed chip thickness = 0.25nm (b)Undeformed chip thickness = 0.26 nm

Figure 1.10. Study of minimum undeformed chip thickness by MD simulation [58]

The normal cutting force makes little contribution to the chip formation since it has the tendency to penetrate the atoms of the surface into the bulk of the workpiece. The chip is formed on condition that the tangential cutting force is larger than the normal cutting force in theory. The relationships between the minimum undeformed chip thickness, cutting edge radius, and cutting forces are studied via MD simulations. The results are highlighted in Table 1.3. The data show that the minimum undeformed chip thickness is about 1/3 to 1/6 of the tool cutting edge radius. The chip formation will be initiated when the ratio of tangential cutting force to normal cutting force is larger than 0.92.

1.4.2.5 Critical cutting radius

It is widely accepted that the sharpness of the cutting edge of a diamond cutting tool directly affects the machined surface quality. Previous MD simulations show that the sharper the cutting edge is, the smoother the machined surface becomes. But this conclusion is based on no tool wear. To study the real effects of cutting edge radius, the MD simulations on nanometric cutting of single crystal aluminum are carried out using a tool wear model [59]. In the simulations the cutting edge radius of the diamond cutting tool varies from 1.57 nm to 3.14 nm with depth of cut of 1.5 nm, 2.2 nm and 3.1 nm respectively. The cutting distance is fixed at 6 nm. The root-mean–square deviation of the machined surface and mean stress on the cutting edge are listed in Table 1.4. Figure 1.11 shows the visualization of the simulated data, which clearly indicates that surface roughness increases with the decreasing cutting edge radius when the cutting edge radius is smaller than 2.31 nm. The tendency is obviously caused by the rapid tool wear when a cutting tool with small cutting edge radius is used. But when the cutting edge is larger than 2.31 nm, the cutting edge is under compressive stress and no tool wear happens. Therefore, it shows the same tendency that the surface roughness increases with decreasing the tool cutting edge radius as in the previous MD simulations.

Table 1.3. Minimum undeformed chip thickness against the tool cutting edge radius and cutting forces [58]

Cutting edge radius (nm)	**1.57**	**1.89**	**2.31**	**2.51**	**2.83**	**3.14**
Minimum undeformed chip thickness (nm)	0.26	0.33	0.42	0.52	0.73	0.97
Ratio of minimum undeformed chip thickness to tool cutting edge radius	0.17	0.175	0.191	0.207	0.258	0.309
Ratio of tangential cutting force to normal cutting force	0.92	0.93	0.92	0.92	0.94	0.93

The MD simulation results also illustrate that it is not true that the sharper the cutting edge, the better the machined surface quality. The cutting edge is destined to wear and results in the degradation of the machined surface quality if its radius is smaller than a critical value. But when the cutting edge radius is higher than the critical value, the compressive stress will take place at the tool edge and the tool condition is more stable. As a result a high quality machined surface can be achieved. Therefore, there is a critical cutting edge radius for stably achieving high-quality machined surfaces. For cutting single crystal aluminum the critical cutting edge radius is at 2.31 nm. The MD simulation approach is applicable for acquiring the critical cutting edge radius for nanometric cutting of other materials.

1.4.2.6 Workpiece materials

In nanometric machining the microstructure of the workpiece material will play an important role in affecting the machining accuracy and machined surface quality. For example, when machining polycrystalline materials, the difference in the elastic coefficients at the grain boundary and interior of the grain causes small steps formed on the cut surface since the respective elastic "rebound" varies [60].

Table 1.4. The relationship between cutting edge radius and machined surface quality [58]

	Cutting edge radius (nm)	**1.57**	**1.89**	**2.31**	**2.51**	**2.83**	**3.14**
Depth of cut: 1.5 nm	S_q (nm)	0.89	0.92	0.78	0.86	0.98	1.06
Depth of cut: 2.2 nm	S_q (nm)	0.95	0.91	0.77	0.88	0.96	1.07
Depth of cut: 3.1 nm	S_q (nm)	0.97	0.93	0.79	0.87	0.99	1.08
Mean stress at cutting edge (GPa)		0.91	0.92	-0.24	-0.31	-0.38	-0.44

The study by Lee and Chueng shows the shear angle varies with the crystallographic orientation of the materials being cut. This will produce a self-excited vibration between cutting tool and workpiece and result in a local variation of surface roughness of a diamond turned surface [61].

A material's destructive behavior can also be affected by nanometric machining. In nanometric machining of brittle materials it is possible to produce plastically deformed chips, if the depth of cut is sufficiently small [62]. It has been shown that a "brittle-to-ductile" transition exists when cutting brittle materials at low load and penetration levels [63]. The transition from ductile to brittle fracture has been widely reported and is usually described as the "critical depth of cut" [62], i.e. generally small up to 0.1 to 0.3 μm. They will result in relatively slow material removal rates [62].

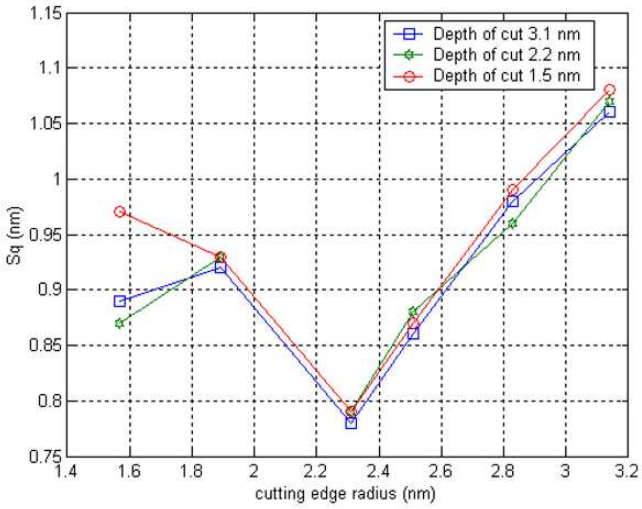

Figure 1.11. Cutting edge radius against machined surface quality [58]

However, it is a cost-effective technique for producing high quality spherical and non-spherical optical surfaces, with or without the need for lapping and polishing [62]. The workpiece materials should also have a low affinity with the cutting tool material. If bits of the workpiece material are deposited onto the tool, this will cause tool wear and adversely affect the finished surface (surface finish and surface integrity). Therefore, workpiece materials chosen must process an acceptable machinability on which nanometric surface finish can thus be achieved. Diamond tools are widely used in nanometric machining because of their excellent characteristics. The materials currently turned with diamond tools are listed in Table 1.5. The materials that can be processed via ductile mode grinding with diamond wheels are listed in Table 1.6.

Table 1.5. Current diamond turned materials [62]

Semiconductors	Metals	Plastics
Cadmium telluride	Aluminum and alloys	Acrylic
Gallium arsenide	Copper and alloys	Fluoroplastics
Germanium	Electroless nickel	Nylon
Lithium niobate	Gold	Polycarbonate
Silicon	Magnesium	Polymethylmethacrylate
Zinc selenide	Silver	Propylene
Zinc sulfide	Zinc	Styrene

Table 1.6. Materials that can be processed via ductile mode diamond grinding [62]

Ceramics/intermetallics		Glasses
Aluminium oxide	Tatanium aluminide	BK7 or equivalent
Nickel aluminide	Tatanium carbide	SF10 or equivalent
Silicon carbide	Tungsten carbide	ULE or equivalent
Silicon nitride	Zirconia	Zerodur or equivalent

1.4.3 Comparison of nanometric machining and conventional machining

Table 1.7 summarizes the comparison of nanometric machining and conventional machining in all major aspects of cutting mechanics and physics.

Table 1.7. The comparison of nanometric machining with conventional machining [55]

		Nanometric machining	**Conventional machining**
Fundamental cutting principles		Discrete molecular mechanics/micromechanics	Continuum elastic/plastic /fracture mechanics
Workpiece material		Heterogeneous (presence of microstructure)	Homogeneous (ideal element)
Cutting physics		Atomic cluster or microelement model $\dot{q}_i = \frac{\partial H}{\partial p_i}$ i=1, 2, … N $p_i = -\frac{\partial H}{\partial q_i}$	Shear plane model (continuous points in material)
		First principal stress $\sigma = \frac{1}{S}\sum_{i=1}^{N_A}\sum_{j=1}^{N_B} f_{ij} - \frac{1}{S}\sum_{i=1}^{N_A}\sum_{j=1}^{N_B} f_{0ij}$ (crystal deformation included)	Cauchy stress principle $\tau_s = \frac{F_s}{A}$ (constant)
Cutting force and energy	Energy consideration	Interatomic potential functional $U(r^N) = \sum_i \sum_{<i} u(r_{ij})$	Shear/friction power $P_s = F_s \cdot V_s$ $P_u = F_u \cdot V_c$
	Specific energy	High	Low
	Cutting force	Interatomic forces $F_I = \sum_{j \neq i}^{N} F_{ij} = \sum_{j \neq i}^{N} -\frac{du(r_{ij})}{dr_{ij}}$	Plastic deformation/friction $F_c = F(b, d_c, \tau_s, \beta_a, \phi_c, \alpha_r)$
Chip formation	Chip initiation	Inner crystal deformation (point defects or dislocation)	Inter crystal deformation (grain boundary void)
	Deformation and stress	Discontinuous	Continuous
Cutting tool	Cutting edge radius	Significant	Ignored
	Tool wear	Clearance face and Cutting edge	Rake face

The comparison highlighted in the table is by no means comprehensive, but rather provides a starting point for further study on the physics of nanometric machining.

Acknowledgements

The chapter contributors wish to thank Inderscience publishers for granting permissions to reproduce work presented in this chapter.

References

[1] Backer WR, Marshall ER, and Shaw MC, 1952, Trans. ASME, **74**, p.61
[2] Taniguchi N, 1994, Precision Engineering, **16**, 5-24.
[3] Shaw MC, 1952, J. Franklin Inst., **254**, 2, 109.
[4] Heidenreich RO, Shockley W, 1948, Report on Strength of Solids, Phys. Soc. of London, 57.
[5] Ernst HJ, Merchant ME, 1941, Trans. Am. Soc. for Metals, **29**, 299.
[6] Merchant ME, 1945, J. Appl. Phys., **16**, 267-275.
[7] Piispanen V, 1937, Teknillinen Aikakaushehti (Finland), **27**, 315.
[8] Merchant ME, 1950, Machining Theory and Practice, Am Soc. for Metals, 5-44.
[9] Merchant ME, 1945, J. Appl. Phys., **16**, 318-324.
[10]Barrett CS, 1943, Structure of Metals, McGraw Hill Co., NY, 295.
[11]Bridgman PW, 1952, Studies in Large Plastic Flow and Fracture, McGraw Hill Co., NY.
[12]Langford G, Cohen M, 1969, Trans. ASM, **62**, 623.
[13]V. Piispanen, 1948, J. Appl. Phys., **19**, p.876.
[14]Blazynski TZ, Cole J M, 1960, Proc. Instn. of Mech. Engrs., **1**, 74, 757.
[15]Shaw MC, 1950, J. AppI. Phys., **21**, 599.
[16]Walker TJ, 1967, PhD Dissertation, Carnegie-Mellon University, PA.
[17]Walker TJ, Shaw M C, 1969, Advances in Machine Tool Design and Research, Pergamon Press, 241-252.
[18]Usui E, Gujral A, Shaw MC 1960, Int. J. Mach Tools and Res., **1**, 187-197.
[19]Vyas A, Shaw MC, 1999, Trans. ASME-J. Mech. Sc., **21**, 1, 63-72.
[20]Eugene F, 1952, Annals of CIRP, **52**, 11, 13-17.
[21]Shaw MC, 1980, Int. Jour. Mech. Sc., **22**, 673-686.
[22] Kwon KB, Cho DW, Lee SJ, Chu CN, 1999, Annals of CIRP, **47**/1, 43-46.
[23]Eyring H, Ree T, and Harai N, 1958, Proc. Nat. Acad. Scs., **44**, 683.
[24] Eyring H, Ree T, 1961, Proc. Nat. Acad. Scs., **47**, 526-537.
[25] Eyring H, Jhon MS, 1969, Significant Theory of Liquids, J. Wiley and Sons, NY.
[26]Kececioglu D, 1958, Trans. ASME, **80**, 149-168.

[27]Kececioglu D, 1958, Trans. ASME, **80**, 541-546.
[28]Kececioglu D, 1960, Trans. ASME-J. Eng for Industry, **82**, 79-86.
[29]Anderson TL, 1991, Fracture Mechanics, CRC Press, Florida.
[30]Zhang B, Bagchi A, 1994, Trans. ASME- J. of Eng for Industry, **116**, 289.
[31]Argon AS, Im J, Safoglu R, 1975, Metallurgical Transactions, **6A**, 825.
[32]Komanduri R, Brown RH, 1967, Metals and Materials, **95**, 308.
[33]Drucker DC, 1949, J. Appl. Phys., **20**, 1.
[34]Fleck NA, Muller GM, Ashby M F, Hutchinson J M, 1994, Acta Metallurgica et Materialia, **41**, 10, 2855.
[35]Stelmashenko NA, Walls M G, Brown L M, Milman Y V, 1993, Acta. Metallurgica et Materialia, **41**, 10:, 2855.
[36]Ma Q, Clarke D R, 1995, J. Materials Research, **46**, 3, 477.
[37]Nix WD, Gao H, 1998, J. Mech. and Physics of Solids, **1**, 4, 853.
[38] Gao H, Huang Y, Nix W D, Hutchinson J W, 1999, Jour. of Mechanics and Physics of Solids, **47**, 1239.
[39] Dinesh D, Swaminathan S, Chandrasekar S, and Farris T N, 2001, Proc ASME-IMECE, NY: 1-8.
[40]Committee on Technology National Science and Technology Council, "National Nanotechnology initiative: Leading to the next industrial revolution, Washington D. C. 2000.
[41] Snowdon K, McNeil C, Lakey J., Nanotechnology for MEMS components. mstNews 2001; **3**, 9-10.
[42] EI-Fatatry A, Correial A., Nanotechnology in Microsystems: potential influence for transmission systems and related applications., mstNews 2003; **3**: 25-26.
[43] Werner M, Köhler T, Grünwald W., Nanotechnology for applications in microsystems. mstNews 2001; **3**: 4-7.
[44] El-Hofy H, Khairy A, Masuzawa T, McGeough J., Introduction. In: McGeough J eds. Micromachining of Engineering Materials. New York: Marcel Dekker, 2002.
[45] Donaldson R, Syn C, Taylor J, Ikawa N, Shimada S., Minimum thickness of cut in diamond turning of electroplated copper. UCRL-97606 1987.
[46] Stephenson DJ, Veselovac D, Manley S, Corbett J., Ultra-precision grinding of hard steels. Precision Engineering 2001; **15**: 336-345.
[47] Rübenach O., Micro technology – applications and trends. Euspen online traininglecture.http://www.euspen.org/training/lectures/course2free2view/02MicroTechApps/demolecture.asp (accessed July 2008).
[48] Diamond milling processes for the generation of complex optical mold inserts. http://www.lfm.uni-bremen.de/html/res/res001/res108.html (accessed July 2008).
[49] Weck M., Ultraprecision machining of microcomponents. Machine Tools 2000; 113-122.
[50] Andreas Schütze, Lutz-Günter John., Nano sensors and micro integration. mstNews 2003; **3**: 43-45.

[51] Ayman EI-Fatatry, Antonio Correial., Nanotechnology in Microsystems: potential influence for transmission systems and related applications. mstNews 2003; **3**: 25.
[52] Ikawa N, Donaldson R, Komanduri R, König W, Mckeown PA, Moriwaki T, Stowers I., Ultraprecision metal cutting – the past, the present and the future. Annals of the CIRP 1991; **40**(2): 587-594.
[53] Shaw MC., Principles of Abrasive Processing. New York: Oxford University Press, 1996.
[54] Komanduri R, Chandrasekaran, Raff L., Effects of tool geometry in nanometric cutting: a molecular dynamics simulation approach. Wear 1998; **219**: 84-97.
[55] Luo X. Cheng K, Guo X, Holt R., An investigation on the mechanics of nanometric cutting and the development of its test-bed. International Journal of Production Research 2003; **41** (7): 1449-1465.
[56] Taniguchi N., Nanotechnology. New York: Oxford University Press, 1996.
[57] Dow T, Miller E, Garrard K., Tool force and deflection compensation for small milling tools. Precision Engineering 2004; **28** (1): 31-45.
[58] Cheng K, Luo X, Ward R, Holt R., Modelling and simulation of the tool wear in nanometric cutting. Wear 2003; **255**: 1427-1432.
[59] Shimada S., Molecular dynamics simulation of the atomic processes in microcutting. In McGeough J, eds. Micromachining of Engineering Materials. New York: Marcel Dekker, 2002: 63-84.
[60] Nakazawa H., Principles of Precision Engineering. New York: Oxford University Press, 1994.
[61] Lee W, Cheung C. A , dynamic surface topography model for the prediction of nano-surface generation in ultra-precision machining. International Journal of Mechanical Sciences 2001; **43**: 961-991.
[62] Corbett J,. Diamond Micromachining. In McGeough J, eds. Micromachining of Engineering Materials. New York: Marcel Dekker, 2002: 125-146.

Chapter 2

Machining Stability

H. H. Zhang, J. Ni and M. J. Jackson

2.1 Introduction

Since the early days of regenerative chatter theory, it has been noticed that the phase difference between the current and the previous passes of machining self-excited vibration is correlated closely to the machining stability. However, an analytical proof of this fact has not been investigated, especially based on a non-linear machining chatter models. In this chapter, an approach for determining the machining stability is presented in terms of the phase difference. The machining stability is demonstrated by a stability criterion in term of the phase difference sensitivity. By investigating the stability of the approximate solution of a non-linear delay differential equation as the machining chatter model under small perturbations about an equilibrium state, the stability criterion is established. Through this approach, a theoretical proof of the relationship between the machining stability and the phase difference is given in terms of internal energy of the machining process. The analysis is in agreement with the numerical simulations and experimental data. Once the parameters of the machining system are identified, the stability criterion can be employed to predict the onset of machining chatter. The stability criterion identified for specific machining operations is of critical importance especially when using nanostructured coated cutting tools in turning and milling operations. It is a well-known fact that the phase difference between the vibration x(t) in the current pass and the vibration x(t-T) in the previous pass determines the machining stability [1-3]. When the phase difference is within 0 to 180 degrees, the machining system is stable, and no regenerative

chatter is observed, while when the phase difference is within 180 to 360 degrees, the machining system is unstable, and regenerative chatter occurs, and the rotating direction of the chatter marks is seen as a right-hand spiral pattern on the workpiece. However, the analytical proof of this phenomenon has not been investigated, especially for the case when the machining chatter is modeled with non-linearities. The study of phase difference and its sensitivity will provide a meaningful approach for machining chatter control: once the parameters of the machining system are identified, the stability criterion based on the phase difference and its sensitivity analysis can be employed to predict the onset of machining chatter. Chatter onset control is even more essential than before when high precision manufacturing becomes the common task, and the flexible, frequently changing working conditions increase the possibility of unstable machining [4].

The machining chatter with finite amplitude involves certain non-linearities [5,6]. The dynamic machining system can be described as the interaction between the elastic structure of the machine tool and the cutting process. In normal machining processes, the elastic structure has only very slight non-linearity, mainly the non-linearities lie in the cutting force. In this chapter, an analysis is based on a well accepted non-linear machining chatter model, which is a non-linear delay differential equation. [7,8] It is difficult to analytically find the exact solution of this equation. Although the solution can be provided by employing numerical integration algorithms and the step method [9], this procedure is only able to show the response of the non-linear machining system to a particular set of initial values and initial function values with a certain set of parameter values. Therefore, the analytical relationship between the phase difference and the machining stability cannot be revealed this way. In order to characterize the relationship, an equivalent linearization technique is employed. Equivalent linearization techniques, which is originally used in ordinary differential equations, is shown to be valid in delay differential equations (called as “difference-differential equations” in early literaries) as well. [10,11] The procedure of the equivalent linearization is to replace the system non-linearity with a linear gain,

which is not constant, but rather a function of the amplitude and frequency of the system oscillation, and which renders the similar system responses to the same sinusoidal input. Based on the equivalent linearization of the non-linear delay differential equation, sensitivity analysis of the phase difference can give a possible way to investigate the relative stability of the self-excited vibration that will provide a theoretical proof of the relationship between the phase difference and the machining stability. As an application, the phase difference sensitivity analysis can be used to interpret the mechanism of the spindle speed variation (SSV) method, which is receiving increasing attention for machining chatter suppression [12-25].

This chapter is organized in four sections. The physical interpretation how the phase difference is related to the machining stability is presented in Section 2. In section 3, the non-linear chatter model with single regenerative effect is introduced, then it is equivalently linearized, the sensitivity analysis of the phase difference is presented, the machining stability is studied based on the information of the phase difference sensitivity, and a stability criterion with the phase difference sensitivity is derived. Section 4 is verification of the stability criterion according to the internal energy calculations. The theoretical results are validated by numerical simulations. A set of the experimental data is also employed to support the stability analysis. The detailed derivation of the stability criterion is given in the Appendix at the end of this chapter.

2.2 Phase Difference and Machining Stability: A Physical Interpretation

During the cutting process, the cutting tool might deviate from its steady motion due to some random disturbances, thus it vibrates relative to the workpiece at that moment. This vibration results in fluctuations in the dynamic cutting force, which drives the cutting tool continuously to oscillate in the cutting passes. If the amplitude of the relative vibration keeps increasing until its vibration

amplitude is limited by the system non-linearities, the machining system is unstable. Otherwise, the machining system is stable. Figure 2.1 displays the thrust component of the cutting force and the relative vibration between the cutting tool and the workpiece surface in the cutting passes. A phase difference angle between the current pass and the previous one is observed. The phase difference angle is the factor that determines whether or not the relative vibration is greater than before, that is, the phase difference determines the machining stability [25].

As is known, the relative vibration is supported by the energy supplied in the cutting process. In a cycle of the relative vibration, when the cutting tool oscillates into the workpiece, the dynamic cutting force is doing positive work, while when the cutting tool oscillates out, the dynamic cutting force is doing negative work (see Figures 2.1 and 2.2). The net work in a cycle of vibration is the sum of the two works. If the net work is positive, the dynamic cutting force injects energy to the vibration system, and the relative vibration becomes larger, thus the machining system is unstable. If the net work is negative, the dynamic cutting force dissipates energy from the vibration system, and the relative vibration decreases, thus the machining system is stable. The value of the net work in a cycle of vibration is determined by the phase difference in the cutting passes.

Figure 2.2 demonstrates several typical cases of the cutting process when the phase difference angle equals to 0, 90, 180, 270 degrees, respectively. The removed area of the workpiece is proportional to the work done by the dynamic cutting force when the cutting tool vibrates in or out the workpiece. For the case shown in Figure 2.2(a), the positive work equals the negative work, so the net work is zero in the vibration cycle, thus the machining system is stable. For the case in Figure 2.2(b), the phase difference is 90 degrees, and the positive work is smaller than the negative work, the net work is negative, that is, the dynamic cutting force is dissipating energy from the system, thus the machining system is stable. When the phase difference is 180 degrees (see Figure 2.2(c)), due to symmetry of the areas when the tool vibrates in and out, no work is

supplied to the machining system. The case of Figure 2.2(d) is the opposite of the Figure 2.2(b), the positive net work done by the dynamic cutting force in a cycle of vibration is injected to the vibration system, and results in a unstable cutting process. In general, it is believed that, when the phase difference varies within 0 to 180 degrees, the machining system is stable, while when the phase difference varies within 180 to 360 degrees, the machining system is unstable.

This is only a physical interpretation. Can we give a theoretical proof on this relationship between the machining stability and the phase difference? Is this relationship still true when the non-linearities are included in the machining system? In the following sections, the analytical relationship between the phase difference and the machining stability is revealed.

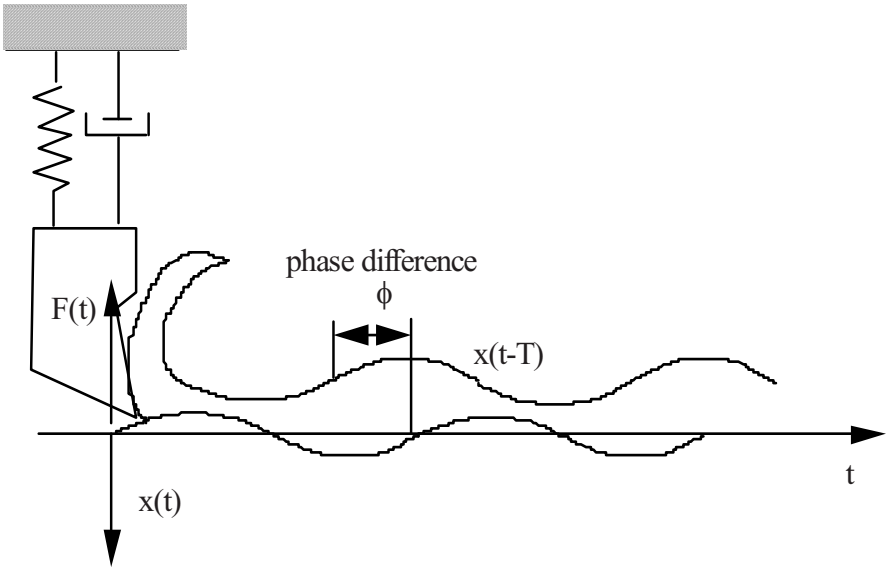

Figure 2.1. Phase difference in the cutting process

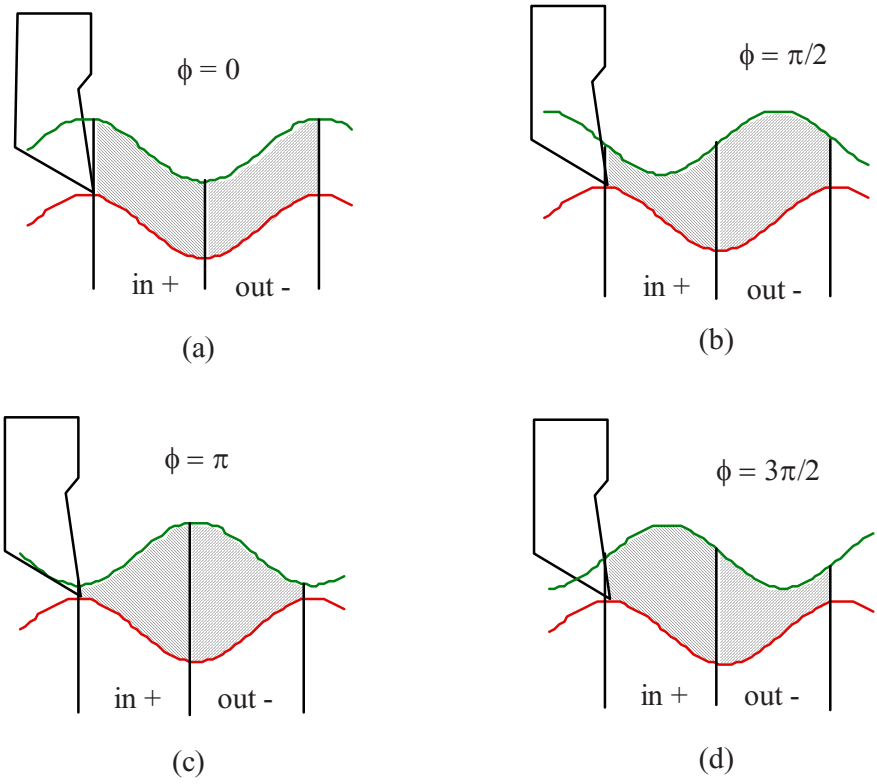

Figure 2.2. Phase difference and net work in a vibration cycle

2.3 Sensitivity Analysis of the Phase Difference of Machining Chatter

In general, there are two main non-linearities in the cutting process, i.e., (1) "the tool leaving the cut" partially in a cycle of vibration when the amplitude of chatter is large enough, and (2) the non-linear relationship between the cutting force and the chip thickness. Single regenerative effect is considered in the following machining chatter model. The single regenerative effect, of course, occurs in the situation of small vibration amplitude, that is, the cutting tool is always in the workpiece during the cutting process, if

$$A < \frac{s_o}{2\sin(\frac{\omega T}{2})} \tag{2.1}$$

Where, A is the chatter amplitude, s_o is the uncut chip thickness, ω is the chatter frequency, and time delay T = 60/N, N is the spindle speed in rpm. But the single regenerative effect could be valid for a special situation of "the tool leaving the cut" as well. In fact the tool leaving the cut does not neccesarily lead to multiple-regenerative effects. It can be proved that, although "the tool leaving the cut" occurs, only single regenerative effect is involved, if

$$\left|\frac{s_o}{2\sin(\frac{\omega T}{2})}\right| < A < \left|\frac{s_o}{\sin(\omega T)}\right| \tag{2.2}$$

The machining system can be described by a nonlinear delay differential equation (NLDDE) with single regenerative effect as follows:

$$\ddot{x}(t) + 2\zeta\omega_n\dot{x}(t) + \omega_n^2 x(t) = -\frac{\omega_n^2}{k}\Delta F(t)\cos\alpha \tag{2.3}$$

$$\Delta F(t) = PW\left\{s^Y(t) - s_o^Y + Ys_o^{Y-1}C\frac{\dot{x}(t)}{N}\right\} \tag{2.4}$$

$$s(t) = x(t) - x(t-T) + s_o, \quad if \quad s(t) > 0;$$
$$else \quad s(t) = 0 \tag{2.5}$$

Under the machining condition of slender shaft turning, the stiffness, k, of the machine tool structure, is mainly contributed by the workpiece stiffness at the cutting point. In Equation (2.4), the first two terms represent the dynamic variation of the cutting force, and the third term is the penetration force. Two constants P and Y are the

cutting force constants. Besides, when "the tool leaving the cut" occurs, the third term equals to zero because there is no metal cutting at this moment. In this equation, since the nose radius of the cutting tool is small in relation to the depth of cut, the depth of cut is assumed as a linear factor in the dynamic cutting force. In this whole study, we focus on studying the non-linearity in chip thickness. Equation (2.5) expresses the instantaneous chip thickness. When the chatter amplitude exceeds a critical value, the tool leaves the workpiece material during part of the chatter cycle. The vibration $x(t -T) - s_o$ in the previous pass has a phase difference with the present one. That makes the instantaneous chip thickness change with time (see Figure 2.2). The uncut chip thickness $s_o = f \sin\kappa$, where f is the feed rate. This model has been verified by experiments and numerical simulation being a valid approach to the real machining process [24,25].

The relative changes in amplitude and frequency of x(t) over one period of the oscillation are assumed small. This is resonable for both chatter onset and fully developed chatter, which are usually a slowly changing process with respect of the requirements for the describing function techniques. According to the modified Krylov-Bogoliubov approach and the equivalently linearization, the real and imaginary parts of the characteristic equation of the NLDDE in steady state case are given as follows:

$$R = -\omega^2 + \omega_n^2 + a_2 - a_2\cos\phi + 3.77\frac{A}{\pi}a_3(1-\cos\phi) + \frac{3}{2}a_4A^2(1-\cos\phi)^2 = 0 \quad (2.6)$$

$$I = a_1\omega + a_2\sin\phi + 3.77\frac{A}{\pi}a_3\sin\phi + \frac{3}{2}a_4A^2\sin\phi(1-\cos\phi) = 0 \quad (2.7)$$

Where,

$$a_1 = 2\varsigma\omega_n + \frac{\omega_n^2}{k} PWYs_o^{Y-1} \frac{C}{N} \cos\alpha$$

$$a_2 = \frac{\omega_n^2}{k} PWYs_o^{Y-1} \cos\alpha$$

$$a_3 = \frac{1}{2}\frac{\omega_n^2}{k} PWY(Y-1)s_o^{Y-2} \cos\alpha$$

$$a_4 = \frac{1}{6}\frac{\omega_n^2}{k} PWY(Y-1)(Y-2)s_o^{Y-3} \cos\alpha$$

$$\phi = \omega T$$

In the above equations, there are three variables chatter amplitude A, chatter frequency ω and the phase difference ϕ. Usually, the functions A(t) and ω(t) can hardly be obtained. Noticing the phase difference $\phi = \omega T$, if the analysis is directed towards determination of the functions $A^2(\phi)$ and ω(ϕ), the steady state response of the nonlinear machining system may be appropriately characterized from Equations (2.6) – (2.7) with respect to the phase difference. Since these equations are nonlinear about the chatter frequency ω, the frequency ω_j and the amplitude A_j can be iteratively updated with respect to the instantaneous phase difference ϕ_j and ω_{j-1} at the j-th time interval.

For the steady state self-excited vibration, the most important features are the amplitude A and the frequency ω of the equilibrium limit cycle state. The stability of the limit cycle can be determined by investigating the system behavior to small disturbances on the amplitude and the frequency of the equilibrium limit cycle state. In order to build the relationship between the phase difference sensitivity and the stability, the proposed sensitivity analysis relates to the differential changes in phase difference ϕ and frequency ω caused by differential changes in the amplitude A, that is,

$$S^{\phi} = \frac{\partial \phi}{\partial A}$$
$$S^{\omega} = \frac{\partial \omega}{\partial A} \tag{2.8}$$

The equations are defined as the phase difference sensitivity and the frequency sensitivity, respectively.

Differentiating Equations (2.6) – (2.7) with respect to the chatter amplitude A, and deriving the close formed expressions of the above sensitivities S^{ϕ} and S^{ω} lead to,

$$\frac{\partial R}{\partial \omega} S^{\omega} + \frac{\partial R}{\partial \phi} S^{\phi} + \frac{\partial R}{\partial A} = 0 \tag{2.9}$$

$$\frac{\partial I}{\partial \omega} S^{\omega} + \frac{\partial I}{\partial \phi} S^{\phi} + \frac{\partial I}{\partial A} = 0 \tag{2.10}$$

Or,

$$\begin{pmatrix} S^{\omega} \\ S^{\phi} \end{pmatrix} = -\begin{pmatrix} \frac{\partial R}{\partial \omega} & \frac{\partial R}{\partial \phi} \\ \frac{\partial I}{\partial \omega} & \frac{\partial I}{\partial \phi} \end{pmatrix}^{-1} \begin{pmatrix} \frac{\partial R}{\partial A} \\ \frac{\partial I}{\partial A} \end{pmatrix} \tag{2.11}$$

Where,

$$\frac{\partial R}{\partial \omega} = -2\omega$$

$$\frac{\partial R}{\partial \phi} = a_2 \sin\phi + 3.77 \frac{A}{\pi} a_3 \sin\phi + 3a_4 A^2 \sin\phi(1 - \cos\phi)$$

$$\frac{\partial R}{\partial A} = 3a_4 A (1 - \cos\phi)^2$$

$$\frac{\partial \mathrm{I}}{\partial \omega} = \mathrm{a}_1$$

$$\frac{\partial I}{\partial \phi} = a_2 \cos\phi + 3.77\frac{A}{\pi} a_3 \cos\phi + \frac{3}{2} a_4 A^2 [\cos\phi(1-\cos\phi) + \sin^2\phi]$$

$$\frac{\partial I}{\partial A} = 3a_4 A \sin\phi(1-\cos\phi)$$

The closed form expressions of the phase difference sensitivity and the frequency sensitivity can be obtained from Equation (2.11). The value of the phase difference sensitivity is related to the stability of the solution. This relationship is revealed in the following section.

Between the machining system and the periodic solution of the nonlinear delay differential equation (NLDDE) there is an interesting duality, that is, no chatter in the machining system corresponds to the stable trivial solution of the NLDDE, and the onset of chatter is the case of the unstable trivial solution of the NLDDE, and the fully developed chatter with a finite amplitude is the steady state non-trivial solution of the NLDDE. The stability of the trivial solution of the NLDDE is more interesting to us. As has been well known, the phase difference ϕ is a parameter that is related to the stability of the trivial solution of the NLDDE. There is a bifurcation value ϕ^* of the phase difference ϕ (0 ~ 360 degrees). If the phase difference ϕ is sufficiently small ($\phi < \phi^*$), the stable trivial solution is obtained. If ϕ increases up to the bifurcation values $\phi = \phi^*$, the system is just on the threshold of instability. For $\phi > \phi^*$, the self-excited vibration appears. Due to the nonlinear relationship of the machining cutting force, it is easier using the sensitivities to determine the relative stability of the machining system.

For steady state case, stability of the limit cycle is determined in terms of the behavior of the system under small perturbations of the limit cycle state, i.e., under small perturbations of the amplitude and/or frequency of the limit cycle. If the limit cycle returns to its original equilibrium state after the perturbations, the system is

considered *stable*, while if either its amplitude or frequency determinedly deviates from the original equilibrium state until another equilibrium state is reached, it is *unstable*. Then, from the variational relationship of replacing A by A+ΔA and ω by ω+Δω+jΔσ, where $\Delta\sigma = -\dot{A}/A$, a stability index ($S_I$) in terms of the phase difference sensitivity S^{ϕ} can be derived as follows (see Appendix):

$$S_I = \left(\frac{\partial I}{\partial \omega} \bullet \frac{\partial R}{\partial A} - \frac{\partial R}{\partial \omega} \bullet \frac{\partial I}{\partial A}\right) + \left(\frac{\partial R}{\partial \phi} \bullet \frac{\partial I}{\partial \omega} - \frac{\partial R}{\partial \omega} \bullet \frac{\partial I}{\partial \phi}\right) S^{\phi} > 0 \qquad (2.12)$$

When the left hand side of the above equation is larger than zero, the machining system is stable. Additionally, the value of the left hand side is also an index of the degree of the relative stability. The greater the value, the more stable the machining process.

In order to investigate the stability of the trivial solution of the NLDDE, we set the amplitude $A \approx 0$, and use the above criterion to determine the stability. A set of parameters used in the chatter model and in the stability criterion are experimentally identified: the damping ratio ζ = 0.0384, the natural frequency of the vibration system ω_n = 101 Hz, the stiffness of the system k = 45000 N/m, the cutting force coefficient P = 1558.4 N, the cutting force exponential Y = 0.77, and the penetration factor C = 0.004 [24,25]. For a certain phase difference ϕ, the amplitude A and the frequency ω are determined by the equations of real values and imaginary values of the steady state characteristic equation. And the phase difference sensitivity S^{ϕ} can be found from Equation (2.11). Figure 3 displays the simulation result of the stability criterion with the phase difference ϕ varying with 0 ~ 360 degrees. The stability criterion indicates that when the phase difference ϕ is within 0 ~ 180 degrees, the trivial solution of the NLDDE is stable, i.e., the machining system is stable; and when the phase difference ϕ is within 180 ~ 360 degrees, the trivial solution is unstable, i.e., chatter occurs. The phase difference bifurcation value ϕ* = 180 degrees. This result of the stability criterion exactly tallies with the physical interpretation

on the phase difference and the machining stability, and it demonstrates that, when the phase difference ϕ is varying within 180 ~ 360 degrees, the machining process is unstable, i.e., the regenerative chatter occurs. This phenomenon remains true for linear cutting processes. For the nonlinear cutting processes, the phase difference bifurcation value is not exactly equal to $\phi^* = 180$ degrees, but it is still very close to 180 degrees. The effect of the non-linearities in the cutting processes on the phase difference bifurcation value will be discussed in the following section.

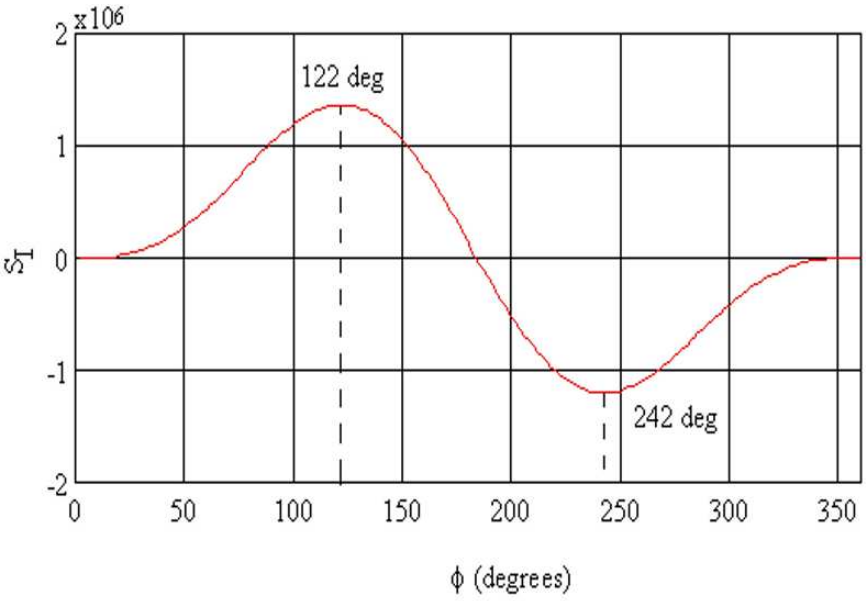

Figure 2.3. Phase difference and the stability of the machining system

2.4 Verification of the Stability Criterion

As mentioned before, the self-excited vibration is supported by the net work done by the dynamic cutting force during a vibration cycle. The net work can be calculated by the following equation:

$$E_f = \int_0^{2\pi/\omega} -\Delta F(t)\cos\alpha\dot{x}(t)dt = -\int_0^{2\pi/\omega} Pw\left\{y(t) + Ys_o^{Y-1}\frac{C}{N}\dot{x}(t)\right\}\cos\alpha\dot{x}(t)dt \quad (2.13)$$

Where, ΔF(t) is given by Equation (2.4), and

$$\begin{aligned} y(t) &= s^Y(t) - s_o{}^Y = [\mathrm{x(t)} - \mathrm{x(t-T)} + \mathrm{s_o}]^{\mathrm{Y}} - \mathrm{s_o^Y} \\ &\approx \mathrm{Y s_o^{Y-1}[x(t) - x(t-T)]} + \frac{1}{2}Y(Y-1)s_o^{Y-2}[x(t)-x(t-T)][x(t)-x(t-T)] \\ &\quad + \frac{1}{6}\mathrm{Y(Y-1)(Y-2)s_o^{Y-3}[x(t) - x(t-T)]^3} \end{aligned} \quad (2.14)$$

The net work in a vibration cycle can be derived as follows:

$$\begin{aligned} E_f &= PWA^2 Y\pi s_o^{Y-1}\left[\frac{C}{60}\phi - \sin\phi\right] \\ &\quad + PWA^4\pi\frac{1}{6}Y(Y-1)(Y-2)s_o^{Y-3}\left[-\frac{3}{4}\sin\phi + \frac{3}{2}\sin\phi\cos\phi - \frac{3}{4}\sin\phi\cos^2\phi - \frac{3}{4}\sin^3\phi\right] \end{aligned} \quad (2.15)$$

Figure 2.4 illustrates the relationship of the net work versus the phase difference ϕ when the chatter amplitude *A* is very small. The numerical simulation shows the work done by the dynamic cutting force during the phase difference varying from 0 ~ 360º (with the chatter amplitude of 0.001 mm, the chatter frequency of 101 Hz, the depth of cut, w = 3 mm, the uncut chip thickness s_o = 0.1 mm, and the spindle speed N = 600 rpm). It can be observed that, for the phase difference angle varying from zero to about 180º, the energy is negative (the dynamic cutting force is dissipating energy from the vibration system in this vibration cycle), thus the vibration amplitude decreases, and if in the successive cycles the dynamic cutting force has tendency to dissipate more or the same energy from the vibration system, the machining process is stable; for the phase difference angle varying from about 180º to 360º, the energy is positive (the dynamic cutting force is injecting energy into the vibration system), thus the vibration amplitude increases, and if in the successive cycles the dynamic cutting force has tendency to input more or the same energy into the vibration system, the machining process is unstable. At about 180º, the energy is zero, and the system is just on the threshold of instability.

The following discussions can be made: (1) For the trivial solution case ($A \approx 0$), if the penetration effect is not considered, we have

$$E_f = PwA^2 Y \cos\alpha\{-s_o^{Y-1}\pi\sin\phi\} \tag{2.16}$$

From $E_f = 0$, the bifurcation value of phase difference angle ϕ_o is found exact 180º. (2) For the trivial solution case ($A \approx 0$), if the penetration effect is considered, we have

$$E_f = PwA^2 Y \cos\alpha\{-s_o^{Y-1}\pi C\frac{\omega}{N} - s_o^{Y-1}\pi\sin\phi\} \tag{2.17}$$

The bifurcation value of phase difference ϕ_o is not exactly 180º, but around 180º (the simulation result gives 180.02º, at the spindle speed of 490 rpm). When the spindle speed is large enough, the penetration effect can be neglected, the bifurcation value of phase difference angle ϕ_o is exactly 180º. For the non-trivial solution with stable amplitude, if the penetration effect is not considered, the bifurcation value of the phase difference angle is calculated as 180.16º.

Figure 2.5 demonstrates the relationship of the net work versus the phase difference ϕ when " the tool leaving the cut" occurs and only single regenerative effect is involved. The following discussions can be made: For the non-trivial solution with stable amplitude, with the penetration effect and the nonlinear approach, the bifurcation value of the phase difference angle is calculated as 180.15º.

Although the non-linearities in the cutting process play a increasingly notable role along with the increment of the chatter amplitude, and yield some distortions of the net work curve, the basic characteristics remain almost unchanged: For the phase difference ϕ varying roughly within 0 ~ 180 degrees, the net work is negative, and the dynamic cutting force is dissipating energy from the vibration system, thus the machining process is stable. For the

phase difference ϕ varying roughly within 180 ~ 360 degrees, the net work is positive, and the dynamic cutting force is supplying energy to the vibration system, thus the machining process is unstable. The bifurcation value of the phase difference ϕ* is about 180 degrees. This result coincides with the conclusion of the stability criterion.

It is obvious that, the phase difference angle ϕ is related to the stability of the machining system. In the following sections, we will derive a stability criterion in terms of the phase difference angle and its sensitivity, which can be used to indicate the degree of stability of the machining system.

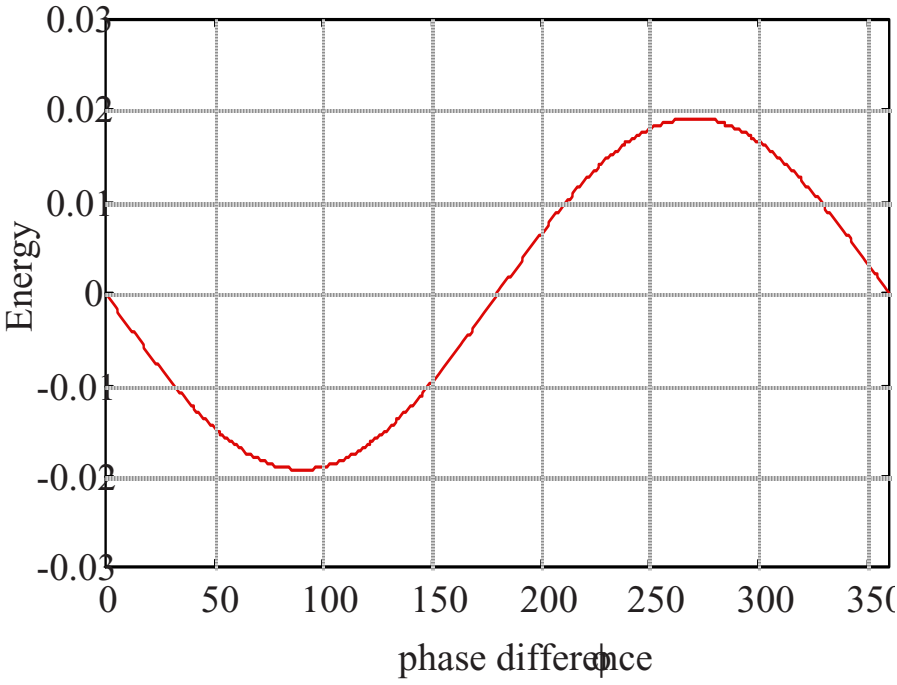

Figure 2.4. The net work versus the phase difference (with A =0.001 mm, energy unit $N \bullet mm$)

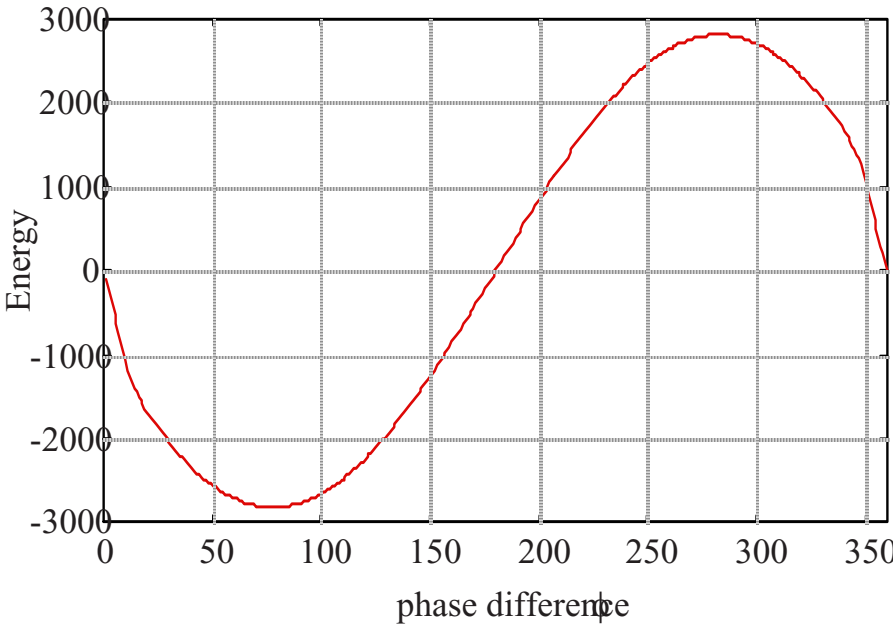

Figure 2.5. The net work versus the phase difference (with A =0.5487 mm, energy unit $N \bullet mm$)

The most stable and unstable phase difference angles can also be studied. Let

$$\frac{\partial E}{\partial \phi} = \int_0^{2\pi/\omega} -\frac{\partial}{\partial \phi} \Delta F(t) \cos \alpha \dot{x}(t) dt \tag{2.18}$$

That is,

$$\begin{aligned} \frac{\partial E}{\partial \phi} &= PWYs_o^{Y-1} A^2 \cos\phi\pi + \frac{1}{2} PWA^4 Y(Y-1)(Y-2) s_o^{Y-3} (\cos\phi \frac{\pi}{4} + \sin\phi \cos\phi\pi \\ &+ \cos^3\phi \frac{3}{4}\pi + \sin^2\phi \cos\phi \frac{3}{4}\pi) + PWYs_o^{Y-1} A^2 \frac{C}{60}\pi \\ &= 0 \end{aligned} \tag{2.19}$$

The phase difference angles that satisfy the above equations are determined by the parameters s_o, Y, A, and C.

Several conditions are studied: (1) For the case of Y=1 (the cutting force is assumed linear), Equation (2.19) can be simplified as

$$PWA^2\pi(\cos\phi + \frac{C}{60}) = 0 \tag{2.20}$$

The most stable phase difference angle, on which the net work done by the dynamic cutting force during a vibration cycle is minimum, is given by

$$\phi_{most\ stable} = 90^o + \cos^{-1}\left(\frac{C}{60}\right) \tag{2.21}$$

And the most unstable phase difference angle, on which the net work done by the dynamic cutting force during a vibration cycle is maximum, is given by

$$\phi_{most\ unstable} = 270^o + \cos^{-1}\left(\frac{C}{60}\right) \tag{2.22}$$

Since the parameter C is very small, the most stable and most unstable phase difference angles are about 90 and 270 degrees, respectively (see Figure 2.6, Case 1). (2) For the case of small chatter amplitude $A \approx 0$, and $Y \neq 1$, Equation (2.19) can be simplified as

$$PWA^2\pi Ys_o^{Y-1}(\cos\phi + \frac{C}{60}) = 0 \tag{2.23}$$

The most stable and unstable phase difference angles are the same as those in case 1, as shown in Figure 2.6 Case 2. (3) For the case of large chatter amplitude and nonlinear cutting force, the most stable and the most unstable difference angles are determined by Equation (2.19). It can be observed in Figure 2.7 that, the most stable and the most unstable phase difference angles are still about 90 and 270 degrees, respectively.

The above discussions imply that, no matter whether the chatter amplitude is large or not, and whether the non-linearities in the cutting process are considered or not, the most stable and the most unstable phase difference angles are around 90 and 270 degrees, respectively. However, as shown in Figure 2.3, the largest positive value of the stability criterion is found at 122 degrees of the phase difference angle (the most stable phase difference angle), and the smallest negative value of the stability criterion is at 242 degrees of the phase difference angle (the most unstable phase difference angle). These differences are due to the fact that the stability criterion is derived from the steady state characteristic equations, and the influences of the derivatives of σ and the derivatives of ω are ignored. Fortunately, this simplification does not interfere with the correct indication of stability. Gelb [4] also claimed that stability criterions derived from the steady state characteristic equations are almost always correct indices of stability.

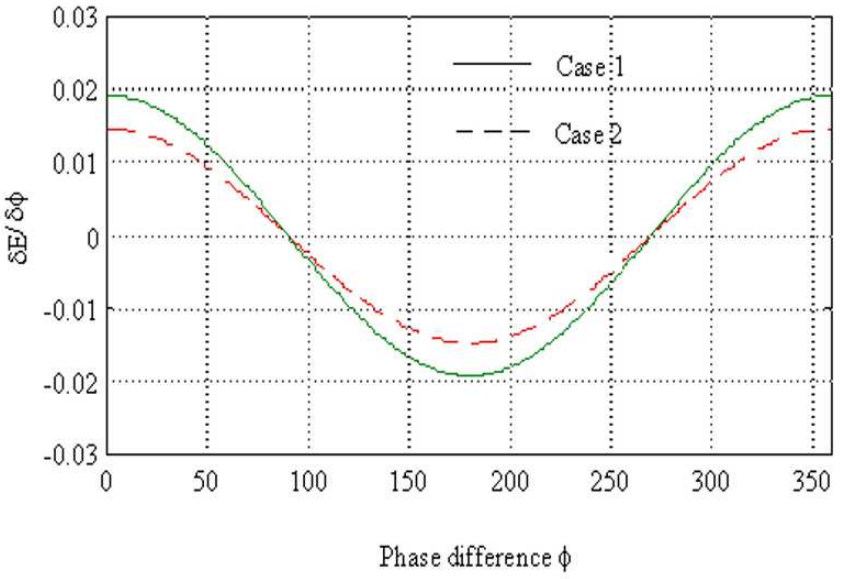

Figure 2.6. The most stable and the most unstable phase difference angles (linear and small chatter amplitude cases)

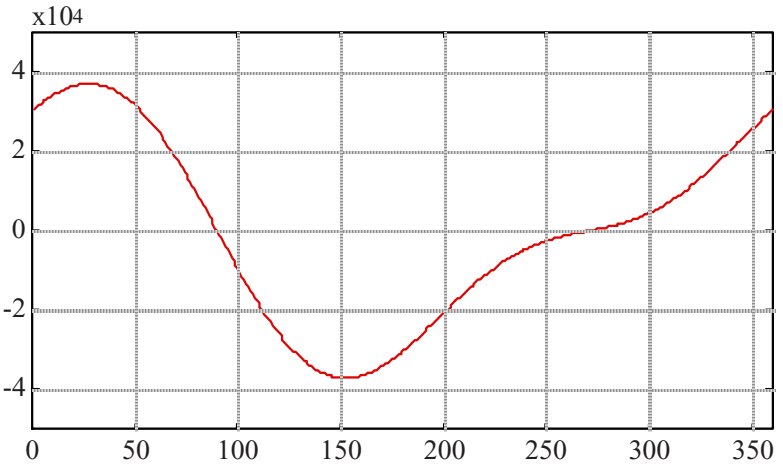

Figure 2.7. The most stable and the most unstable phase difference angles (non-linear case with large chatter amplitude A=0.5487mm)

The above results of machining stability and phase difference can also be verified by experimental results. Kasahara et al. [11] made their effort to investigate the phase characteristics of self-excited vibration in cutting. It is meaningful to point out, that Kasahara's results provided an experimental support to our theoretical analysis. Figure 2.8 displays the spindle speed N, self-excited vibration signal x(t), chatter frequency ω, and phase difference ν. In Figure 2.8, four unstable machining conditions can be observed (let A represents the fully developed machining chatter amplitude):

(a) N = 580 rpm, ω = 162Hz, $\phi = 270^o$, A = 50 μm.
(b) N = 475 rpm, ω = 157Hz, $\phi = 320^o$, A = 90 μm.
(c) N = 600 rpm, ω = 162Hz, $\phi = 290^o$, A = 70 μm.
(d) N = 750 rpm, ω = 156Hz, $\phi = 264^o$, A = 52 μm.

Noticing that the phase difference $\phi = 2\pi\tilde{}\ \nu$, where ν is the defined phase difference in Kasahara et al. [11], and ϕ is the defined phase difference in this work in agreement with the time delay concept. Nr

is the number of designated revolution during the measurement. First of all, the experimental results display that, when the phase difference ϕ is within 180 – 360 degrees, the machining process is unstable. In all of these four cases, the fully developed chatters occurred.

Secondly, the effectiveness of our stability criterion equation can also be verified: According to Kasahara's work, the feed rate f = 0.05 mm/rev, the depth of cut W = 0.5 mm, the natural frequency ω_n = 156 Hz, and the stiffness k = 2 N/μm. Assuming the cutting force parameters Y and P, and the penetration factor C are the same as that identified in our laboratory researches, i.e., Y = 0.77, P = 1558.4 N, and C = 0.004. Then the stability index S_I can be calculated as follows: (a) S_I = -3185.1, (b) S_I = -747.7, (c) S_I = -2885.7, and (d) S_I = -3683.9. All of them are negative, that is, according to the stability criterion with the phase difference sensitivity, these four cutting processes are unstable. It tallies with the experimental results. Furthermore, with the experimental parameters identified by Kasahara, the similar stability chart as shown in Figure 2.3 can also be obtained with the bifurcation phase difference angle at about 180 degrees.

2.5 Conclusions

A theoretical proof on the well-known phenomenon of the phase difference and the machining stability is provided. The bifurcation value of the phase difference is about 180 degrees in both linear and nonlinear cases. The phase difference sensitivity analysis can be used to investigate the stability of the machining system. A stability criterion in terms of the phase difference sensitivity is derived, and verified by numerical simulation and experimental data. Energy analysis on the well-known relationship of the phase difference is performed as a proof of the stability criterion. Once the parameters of the machining system are identified, the stability criterion could be used to predict the onset of machining chatter.

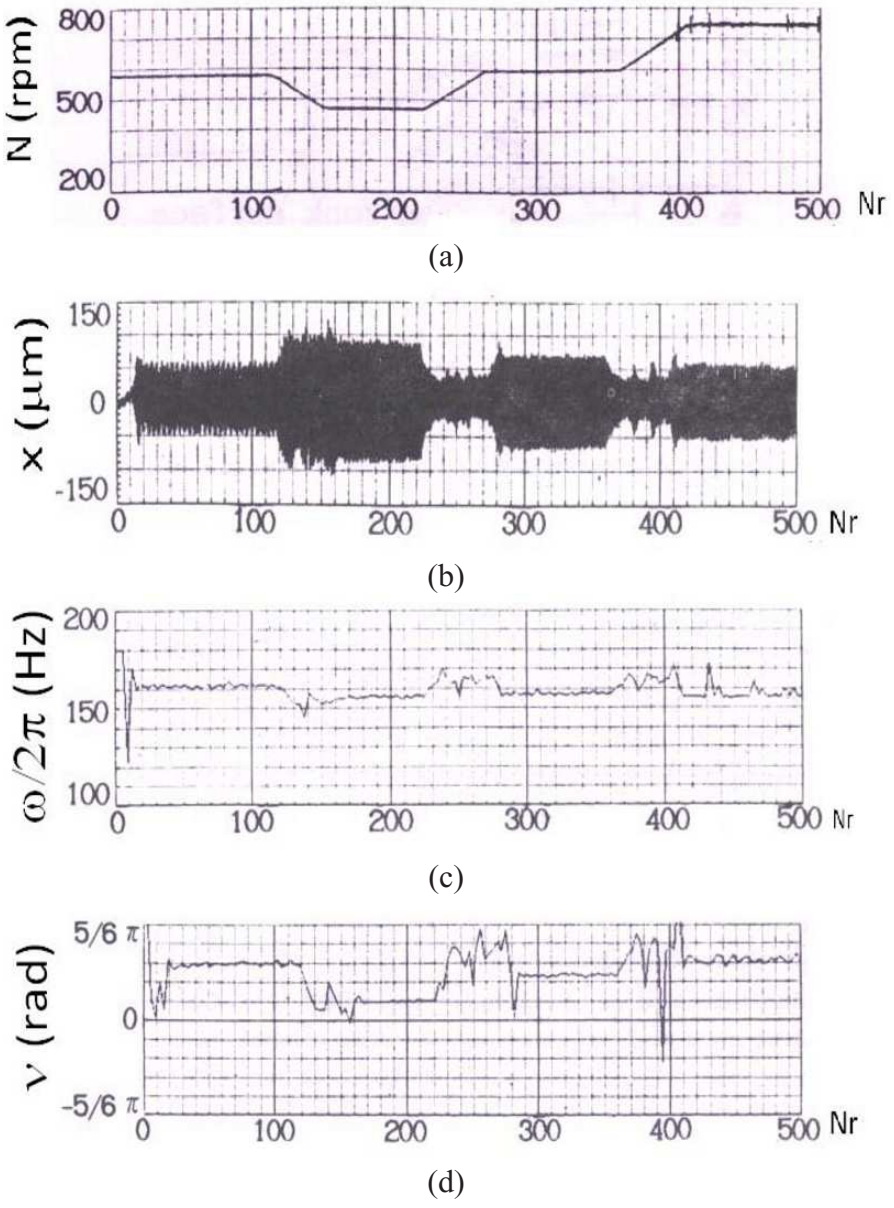

Figure 2.8. Machining chatter experimental results (see Kasahara et al. [11])

Acknowledgements

The chapter contributors wish to thank Inderscience publishers for granting permissions to reproduce work presented in this chapter.

References

[1] Boothroyd, G., and Knight, W.A., 1989, *Fundamentals of Machining and Machine Tools*, Second edition, Marcel Dekker, Inc.

[2] Drozda, T., 1983, *Tool and Manufacturing Engineers Handbook*, 4th edition, SME, pp. 1-15

[3] ElMaraghy, H.A., 2007 "Reconfigurable Process Plans for Responsive Manufacturing Systems", *Digital Enterprise Technology: Perspectives & Future Challenges*, Edited by P.F. Cunha and P.G. Maropoulos, Springer Science, pp. 35-44

[4] Gelb, A. and VanderVelde, W.E., 1968, *Multiple-Input Describing Functions and Nonlinear System Design*, New York, McGraw-Hill

[5] Gurney, J.P. and Tobias, S.A., 1962, "A Graphical Analysis of Regenerative Machine Tool Instability", Trans. of ASME, *Journal of Engineering for Industry*, Vol. 84, pp. 103-12

[6] Hahn, R.S., 1954, "On the Theory of Regenerative Chatter in Precision-Grinding Operations", Trans. of ASME, Vol. 76, pp. 593-7

[7] Inamura, T., and Sata, T. , 1974, "Stability Analysis of Cutting Under Varying Spindle Speed", *Annals of CIRP*, Vol. 23, pp. 119-120

[8] Jemielniak, K., and Widota, A., 1984, "Suppression of Self-Excited Vibration by the Spindle Speed Variation Method", *Int. J. Mach. Tools Res.*, Vol. 24, No. 3, pp. 207-214

[9] Jemielniak, K., and Widota, A., 1989, "Numerical Simulation of Nonlinear Chatter Vibration in Turning", Int. J. Mach. Tools Manufact., Vol. 29, No. 2, pp. 239-247

[10] Kalmanovskii, V. and Myshkis, A., 1992, *Applied theory of Functional Differential Equations*, Kluwer Academic Publishers

[11] Kasahara, N., Sato, H. and Tani, Y., 1992, "Phase Characteristics of Self-excited Chatter in Cutting", Trans. of ASME, *J. of Engineering for Industry*, pp. 393-399

[12] Kato, S. and Marui, E., 1972, "On the Cause of Regenerative Chatter Due to Workpiece Deflection", Trans. of ASME, *J. of Engineering for Industry*, pp. 179-134

[13] Lin, S. C., Devor, R. E., and Kapoor, S. G., 1990, "The Effects of Variable Speed Cutting on Vibration Control in Face Milling", *Trans. of the ASME*, *J. of Eng. for Ind.*, Vol. 112, pp. 1-11

[14] Minis, I., Yanushevsky, R., and Tembo, A., 1990, "Analysis of the Linear and Nonlinear Chatter in Milling", *Annals of CIRP*, Vol. 39

[15] Minorsky, N., 1962, *Nonlinear Oscillations*, D. Van Nostrand Company, Inc., Princeton, N.J.

[16] Saaty, T.L., 1967, *Modern Nonlinear Equations*, McGraw-Hill, Inc.

[17] Sexton, J. S., Miline, R. D., and Stone, B. J., 1977, "A Stability Analysis of Single-point Machining with Varying Spindle Speed", *Appl. Math. Modeling*, Vol. 1, pp. 311-318

[18] Shi, H. M. and Tobias, S. A., 1984 "Theory of Finite Amplitude Machine Tool Instability", *Int. J. Mach. Tool Des. Res.*, Vol. 24, No. 1, 45-69

[19] Shi, H. M., Xie, Y.Y., and Lu, T.G., 1987, "Microcomputer-Based Digital Simulation of Machine Tool Chattering", *J. of Huazhong Univ. of Sci. & Tech.*, Vol. 15, No. 2

[20] Takemura, T., Kitamura, T., and Hoshi, T., 1974, "Active Suppression of Chatter by Programmed Variation of Spindle Speed", *Annals of CIRP*, Vol. 23, pp. 121-122

[21] Tlusty, J., and Ismail, F., 1981, "Basic Non-linearity in Machining Chatter", Annals of the CIRP, Vol. 30, 299-304

[22] Tobias, S. A., 1965, *Machine Tool Vibration*, John Wiley & Sons, Inc., New York

[23] Wu, D. W., and Liu, C. R., 1985, "An Analytical Model of Cutting Dynamics. Part 2: Verification", *Transaction of the ASME*, Vol. 107, pp. 112-118

[24] Zhang, H., Ni, J., and Shi, H., 1994, "Machining Chatter Suppression by Means of Spindle Speed Variation", Part I & Part II, S.M. Wu Symposium on Manufacturing Science, Vol. 1, 161-167, & 169-175

[25] Zhang, H., 1996, "Chatter Modeling, Analysis and Control for CNC Machining Systems", Ph.D. dissertation, The University of Michigan – Ann Arbor.

Appendix A: Derivation of the Stability Criterion with the Phase Difference Sensitivity

The steady state characteristic equation can be expressed as:

$$R(A, \omega, \phi) + j\, I(A, \omega, \phi) = 0 \tag{A1}$$

Where A and ω are the steady state amplitude and frequency of the machining chatter, and ϕ is the phase difference angle. Assume that the small perturbations in the chatter amplitude A, the change rate of the chatter amplitude Δσ, and frequency ω are caused by the small deviation of the phase difference angle Δϕ. The chatter amplitude A and frequency ω with small perturbations are given as

$$A \rightarrow A + \Delta A, \text{ and } \omega \rightarrow \omega + \Delta\omega + j\,\Delta\sigma \tag{A2}$$

It is noticed that the small perturbation in the chatter frequency is associated with the change rate of the chatter amplitude, that is, $\Delta\sigma = -\dot{A}/A$, if the approximate solution of the NLDDE machining chatter model is given by the first order approach. Hence, we have

$$R(A+\Delta A,\ \omega + \Delta\omega + j\ \Delta\sigma,\ \phi+\Delta\phi) + I(A+\Delta A,\ \omega + \Delta\omega + j\ \Delta\sigma,\ \phi+\Delta\phi) = 0 \tag{A3}$$

The Taylor series first order expansion of Equation (A3) about the equilibrium state yields

$$\begin{aligned} &\frac{\partial R}{\partial A}\Delta A + \frac{\partial R}{\partial \omega}(\Delta\omega + j\Delta\sigma) + \frac{\partial R}{\partial \phi}\Delta\phi \\ &\quad + j\frac{\partial I}{\partial A}\Delta A + j\frac{\partial I}{\partial \omega}(\Delta\omega + j\Delta\sigma) + j\frac{\partial I}{\partial \phi}\Delta\phi = 0 \end{aligned} \tag{A4}$$

Both the real and the imaginary parts will vanish separately, if the above equation is satisfied:

$$\begin{aligned}\frac{\partial R}{\partial A}\Delta A+\frac{\partial R}{\partial \omega}\Delta\omega+\frac{\partial R}{\partial \phi}\Delta\phi-\frac{\partial I}{\partial \omega}\Delta\sigma=0\\ \frac{\partial R}{\partial \omega}\Delta\sigma+\frac{\partial I}{\partial A}\Delta A+\frac{\partial I}{\partial \omega}\Delta\omega+\frac{\partial I}{\partial \phi}\Delta\phi=0\end{aligned} \tag{A5}$$

A single relationship among $\Delta\sigma$, ΔA and $\Delta\phi$ can be obtained by eliminating $\Delta\omega$ from the equation set (A5):

$$\left[\left(\frac{\partial I}{\partial \omega}\right)^2+\left(\frac{\partial R}{\partial \omega}\right)^2\right]\Delta\sigma=\left(\frac{\partial R}{\partial A}\frac{\partial I}{\partial \omega}-\frac{\partial I}{\partial A}\frac{\partial R}{\partial \omega}\right)\Delta A+\left(\frac{\partial R}{\partial \phi}\frac{\partial I}{\partial \omega}-\frac{\partial I}{\partial \phi}\frac{\partial R}{\partial \omega}\right)\Delta\phi \tag{A6}$$

Notice that the phase difference sensitivity S^{ϕ} is defined as

$$S^{\phi}=\frac{\partial \phi}{\partial A}\approx\frac{\Delta\phi}{\Delta A} \tag{A7}$$

Hence, Equation (A6) can be rewritten in the form

$$\left[\left(\frac{\partial I}{\partial \omega}\right)^2+\left(\frac{\partial R}{\partial \omega}\right)^2\right]\Delta\sigma=\left[\left(\frac{\partial R}{\partial A}\frac{\partial I}{\partial \omega}-\frac{\partial I}{\partial A}\frac{\partial R}{\partial \omega}\right)+\left(\frac{\partial R}{\partial \phi}\frac{\partial I}{\partial \omega}-\frac{\partial I}{\partial \phi}\frac{\partial R}{\partial \omega}\right)S^{\phi}\right]\Delta A \tag{A8}$$

If the equilibrium state is stable, a positive increment ΔA must result in a negative derivative of the chatter amplitude $\dot{A}$, thus a positive relative change rate of the chatter amplitude $\Delta\sigma$; and similarly, a negative increment ΔA must lead to a negative relative change rate of the chatter amplitude $\Delta\sigma$. Stated another way, for a stable equilibrium state, the following condition must be satisfied:

$$\left(\frac{\partial R}{\partial A}\frac{\partial I}{\partial \omega}-\frac{\partial I}{\partial A}\frac{\partial R}{\partial \omega}\right)+\left(\frac{\partial R}{\partial \phi}\frac{\partial I}{\partial \omega}-\frac{\partial I}{\partial \phi}\frac{\partial R}{\partial \omega}\right)S^{\phi}>0 \qquad \text{(A9)}$$

This is the stability criterion with the phase difference sensitivity.

Chapter 3

Machining Chatter Suppression

H. H. Zhang, J. Ni and M. J. Jackson

3.1 Introduction

This chapter presents a systematic stability analysis of spindle speed variation (SSV) method for machining chatter suppression based on a machining chatter model of non-linear delay differential equation. The theoretical results are verified by results of numerical simulations and experiments. Some important results are achieved: the stability increment index (SII) of SSV cutting over constant speed cutting is derived; a formula for selecting the SSV amplitude is proposed based on the internal energy analysis of the SSV cutting and the instantaneous sideband effect, which is meaningful for practical application of SSV cutting, especially using nanostructured coated cutting tools where chatter can cause the thin solid film to fail by chipping.

Machining processes are often accompanied by chatter, essentially regenerative chatter (see Figure 3.1) that results in rough surface finish, poor accuracy, and shortened tool life. Chatter becomes even more critical, when workpiece materials are difficult to cut. Some advanced cutting tool materials such as ceramic, silicon nitride and CBN require strict chatter control to prevent breakage of the tool and its coating [1,2]. For high precision manufacturing, even mild vibration is undesirable. Furthermore, since modern machining systems have become more flexible, the frequently changing working conditions increase the possibility of bringing machining process into unstable operating regions [3,4]. In order to avoid chatter, the metal-removal rate of machining systems is often kept undesirably low.

Various methods have been developed to control chatter without reducing metal-removal rate. Some of them involve in modification of the cutting tool, for instance using variable-pitch cutters [5] or bi-helical cutters [6], and others attach supplementary equipments to the machine tool structure in the vicinity of chip producing area, such as vibration absorbers or actuators and sensors with expensive control processors. In the former case, the design of cutter insert spacing is dependent upon the cutting conditions and workpiece geometry, which could be changing during the machining process. However, the insert spacing cannot be in-process adjusted to maintain the desired effect. In addition, insert spacing technique is applicable only to multi-tooth cutters, not to single-point cutters in turning or boring. In the latter case, the control laws are usually designed with state variables, such as position variables and forces, by feedback of the error signals to control the relative vibration between the cutting tool and the workpiece [7,8], which still fall short of practical industrial application. Actually, the control laws can be also designed with the cutting parameter variables, such as the spindle speed and the feed, since the stability of the machining process is directly affected by the cutting parameters. Adjusting the cutting parameters is a natural way to control machining chatter, and in CNC environment, it can be easily realized without necessity of supplementary equipments.

Among machining chatter control methods, Spindle Speed Variation (SSV) method overcomes the above-mentioned difficulties, and eliminates regenerative chatter by means of continuously and periodically adjusting the spindle speed only. SSV has strong potentials for practical applications due to its following features: (1) Diversity: Continuously varying the spindle speed provides similar effects of modifying the cutting tool, and is applicable not only for multi-point cutting, but also for single-point cutting. It can be utilized in many machining operations. (2) Flexibility: Instead of replacing cutters with different insert spacing for various cutting conditions and workpiece geometry, the same effect can be achieved only by adjusting the SSV amplitude and/or the SSV frequency in software. (3) Effectiveness: SSV increases

machining stability against vibrations, and improves the surface finish on the workpiece for roughing or semi-roughing operations with relatively small and slow speed variations. (4) Simplicity: No supplementary equipments such as vibration absorbers or actuators are needed. All the required hardware is already available in CNC machining systems.

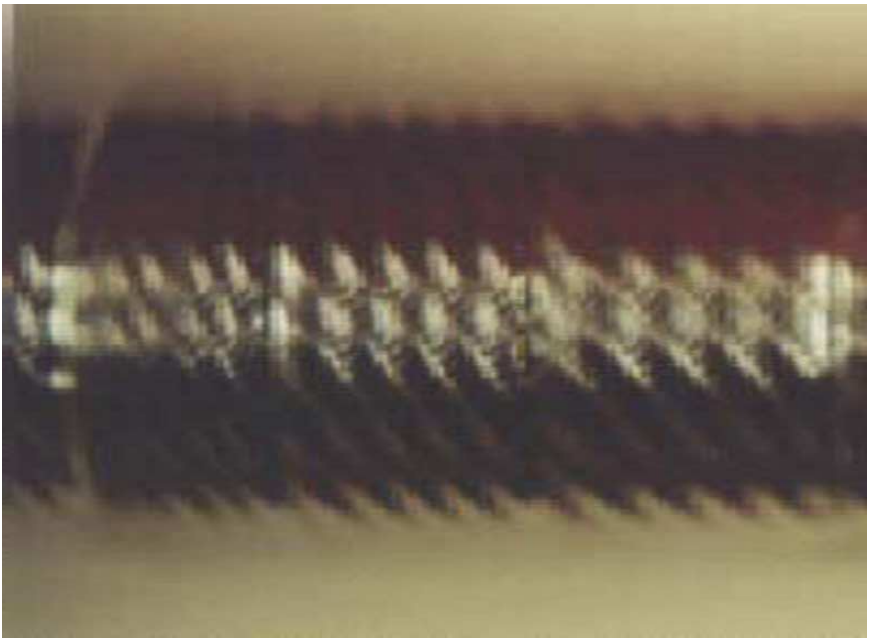

Figure 3.1. Typical machining chatter in turning (at constant cutting speeds)

Once in-process estimation technique of the SSV parameters is developed with identifying the elastic structure parameters and detecting chatter signals, SSV closed loop control can be readily integrated into CNC machining systems.

The spindle speed variation (SSV) method originated from the discovery that uneven distribution of the chip load in machining is a means to break the regenerative effect for chatter suppression. For multi-point cutting, it was accomplished with uneven insert spacing technique applied to milling cutters, while for single point cutting, it was realized by continuously and periodically varying the spindle

speed (SSV). The first suggestion of the concept of SSV is credited to Stone as a result of his study of bi-helical cutters, and Stoferle and Grab first presented its application in turning. In recent years, SSV has been brought to increasing attention.

Takemura et al. [9] proposed a theory to interpret chatter suppression by SSV, but in their analysis the cutting stiffness transfer function locus was assumed a closed circle, which is true only for constant speed cutting, but not for SSV cutting. Inamura and Sata [10] investigated the mechanism of improving machining stability by SSV based on Hilbert Space theory, but their prediction of up to 10 times stability increment was an overestimate. In their second report, Takemura et al. [11] studied the effects of SSV parameters such as SSV amplitude and SSV frequency in turning. And the effect of complex SSV waveforms on chatter suppression was studied in their third report, the spindle speed trajectory was described by a nominal speed modulated with multi-frequency and multi-amplitude periodic waves, for instance, multi-stepped, triangular, rectangular and sinusoidal waves, and it was believed that more effective wave form of SSV can be found theoretically [9]. Through a series of experiments in turning and boring, Hoshi et al. [10] verified the reported SSV effect on chatter suppression. Sexton and Stone [11-13] applied orthogonal projection theory on almost-periodic functions of a linear machining chatter model, and determined the stability borderline of constant speed cutting, however, for SSV cutting the stability increment was underestimated comparing with their analogue and digital simulations. Jemielniak and Widota [14] pointed out, the reason for SSV not being well accepted in practice was due to contradictory conclusions concerning the effect of SSV parameters on chatter suppression and no satisfactory agreement between theoretical and experimental results. They proposed the amplitude amplification coefficient to monitor the system stability for constant speed cutting and SSV cutting. For multi-point cutting, Engelhardt et al. [15] and Wu and Yu [16] verified the effectiveness of SSV with simple periodic trajectory on chatter suppression in face milling. Lin et al. [17] investigated speed trajectory design with different periodic waveforms in face milling. Tsao et al. [18] analyzed machining

stability utilizing the spectrum radius of the companion matrix in the finite difference approximation of the machining chatter model, which was used to determine the stability borderlines for constant speed and SSV cuttings. However, a tradeoff was made between the accuracy and computational load, since its accuracy was dependent on the number of finite difference segments one spindle rotation was divided into. Jayaram et al. [19] based on a linear chatter model with time delay to design optimal SSV machining parameters. Yilmaz et al. [20] and Li et al. [21] studied a variation of SSV and demonstrated its effectiveness of chatter suppression.

Evidently, with its substantial values in industrial applications, SSV method is still under development [22-28]. The motivation behind this work is to develop a systematic approach that address the following issues: (1) Derivation of an analytical index for machining stability increment, which can be used to predict the critical depth of cut for different SSV parameters under various cutting conditions. (2) Theoretical prediction of the minimum SSV parameters that are needed to suppress the chatter based on chatter signals, which can be used for closed loop SSV control. (3) Analytical energy expressions correlated to the cutting process and the elastic structure of the machine tool during SSV cutting, which can be used to interpret the mechanism of SSV cutting on chatter suppression. In this work, only the investigation of simple sinusoidal waveform of SSV cutting is presented without loss of generality.

3.2 Non-linear Machining Chatter Model

A well-accepted nonlinear regenerative machining chatter model with single time-delay [29-31] is employed in this study. In the dynamic interaction of the machine tool elastic structure and the cutting process, the elastic structure is presumed a linear sub-system

$$\ddot{x}(t)+ 2\varsigma\omega_n\dot{x}(t) + \omega_n^2 x(t) = -\frac{\omega_n^2}{k}\Delta F(t)\cos\alpha \tag{3.1}$$

Where ζ, ω_n and k are the damping ratio, the natural frequency and the stiffness of the elastic structure, $\Delta F(t)$ is the dynamic cutting force.
The cutting process is modeled as a nonlinear subsystem

$$\Delta F(t) = Pw\left\{ s^{Y}(t) - s_o^{Y} + Y s_o^{Y-1} C \frac{\dot{x}(t)}{N} \right\} \tag{3.2}$$

Where, P is the force coefficient, Y is the force exponential, C is the penetration coefficient, w is the depth of cut, s(t) is the instantaneous chip thickness, s_o is the uncut chip thickness, N is the spindle speed, m is the number of regenerative passes. The instantaneous chip thickness $s(t)$ can be expressed as

$$s(t) = x(t) - x(t-T) + s_o \tag{3.3}$$

Where, s_o is the nominal chip thickness. Equations (3.1) – (3.3) give a nonlinear delay differential equation (NLDDE) as the model of regenerative machining chatter.

3.3 Characteristic Equation of SSV Cutting

3.3.1 Equivalently linearized differential equation

First of all, it is noticed that the nonlinear part $s^{Y}(t) - s_o^{Y}$ can be approximated by a 3-rd order polynomial:

$$\begin{aligned} s^{Y}(t) - s_o^{Y} &= [x(t) - x(t-T) + s_o]^{Y} - s_o^{Y} \\ &\approx Y s_o^{Y-1}[x(t) - x(t-T)] + \frac{1}{2} Y(Y-1) s_o^{Y-2} |x(t) - x(t-T)| [x(t) - x(t-T)] \\ &\quad + \frac{1}{6} Y(Y-1)(Y-2) s_o^{Y-3} [x(t) - x(t-T)]^3 \end{aligned} \tag{3.4}$$

The input-output characteristics of $s^{Y}(t)-s_{o}^{Y}$ with respect to x(t)-x(t-T) basically possesses odd symmetry.
Furthermore, the NLDDE machining chatter model can be approached by the equivalently linearized differential equation:

$$\begin{aligned}&\ddot{x}(t)+ a_1\dot{x}(t)+(\omega_n^2+a_2)x(t)\\&=a_2(1-\sigma T)e^{j[-\omega(t)T+\frac{1}{2}\dot{\omega}(t)T^2]}x(t)-3.77\frac{A}{\pi}a_3[(1-\cos\omega T)+j\sin\omega T]x(t)\\&\quad-1.5A^2a_4(1-\cos\omega T)[(1-\cos\omega T)+j\sin\omega T]x(t)\end{aligned} \tag{3.5}$$

Where,

$$a_1=2\varsigma\omega_n+\frac{\omega_n^2}{k}PwYs_o^{Y-1}\frac{C}{N}\cos\alpha$$

$$a_2=\frac{\omega_n^2}{k}PwYs_o^{Y-1}\cos\alpha \qquad \sigma=\frac{\dot{A}(t)}{A(t)}$$

$$a_3=\frac{1}{2}\frac{\omega_n^2}{k}PwY(Y-1)s_o^{Y-2}\cos\alpha$$

$$a_4=\frac{1}{6}\frac{\omega_n^2}{k}PwY(Y-1)(Y-2)s_o^{Y-3}\cos\alpha$$

Noticing the first order approximation of the solution $x(t)=A(t)e^{j\varphi(t)}$, with steady state conditions, Equation (3.5) yields the following equation:

$$\begin{aligned}&-\omega^2A\cos\omega t-a_1A\omega\sin\omega t+(\omega_n^2+a_2)A\cos\omega t\\&=a_2(A\cos\omega T\cos\omega t+A\sin\omega T\sin\omega t)\\&\quad-3.77\frac{A^2}{\pi}a_3[(1-\cos\omega T)\cos\omega t-\sin\omega T\sin\omega t]\\&\quad-1.5A^3a_4(1-\cos\omega T)[(1-\cos\omega T)\cos\omega t-\sin\omega T\sin\omega t]\end{aligned} \tag{3.6}$$

3.3.2 Time delay of SSV cutting

For SSV cutting, the time delay T is varying with time. However, it is a slowly varying variable, because the SSV frequency is only about 0.5% ~ 2% of the chatter frequency and also a small portion of the nominal spindle speed. For the sinusoidal spindle speed variation, the time delay is sinusoidally varying as well:

$$T = \frac{60}{N} = \frac{60}{N_o} \frac{1}{1 + \frac{\Delta N}{N_o} \sin(2\pi f_\tau t)} \approx T_o - \tau \sin(\omega_\tau t) \tag{3.7}$$

Where, N_o is the nominal spindle speed, ΔN is the SSV amplitude, and f_τ is the SSV frequency, the time delay T is sinusoidally varying as well, $T_o = 60/ N_o$ is the nominal time delay. The amplitude of the varying time delay is

$$\tau = \frac{60 \Delta N}{N_o^2} \tag{3.8}$$

And, $\omega_\tau = 2\pi f_\tau$ is the frequency of the varying time delay, which is much lower than the chatter frequency ω, and $\omega = M\omega_\tau$ (M is a large number).

3.3.3 Characteristic equation

In Equation (3.6), sinωT and cosωT can be expanded with Bessel functions of the first kind, of order n, and is defined as follows

$$J_n(\omega\tau) = \frac{1}{2\pi} \int_0^{2\pi} \cos(n\theta - \omega\tau \sin\theta) d\theta, \text{ n} = 0, 1, 2, 3, ... \tag{3.9}$$

Figure 3.2 displays the accuracy comparison between $\sin \omega T$ and $\cos \omega T$ and their series approximations. Finding the inner product of Equation (3.6) with an orthonormal basis set $\{\cos \omega t, \sin \omega t\}$ for $\omega_\tau t \in (0, 2\pi)$ or $\omega t \in (0, 2M\pi)$, where $M = \omega / \omega_\tau$, substituting the inner product results into it produce the characteristic equations of SSV cutting:

$$-\omega^2 + \omega_n^2 + a_2 - a_2 J_o(\omega\tau)\cos\omega T_o + a_3 3.77\frac{A}{\pi}[1 - J_o(\omega\tau)\cos\omega T_o] + \frac{3}{2}A^2 a_4\{(1 - 2J_o(\omega\tau)\cos\omega T_o) + [J_o^2(\omega\tau) + 3J_M^2(\omega\tau)]\cos^2\omega T_o]\} = 0 \tag{3.10}$$

$$a_1\omega + a_2 J_o(\omega\tau)\sin\omega T_o + a_3 3.77\frac{A}{\pi}J_o(\omega\tau)\sin\omega T_o + \frac{3}{2}A^2 a_4[J_o(\omega\tau)\sin\omega T_o - J_o^2(\omega\tau)\sin\omega T_o\cos\omega T_o] = 0 \tag{3.11}$$

Solving the above two equations for chatter amplitude, A, and chatter frequency, ω, produces the approximate steady state solution $x(t) = A(t)e^{j\varphi(t)}$ of the NLDDE. For constant speed cutting, i.e., $\omega\tau = 0$, we have $J_o(0) = 1$, and $J_M(0) = 0$, the above two equations become the characteristic equation of constant speed cutting.

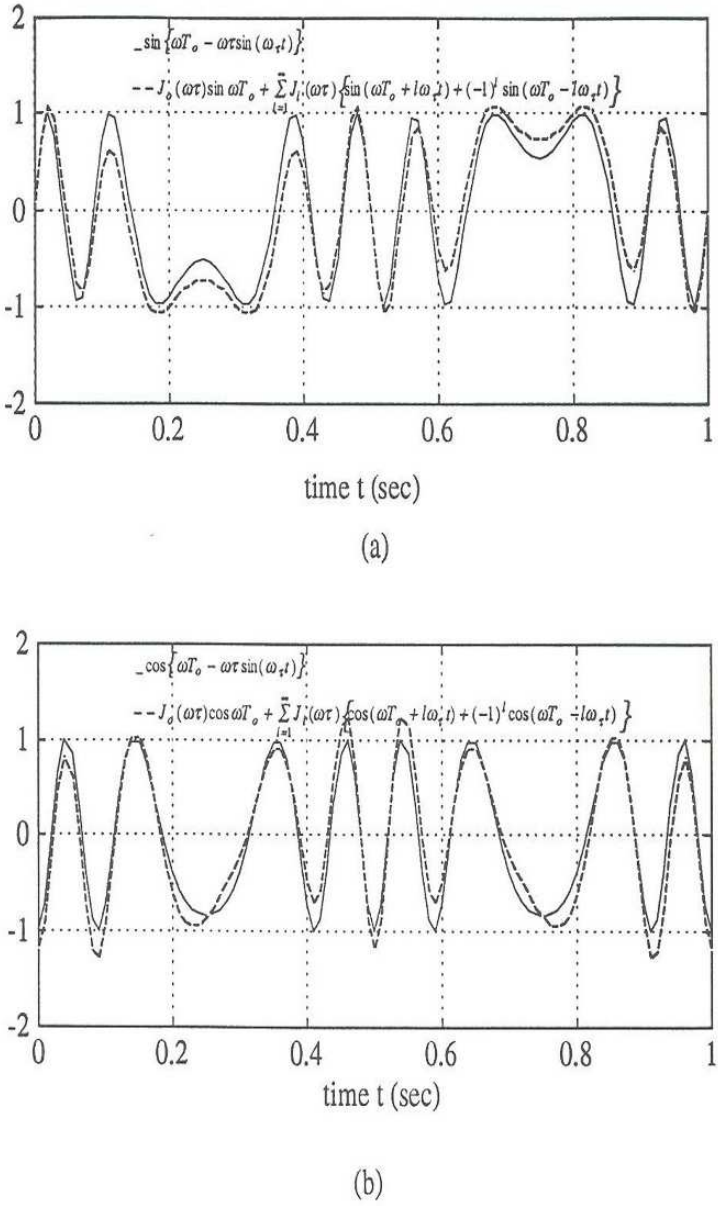

Figure 3.2. Series approximations with $\omega\tau = 12$

3.4 Stability Increment by SSV Cutting

In this section, we will find the stability regions of constant speed cutting and SSV cutting, and compare changes of the stability regions. During the transient state of the chatter onset, the chatter amplitude A(t) can be described by

$$\frac{dA(t)}{dt} \approx \frac{A}{2\omega - a_2 T \sin \omega T}[-a_1 \omega - a_2 \sin \omega T - 3.77\frac{A}{\pi} a_3 \sin \omega T - \frac{3}{2} A^2 a_4 \sin \omega T(1 - \cos \omega T)] \tag{3.12}$$

For constant speed cutting, it can be found that the trivial solution is stable, if

$$a_1 \omega + a_2 \sin \omega T > 0 \tag{3.13}$$

And the chatter frequency ω is determined in Equation (3.10), the real part of the characteristic equation:

$$\omega_n^2 - \omega^2 + a_2(1 - \cos \omega T) = 0 \tag{3.14}$$

Equations (3.13) and (3.14) determine the stability borderline of constant speed cutting as shown in Figure 3.3. For SSV cutting, the stability borderline of the trivial solution is determined by the characteristic equations and Equation (3.12):

$$a_1 \omega + a_2 \sin(\omega T_o) J_o(\omega \tau) > 0 \tag{3.15}$$

$$\omega_n^2 - \omega^2 + a_2[1 - \cos(\omega T_o) J_o(\omega \tau)] = 0 \tag{3.16}$$

A simulated comparison between the stability borderline of SSV cutting and that of constant speed cutting is displayed in Figure 3.3

(feed f of 0.1 mm/rev, natural frequency ω_n of 202π rad/sec, SSV amplitude ΔN of 60 rpm, SSV frequency f_τ of 0.9 Hz). It is observed that SSV cutting has a different stability borderline from that of constant speed cutting, and SSV stability region is larger than and covers that of constant speed cutting. According to Equation (3.5), a_1 is proportional to the damping ratio, and a_2 is proportional to the depth of cut. As is shown in Figure 3.3, for a given damping ratio, the critical depth of cut of SSV cutting is larger than that of constant speed cutting. Similarly, for a given depth of cut, the critical damping ratio of SSV cutting is less than that of constant speed cutting. Thus SSV cutting does increase stability over constant speed cutting.

Given a point on a_1 axis in Figure 3.3, a typical lobe type stability chart can be induced (see Figure 3.4). In Figure 3.4, the theoretical stability borderline of constant speed cutting which is verified by simulated constant speed cuttings denoted with circles (o), and the theoretical stability borderline of simulated SSV cutting with amplitude 60 rpm and frequency 0.9 Hz denoted with asterisks (*). It shows that the SSV stability borderline is elevated in comparison with the constant speed stability borderline through the whole region. The critical depth of cut of SSV cutting is larger than that of constant speed cutting. Therefore, SSV increases the machining stability. Experiments are performed to verify the above comparison. The three squares (□) in Figure 3.4 denote three unstable constant speed cuttings and three stable SSV cuttings (SSV amplitude of 60 rpm, SSV frequency of 0.9 Hz). Since they are located in the unstable region of the constant speed cutting, chatter occurs in those cases. However, with respect to the SSV stability borderline, they are in the stable region, therefore no chatter is observed.

It is also shown that the SSV stability borderline gradually decreases along with increasing nominal spindle speed. For a given SSV amplitude, the higher the nominal spindle speed, the lower the SSV stability borderline. Although in some minor areas SSV cuttings may have lower stability at high nominal spindle speed than

corresponding constant speed cuttings, in low and medium speed regions, SSV method significantly improves machining stability.

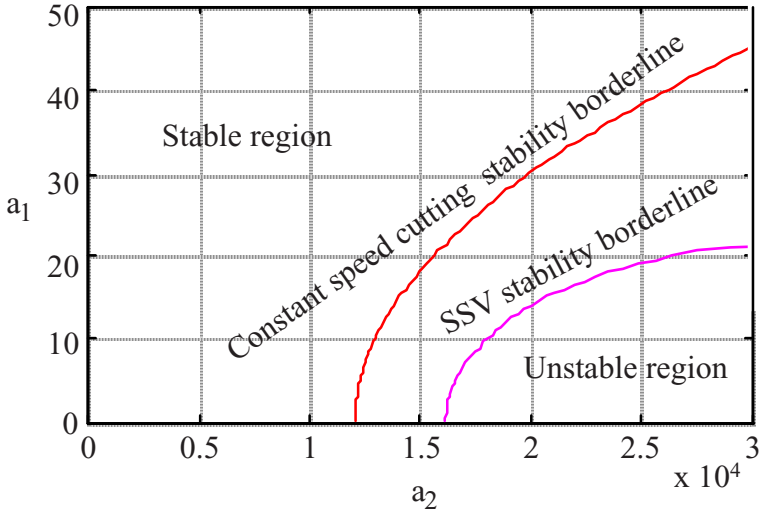

Figure 3.3. Stability regions of constant speed and SSV cuttings

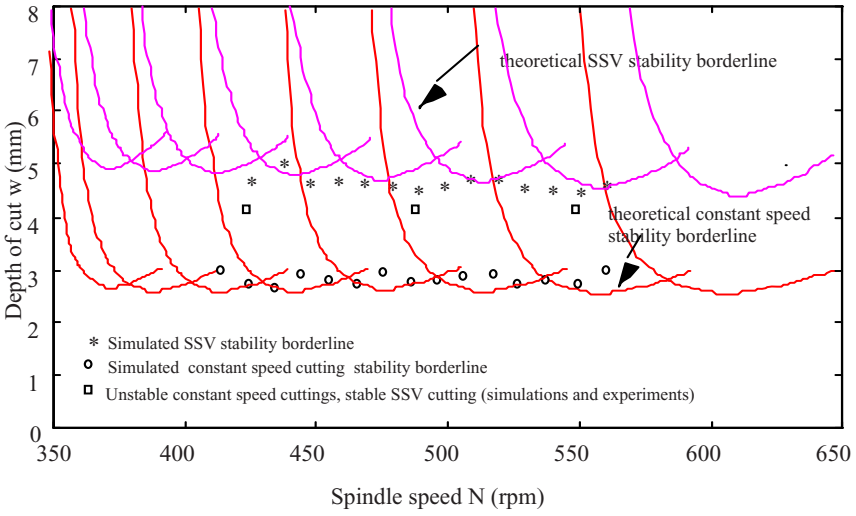

Figure 3.4. Stability increment by the SSV cutting. Cutting conditions: spindle speed $N = N_o + 60\sin(2 \quad 0.9t)$, nominal spindle speed $N_o = 430 \sim 560$ rpm, feed f = 0.1 mm/rev

3.5 Determination of Stability Increment Index

It can be derived that, for constant speed cutting, the stability borderline is determined by

$$E_{fconst} = E_{dconst} \tag{3.17}$$

Where E_{fconst} is the net work done by the dynamic cutting force in a vibration cycle during the constant speed cutting, and E_{dconst} is the damping dissipated energy in a vibration cycle during the constant speed cutting. The critical depth of cut for constant speed cutting is roughly given by

$$w_{const} \approx \frac{2k\varsigma(\omega_{const} / \omega_n)}{PYs_o^{Y-1}\cos\alpha\sin\omega T_o} \tag{3.18}$$

Where ω_{const} is the chatter frequency at the critical depth of cut during constant speed cutting. Similarly, for SSV cutting, the stability borderline is contingent on

$$E_{fssv} = E_{dssv} \tag{3.19}$$

Where E_{fssvt} is the net work done by the dynamic cutting force in a vibration cycle during the SSV cutting, and E_{dconst} is the damping dissipated energy in a vibration cycle during the SSV cutting. And the critical depth of cut for SSV cutting is roughly expressed as

$$w_{ssv} \approx \frac{2k\varsigma(\omega_{ssv} / \omega_n)}{J_o(\omega_{ssv}\tau)PYs_o^{Y-1}\cos\alpha\sin\omega T_o} \tag{3.20}$$

Where ω_{ssv} is the chatter frequency at the critical depth of cut during SSV cutting. ω_{ssv} is determined as follows: From Equations (3.15) and (3.16), we have

$$\omega_{ssv} = \sqrt{\frac{1}{2}\left\{2(\omega_n^2 + a_2) - a_1^2] \pm \sqrt{a_1^4 - 4a_1^2(\omega_n^2 + a_2) + 4a_2^2 J_o^2}\right\}} \qquad (3.21)$$

Define the parameters a_1 and a_2 in the following way with more physical meanings:

$$\begin{aligned} a_1 &= 2\varsigma_d \omega_n \\ \varsigma_d &= \varsigma + \frac{1}{2}\frac{\omega_n^2}{k} Pw_{ssv} C \frac{1}{N}\cos\alpha \\ a_2 &= \omega_n^2 \frac{k_d}{k} \\ k_d &= Pw_{ssv} Ys_o^{Y-1}\cos\alpha \end{aligned} \qquad (3.22)$$

Where ζ_d is the dynamic damping ratio, and k_d is the dynamic stiffness. Then the chatter frequency during SSV cutting can be rewritten as

$$\omega_{ssv} = \omega_n \sqrt{\frac{k_d}{k} + (1 - 2\varsigma_d^2) \pm \sqrt{\varsigma_d^4 - (2\varsigma_d)^2 (1 + \frac{k_d}{k}) + \left(\frac{k_d}{k}\right)^2 J_o^2}} \qquad (3.23)$$

This estimation shows that, although there might be a variation of the chatter frequency, the chatter frequency is always slightly larger than the natural frequency of the elastic structure. Figure 3.5 displays the simulated chart of the chatter frequency versus the depth of cut during SSV cuttings. Therefore, the stability increment index (SII), defined as the ratio of the critical depth-of-cut of SSV cutting to that of constant speed cutting, can be expressed as

$$SII = \frac{w_{ssv}}{w_{const}} = \frac{\omega_{ssv} / \omega_n}{J_o(\omega_{ssv}\tau)(\omega_{const} / \omega_n)} \qquad (3.24)$$

It is essentially related to Bessel function value of the 0-th order associated with the chatter frequencies at the depth of cuts and SSV amplitude.

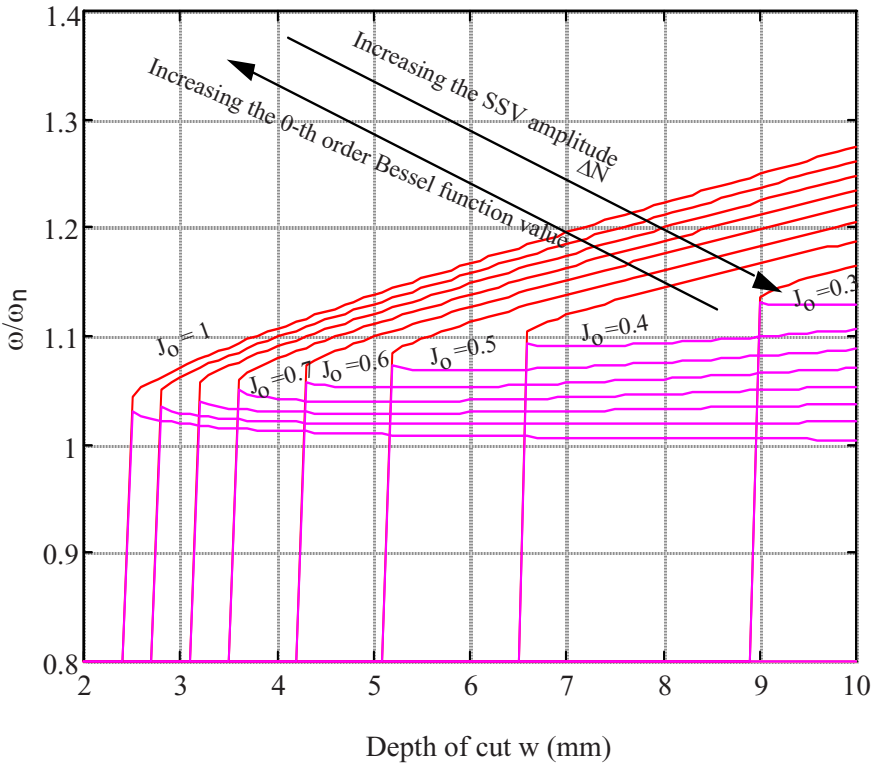

Figure 3.5. Chatter frequency during SSV cutting

Figure 3.6 shows the simulated stability increase chart, showing the relationship between the stability increment index (SII) and the 0-th order Bessel function value $J_o(\omega\tau)$. The estimated SII values are very close to the simulated stability increase. Along with increasing $\omega\tau$, the value of $J_o(\omega\tau)$ becomes smaller, and SII becomes larger. However, one has to realize that, SSV parameters are with constraints of the surface finish requirement, spindle system frequency bandwidth, and power of the DC motor of spindle system. Therefore, in normal cutting conditions, SII is often observed as 1.5 ~ 3 times.

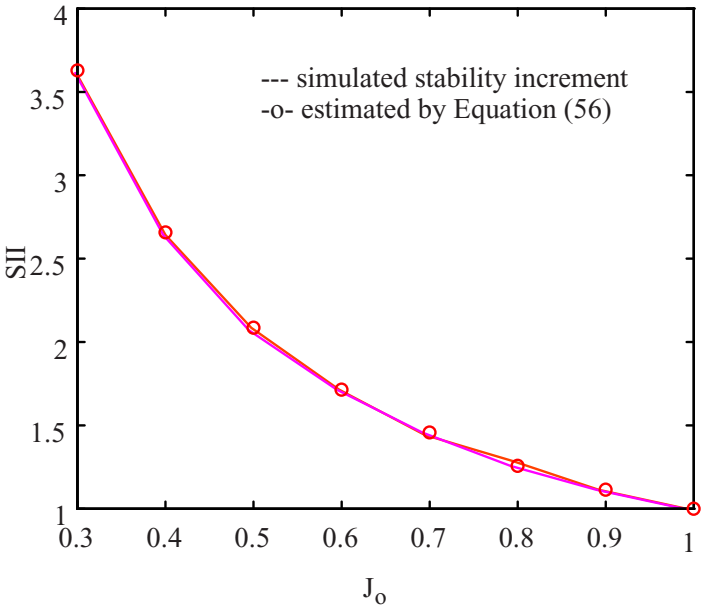

Figure 3.6. Stability Increment vs. J_O

3.6 Selecting SSV Amplitude from Energy Analysis

As shown, most of the information of SSV frequency, ω_τ, is "lost" during averaging procedure on the range of $\omega_\tau t \in (0, 2\pi)$. This does not imply that SSV frequency, ω_τ, is not important. In fact, for effective chatter suppression, SSV frequency is only about 0.5% ~ 2% of the chatter frequency. If $M = \omega / \omega_\tau$ is too large, the small SSV frequency might weaken the effect of chatter suppression. Normally, larger SSV frequency is modestly more effective than smaller SSV frequency. However, the SSV frequency ω_τ will be limited by the frequency bandwidth of CNC machining systems. Therefore, M should not be too small either. In general, $M = \omega / \omega_\tau = 50 \sim 200$ is suggested, and it can be easily achieved in CNC machining systems.

Comparing with the selection of SSV amplitude, there is not much room for the selection of SSV frequency ω_τ. SSV amplitude is the more dominant factor for chatter suppression, thus more commonly requested.

3.6.1 Preliminary procedure of selecting SSV amplitudes

In this section, our goal is to select a proper SSV amplitude ΔN (with an adequate SSV frequency ω_τ) such that the following equation is satisfied:

$$\Delta E = E_{fssv} - E_{dssv} \le 0 \tag{3.25}$$

Although the critical chatter frequency ω_{ssv} during SSV cutting is slightly larger than the chatter frequency, ω, during constant speed cutting, for rough estimation, E_{dssv} can be approximately treated as E_{dconst}. It can be derived from Equation (3.25):

$$PwYs_o^{Y-1}\left\{-\pi J_o(\omega\tau)\cos\alpha\sin\omega T_o - C\frac{\omega}{60}\cos\alpha\left(\pi T_o + \frac{1}{2}\tau\frac{\omega}{\omega_\tau}[\cos(\frac{\omega_\tau}{\omega}2\pi)-1]\right)\right\}$$
$$-2\pi\omega\varsigma\frac{k}{\omega_n} \le 0 \tag{3.26}$$

The 0-th order Bessel function value should satisfy

$$J_o(\omega\tau)\sin\omega T_o \le \left|\frac{2\pi\omega\varsigma\frac{k}{\omega_n} + PwYs_o^{Y-1}C\frac{\omega}{60}\cos\alpha\left(\pi T_o + \frac{1}{2}\tau\frac{\omega}{\omega_\tau}[\cos(\frac{\omega_\tau}{\omega}2\pi)-1]\right)}{PwYs_o^{Y-1}\pi\cos\alpha}\right| \tag{3.27a}$$

Which is, obviously, a function of the cutting conditions (the spindle speed, N, the feed, f, and the depth of cut, w) , the cutting force parameters (the force exponential Y, the force constant P, the penetration parameter, C) , the elastic structure parameters of the machine tool and the workpiece (the equivalent stiffness, k, the damping ratio, ζ, and the natural frequency ω_n), the chatter frequency, ω, and SSV frequency, ω_τ.

Noticing $\frac{1}{2}\tau\frac{\omega}{\omega_\tau}[\cos(\frac{\omega_\tau}{\omega}2\pi)-1] << \pi T_o$, Equation (3.27a) can be simplified

$$J_o(\omega\tau)\sin\omega T_o \le \left|\frac{2\pi\omega\varsigma\frac{k}{\omega_n}+PwYs_o^{Y-1}C\frac{\omega}{60}\cos\alpha\pi T_o}{PwYs_o^{Y-1}\pi\cos\alpha}\right| \qquad (3.27b)$$

Theoretically, from the value of the 0-th order Bessel function, we can obtain a value of $\omega\tau$. And, if the chatter frequency ω is on-line identified, the SSV amplitude can be determined from $\Delta N=\frac{\tau N_o^2}{60}$. However, three concerns have to be emphasized: (1) Unconditional stability increment: Since stability increment index (SII) is inversely proportional to the 0-th order Bessel function $J_o(\omega\tau)$, and for a given $J_o(\omega\tau)$, there are usually more than one value of $\omega\tau$, SII curve consists of a series of lobes. The readings between two lobes stand for conditional stability increment, while the profile curve of these lobes implies unconditional stability increment. The unconditional stability increment values should be used to estimate the effective SSV amplitude. The unconditional stability increment corresponds to the profile curve of 0-th order Bessel function $J_o(\omega\tau)$. Utilizing the profile curve of the 0-th order Bessel function $J_o(\omega\tau)$, we can read a single value of $\omega\tau$. (2) Sideband effect: As shown, there is an infinite number of sidebands $\{J_1(\omega\tau), J_2(\omega\tau),\ldots,J_n(\omega\tau)\}$ with multiple SSV frequency.

Although in the range of $\omega_\tau t \in (0, 2\pi)$, the sideband averaging effect is almost zero, they still have instantaneous effect in a vibration cycle, since the SSV frequency ω_τ is much smaller than the chatter frequency ω. Further discussion can be found in the following section. (3) Final suppression and immediate suppression: The minimum SSV amplitude determined by the energy analysis is SSV amplitude that can finally suppress chatter as $t \to \infty$, which might be meaningless for practical applications. The minimum SSV amplitude for immediate chatter suppression is desired in the numerical simulation and the corresponding experiments. When choose the minimum SSV amplitude for immediate chatter suppression, the instantaneous sideband effect has to be considered.

3.6.2 Bessel function values and their profile curves

Let's first investigate Bessel functions of the first kind, of order n (see Equation (3.15)), the values of $J_n(\omega\tau), n = 0,1,2,3,...$ can be numerically simulated. It will be noted that some of the values appear as negative quantities. If two sidebands have Bessel function values of opposite sign, it indicates that their vectors have opposite polarity. Figure 3.7 displays the amplitude of 0-th order Bessel function and sidebands. For a given ωτ, at the moment, t, the sidebands with opposite polarity weaken even cancel each other, and the instantaneous sideband effect can be roughly determined by the profile curve. We assume that, within the region of commonly used SSV amplitudes and frequencies, the profile curve of the sidebands can be approximated by

$$J_{profside}(\omega\tau) = ae^{b\omega\tau} + c \tag{3.28}$$

Where, the constants a, b, and c can be determined with the following constraints:

$$\frac{d}{d(\omega\tau)} \max[J_n(\omega\tau), n = 1,2,3,...] = \frac{d}{d(\omega\tau)} J_{profside}(\omega\tau) \tag{3.29}$$

$$\max[J_n(\omega\tau), n = 1, 2, 3, \ldots] = J_{profside}(\omega\tau) \tag{3.30}$$

For simplicity, the parameters a, b, and c are found by the least square estimation: $a \approx 0.5, b \approx -0.29, c \approx 0.3$. So, the profile curve is described by

$$J_{prof}(\omega\tau) = 0.5e^{-0.29\omega\tau} + 0.3 \tag{3.31}$$

Similarly, we can find the profile curve of the 0-th order Bessel function, which ensures the minimum stability increment:

$$J_{profo}(\omega\tau) = 0.85e^{-0.32\omega\tau} + 0.22 \tag{3.32}$$

With the effect of the sidebands, Equation (3.27) is modified as

$$J_{profo}(\omega\tau)\sin\omega T_o + J_{profside}(\omega\tau) \le \left| \frac{2\pi\omega\varsigma\dfrac{k}{\omega_n} + PwY\mathrm{s}_{\mathrm{o}}^{\mathrm{Y}-1}C\dfrac{\omega}{60}\cos\alpha\pi T_o}{PwYs_o^{Y-1}\pi\cos\alpha} \right| \tag{3.33}$$

3.6.3 Selecting SSV Amplitude

For a given SSV frequency ω_τ, a practical procedure of selecting SSV amplitude is proposed as follows: (1) According to the cutting conditions, the cutting force parameters, the elastic structure parameters, the chatter frequency and the selected SSV frequency, calculate the value of

$$\left| \frac{2\pi\omega\varsigma\dfrac{k}{\omega_n} + PwY\mathrm{s}_{\mathrm{o}}^{\mathrm{Y}-1}C\dfrac{\omega}{60}\cos\alpha\pi T_o}{PwYs_o^{Y-1}\pi\cos\alpha\sin\omega T_o} \right| \tag{3.34}$$

(2) Let $J_{profo}(\omega\tau)\sin\omega T_o + J_{profside}(\omega\tau)$ be less or equal to the above value. Then the value of ωτ, thus the value of τ, can be determined.

(3) The minimum SSV amplitude is selected from $\Delta N = \frac{\tau N_o^2}{60}$.

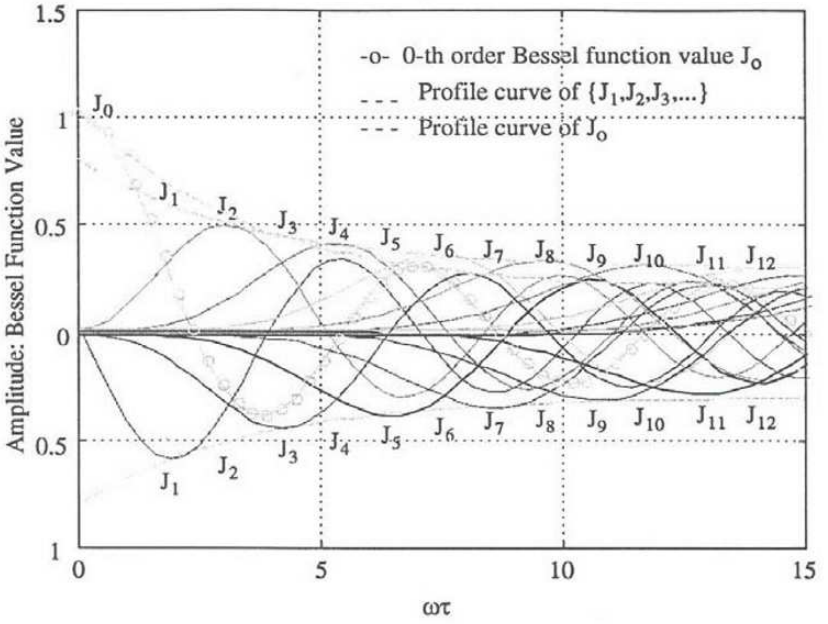

Figure 3.7. Bessel function values and profile curve

The above procedure of selecting SSV amplitude can be in-line implemented to construct a closed loop SSV cutting. In industrial machining processes, the cutting conditions are changing with operation requirements (for instance, forming the OD profile of a shaft, roughing and finishing), and the elastic structure and the chatter frequency are also varying with time, closed loop SSV cutting is definitely necessary.

Examples:

The above procedure of selecting SSV amplitude is demonstrated by the following example: An unstable constant speed cutting process with the following cutting conditions is demonstrated: the spindle speed N=490 rpm, the feed f=0.1 mm/rev,

the depth of cut w=4 mm. The chatter frequency ω is identified as 653 rad/sec (104 Hz), and SSV frequency ω_τ is selected as 5.65 rad/sec (0.9 Hz), find the required SSV amplitude for chatter suppression.

(1) Calculate

$$\left| \frac{2\pi\omega\varsigma\dfrac{k}{\omega_n} + PwYs_o^{Y-1}C\dfrac{\omega}{60}\cos\alpha\pi T_o}{PwYs_o^{Y-1}\pi\cos\alpha\sin\omega T_o} \right| = 0.61$$

(2) From $J_{profo}(\omega\tau)\sin(\omega 60 / N_o) + J_{profside}(\omega\tau) = 0.61$, $\omega\tau = 8.8$ is obtained, and thus $\tau = 8.8/\omega = 0.0135$ is found.

(3) The minimum SSV amplitude

$\Delta N = \dfrac{\tau N_o^2}{60} = 54$ rpm and is predicted for immediate chatter suppression. Denoted as 'o', this point is shown in Figure 3.8.

According to simulated SSV cuttings, the minimum effective SSV amplitude is about 60 rpm (see Figure 3.9d). This SSV amplitude is verified by machining experiments (see Figure 3.10, record on tape 3:58). Figures 3.9 and 3.10 display chatter displacement signals and the spindle speed under the following cutting conditions: spindle speed N = 430, 490, 550, 490+60sin(2π0.9t) rpm, feed f = 0.1 mm/rev, depth of cut w = 4 mm. The simulations and corresponding experiments demonstrate that the SSV method does increase the machining stability, that is, the machining process is stable with SSV cutting when the process is expected to be unstable under constant speed cutting. As shown, three constant speed cuttings are unstable, however, the SSV cutting, with its spindle speed varying within the unstable region, is stable.

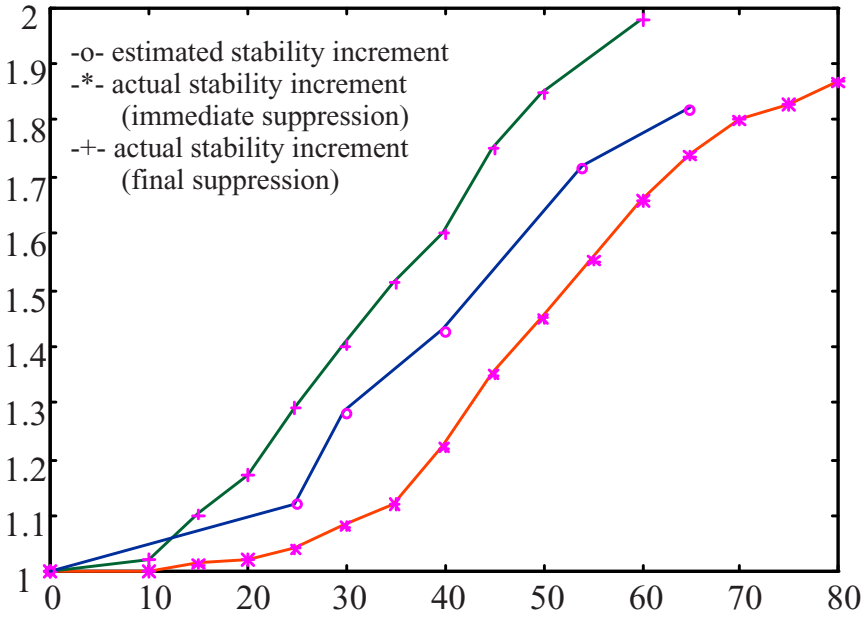

Figure 3.8. Verification by simulated SSV cuttings

Actual stability increment for immediate chatter suppression is slightly smaller than the estimated. In Figure 8, the actual stability increment for immediate chatter suppression is shown as '*'. Another set of data corresponding to final chatter suppression are also obtained (denoted as '+' in Figure 3.8), it can be observed that, actual stability increment for final chatter suppression is slightly larger than the estimated. Therefore, the estimated effective SSV amplitude is a value between the actual SSV amplitude for final chatter suppression and the actual SSV amplitude for immediate chatter suppression. More examples are summarized in Figure 3.8.

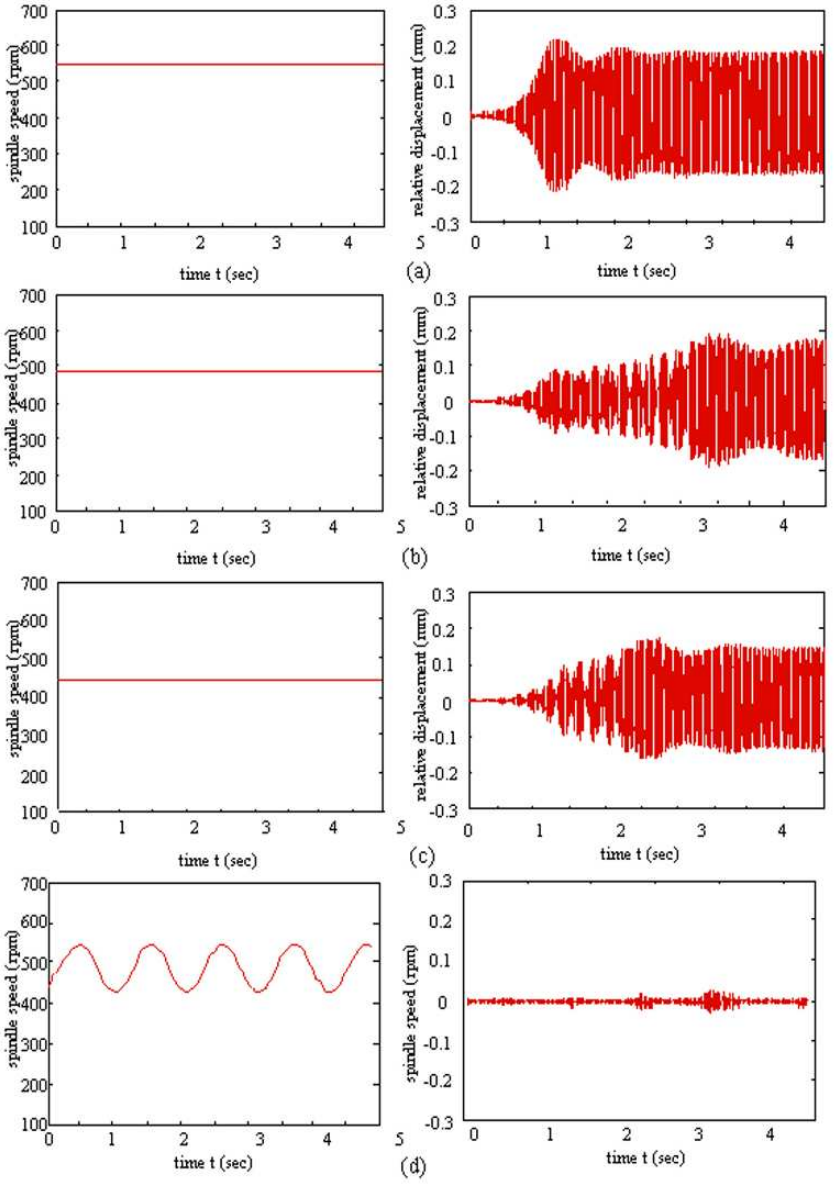

Figure 3.9. Simulated constant speed and minimum SSV cuttings: Cutting conditions: N = $490 \pm 60 \sin(2\pi 0.9t)$ rpm, f = 0.1 mm/rev, w = 4 mm

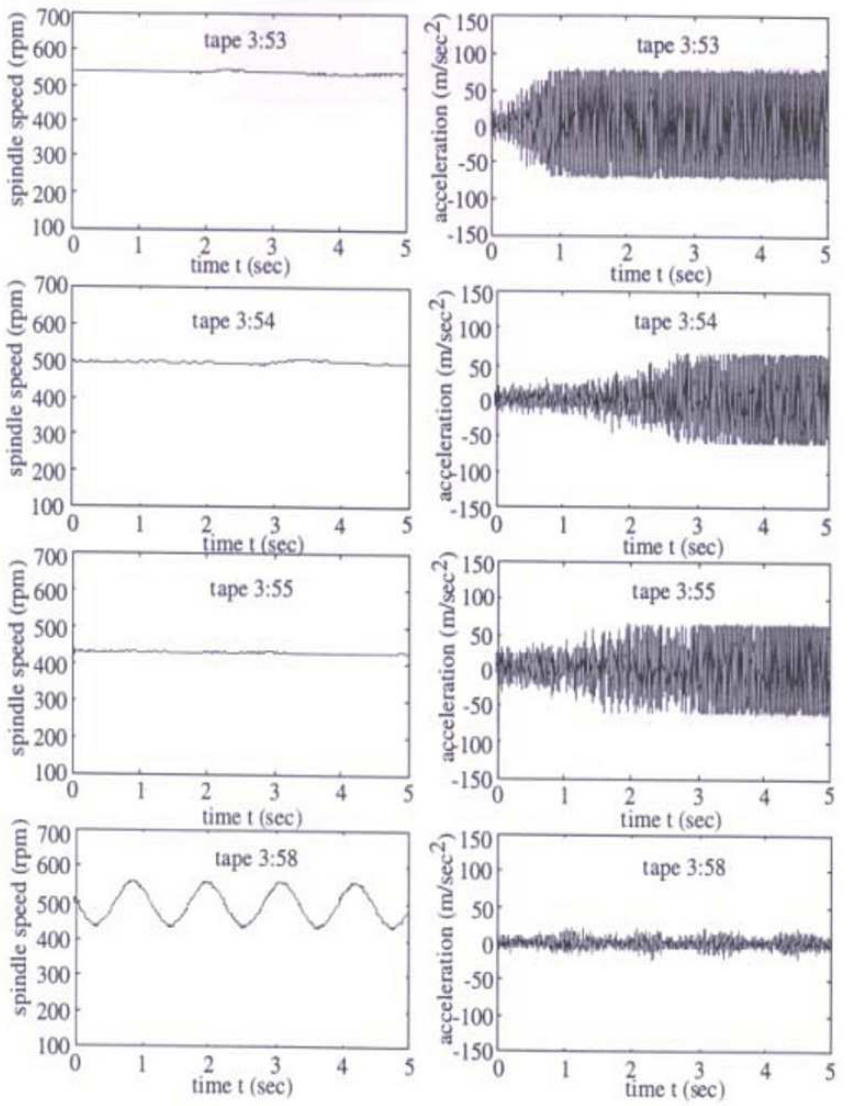

Figure 3.10. Experiment of constant speed and minimum SSV cuttings. Cutting conditions: N = $490 \pm 60\sin(2\pi 0.9t)$ rpm, f = 0.1 mm/rev, w = 4 mm

3.7 Conclusions

In this chapter, through a systematic approach for theoretical analysis on SSV cutting analysis, the following results are achieved: The characteristic equation of SSV cutting is derived. From the characteristic equation, the stability region of SSV cutting is determined, which is proved being larger than the stability region of constant speed cutting. The stability increment index (SII) is proposed to measure the stability increase by means of SSV cutting. This is not only a proof of SSV method but also a measurement of its stability augment.

A procedure of selecting SSV amplitude is proposed based on the energy analysis. This procedure is validated by experimental results. During the machining process, the cutting condition, the cutting force parameters, the elastic structure and the chatter frequency are varying with time, a closed loop SSV cutting is desired. This procedure of selecting SSV amplitude can be in-line implemented to construct a closed loop SSV cutting. This is a very important result for industrial applications of SSV method.

Acknowledgements

The chapter contributors wish to thank Inderscience publishers for granting permissions to reproduce work presented in this chapter. Authors acknowledge the helpful discussions with Professor Hanmin Shi regarding SSV method.

References

[1] ElMaraghy, H.A., 2007 “Reconfigurable Process Plans for Responsive Manufacturing Systems”, Digital Enterprise Technology: Perspectives & Future Challenges, Edited by P.F. Cunha and P.G. Maropoulos, Springer Science, pp. 35-44

[2] El’yasberg, M.E., and Binder, M.G., 1989 “Reducing Self-excited Vibration of Machining Tools by Periodic Low-frequency Changes in Cutting Speed”, Soviet Engineering Research, pp. 102-106

[3] Englehardt, R., Lin, S. C., Devor, R. E., and Kapoor, S. G., 1989 "A Verification of the Use of Variable Spindle Speed for Vibration Reduction in

Face Milling", Proc. of the 17th NAMRI/SME Conference, Vol. 17, pp. 115-122

[4] Hoshi, T., Sakisaka, N., Moriyama, I., and Sato, M., 1977 "Study for Practical Application of Fluctuating Speed Cutting for Regenerative Chatter Control", *Annals of the CIRP*, Vol. 25, pp. 175 - 179

[5] Inamura, T. and Sata, T., 1974 "Stability Analysis of Cutting under Varying Spindle Speed", *Annals of CIRP*, Vol. 23

[6] Jayaram, S., Kapoor, S. G., Devor, R.E., 2000 "Analytical Stability Analysis of Variable Spindle Speed Machining", J. of Manufacturing Science and Engineering, Vol. 122

[7] Jemielniak, K., and Widota, A. 1984 ",Suppression of Self-Excited Vibration by the Spindle Speed Variation Method", *Int. J. Mach. Tools Res.*, Vol. 24, No. 3

[8] King, R. I., 1985 *Handbook of High Speed Machining Technology*, Chapman and Hall

[9] Li, C.J., Ulsoy, A.G., Endres, W.J., 2006 "The Effect of Spindle Speed Variation on Chatter Suppression in Rotating-Tool Machining", Material Science Forum, Vols. 505-507, pp. 859-864

[10] Lin, S. C., Devor, R. E. and Kapoor, S. G., 1990 "The Effects of Variable Speed Cutting on Vibration Control in Face Milling", Trans. of the ASME, *J. of Eng. for Ind.*, Vol. 112, pp. 1-11

[11] Liu, K. J., and Rouch, K. E., 1992 "Optimal Cutting Process Stability in Milling Using Active Dynamic Absorber", *Active Control of Noise and Vibration*, DSC-Vol. 38, ASME, pp. 275-283

[12] Namachchivaya, N.S., and Beddini, R., 2003 "Spindle Speed Variation for the Suppression of Regenerative Chatter", *J. of Nonlinear Science*, Vol. 13, pp. 265-288

[13] Sandvik Coromant, 1985 *Turning Guide*, Fair Lawn, N. J.

[14] Sexton, J. S., Miline, R. D. and Stone, B.J., 1977 "A Stability Analysis of Single-point Machining with Varying Spindle Speed", *Appl. Math. Modelling*, Vol. 1

[15] Sexton, J. S. and Stone, R. J., 1978 "The Stability of Machining with Continuously Varying Spindle Speed", *Annals of CIRP*, Vol. 27, pp. 321-326

[16] Sexton, J. S. and Stone, R. J., 1980 "An Investigation of the Transient Effects during Variable Speed Cutting", *J. Mechanical Engineering Science,* Vol. 22, No. 3

[17] Shi, H. M., 1986 "Effects of Some Nonlinear Factors on Machine Tool Chattering and Their Mathematical Models", *J. of Huazhong Univ. of Sci. & Tech.*, Vol. 7, No. 1, pp. 9-22

[18] Shi, H. M. and Tobias, S. A., 1984 "Theory of Finite Amplitude Machine Tool Instability", *Int. J. Mach. Tool Des. Res.*, Vol. 24, No. 1, pp. 45-69

[19] Shiraishi, M., Yamanaka, K., and Fujita, H., 1991 "Optimal Control of Chatter in Turning", Int. J. Mach. Tools Manufact., Vol. 31, No. 1, pp. 31-43

[20] Slavicek, J., 1965 "The Effect of Irregular Tooth Pitch on Stability of Milling", 6th MTDR Conference

[21] Stoferle, T., and Grab, H., 1972 "Vermeiden von Ratterschwingungen durch periodische Drehzahlanderung", Werkstatt und Betrieb, Vol. 105
[22] Stone, B. J., 1970 "The effect on the chatter behaviour of machine tools of cutters with different helix angles on adjacent teeth", *Proc. M.T.D.R.*
[23] Takemura, T., Kitamura, T. and Hoshi, T., 1974 "Active Suppression of Chatter by Programmed Variation of Spindle Speed", *Annals of CIRP*, Vol. 23
[24] Takemura, T., Kitamura, T. and Asada, H., 1976 "Active Suppression of Chatter by Programmed Variation of Spindle Speed (Second Report)", *Precision Machinery* , Vol. 42, No. 11
[25] Takemura, T., Kitamura, T. and Hoshi, T., 1977 "Active Suppression of Chatter by Programmed Variation of Spindle Speed (Third Report)", *Precision Machinery*, Vol. 43, No. 10
[26] Tsao, T. C., McCarthy, M., and Kapoor, S. G., 1993 "A New Approach to Stability Analysis of Variable Speed Machining Systems", *International Journal of Machine Tools and Manufacturing*, Vol. 33, pp. 791-808
[27] Valenite Inc., 1993 *Handy Reference Guide*, Troy, Michigan
[28] Wu, B., Yang, G., and Yu, J., 1992 "The Influence of Speed Variation Parameters on the Effect of Chatter Suppression in Vari-Speed Face Milling", *2nd International Conference on Machine Dynamics and Engineering Applications*, Zhenjiang, China
[29] Yilmaz, Alpay, Al-Regib, Emad, Ni, Jun, 2002 “Machine Tool Chatter Suppression by Multi-Level Random Spindle Speed Variation”, J. of Manufacturing Science and Engineering, Vol. 124
[30] Zhang, H., Ni, J., and Shi, H., 1994 "Machining Chatter Suppression by Means of Spindle Speed Variation", Part I & Part II, S.M. Wu Symposium on Manufacturing Science, Vol. 1, pp. 161-167, & pp. 169-175
[31] Zhang, H., 1996 "Chatter Modeling, Analysis and Control for CNC Machining Systems", Ph.D. dissertation, The University of Michigan – Ann Arbor.

Chapter 4

Micromachining from a Materials Perspective

M. J. Jackson, W. Ahmed and G. M. Robinson

4.1 Introduction

Mechanical micro machining is a technique that has the potential to become a successful small scale manufacturing process. If the abilities of macro machining can be scaled down to the micro scale then a versatile manufacturing technique will be created that is capable of processing a wide variety of materials. However, simply scaling down machines is not the solution, reducing the scale from macro-to-micro presents unique problems that must be overcome that include eliminating tool wear, machining heterogeneous workpiece materials in a uniform manner, and advances in machine tool design. Therefore, a review of the aspects of machining is presented that focuses on the machining process from a materials perspective.

4.2 Machining Theory

In the 1940's Ernst and Merchant [1], Merchant [2,3], developed models for orthogonal cutting, i.e. the situation where the tool and the workpiece are both perpendicular to each other (Figure 4.1), where undeformed material shears as it passes through a primary shear zone (Figure 4.2). The simplified model ignores secondary shear that exists between the tool and chip. Earlier work by Piispanen [4] stated that the shearing process of metal is similar to cutting a deck of stacked cards (Figure 4.3). The cards are inclined at an angle φ that matches the shear angle. As the cards approach the

tool they are forced to slide over each other when they encounter the resistive force provided by the tool. There are many assumptions made to reach this point but the analogy helps visualize the cutting process. Merchant [2] began the metal cutting analysis by making the following assumptions.

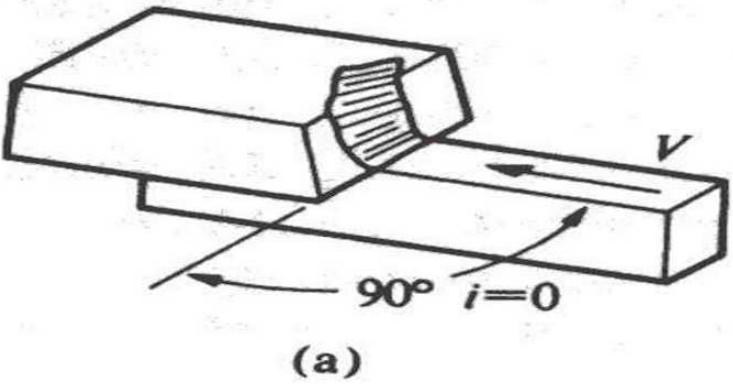

Figure 4.1. Orthogonal Cutting Conditions [5]

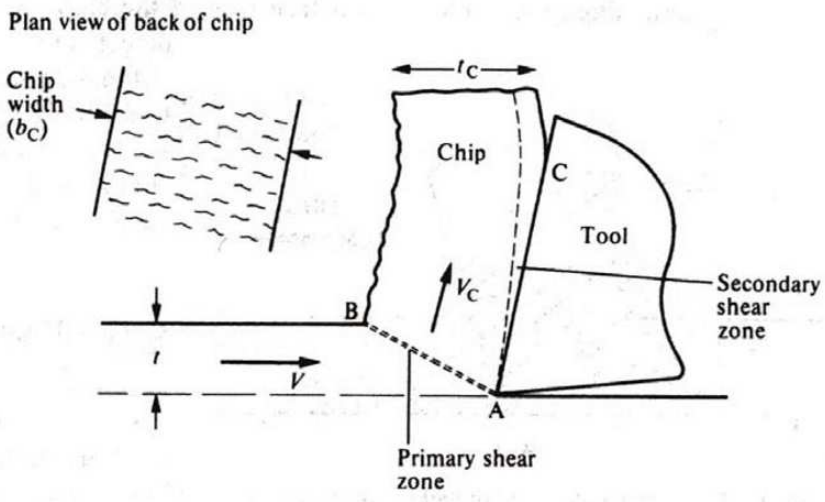

Figure 4.2. Undeformed Material Passes Through the Shear Zone [5]

The following analysis is taken from Shaw [5] and is based on Merchant's approach:

1. The tool is perfectly sharp and there is no contact along the clearance face;
2. The shear surface is a plane extending upward from the cutting edge;
3. The cutting edge is a straight line extending perpendicular to the direction of motion and generates a plane surface as the work moves past it;
4. The chip does not flow to either side;
5. The depth of cut is constant;
6. The width of the tool is greater than the width of the workpiece;
7. The work moves relative to the tool with uniform velocity;
8. A continuous chip is produced with no built-up edge;
9. The shear and normal stresses along the shear plane and tool are uniform.

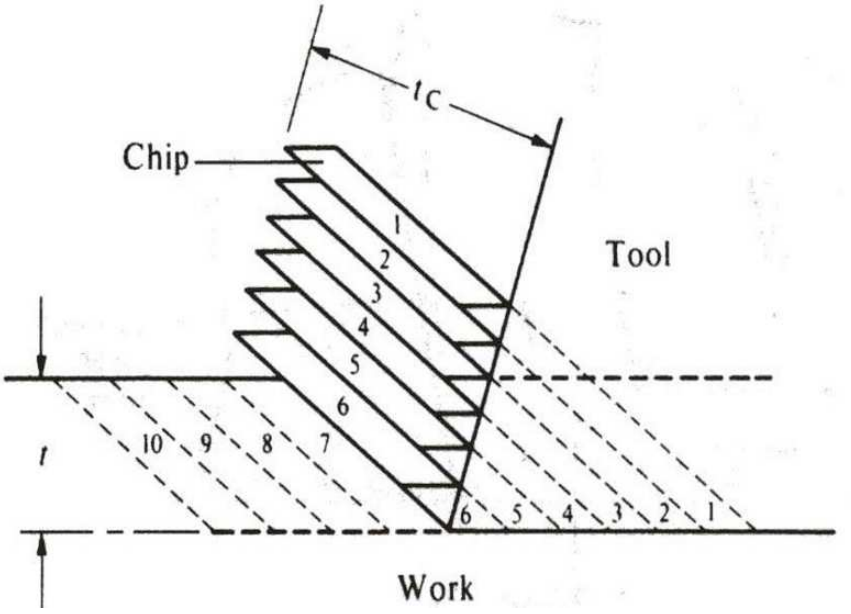

Figure 4.3. Piispanen's [4] Stacked Card Analogy of metal cutting

The forces acting between the chip and tool can be identified and isolated in a free body diagram (Figure 4.4). At equilibrium the force between the tool and chip R, is equal to the force between the workpiece and chip, R'. These resultant forces can be broken up into their constituent components.

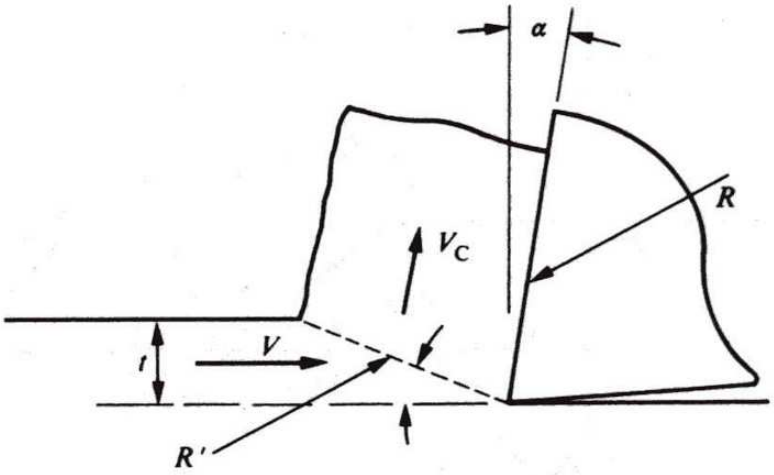

Figure 4.4. Isolation of Forces on a Free Body Diagram [5]

R is broken up in to forces perpendicular, N_C and along, F_C the tool face. R' can be broken up into two sets of components, horizontal, F_P and vertical, F_Q relative to the direction of motion and along, F_S and perpendicular, N_S to the shear plane (Figure 4.5). These forces can be rearranged and applied at the tool tip while being contained within a circle. This is Merchant's [2,3] circle of cutting forces and is fundamental to metal cutting theory (Figure 4.6). From this circle a range of equations can be generated that describe the cutting process. Only a few forces need to be measured with a dynamometer before these equations can be applied; the equations are listed below where α is angle between the vertical and the tool face called the rake angle and φ is the shear plane angle.

$$F_S = F_P \text{Cos}\varphi - F_Q \text{Sin}\varphi \quad (4.1)$$

$$N_S = F_Q \mathrm{Cos}\varphi + F_P \mathrm{Sin}\varphi \tag{4.2}$$

$$N_S = F_S \mathrm{Tan}(\varphi + \beta - \alpha) \tag{4.3}$$

Where β is the friction angle and μ the coefficient of friction and is given by;

$$\mu = \mathrm{Tan}\beta \tag{4.4}$$

$$F_C = F_P \mathrm{Sin}\alpha + F_Q \mathrm{Cos}\alpha \tag{4.5}$$

$$N_C = F_P \mathrm{Cos}\alpha - F_Q \mathrm{Sin}\alpha \tag{4.6}$$

$$\mu = \frac{F_C}{N_C} \tag{4.7}$$

$$\mu = \frac{F_P \mathrm{Sin}\alpha + F_Q \mathrm{Cos}\alpha}{F_P \mathrm{Cos}\alpha - F_Q \mathrm{Sin}\alpha} \tag{4.8}$$

$$\mu = \frac{F_Q + F_P \mathrm{Tan}\alpha}{F_P - F_Q \mathrm{Tan}\alpha} \tag{4.9}$$

The shear stress τ is given by;

$$\tau = \frac{F_S}{A_S} \tag{4.10}$$

Where,

$$A_S = \frac{bt}{\mathrm{Sin}\varphi} \tag{4.11}$$

Here, b is the width of cut and t is the depth of cut, therefore the shear stress is;

$$\tau = \frac{(F_P Cos\varphi - F_Q Sin\varphi)Sin\varphi}{bt} \tag{4.12}$$

Similarly, the normal stress σ is given by.

$$\sigma = \frac{N_S}{A_S} \tag{4.13}$$

$$\sigma = \frac{(F_P Sin\varphi + F_Q Cos\varphi)Sin\varphi}{bt} \tag{4.14}$$

An equation for φ is still required. It is found experimentally that when certain metals are cut there is no change in density. The subscript C refers to the chip and l is the length of cut.

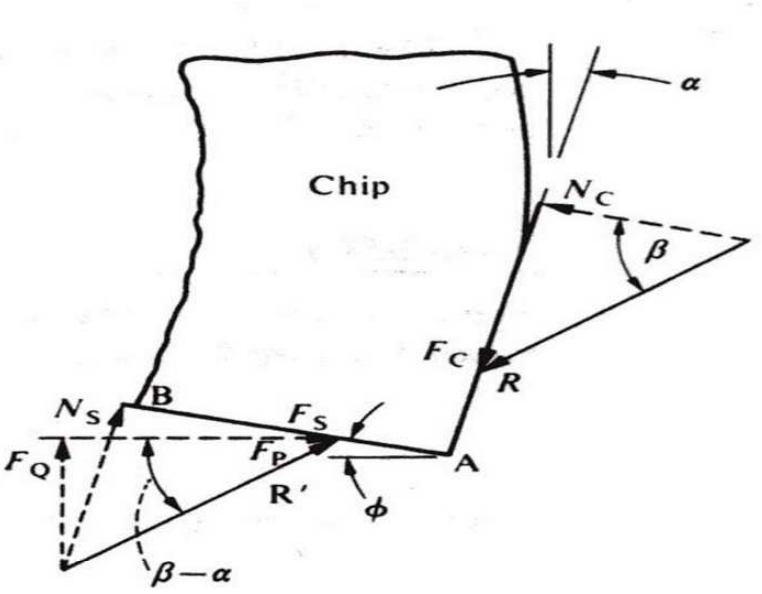

Figure 4.5. Identification of the Constituent Components of Force [5]

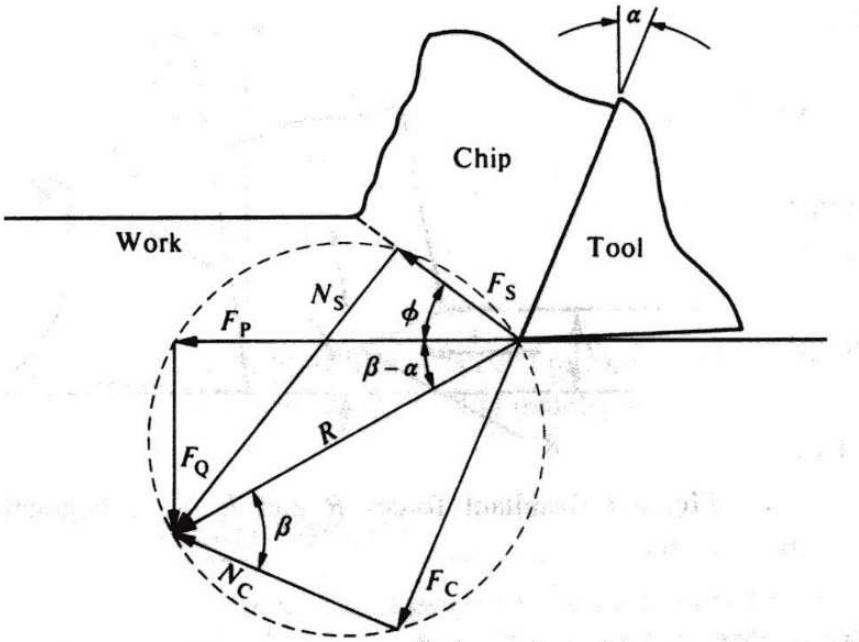

Figure 4.6. Merchant's Circle of Cutting Forces [2,3]

Therefore;

$$tbl=t_C b_C l_C \tag{4.15}$$

It is found experimentally that if b/t≥5 the width of the chip is the same as the workpiece thus.

$$\frac{t}{t_C} = \frac{l_C}{l} = r \tag{4.16}$$

Where, r is the cutting ratio, or chip thickness ratio;

$$r = \frac{t}{t_C} = \frac{ABSin\varphi}{ABCos(\varphi - \alpha)} \tag{4.17}$$

Where, AB refers to the length of the shear plane. Solving for the shear angle φ.

$$\text{Tan}\varphi = \frac{r\text{Cos}\alpha}{1 - r\text{Sin}\alpha} \tag{4.18}$$

The work length may be determined by weighing the chip, if the chip weighs w_C and γ' is the specific weight of the metal then.

$$l = \frac{w_C}{tb\gamma'} \tag{4.19}$$

The shear strain γ is given by;

$$\gamma = \frac{\text{Cos}\alpha}{\text{Sin}\varphi\text{Cos}(\varphi - \alpha)} \tag{4.20}$$

Expressions can also be developed for the cutting velocity V, which is the velocity of the tool relative to the work and directed parallel to F_P. The chip velocity V_C is the velocity of the chip relative to the tool and directed along the tool face. The shear velocity V_S is the velocity of the chip relative to the workpiece and direct along the shear plane.

$$V_C = \frac{\text{Sin}\varphi}{\text{Cos}(\varphi - \alpha)} V \tag{4.21}$$

Or,

$$V_C = rV \tag{4.22}$$

$$V_S = \frac{\text{Sin}\alpha}{\text{Cos}(\varphi - \alpha)} V \tag{4.23}$$

Or,

$$V_S = \gamma \mathrm{Sin}\varphi V \tag{4.24}$$

The shear strain rate γ" is given by

$$\gamma'' = \frac{\mathrm{Cos}\alpha}{\mathrm{Cos}(\varphi - \alpha)} \frac{V}{\Delta y} \tag{4.25}$$

Where Δy is the thickness of the shear zone and is often approximated by assuming its value is equal to the spacing between slip planes. It is not always convenient to measure all the quantities required to apply the equations. Therefore, Merchant and Zlatin [6] produced a number of nomographs that can be used to obtain some of these quantities without the need for extensive experiments (Figure 4.7).

Not all machining operations are similar to these idealized cutting conditions, for example the process of milling. Not only are the contact conditions not orthogonal, they are oblique, but there are multiple cutting points. The surface marks produced by milling can be seen but feel smooth to touch however there are peaks and valleys similar to surface roughness. The height of these peaks and troughs or scallops, h can be determined by,

$$h = \frac{f}{4(D/f) \pm (8n/\pi)} \tag{4.26}$$

Where, D is the diameter of the cutter, f is the feed per tooth and n is the number of cutting teeth. Expressions are also available for the undeformed chip thickness and the length of cut. Under certain cutting conditions complications can arise with the assumptions made for ideal cutting. The strain and heat generated at the interface between the chip and tool, called the secondary shear zone, can be so high that part of the chip welds to the tool. This welded material effectively becomes part of the tool that changes its overall geometry and cutting conditions; this is called a built-up edge. In turn this affects the depth of cut and quality of surface finish. With time the built-up edge grows so large that the shear forces are high enough to

remove it and another built-up edge begins to form, the process is therefore dynamic.

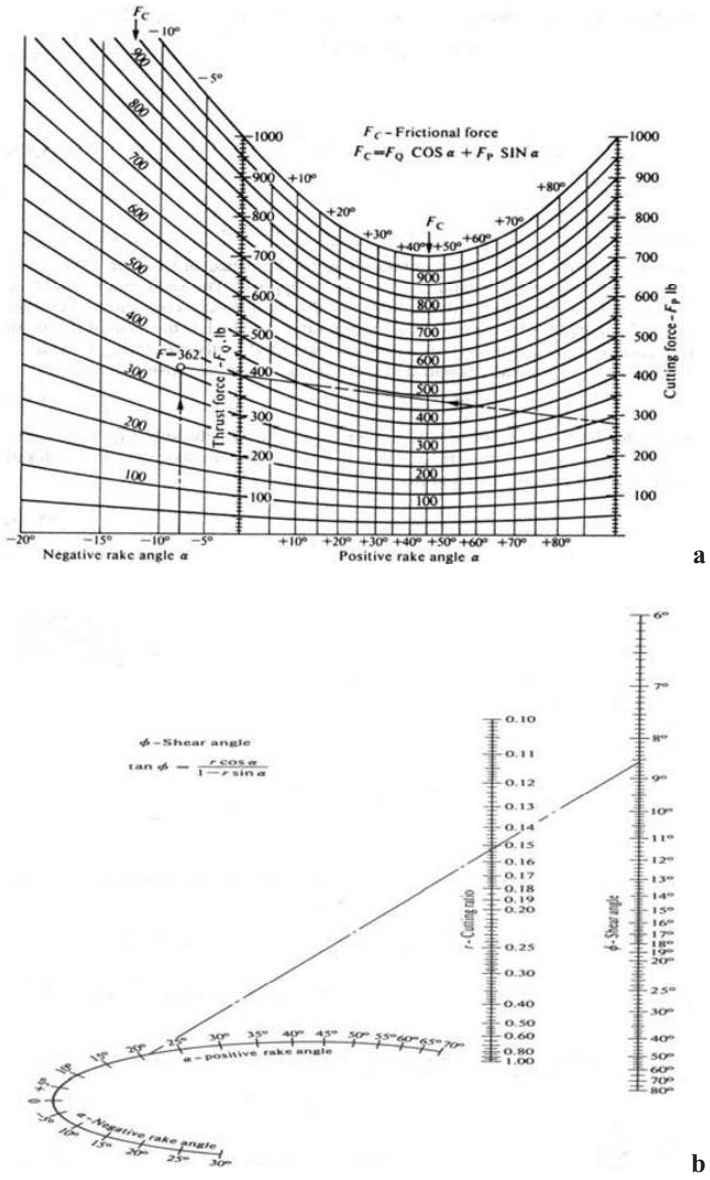

Figure 4.7 (a) and (b). Merchant and Zlatin's Nomographs [6]

A secondary effect of a built-up edge is additional heat is generated. At the point where the chip adheres to the tool its velocity is zero. At the free surface of the chip, the velocity of the chip is at a maximum and in between there is a velocity gradient. This gradient is made possible by internal shear of the chip, which is the source of additional heating. Therefore, the presence of a built-up edge disrupts the cutting process and ideally should be avoided.

In order to predict cutting forces the shear plane angle must be determined, Merchant continued his reasoning and assumed that the shear plane angle would take a value so that the total power consumed would be a minimum. Merchant also reasoned that the shear stress would be influenced by the normal stress, he arrived at an equation that Piispanen [4] had previously independently determined. However, depending on the assumptions made a variety of equations can be generated for the shear angle. Stabler [7], Lee and Shafer [8] and Oxley [9] developed such equations. For the conditions likely to be encountered an approach that best matches the assumptions and constants can be selected and acceptable results gained. The failure to generate a widely accepted single model therefore highlights the complexity of the cutting process due to the vast number of variables involved. A comprehensive review of the machining process at the microscale that takes account of the size effect has been provided by Shaw [10] and Shaw and Jackson [11]. A comprehensive review of metal cutting at the macroscale has been recently published by Shaw [5].

4.3 High Speed Machining

High speed machining is usually defined by spindle speeds between 30,000 and 100,000 revolutions per minute (rpm). Machining at high speed yields advantages such as increased metal removal rate, reduced cutting forces, increased dissipation of heat and better surface roughness. Schulz [12] discussed the advantages that can only be gained by machining at high speed; which are summarized in Table 4.1. An unwanted effect of high speed machining is that tool wear rate often increases.

Benefit	Application Field	Application Examples
Large cutting volume per machining time.	Light metal alloys, steel and cast iron.	Aircraft and aerospace production, die and mould manufacturing.
High surface quality.	Precision machining, special workpieces.	Optical industry, fine mechanical parts.
Low cutting forces.	Processing thin walled workpieces.	Aircraft and aerospace industry, automotive industry.
High frequencies of excitation.	No machining in critical frequencies.	Precision mechanisms and optical industry.
Heat transported by the chips.	Machining of workpieces with critical heat influence.	Precision mechanisms magnesium alloys.

Table 4.1. Summary of the Advantages of High Speed Machining Discussed by Schulz [12]

However, Schulz [12] found that improving the following can extend tool life: (1) Cutting parameters, i.e. machine at an optimized feed rate and cutting speed; (2) Contact conditions, i.e. optimizing tool angles and tool/workpiece contact geometry; (3) Workpiece material, i.e. use an easy to machine workpiece where possible; (4) Cutting tool, i.e. ensure sharpness, correct geometry, and isolation from vibrations, also select a cutting tool material that has a low potential for diffusion into the workpiece; (5) Machining strategy, i.e. ensure the tool path does not impart large forces on the tool or workpiece. Schulz [12] found that if these five areas are optimized then surface roughness produced is often better than roughness operations such as grinding. Eliminating post processing decreases lead-time and cost thus providing high speed machining with an

advantage over conventional machining operations. The first application of high speed machining was to cut aerospace materials such as titanium and nickel-based alloys; cutting speeds between 30 and 100m/min were achieved with conventional carbide tools. However, these speeds can be significantly increased if ceramic tools are used. Usui, Hirota and Masuko [13] constructed a cutting model based on an energy approach; later Usui and Hirota [14] extended the model to examine chip formation and cutting forces with a single point tool. Finally, Usui, Shirakashi and Kitagawa [15] investigated thermally activated wear mechanisms for ceramic tools. To establish the tool edge temperature a 25μm diameter wire was inserted into a Si_3N_4 tool, which is subsequently sintered and ground until the wire is exposed at the rake face. Experimental work by Kitagawa, Kubo and Maekawa [16] showed that tool temperature increases with cutting speed (Figures 4.8 and 4.9) and that rake face temperature is higher than the flank face temperature. Usui [13,14] points towards evidence suggesting that tool wear is triggered by thermally activated processes and to a lesser extent by abrasive processes. Burr height decreases and the quality of surface roughness is found to increase with increasing cutting speed. Usui [13,14] also observed at a cutting speed of 150m/min that the temperature was 1200^0C, which is close to the melting temperature of the workpiece alloy. The dominant wear mechanisms for Al_2O_3+TiC and Si_3N_4 ceramic tools were found to be notch and crater wear respectively, with the Al_2O_3+TiC tool having the lowest wear rate. Kitagawa [16] also found that Taylor's tool life equation could be used for calculating the life of ceramic tools.

Ozel and Altan [17] produced finite element models of high speed machining by using a variable coefficient of friction to take account of the dynamic cutting situation at the tool-chip interface. The model predicts chip curl that is a result of large strains and thermal expansion. The degree of chip curl is found to be heavily dependent on cutting speed; above 300m/min chip curl develops early, but if the feed per tooth is increased chip curl begins later. Higher cutting speeds therefore reduce the chip thickness. The model produced by Ozel [17] predicts cutting forces decrease with increasing cutting speed in the high-speed machining regime. Ozel's

model also predicts a rise in feed rate increases the cutting forces along the tool edge due to an increased chip load. An application of such models is their use in predicting some of the constants required by metal cutting theory.

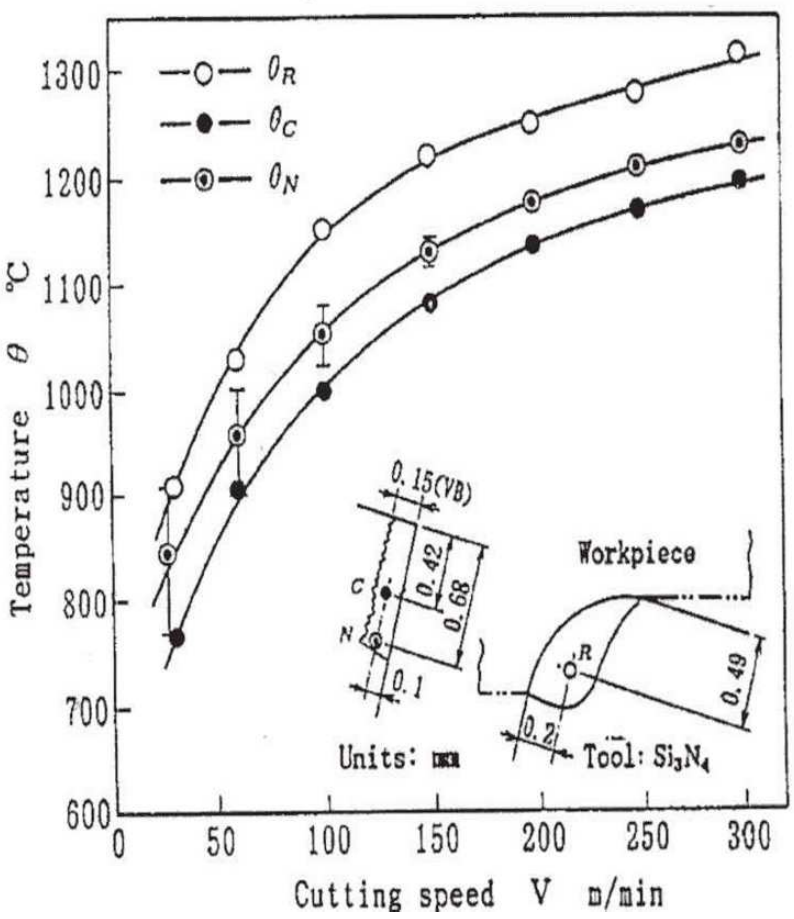

Figure 4.8. A Graph of the work of Kitagawa et al. [16] Showing that an Increase in Cutting Speed Produces an Increase in Temperature.

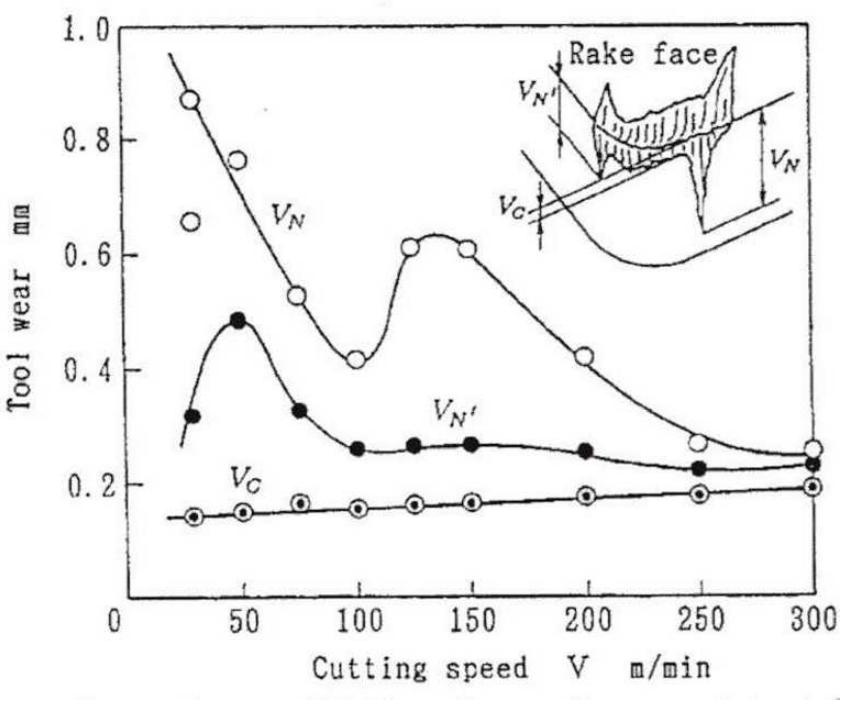

Figure 4.9. A Graph of the work of Kitagawa et al. [16] Showing the Variation of Temperature on the Tool with Increasing Cutting Speed

Traditional approaches to machining yield useful information about the cutting forces but little regarding the stress distribution. A finite element approach can be used to predict stress distribution across the tool. It is shown that critical chip loads are applied when the cutting edge enters and exits the workpiece; stresses during chip formation are not significant. The rake face temperature is predicted to be higher than the primary shear zone temperature and the maximum tool tip temperature is found a short distance from the tool edge. This implies that frictional contact provides a further source of heating as the chip slides over the tool. During high speed machining heat is generated in the primary shear zone and at the tool-chip interface. For steel, cutting temperatures are predicted to reach between 500^{O}C and 1000^{O}C as shown by Moufki, Molinari and Dudzinski [18]. The coefficient of friction has a significant effect on heat generation but its value is not constant because it depends on

dynamic factors such as the rake angle, feed and cutting speed, Bailey [19]. Therefore, precisely measuring or predicting the tool-chip interface temperature is a challenging problem. Montgomery [20] showed that at large sliding velocities a reduction in the coefficient of friction is observed when the normal pressure or sliding velocity is similarly increased. Therefore, despite the large number of models that have been generated using finite element analysis to predict cutting forces, tool wear and temperature, no existing model adequately accounts for all aspects of cutting and results are not always satisfactory, in particular predictions of temperature. The models are validated by comparing predicted temperatures to directly measured experimental data obtained using thermocouples demonstrated by Groover and Kane [21], infrared sensors demonstrated by Wright and Trent [22] and chip microstructure analysis demonstrated by Fourment, Oudin, Massoni, Bittes, and Le Calvez [23]. The models are then used to calculate cutting temperature in an attempt to determine if machining problems are likely to be encountered. For example high temperatures can cause an unacceptable change in the workpiece microstructure or thermal softening of the tool. If either problem is predicted corrective action can be taken prior to the onset of machining. Although Moufki [18] has shown that thermal softening is not usually sufficient to overcome strain hardening in the workpiece material. Finite element analysis by Kim and Sin [24] can accurately predict the way in which chips form. However, it is difficult to quantify the contributions made by different mechanisms because the situation is dynamic, i.e. the coefficient of friction is dependent on the sliding velocity or normal pressure, which changes as the tool advances (Figure 4.10 and 4.11). Trent and Wright [25] observed during slow speed machining that the condition of chip sliding is dominant, during high speed machining the condition of seizure is dominant and somewhere in between there is a transition between sliding and seizure. Seizure occurs when the apparent area of contact equals the actual area of contact; this is in agreement with the work on friction carried out by Doyle, Horne and Tabor [26]. Seizure takes place when the normal stress exceeds the materials shear strength allowing complete contact between tool and chip. Seizure therefore is a major source of tool wear and is characterized

by craters located near to the tool edge. Gekonde and Subramanian [27] predicted that these craters have a maximum depth that correlates to the phase change temperature rather than the maximum temperature as first thought. The phase change temperature is sufficient to cause dislocation generation, which leads to diffusion wear. Gekonde [27] also found that total tool wear is the net results of mechanical and chemical wear. Mechanical wear remains constant and is independent of the cutting speed, whereas chemical wear in the form of diffusion increases with cutting speed because conditions of seizure are more prevalent at higher speed. Therefore, at high speed the contribution to tool wear made by mechanical wear is inconsequential compared to the contribution made by chemical wear. Metal cutting theory is well established but its application can sometimes be difficult, especially when applied to milling; for example Gygax [28] found the rapid periodic impact of each cutter often makes reading a dynamometer challenging.

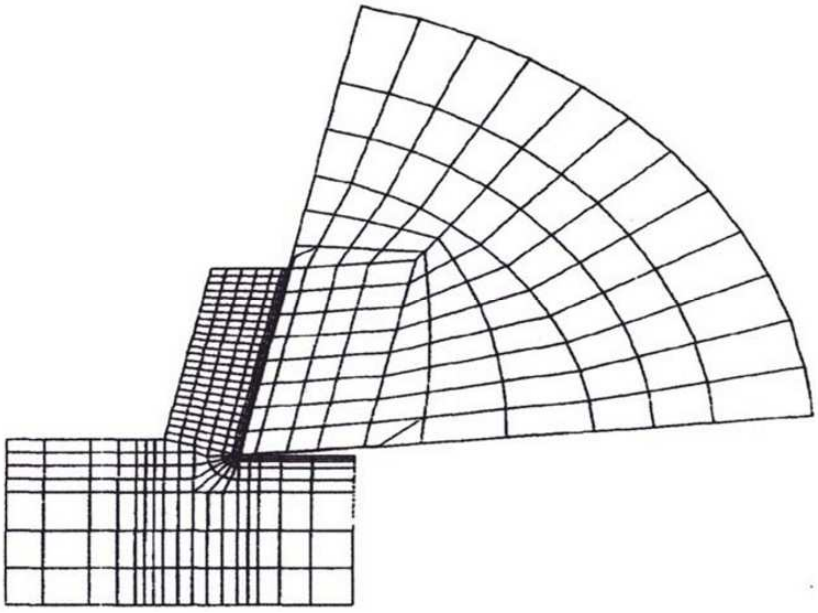

Figure 4.10. The Finite Element Mesh Produced by Kim and Sim [24] to Model the Cutting Process

Some metal cutting approaches require a number of variables to be measured before the theory can be applied in earnest. Such approaches are accurate but require a great deal of experimental time and effort. Other approaches only measure a few parameters and consequently are less accurate but easier to work with. Rotberg [29] decided the best approaches utilize a large number of sensors, a few experimental results and idealized cutting conditions to generate a complete range of machining data. These models are useful because they can predict cutting forces and determine what conditions are likely to be encountered prior to machining e.g. seizure or sliding. Schmitt [30] points out that high-speed milling is not always the most suitable method for machining.

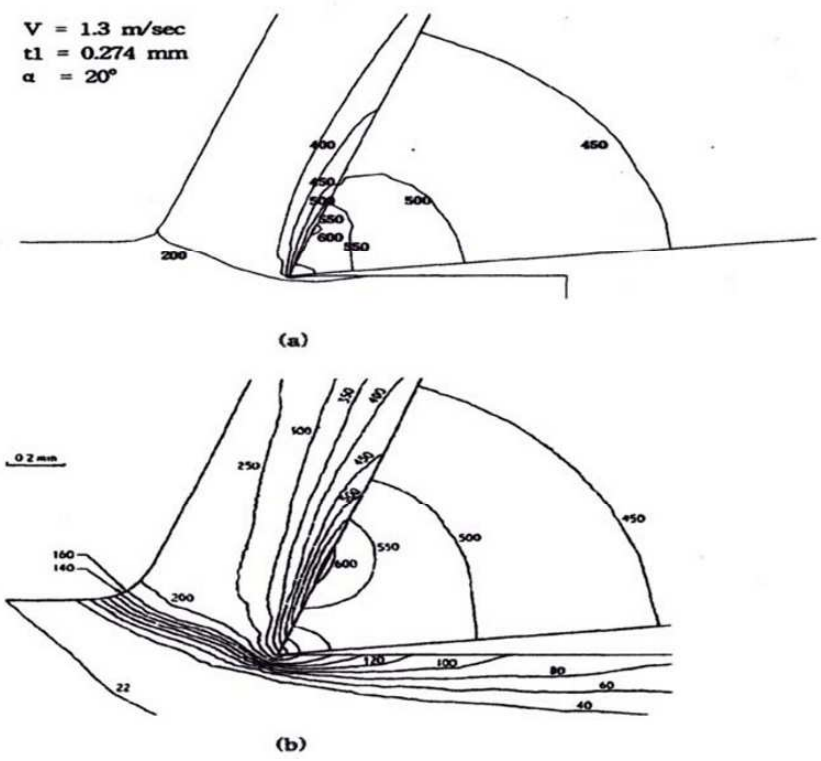

Figure 4.11. The Cutting Temperature Distribution Produced by Kim and Sim's [24] Finite Element Analysis to Model the Cutting Process

It is usually employed specifically where its attributes are critical for successful machining of the part, e.g. thin ribs in the aerospace industry. Spindles are often selected by their power because this gives them the capability to machine a certain material. One of the main restrictions on spindle speed is the bearings capacity to operate at high speed. Schmitt [30], Weck and Staimer [31] and Ibaraki et al. [32] considered different methods of creating the working envelope. It was found that a hexapod structure is more stable than the construction of a conventional milling machine and produces better results in terms of surface roughness. This is because the hexapod (Figure 4.12) does not suffer from vibrations caused by jerk (the rate of change of acceleration) that result from the high accelerations and speeds required for high speed machining.

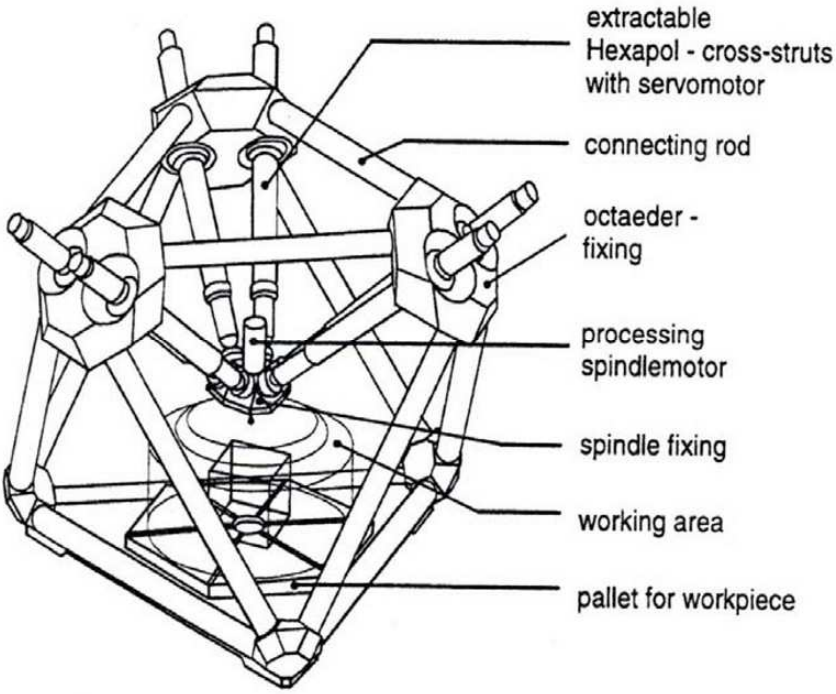

Figure 4.12. The Hexapod Machine Structure Considered by Schmitt [30]

Moller [33] summarized the special requirements of high-speed spindles. He found that the best designs had no transmission, achieved high speeds with low vibration, were liquid cooled leading to high thermal stability and had low inertia which allows high accelerations and decelerations. Another significant challenge identified by Moller [33] is the problem of selecting bearings suitable for operation at high speed. It is suggested bearings should be lubricated to reduce friction and aid heat dissipation, however at high speeds ceramic bearings perform better and the use of lubrication is brought into question. Moller [33] also showed the advantages of cutting at high speed include a reduction in force (Figure 4.13). Cohen and Ronde [34] have proposed that hydrostatic bearings could operate successfully at high speed. A pressurized fluid held in reservoir by localized pockets provides the force to separate two surfaces. The hydrostatic bearing has a load capacity determined by the product of its pocket area and pocket pressure; this places a restriction on the size and shape of the bearing. Optimum rigidity occurs when the gap between both surfaces is a minimum. However a smaller gap produces a greater pressure loss, which results from a velocity profile created across the fluid by the high shaft speed. Additionally hydrostatic bearings eliminate run out, hence they are often used on machine tools that machine optical materials.

4.4. Cutting Tool Wear

Establishing the point at which the tool is considered worn is important because after this point machining results are no longer acceptable. If the onset of unacceptable tool wear can be identified, the tool can be changed with no impact upon the part. Tansel et al. [35] applied neural networks to this problem, by training neural networks to monitor cutting forces and based on past failures the critical point of future tool wear could be identified. However, Tansel et al. [35] found this method was only reliable with a soft workpiece. Ingle, Subramanian, and Kay [36] investigated crater wear, which is a major contributor to overall tool wear, which is composed of chemical and mechanical wear (Figure 4.14).

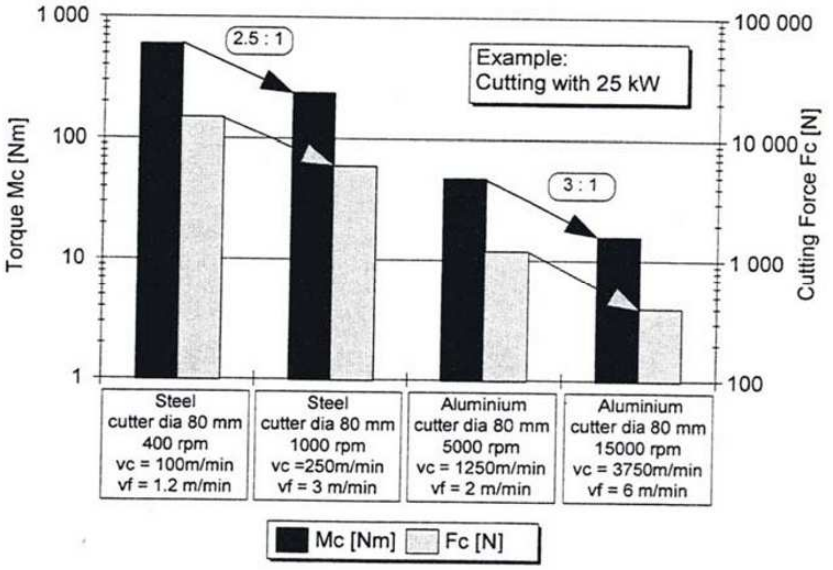

Figure 4.13. Force Reduction by Using High Speed Cutting [33]

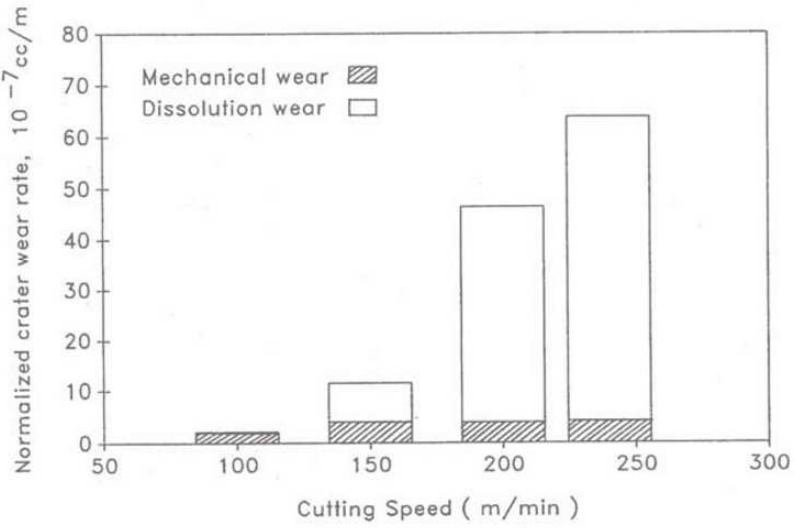

Figure 4.14. The Contribution Made to Overall Wear by Chemical and Mechanical Sources [36]

Ingle [36] machined calcium treated AISI 1045 grade steel with a cemented carbide tool containing 97% tungsten carbide, 0.4% Ta(Nb)C and 2.6% cobalt. An expression based on the work of Bhattacharyya and Ham [37] and Bhattacharyya, Gosh and Ham [38] was developed to estimate the amount of tungsten transported by diffusion during the cutting time.

$$W = 1.1284C_o.f.t.(D/\tau)^{1/2}(\text{contact area}) \quad (4.27)$$

Where, W is the amount of tungsten dissolved, C_o is the equilibrium concentration of W at interface, F is the ferrite volume fraction, t is the cutting time, D is the diffusivity of tungsten in ferrite, and τ is the tool chip contact time. It was found if a tungsten carbide tool was used to machine steel, a TiN coating decreased the thermodynamic potential for dissolution by six orders of magnitude compared to the uncoated case. Ingle [36] also found that cutting speed affected the cutting temperature; at 50m/min the temperature was $1337^{O}K$ and at 240m/min the temperature was $1512^{O}K$. A reason contributing to this temperature rise is the tool chip contact area also increases with increased cutting speed. In related work, Subramanian, Ramanuhacher, and Ingle [39] found diffusion is the main source of crater wear when machining AISI 1040 grade steels with a tungsten carbide tool at speeds of 175m/min and higher. At these high cutting speeds the tribological condition of seizure dominates tool wear and therefore defines tool life. Subramanian [39] found that during chip deformation thermoplastic shear occurs causing localized heating which is sufficient to allow diffusion of the tool material into the chip. Naerheim and Trent [40] observed a concentration gradient of tool material in the chip, specifically W and Co near the chip-tool interface. Subramanian [39] conducted experiments coated and uncoated tools made from K1 cemented tungsten carbide containing 85%WC, 4%(TaC/NbC) and 11%Co. For uncoated and coated tools the amount of tungsten present in the chips is measured by neutron activation analysis. Total tool wear is composed of mechanical wear and chemical wear. A loss of tungsten carbide particles from the workpiece characterizes mechanical wear and a loss of tungsten carbide by dissolution characterizes chemical

wear. The initial amount of tungsten in the workpiece was 11+/-0.5ppm (parts per million). For the uncoated tungsten carbide tool at 150m/min the amount of tungsten dissolved in the chip is 1.5ppm whereas at 240m/min this amount is 10.5ppm. However, the amount of tungsten carbide found in the chip is approximately constant, regardless of the cutting speed, around 0.8ppm.

To test the effectiveness of a 10μm thick CVD deposited HfN coating, experiments were performed at cutting speeds of 220 and 240m/min and the concentrations of tungsten in the chips was found to be 11.3+/-0.1 and 11.2+/10.1ppm, respectively. It was therefore concluded that at high cutting speeds a thin HfN coating was successful at preventing dissolution of tungsten from the workpiece. Therefore, Subramanian [36] predicted that dissolution is prevented by coating the tool with a barrier layer that has the least thermodynamic potential for dissolution. For example, neutron activation analysis has shown a cemented carbide tool with a CVD deposited HfN coating drastically reduces diffusion. An alternative method to provide a diffusion barrier can be to engineer inclusions into the workpiece, e.g., oxides and sulphides, which can also aid chip formation. During testing of the HfN coated tools, Subramanian [39] employed a technique suggested by Hastings, Mathew and Oxley [41] that was based on a method developed by Boothroyd [42] to determine the chip temperature. Coated tools were found to be $75^{O}C$ lower in temperature and regardless of cutting speed it was found that HfN coatings prevented dissolution crater wear.

Subramanian [36] also tested the effectiveness of adding inclusions in the workpiece, it was found that they were equally as effective as the HfN coating at cutting speeds between 220-240m/s. However as cutting speed increased the effectiveness of the inclusion barrier is reduced and diffusion wear increases. The contribution made by mechanical wear to the amount of tungsten in the chips is 0.8ppm and is independent of cutting speed. However, the contribution of tungsten in the chips made by dissolution increases sharply with increasing cutting speed, e.g., at 150m/min there is 66% dissolution wear but at 240m/min there is 93% dissolution wear. Subramanian [36] concludes by stating that when

machining steels, the solubility of tungsten carbide in austenite is increased at higher temperatures, which results from the condition of seizure. Additionally, the presence of ultra fine grain boundaries provides high diffusivity paths, which increase dissolution wear. If there is no coating the tool can loose a large amount of tungsten by dissolution to the chips. Sherby, Orr and Dorn [43] found that creep resistance of a metal is higher than its self-diffusion activation energy. Sherby [44] found during high temperature deformation that the formation of sub boundaries, grain boundary shear, and fine slip are related to interatomic diffusion. These static diffusion studies by Sherby [44] can help explain the dynamic diffusion present at the tool-chip interface. Gregory [45] studied diffusion between a cemented carbide tool of composition WC74%, Co10% and TiC16% and a workpiece material of Armco iron of composition C0.05%, Mn0.05%, S0.028%, P0.01% and Fe balance. Specimens were diffused under vacuum at temperatures of 1100, 1175, 1250 and $1325^{O}C$ (Figures 4.15 (a) and (b)). These results were compared to a tool subjected to orthogonal cutting of the Armco iron at 370ft/min for one hour with a feed rate of 0.0015in/min. Gregory [45] produced graphs charting the composition of the diffusion couples indicate the first stage of diffusion is the outward migration of the cobalt binder phase followed by a build-up of titanium carbide in the reaction zone. The activation energy triggering cobalt diffusion was found to be 83k.cal/mole, which is comparable to 72.9k.cal/mole determined in another study by Suzuoka [46]. After the diffusion phase, a period of stable of wear sets in; this can be considered comparable to the run-in of a tool. Trent [47] suggests the stable period of wear is due to the presence of titanium carbide, which is more difficult to take into solution in steel compared to tungsten carbide. For titanium carbide to leave the tool material a thermal activation energy of 124k.cal/mole is required. However, for titanium carbide to diffuse into the iron-cobalt reaction zone energy levels of 150k.cal/mole are needed. Upon further examinations of the diffusion couples, Gregory [45] decided that wear resistance was also aided by a titanium carbide rich zone that builds up close to the wearing surface. Gregory [45] argued that final wear is explained by the continual diffusion of the titanium carbide zone.

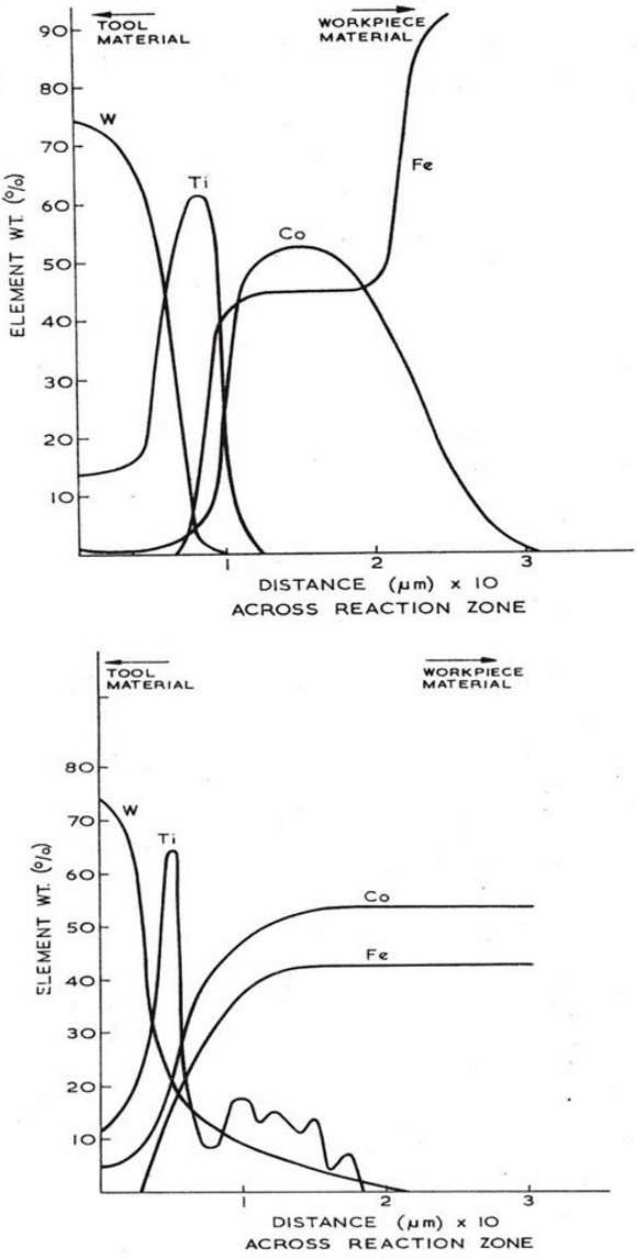

Figure 4.15 (a) and (b). Examples of Diffusion Couples Tested by Gregory [45]

The activation energies of its constituents are: 98k.cal/mole for the inward diffusion of iron, 142k.cal/mole for the volume diffusion of iron in tungsten and 77.5k.cal/mole for the outward diffusion of tungsten during the whole process. These energies point towards grain boundary diffusion mechanisms because Danneberg [48] found that the volume self-diffusion energy of tungsten was between 110 and 121k.cal/mole.

Nayak and Cook [49] reviewed some thermally activated methods of tool wear. Nayak [49] found models attempting to predict thermally triggered wear mechanisms using continuum diffusion theory experience difficulties when the workpiece material and tool material are similar e.g. cutting steels with high-speed tool steel. This is because the model assumes diffusion is driven by the concentration gradient of the diffusing material; hence there is a problem when this gradient is small. An alternate approach is to assume that vacancy concentration is the mechanism driving diffusion. This approach is successful in describing the wear of cemented tungsten carbide cobalt tools. Another approach is to explain wear as the result of a loss of hardness due outward diffusion of interstitial atoms into the chip, however this method is in poor agreement with experiments conducted. Consideration was given to a number of thermally activated processes that could trigger wear. Characteristics identifying the wear mechanism were determined so that an examination of experimental results would reveal the process responsible. Nayak [49] conducted a series of experiments and data was obtained using M2 tool steel hardened to HRC 65. Initially wear, temperature, and cutting forces increased rapidly followed by a prolonged steady state period; eventually catastrophic wear occurs. Wear rate was defined as the rate of increase of crater depth. It was concluded from the best information available; whilst crater temperature distribution is uniform the wear rate is uniform. The size distribution of the wear particles was examined because this can yield information about the wear mechanism. For example if large wear particles are observed it is inferred that they result from asperity fracture caused by plastic flow. However, if different wear particles are observed then plastic flow cannot have occurred and an alternative wear mechanism must be present. There is no evidence that an asperity fracture model can predict wear. A creep model

could explain the triggering of wear but the wear rate is calculated at $4x10^{-12}$in/sec, which is six orders of magnitude less than that observed; this trigger mechanism is therefore rejected. Depletion of interstitial carbon atoms was also investigated; if this mechanism were active a loss of hardness leading to wear by plastic flow would be observed. Diffusion couples were constructed to test this possibility. 0.18%C and 0.9%C steels were heated to temperatures between 1200^{O}F and 1300^{O}F for several hours. Carbon diffusion was in the opposite direction to that expected; it was found that high-speed steel was carburized by low and high carbon content steel. Therefore, this mechanism is rejected because the tool should loose and not gain carbon.

Wear by the removal of oxide films is rejected because no change is observed when machining in an oxygen free environment and there is not enough oxygen in the material to cause the required effect. Nayak [49] also considered tempering wear. At critical temperatures transition carbides such as W_2C and Mo_2C can form, thus reducing tool hardness due to tempering. The equation, $V = 1.4x10^{15}e^{-90000/RT}$ in/sec can be derived for the tool wear rate, V, which agrees reasonably well with experiments conducted. R is the universal gas constant (cal/mol) and T is the absolute temperature (Kelvin). However, equations predicting other machining parameters generated during the derivation of this equation predict significantly different results to those observed. Atomic wear is also investigated, the energy required for atomic wear is provided thermally rather than mechanically by the applied stresses. Because tool atoms are in a higher energy state than chip atoms overall migration is from tool to chip where atoms flow to low energy sites in the chip such as vacancies. This mechanism depends on the difference in free energy, the concentration of low energy sites in the chip, the activation energy required for an atom to jump from the tool to the chip, the available thermal activation energy and the frequency of atomic vibration. If these factors are considered an equation describing the wear rate V, can be developed, thus V is equal to $\upsilon Ae^{-Q/RT}$, where υ is the atomic vibration frequency (1/s), a is the atomic spacing (in), Q is the energy barrier for the atomic jump (kcal/mol), R is the universal gas constant (cal/mol) and T is the absolute temperature

(Kelvin). Q and A variables are dependent on the work material. The tool-chip interface is considered similar to a grain boundary interface and therefore the activation energy Q required for an atomic jump is also similar; this is in the order of 40-45kcal/mole as determined by Leymonie and Lacomb [50]. The atomic vibration frequency is approximately10^{14}/sec and the atomic spacing approximately 10^{-8}inch, yielding, $v=10^{6}e^{-42000/RT}$in/sec which is in excellent agreement when cutting 1018, 1045, 4140 and 10C-40C steels. At low cutting speeds mechanical wear is dominant, it can take two forms; abrasion due to ploughing and adhesion due to the formation and subsequent breakage of metallic bonds. These wear mechanisms depend on the hardness ratio between the tool and workpiece, environmental pressure and temperature, the presence of hard constituents and the presence of severe reagents.

A statistical model for the predictions of tool wear can be developed; Davis [51] suggested a Monte Carlo approach for modeling mechanical wear based on the following assumptions. Quanta of energy are added to the rubbing particles all of which leave the same site. The quanta of energy are added to the particles at domains randomly spaced over the surface at moments randomly spaced in time. The quantized energy of a particle over the surface diffuses continuously into the material at a known rate. Finally the surface energy of a particle causes it to detach as a wear particle. Bhattacharya and Ham [37] extended this approach developing expressions for the width of flank wear due to mechanical wear from abrasive and adhesive sources. The width of the flank wears, $H_f(T)$, at time T is given by:

$$H_f(T) = K''V_C T^{1-\alpha} \tag{4.28}$$

Where, V_c is the cutting velocity, T is the cutting time, α is the clearance angle, and K" is given by:

$$K''=3K'/2C'(1-\alpha) \tag{4.29}$$

Where, C' is given by:

$$C'=C^2/\sigma^2 \tag{4.30}$$

Where C is a constant, σ is the deviation from the mean and K' is given by:

$$K'=\frac{Km}{\rho\left(\frac{Tan\alpha}{1-Tan\gamma Tan\alpha}\right)} \tag{4.31}$$

Where ρ is the density of tool material, m is the mass of the wear particle, γ is the true rake angle, and K is the constant governing decay rate. The height of flank wear, h_f, can also be determined by:

$$h_f=\left[\frac{5}{4}\frac{KV_cA^{\frac{3}{4}}(1-Tan\alpha Tan\gamma)T}{bTan\alpha}\right] \tag{4.32}$$

Where A is a constant based on the tool and workpiece combination and b is the width of cut. This model worked well when applied to experiments conducted by Bhattacharyya, Ghosh and Ham [38] and experiments conducted by the internationally recognized tool wear collection body OECD/CIRP. However, a large amount of data for specific tool and workpiece combinations must be collected before this approach can be used. Bhattacharyya [38] points out the reliability of the model depend on the accuracy of the data, making this approach susceptible to compounded errors. It is also inconvenient to collect a large amount of data every time new machining conditions are encountered.

4.5 Tool Coatings

In environments where tools experience high wear forces and extreme pressure sintered tungsten carbide tools are used. However, ultra hard materials such as silicon alloys, abrasive materials, synthetic materials and composites can only be machined with

diamond-coated tools. Faure, Hanni, Schmutz and Gerovanoni [52] discussed the main issues involving diamond coatings.

Thin uncoated tool edges are susceptible to rounding and therefore must be protected. Coating the tool with a hard material such diamond does not offer sufficient protection because there is a sharp hardness gradient between the tool and its coating. Upon impact this gradient causes the coating to break therefore exposing tool material to the usual wear mechanisms. This effect can be reduced if an interlayer is introduced with a hardness between the tool material and diamond e.g. TiC/TiN. Such an interlayer reduces the severity of the hardness gradient and enhances adhesion between the diamond and tool. Diamond is an ideal coating material; it has high hardness, high wear resistance and is chemically inert. However it is difficult to coat steels, Ni alloys, cemented carbides and alloys containing transition metals with diamond. It is possible to coat WC-Co, but the cobalt must be etched away or a diffusion barrier introduced Jackson et al [53].

Faure [52] applied a $TiCl_4$ precursor to the tool before depositing an interlayer in a CVD reactor at a temperature between $900^{O}C$ and $1000^{O}C$. 1% methane in hydrogen gas is introduced at a flux of 2000 sccm at a pressure of 20mbar to a CVD chamber that has a tantalum filament, graphite work holders and a working surface area of $200cm^2$. These conditions allow a diamond film to grow on the tool. The tool material coated was a 6% Co tungsten carbide. A cobalt etch was undertaken before deposition of a TiN interlayer and a TiN/TiC multilayer. Seeding with a solution of diamond micro grains was performed prior to deposition of the diamond coating. The coating effectiveness was assessed by a 'Revetest' test device and drilling experiments. The 'Revetest' device applies a constant force to an indenter during constant velocity displacement of the sample and critical loads are identified by an acoustic signal (Figure 4.16 (a) and (b)). Drilling tests were performed at 69,000rpm at 3.5m/min with a 1mm diameter drill. The critical load causing coating failure is a function of the substrate hardness and the strength of adhesion between coating and tool. It is common for a soft substrate to deform plastically while its coating does not

because it has a high Young's modulus. The coating alone bears the load and fails thus exposing tool material to wear mechanisms (Figure 4.17). Diamond coatings with a TiN interlayer (Figure 4.18) can withstand 10 times more force compared to diamond coatings without the interlayer; adhesion is not necessarily better but toughness is improved. Both cases with and without an interlayer offer a significant improvement over tools with no coating where rounding of the tool edge is observed after drilling only one hole (Figure 4.19). If a TiC/TiN/TiC multilayer is applied large forces, around 100N, are required to break the surface. It was found that thicker interlayers improved adhesion between the tool and diamond coating and interlayers with a Young's modulus between that of the tool and diamond coating produced better machining results. Uncoated tools were able to drill 10,000 holes and coated tools drilled 20,000 holes before they were considered worn. Uncoated tools experienced rounding of the cutting edge.

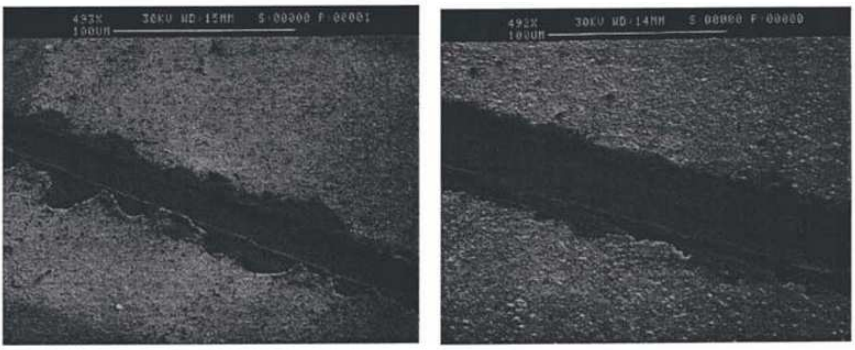

Figure 4.16 (a) and (b). Scratch Tests Performed by Faure [52] to Determine the Adhesion of Diamond Coatings

Bell [54] categorized tool materials into three basic groups, high-speed steels, cemented carbides and ceramic and super hard materials including alumina based composites, sialons, diamond and cubic boron nitride. In addition the surface properties of these materials can be modified with the coatings varying in thickness between 10^{-1} – 10^{4}μm (Figure 4.20). Tool wear can be defined by the following description, 'A cutting tool is considered to have failed

when it has worn sufficiently that dimensional tolerance or surface roughness are impaired or when there is catastrophic tool failure or impending catastrophic tool failure'. To prevent failure Mills [55] suggests surface modification techniques such as coating should be employed to improve tool performance. PVD has the capability to deposit wear resistant ceramic layers on high-speed tool steels. Although CVD can be used PVD appears to be advantageous in terms of coating adhesion and producing coatings with compressive stresses. It is increasingly being discovered that cubic boron nitride is an effective tool coating. Different machining processes are characterized by different wear mechanisms (Figure 4.21) and the choice of tool coating should be selected to offer the best protection for a particular set of machining conditions; e.g. the combination of wear rate, bearing pressure and tool material (Figure 4.22).

Figure 4.17. Fracture of the Coating [52]

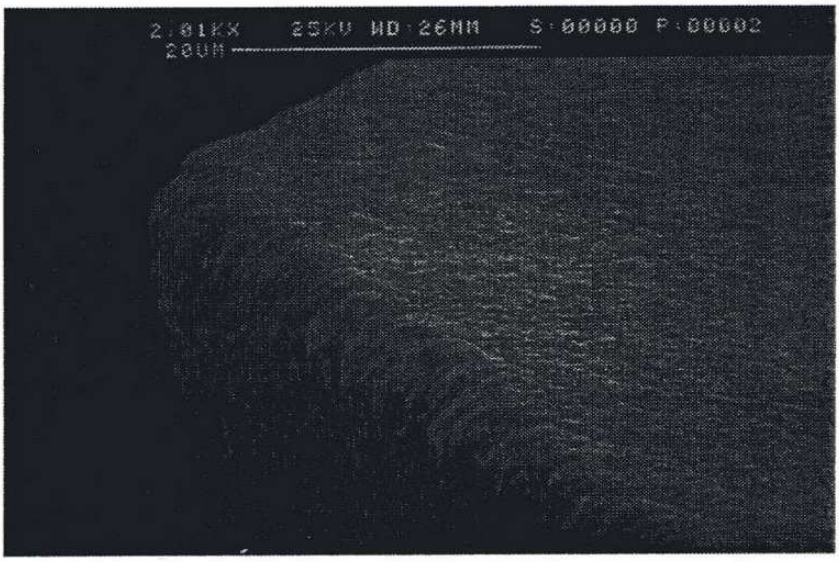

Figure 4.18. A Drill Produced by Faure [52] with an Interlayer and a Diamond Coating Before Testing

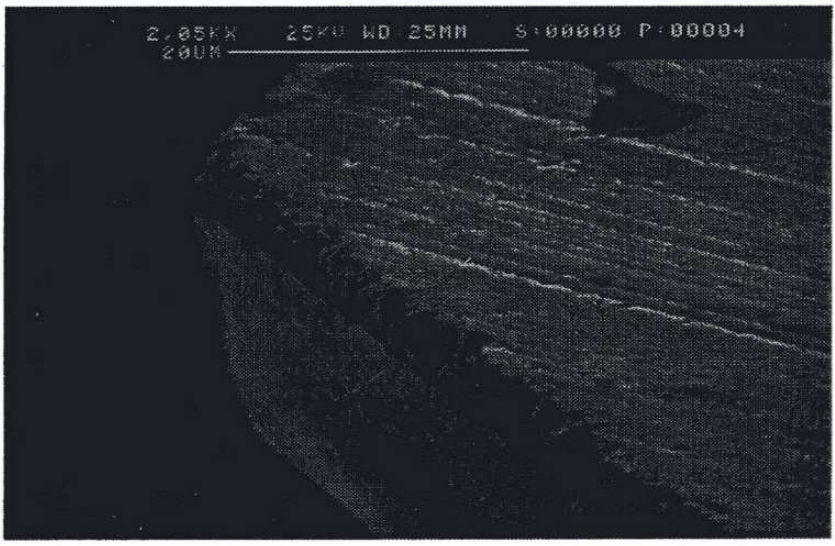

Figure 4.19. An Uncoated Drill After Drilling One Hole [52]

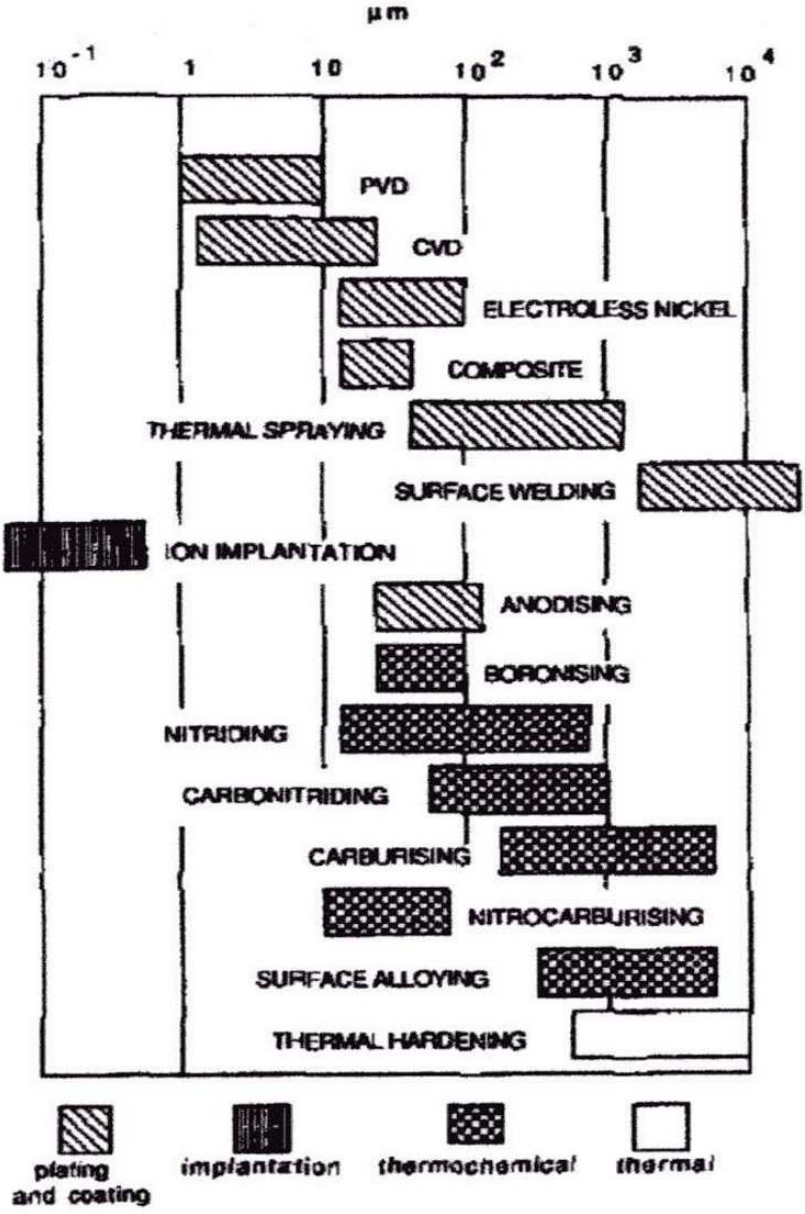

Figure 4.20. Thickness of Surface Layers and their Method of Manufacture [54]

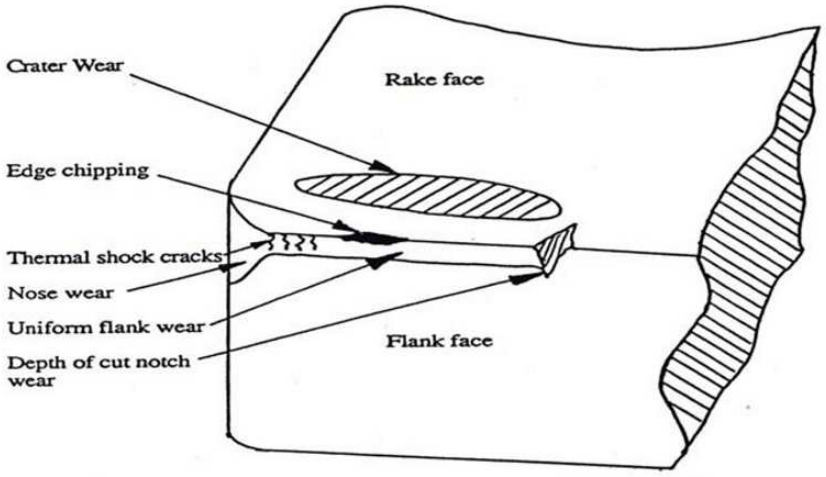

Figure 4.21. Different Wear Mechanisms on a Cutting Tool [55]

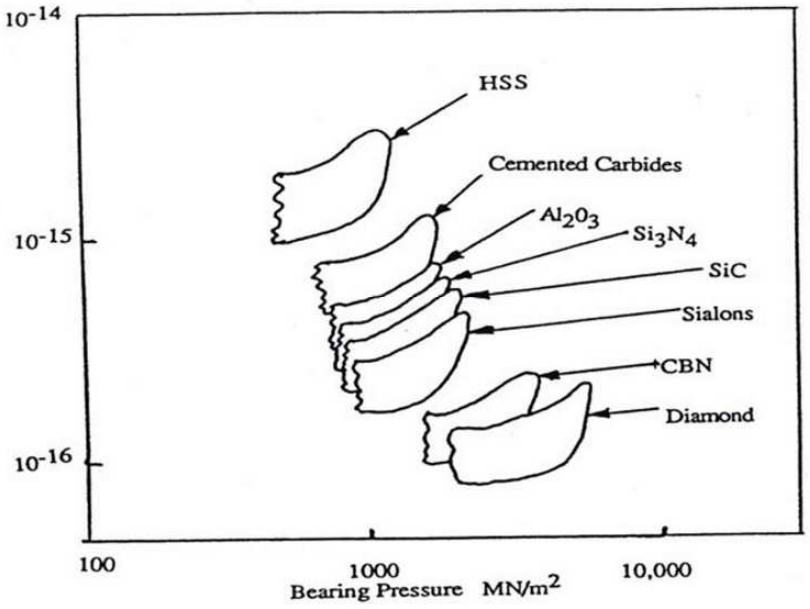

Figure 4.22. Normalized Wear Rate, Ka, Plotted Against Bearing Pressure for a Range of Tool Materials [55]

Tool coatings can modify contact conditions which alters the coefficient of friction, in turn this alters heat generation and heat flow; there are four main types of coating. The first category is titanium-based coatings such as TiAlN; other elements are added to improve hardness and oxidation resistance. Titanium based coatings are popular because they provide a wide range of average protection properties, have good adhesion and are relatively easy and quick to coat. The second category is ceramic-based coatings, e.g. Al_2O_3, except for this example ceramics have good thermal properties and excellent resistance to wear but are difficult to deposit. The third category is super hard coatings such as CVD diamond. The fourth category is solid lubricant coatings such as amorphous metal carbon, Me-C:H. Combinations of these coatings can give the best wear resistance; for example a recent development has been to take super hard coatings and deposit low friction MoS_2 or pure carbon on their surfaces.

Kub aschewski and Alcock [56] concluded that to prevent the onset of diffusion the enthalpy of the coating must be as negative as possible to increase the temperature at which diffusion is triggered. From this point of view most carbide coating materials such as TiC, HfC, ZrC are more suitable for cutting steel than tungsten carbide, similarly for the nitrides except CrN up to a temperature of $1500^{O}C$. The technique used to coat the tool can affect its performance; CVD requires high temperatures that can have an annealing effect on the tool. This affects the tool's toughness and rupture strength because a brittle η phase $(Co_XW_YC_Z)^2$ forms. A standard CVD process operating at $1100^{O}C$ can reduce the materials strength by 30%. PVD techniques such as evaporation, sputtering and ion plating usually take place between $200\text{-}500^{O}C$ avoiding such problems.

Eventually, multilayer coatings were developed. Klocke and Krieg [57] summarized their three main advantages: (1) Multilayer coatings have better adhesion to the tool. This is because the adhesion between the tool, intermediate layer and coating is better than the adhesion between the tool and coating alone; for example the presence of TiC in a CVD TiC-Al_2O_3-TiN coating system; (2) Multilayer coatings have improved mechanical properties such as

hardness and toughness. For example, the advantages of a (Ti,Al)N layer can be combined with advantages of a TiN layer (good bonding and high toughness) by building up alternate layers of each coating. Layering is also thought to provide a barrier to resist crack propagation; and (3) Each level of a multilayer coating can provide a different function. For example, a coating could consist of a mid-layer with high thermal stability and a top layer with high hardness to produce a coating that maintains its hardness at high temperatures. It is possible for coatings to protect the substrate from heat if they are good insulators, have low thermal conductivity and a low coefficient of heat transfer. An example of such an improvement is a TiN-NaCl multilayer, which has hardness that is 1.6 times greater than a single TiN layer. (Al,Ti)N coated tools have been compared to TiN and uncoated tools when milling at 600m/min. The (Al,Ti)N coated tools exhibit much less flank wear, which correlates to a higher hardness, 2720HV for (Al,Ti)N vs 1930HV for TiN and an improved oxidation temperature, $840^{O}C$ for (Al,Ti)N v $620^{O}C$ for TiN. The improved performance of (Al,Ti)N coated tools is due to their ability to maintain a higher hardness at elevated temperatures.

It has been noted that in some extreme cases of machining highly abrasive materials, e.g. hypereutectic Al-Si alloys where the Si particles are highly abrasive, variations of Ti based coatings do not improve the tool life. In such cases only the hardness of diamond coatings can improve the abrasion resistance and therefore prolong tool life. Quinto, Santhanam and Jindal [58] investigated coatings deposited by CVD and PVD techniques on two alloys A and B (Figures 4.23 - 4.26). Coatings with an Al content tend to perform better regardless of the application, coating process or chemical content of other the coating constituents. This is because abrasive resistance, oxidation resistance and hardness are all improved. Thermal relief experienced by the substrate is of special interest in terms of volume effects like fatigue and diffusion. Examples of coatings offering this relief are PVD (Ti,Al)N and CVD TiC-Al_2O_3-TiN. Quinto [58] found that PVD coatings outperform CVD coatings that outperform uncoated tools (Figures 4.27 - 4.29).

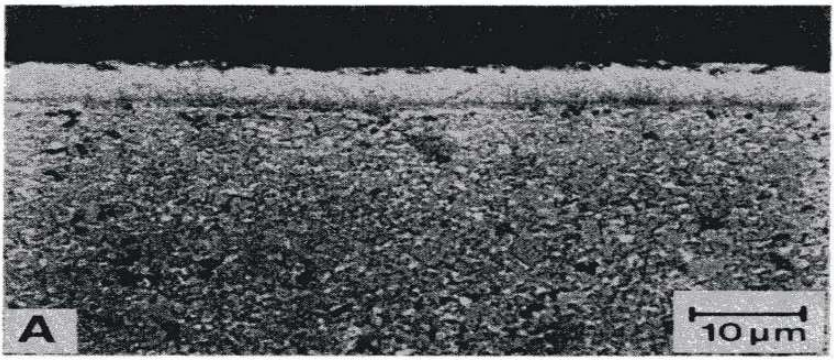

Figure 4.23. CVD Deposited TiN on Alloy A [58]

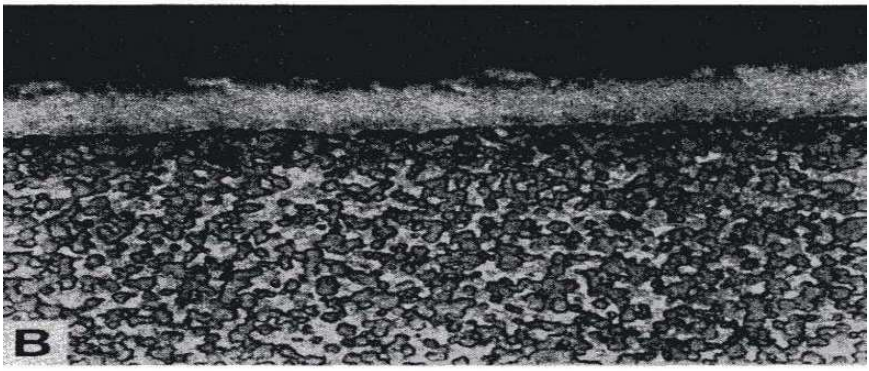

Figure 4.24. CVD Deposited TiN on Alloy B [58]

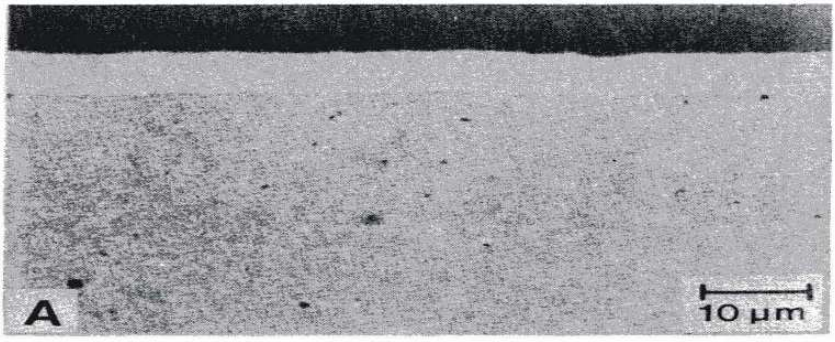

Figure 4.25. PVD Deposited TiN on Alloy A [58]

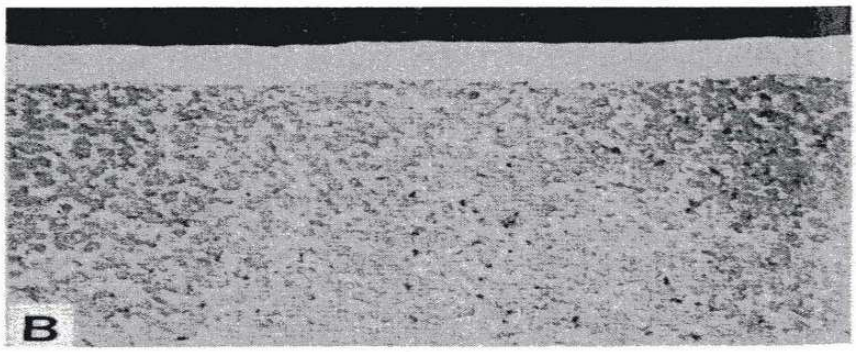

Figure 4.26. PVD Deposited TiN on Alloy B [58]

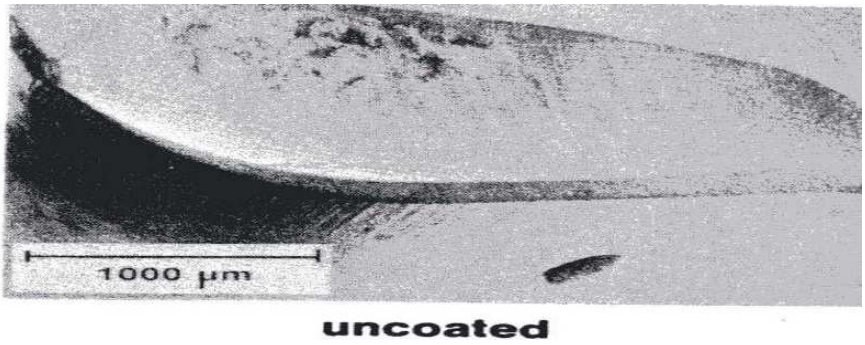

Figure 4.27. Appearance of an Uncoated Insert at the end of Tool Life After Machining 1045 AISI Steel [58]

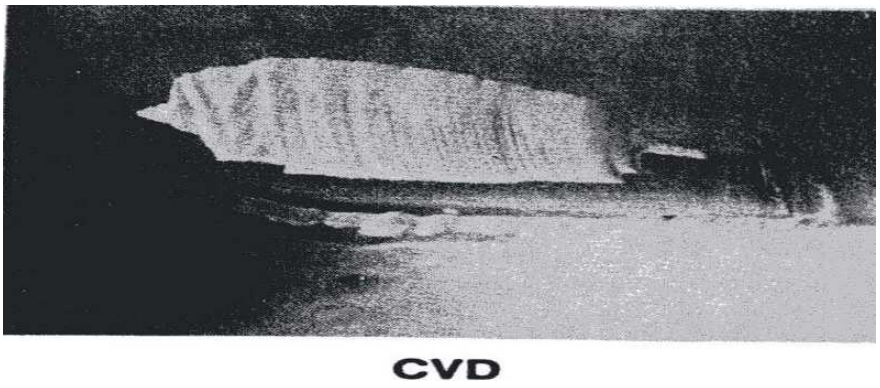

Figure 4.28. Appearance of an TiN CVD Coated Insert at the end of Tool Life After Machining 1045 AISI Steel [58]

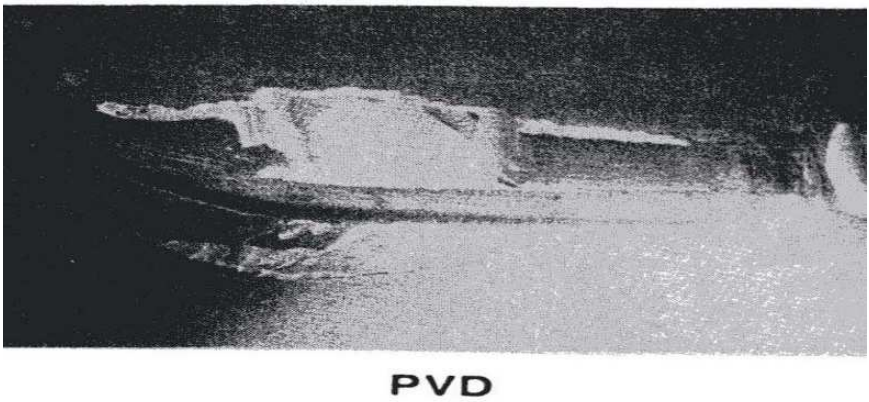

Figure 4.29. Appearance of an TiN PVD Coated Insert at the end of Tool Life After Machining 1045 AISI Steel [58]

Dry machining of steels in the range of 55-62HRC at 15,000-25,000 rpm generates cutting temperatures of 1000^{O}C and the tool must be protected from oxidation wear. Previous work by Munz, Smith, Donohue, Deeming and Goodwin [59] has shown that above 800^{O}C diffusion of stainless steel is triggered and cavities begin to form between the substrate and coating, although this can be prevented by adding 1% yttrium. One method used by Constable, Yarwood and Munz [60] to analyze the integrity of coatings is Raman microscopy. It has been used to study wear, wear debris, stress, oxidation, and the structure of single layer PVD coatings; it is now being used to study multilayer PVD coatings. Raman microscopy works by analyzing photon interactions with the lattice to determine the characteristic vibrations of the molecules. Thus the process is sensitive to lattice re-arrangement that can occur as a result of local changes in material properties due to high cutting temperatures. Constable, Yarwood, Hovsepian, Donohue and Lewis [61] demonstrated the usefulness of Raman microscopy when a PVD combined cathodic arc/unbalanced magnetron deposition system was used to coat high-speed steel and stainless steel for abrasion tests. The coatings had a thickness between 2.5-4μm with a surface

roughness of 0.02-0.03μm Ra (roughness average). Polycrystalline corundum with a hardness of 1900HVN and Ra of 0.2μm was brought into contact with the PVD coating. A constant load of 5N was applied and the relative sliding speed between the two surfaces was 10cm/s. A 25mW HeNe laser with an excitation wavelength of 632.8nm was used to obtain Raman results. The PVD coating consisted of a 1.5μm thick TiN base layer with alternating layers of TiCN, 0.4μm thick and TiN, 0.6μm thick; the total thickness was 3.9μm. The expected wear debris was rutile, TiO_2, which yields a peak at 426cm^{-1}; however peaks were also detected at 512 and 602cm^{-1} indicating anastase debris. This would suggest the contact temperature was lower than expected, indicating the coefficient of friction was also lower than expected. Deeming, Munz and Smith [62] investigated the effect different coatings have on delaying the onset of oxidation. During high speed machining, temperatures regularly exceed 900^0C. Deeming found a TiN coating delayed oxidation until 500^0C, a TiAlN coating delayed oxidation until 700^0C and a multilayered system delayed oxidation formation until 950^0C. The final coating tested was TiAlCrYN, prior to deposition Cr is added to etch the tool thereby achieving the smoothest, most strongly adhered, dense coatings possible. The addition of yttrium increases wear at low temperatures, however at higher temperatures yttrium causes maximum wear to occur at 600^0C and minimal wear to occur at 900^0C. Without the addition of yttrium the wear rate continually increases with temperature. Deeming [62] suggests yttrium diffuses into the grain boundaries and at high temperatures there is some stress relaxation. Heat-treated TiAlCrYN therefore has lower internal compressive stresses than regular TiAlCrYN. TiAlCrYN also has a lower coefficient of friction with increasing temperature compared to TiN (Figure 4.30) and also has a lower wear rate at elevated temperatures (Figure 4.31).

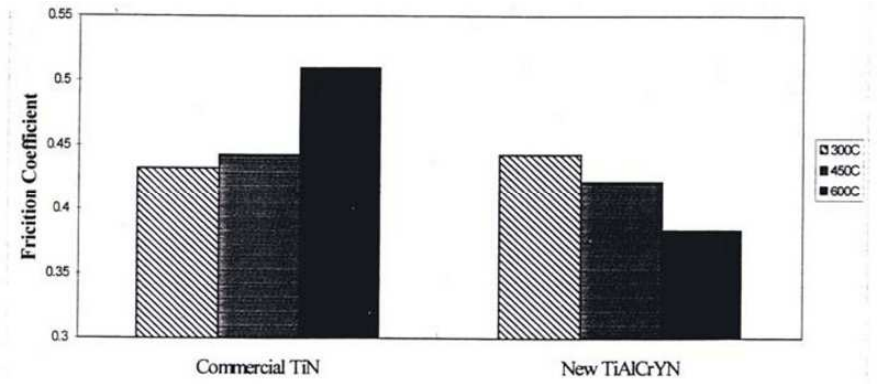

Figure 4.30. Comparison of the Coefficient of Friction Produced by TiN and TiAlCrYN Coatings [62]

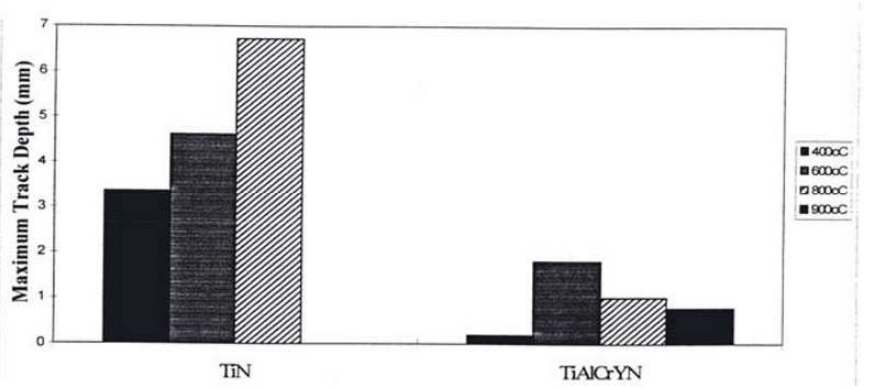

Figure 4.31. Comparison of the Wear Rate Produced by TiN and TiAlCrYN Coatings at Elevated Temperatures [62]

A problem with PVD coatings identified by Creasey, Lewis, Smith and Munz [63] is when ion etching is used to evaporate target materials; subsequent deposition by magnetron sputtering can lead to the formation of droplets which adhere badly to the surface and cause weaknesses in the coating. This is particularly problematic when depositing TiAlN. It has been shown by Munz, Smith, Lewis and Creasey [64] the melting temperature of the cathode material influences the number and size of these droplets. Munz compared TiAl and Cu targets, TiAl had a higher melting point and produced a droplet density of $100x10^3/mm^2$ compared to a droplet density of

$60x10^3/mm^2$ for the lower melting point Cu. Comparing droplet size, up to 1μm TiAl had twice the number of droplets as Cu. Between 2-4μm the number of droplets was the same and between 4-8μm more Cu droplets were detected. It was expected Cu would produce more particles for all sizes of droplet, but due to its high vapor pressure Cu can escape the surface and is therefore not deposited. It is noted higher melting point targets exhibit spherical droplets suggesting they have solidified before contact with the surface and are subsequently included between the layers. Lower melting point targets show none spherical droplets. Generally higher melting point targets reduce the number and size of defects when depositing TiAlN with UBM. An alternate to the Ti based coatings is CrN_x, which can be deposited at temperatures as low as 200^OC, the oxidation temperature for this coating is 700^OC. There are a number of ways to deposit this coating in addition to magnetron sputtering. Gahlin, Bromark, Hedenqvist, Hogmark and Hakansson [65] have demonstrated cathodic arc deposition and Wang and Oki [66] have demonstrated low voltage beam evaporation deposition. The pressure of the N_2 gas defines which of the different phases result, Cr, Cr-N solid solution, Cr_2N, Cr_2N+CrN or CrN. Cr_2N has the hardest coating between 1700-2400HV. Hurkmans, Lewis, Brooks and Munz [67] deposited the coatings using a combined steered arc/unbalanced magnetron-arc bond sputtering (ABS) technique. Ferritic stainless steel (Cr18) and high-speed steel (M2) were etched either by inert Ar ion or Cr metal ion, and then polished to a Ra of 0.01μm. The coating temperature was a constant 250^OC and the thickness a constant 3μm. It has been found low adhesion problems can be overcome by using the ABS technique and conducting a pre-etch at 1200eV Cr prior to UBM film deposition; this can more than double the adhesive force from 25N to 50N. Both TiAlN and CrN coatings exhibit good properties for dry high temperature machining; Wadsworth, Smith, Donohue and Munz [68] reasoned that a multilayer composed of these materials would produce an optimal coating for preventing tool wear; such a coating can be produced using PVD techniques. Wadsworth deposited coatings with and ABS system at 450^OC and a base pressure of $1x10^{-5}$mbar. The targets were three $Ti_{0.5}Al_{0.5}$ plates and a Cr plate, the substrates were various sized sheets of 304 austenitic stainless steel and 10mm

diameter 10mm long cylinders of heat treated M2 high speed steel (HRC~62), polished to an Ra of 0.01µm. A 0.2µm thick TiAlN base layer was deposited prior to the TiAlN-CrN multilayer; the final coating thickness was 3.5µm.

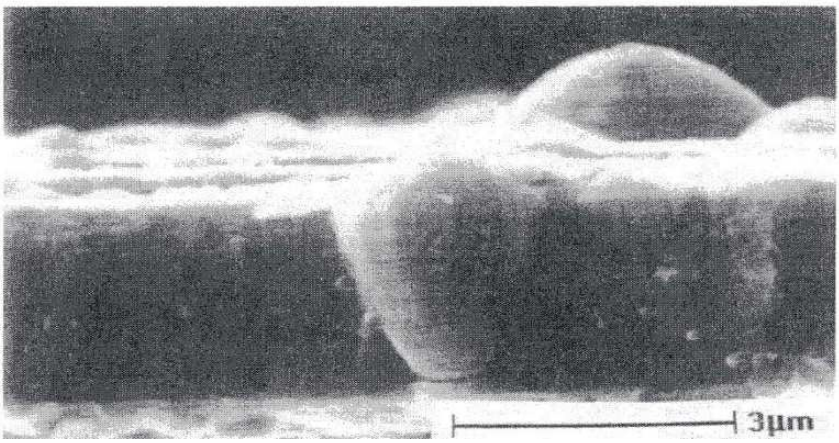

Figure 4.32. Cross Section Showing Growth Defects in a TiAl Coating [69]

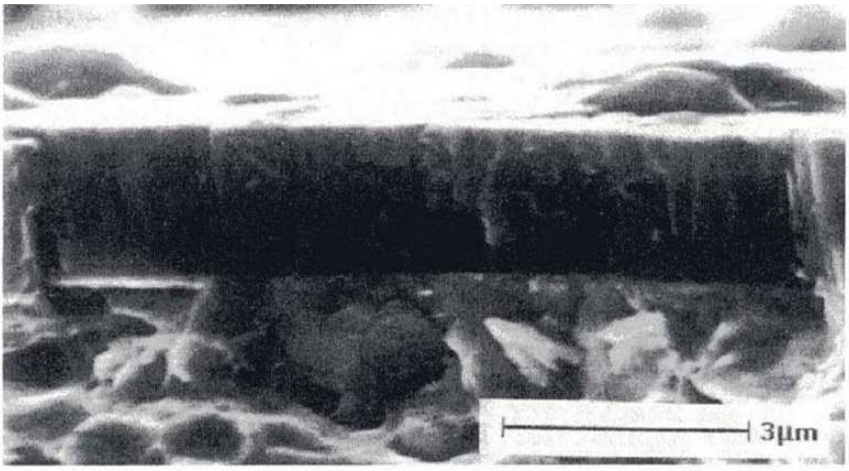

Figure 4.33. Cross Section of a Cr Etched TiAlN Coating [69]

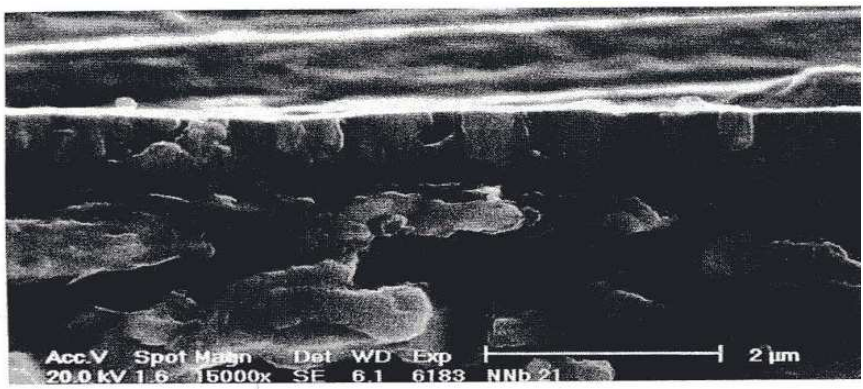

Figure 4.34. Coatings Deposited at –25V Bias [71]

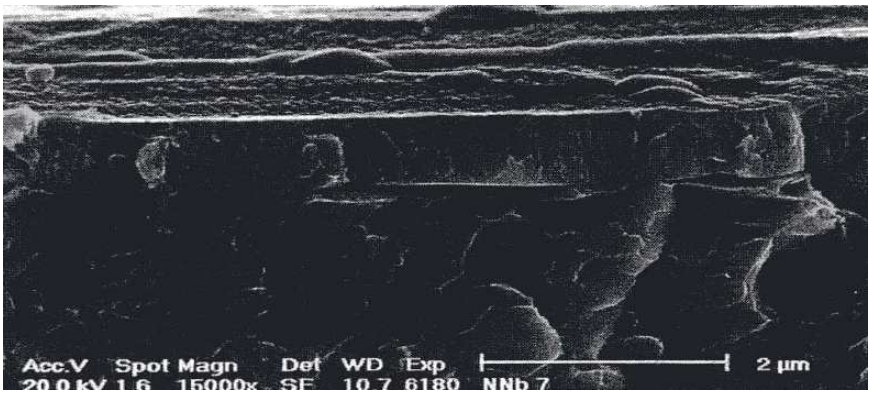

Figure 4.35. Coatings Deposited at –75V Bias [71]

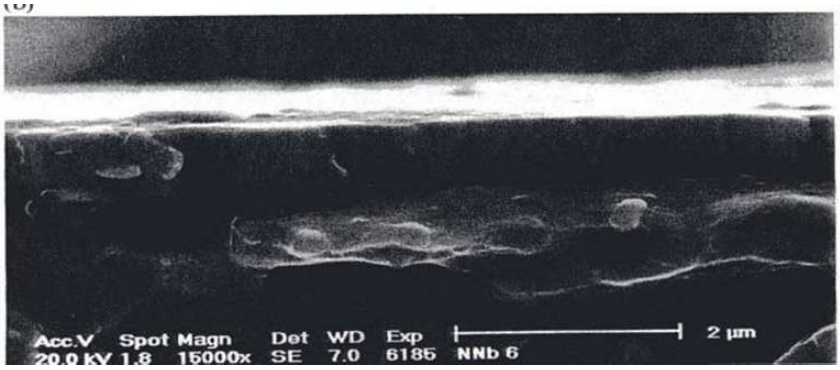

Figure 4.36. Coatings Deposited at –125V Bias [71]

A series of coatings were tested at elevated temperatures. It was found that up to 700^{O}C the coatings were unaffected, with the hardness dropping from an initial 3500 to 2800 Knoop hardness ($HK_{0.01}$) after 16 hours. However if the coatings were held only 50^{O}C higher for the same length of time the hardness dropped to 475 $HK_{0.01}$. The reduction in hardness is thought to coincide with a breakdown in the multilayers and oxidation of the exposed surface. The addition of Cr however reduces the onset and rate of oxidation. Smith el al [69] coated various substrates and performed a series of tests. The two coatings tested were TiAl and TiAlN with a Cr etch. The growth defects previously discussed were highlighted in the TiAl coating (Figure 4.32) while the Cr etched TiAlN coatings was defect free (Figure 4.33). The substrates coated were 30mm diameter and 5mm thick cylinders made from M2 high speed steel (HRC~65) with an of Ra=0.005μm, 25x25x0.8mm bright annealed 304 stainless steel plates and 8mm diameter HSS twist drills. The drills are of particular interest and were initially tested at 835rpm and a feed rate of 0.28mm/rev, for each subsequent test the spindle speed was incrementally increased. It was found TiAlN coated drills out performed commercially available drills. This improvement was partially attributed to the smoother surface observed on the TiAlN coating, which was enhanced further with a Cr etch.

Petrov el al [70] also experienced the droplet formation described by Munz during the coating procedure. Polycrystalline $Ti_{1-x-y}Al_xN$ alloys and $Ti_{1-x}Al_xN/Ti_{1-y}Nb_yN$ multilayers exhibiting smooth flat layers up to a total film thickness of 3μm were grown on ferritic b.c.c. stainless steel substrates at temperatures around 450^{O}C using unbalanced magnetron sputtering and cathodic arc deposition. Petrov [70] prepared the substrate for final deposition by performing a cathodic arc etch using a $Ti_{0.5}Al_{0.5}$ or $Ti_{0.85}Nb_{0.15}$ target. $Ti_{0.5}Al_{0.5}$ has a lower melting point and results in large droplet formation, which decreases the integrity of the film. $Ti_{0.85}Nb_{0.15}$ however has a higher melting point and produces less droplets that are much smaller in size. Under UBM deposition conditions the films exhibited columnar growth with a compressive stress around 3GPa

and around 1.5% trapped Ar. For a thickness of 3μm peak-to-peak roughness was observed at 50nm. Using a UBM/CA deposition technique a thickness of 3μm peak-to-peak roughness was observed at only 5nm. Higher compressive stresses were observed, 9GPa with an Ar concentration of 0.5%. Further materials that would be suitable for coating applications are niobium and tantalum because they are extremely stable; but they are difficult to deposit using conventional methods. However an ion beam assisted deposition technique has developed that takes place at 250eV and leads to niobium coatings that are fully dense.

Salagean el al [71] also deposited such coatings using an arc and unbalanced magnetron-sputtering cathode equipped with an Nb target; base pressure $5x10^{-5}$, 10kW and a 6A coil at $400^{O}C$. It was found prior etching treatment defined the quality of the new surface as well as the voltage bias during deposition (Figures 4.34 – 4.36). Salagean [71] found niobium whose melting point is $2468^{O}C$ could be deposited on a substrate with a temperature of $400^{0}C$. Donohue, Smith, Munz, Petrov and Greene [72] preferred TiAlN to TiN coatings due to their greater resistance of oxidation (Figures 4.37 and 4.38). Donohue [72] also found $Ti_{l-x-y-z}Al_xCr_yY_zN$ deposited by magnetron sputtering offered even greater oxidation resistance due to the additional alloying elements. Substrates coated were M2 tool steel with Ra of 10nm and cold-rolled 304 austenitic stainless steel. Prior to coating the samples were Cr ion etched at –1.2kV for 20mins at a pressure of $6x10^{-4}$ mbar to reduce droplet formation. A 0.2μm thick $Ti_{l-x-y}Al_xCr_yN$ base layer was then deposited, three separate coatings were then grown on top of this base layer to a thickness of 3μm; they were $Ti_{l-x-y-z}Al_xCr_yY_zN$, $Ti_{l-x-y}Al_xCr_yN$ and $Ti_{l-x}Al_xN$. In all cases the bias was –75V. The exact compositions were $Ti_{0.43}Al_{0.52}Cr_{0.03}Y_{0.02}N$, $Ti_{0.44}Al_{0.53}Cr_{0.03}N$ and $Ti_{0.46}Al_{0.54}N$. The surface roughness for all films had Ra values between 0.038-0.04μm. The hardness of the coatings was $Ti_{0.43}Al_{0.52}Cr_{0.03}Y_{0.02}N$ = $HK_{0.025}$ = 2700kgmm^2, $Ti_{0.44}Al_{0.53}Cr_{0.03}N$ = $HK_{0.025}$ = 2400kgmm^2 and $Ti_{0.46}Al_{0.54}N$, = $HK_{0.025}$ = 2400kgmm^2. Donohue [72] also investigated the oxidation temperature, for TiN it was $600^{O}C$, for $Ti_{0.46}Al_{0.54}N$ it was $870^{O}C$, for $Ti_{0.44}Al_{0.53}Cr_{0.03}N$ it was $920^{O}C$ and for $Ti_{0.43}Al_{0.52}Cr_{0.03}Y_{0.02}N$ it was $950^{O}C$. He therefore concluded the

extra alloying elements were significant. Annealing of the $Ti_{0.44}Al_{0.53}Cr_{0.03}N$ at $950^{O}C$ for 1hour showed significant oxidation with micron sized voids however annealing of the same conditions of the $Ti_{0.43}Al_{0.52}Cr_{0.03}Y_{0.02}N$ shows no effect, highlighting the importance of yttrium.

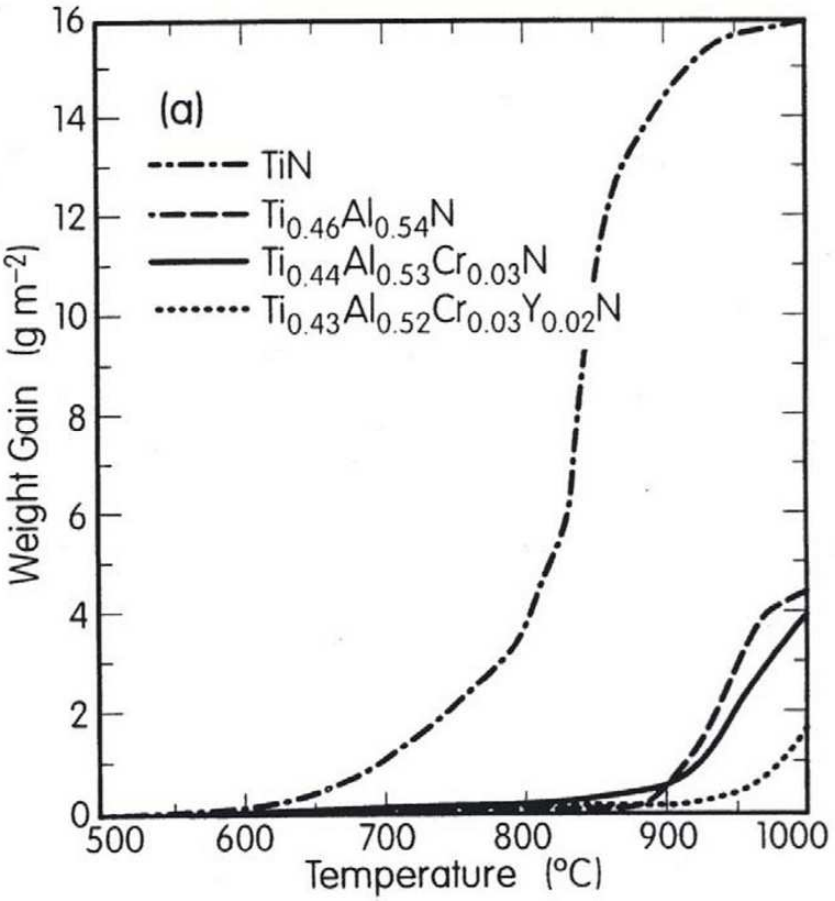

Figure 4.37. Thermo-Gravimetric Oxidation Rate Measurements in Air During a Linear Temperature Ramp at $1^{0}C\ min^{-1}$ [72]

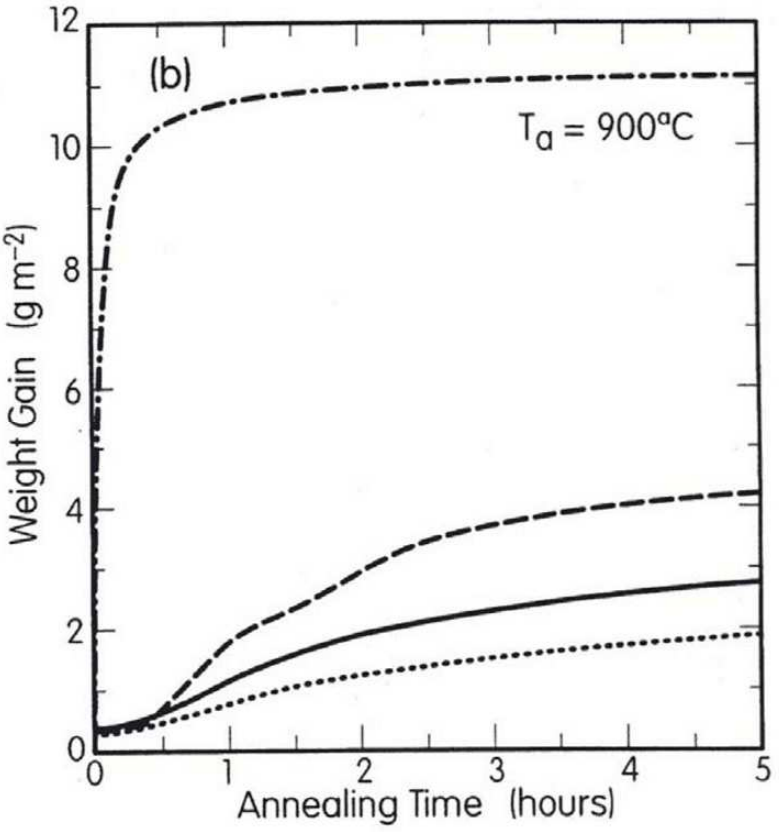

Figure 4.38. Thermo-Gravimetric Oxidation Rate Measurements in Air During an Isothermal Anneal at 900^0C [72]

4.6. Micromachining

Inamura, Takezawa and Kumaki [73] found it difficult to apply finite element analysis to micromachining processes around 1nm (Figure 4.39); they found that a more successful approach is to use molecular dynamics simulations. Molecular dynamics works by establishing the position of each atom by resolving Newtonian dynamics for the system. Such simulations highlight the need for sharp tools because dull tools are predicted to generate a large shear area (some area either side of the defined shear plane) and this leads

to significant work hardening of the material. It has been shown faster cutting speeds produce thinner chips and sharp tools operated at high cutting speeds impart low forces to the tool. However, Kim and Moon [74] found that when considering the cutting zone (Figure 4.40), if the tool becomes blunt the forces generated by a blunt tool at high speed are significantly higher than forces produced by a blunt or sharp tool at low speed. Therefore, if the full benefits of micro cutting are to be utilized according to predictions made by molecular dynamics simulations of chip flow (Figure 4.41) the cutting tool must be sharp and cutting speeds must be high.

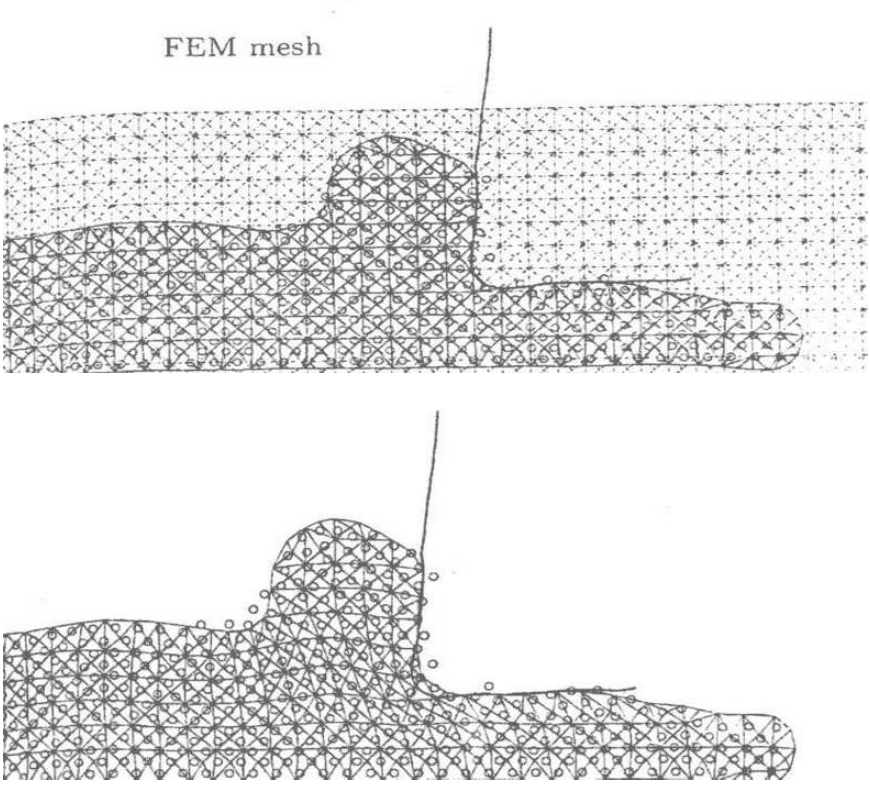

Figure 4.39. Finite Element Mesh to Simulate Micromachining [73]

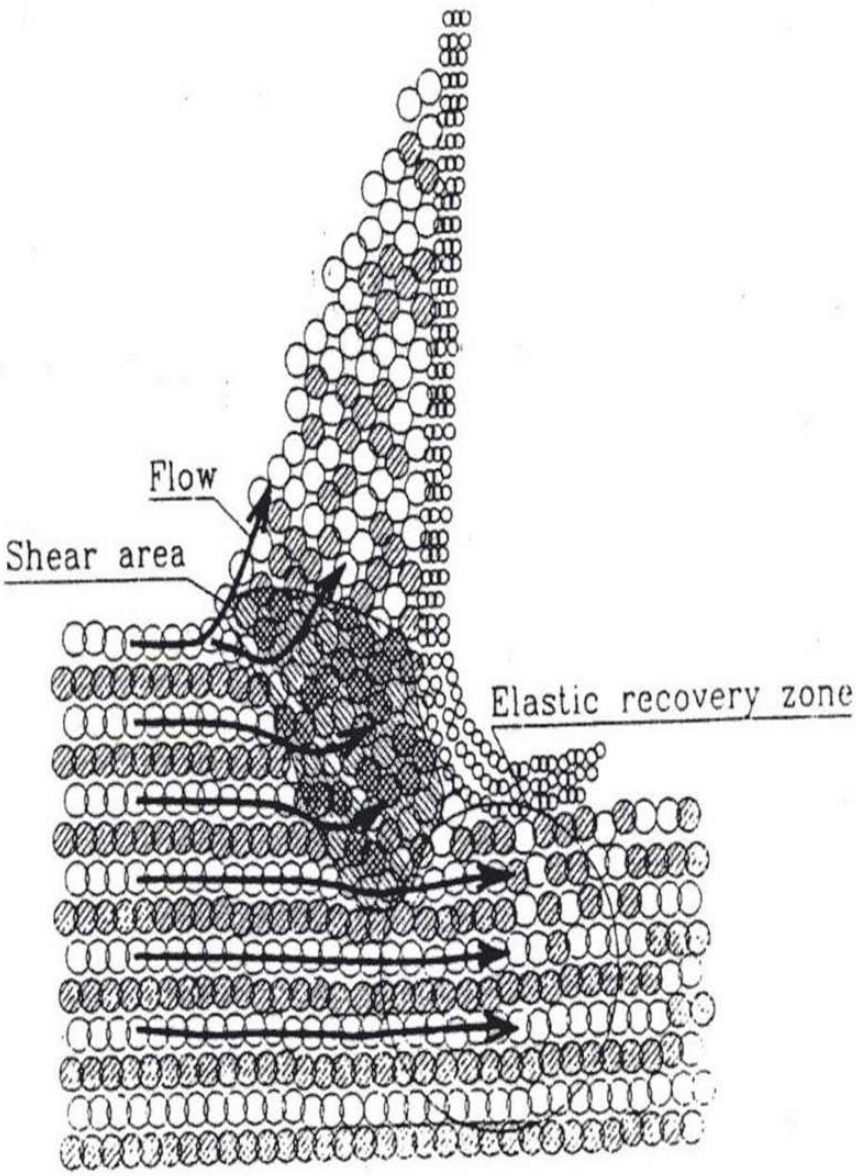

Figure 4.40. Molecular Dynamics Simulation of the Cutting Zone [74]

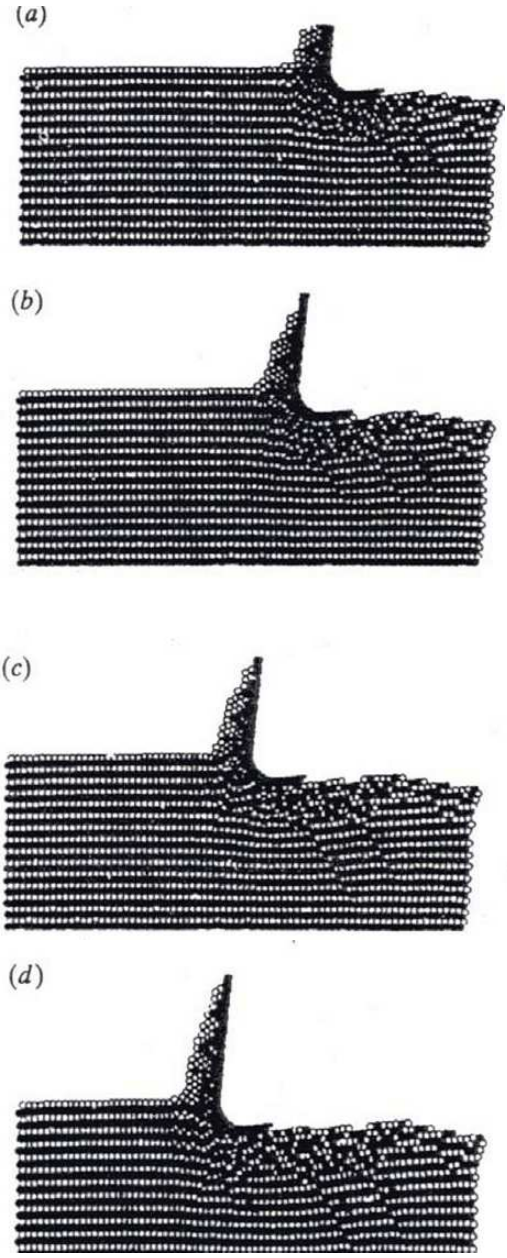

Figure 4.41. Chip Formation Predicted by Molecular Dynamics Simulation [74]

Burr formation is observed at the macro scale and can contribute up to 30% of the time and cost it takes to produce a part. Burr formation is also observed at the micro scale, but Gillespie [75] discovered macro scale burr removal techniques could not be applied because dimensional inaccuracies and residual stresses may be induced. Smaller burrs are more difficult to deal with; therefore investigations into burr formation and burr reduction have been undertaken. Gillespie and Blotter [76] stated there are three generally accepted burr formation mechanisms: lateral deformation; chip bending and chip tearing.

Most micro burr formation studies are at a disadvantage by operating well below the recommended cutting speed, for example machining aluminum with a 50μm tool demands a cutting speed of 105m/min which would require a spindle speed of 670,000rpm. At the macro scale, once formed, burrs can be quantified; for example burr height and burr width can be measured. However, at the micro scale such techniques are difficult to employ; if they are employed then Kim [77] found accuracy and repeatability are lost. Work by Ko and Dornfield [78] described a three-stage process for the burr, initiation, development and formation. They developed a model for the burr formation mechanism that worked well for ductile materials such as Al and Cu. However, at this time burr formation is not well understood but correlations between machining parameters can identify key variables that help reduce burr size; for example observations of burrs (Figure 4.42) by Lee and Dornfeld [79], indicate that up-milling generally creates smaller burrs than down milling and these observations along the length of a track led to the categorization of different burr types (Figure 4.43).

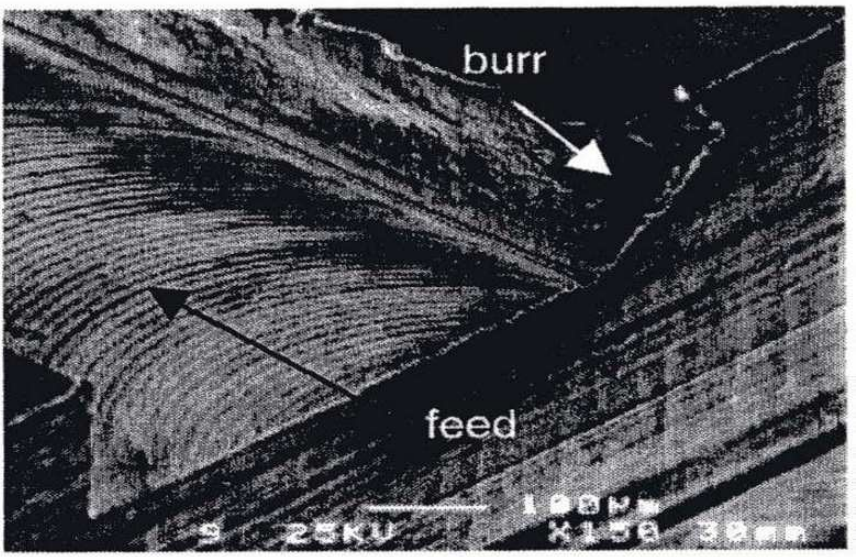

Figure 4.42. An Exit Burr [79]

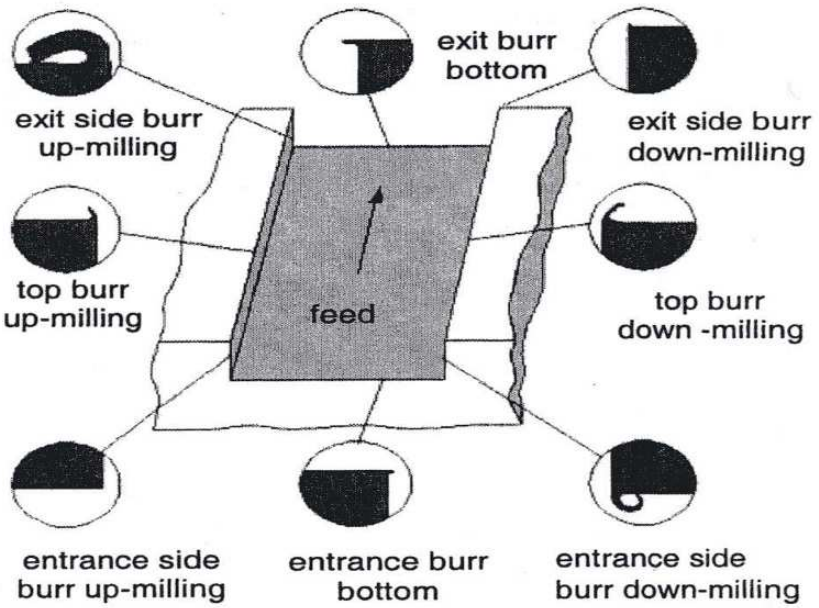

Figure 4.43. Categorization of Burr Types [79]

It cannot be assumed that if milling is scaled down to the micro level, then machining characteristics will scale by the same amount. During macro machining the feed per tooth is larger than the cutting edge radius, however during micro machining the feed per tooth is equal to or less than the cutting edge radius. Conventional milling tools have a slenderness ratio that prevents bending whereas micro tools are susceptible to bending because their diameters are only a few hundred microns. During macro scale cutting the leading tool edge encounters bulk material and therefore avoids contact with hard particles; in comparison a micro cutting edge encounters individual grains ensuring contact with hard particles.

The results of Ikawa, Shimada and Tanaka [80] suggest there is a critical minimum depth of cut, below which chips do not form. The analysis of Yuan, Zhou and Dong [81] indicates chip formation is not possible if the depth of cut is less than 20-40% of the cutting edge radius. Micro machining at 80,000rpm produces chips similar to those created by macro scale machining, where chip curl and helix effects are observed, Kim, Bono and Ni [82]. Kim also observes if the feed rate is too low a chip is not necessarily formed by each revolution of the tool. This anomaly can be demonstrated by calculation; if the feed rate is low enough, the volume of material removed is predicted to be greater than the volume of chips created. Thus some rotations that were assumed to create a chip could not have done so. This effect can also be demonstrated by experimental evidence. Sutherland and Babin [83] found that feed, or machining marks, are separated by a spacing equal to the maximum uncut chip thickness. Results show at small feeds per tooth the distance between feed marks is larger than the uncut chip thickness indicating no chip has been formed. Kim [82] concludes that a tool rotation without the formation of a chip is due to the combined effects between the ratio of cutting edge radius to feed per tooth and the lack of rigidity tool of the tool.

Work by Ikawa, Shimada, Tanaka and Ohmori [84] and Mizumoto, Arii. Yoshimoto, Shimizu and Ikawa [85] showed single point diamond turning can machine surface roughnesses to a

tolerance of 1nm; the critical parameter was found to be repeatability of the depth of cut. It is useful to model the cutting process using a molecular dynamics simulation approach. Ikawa and Mizumoto [84] found that the behaviour and flow of the material can be predicted by the laws governing interactions between neighboring atoms. Ikawa's simulations [85] suggest the depth of cut and cutting edge radius are critical parameters that determine chip formation (Figure 4.44). The velocities of these atoms can be calculated for each time step.

$$v_i' = v_i \sqrt{\frac{NkT}{\sum_i \frac{m_i v_i^{\,2}}{2}}} \tag{4.33}$$

Where v_i is the atom velocity, N is the number of atoms, k is Boltzmann's constant, T is temperature, and m is the atomic mass. By dividing the process into small intervals it is possible to compute the position of each atom, in this way material flow during the chip formation process can be predicted. Because a molecular dynamics simulation does not account for electron behavior temperature predictions are unreliable. Temperature gradients are overestimated; therefore an adjustment is required to predict heat flow more accurately. The adjustment process is conducted using the following steps, to convert the atom velocity to atom temperature T_i.

$$T_i = \frac{m v_i^{\,2}}{2k} \tag{4.34}$$

The scaled temperature is given by.

$$T_i' = T^i - (T_i - T_m)\beta \tag{4.35}$$

Where T_m is the average temperature of the atoms and is given by.

$$T_m = \frac{1}{N} \sum_i T_i \tag{4.36}$$

Eventually forces on the tool tip and the cutting forces can be calculated. Shimada, Ikawa Tanaka, Ohmori and Uchikoshi [86] compared their predicted results with experimentally determined values for a copper workpiece and found them to be accurate. If the strain applied to the workpiece by the tool is large enough, forced lattice rearrangement will occur therefore generating dislocations. As the tool advances more dislocations form at the tool-chip interface and if enough join at the primary shear zone then a chip is formed. After the tool has finished cutting, dislocations that penetrated the workpiece migrate out towards the surface because the lattice can relax. This phenomenon can be observed as atomic sized steps on the surface, which represent the best surface roughness possible Shimada [87]. Shimada also showed machining accuracy can be defined by the minimum undeformed chip thickness, below a depth of 0.2nm simulations have shown chips will not form for a tool edge radius of 5nm, although this depth varies with tool size and material.

In macro scale machining the tool edge sees bulk properties of the workpiece, however in micromachining the tool edge sees features of the material matrix such as grain boundaries. Shimada, Inoue, Uchikoshi and Ikawa [88] used molecular dynamic models to simulate this interaction. Simulations running cutting speeds at 2000m/s show the kinetic energy imparted to the workpiece is far greater than the cohesive energy of the workpiece. Other molecular dynamic simulations have identified four stages of the cutting process: (1) Compression of the work material ahead of the tool; (2) Chip formation; (3) Side flow; and (4) Subsurface deformation of the workpiece. Komanduri, Chandrasekaran, and Raff [89] conducted simulations that help highlight differences between macro and micro scale cutting, for example a volume change is observed when machining silicon. A pressure induced phase change modifies the structure from cubic to body centered tetragonal resulting in a 23% denser chip.

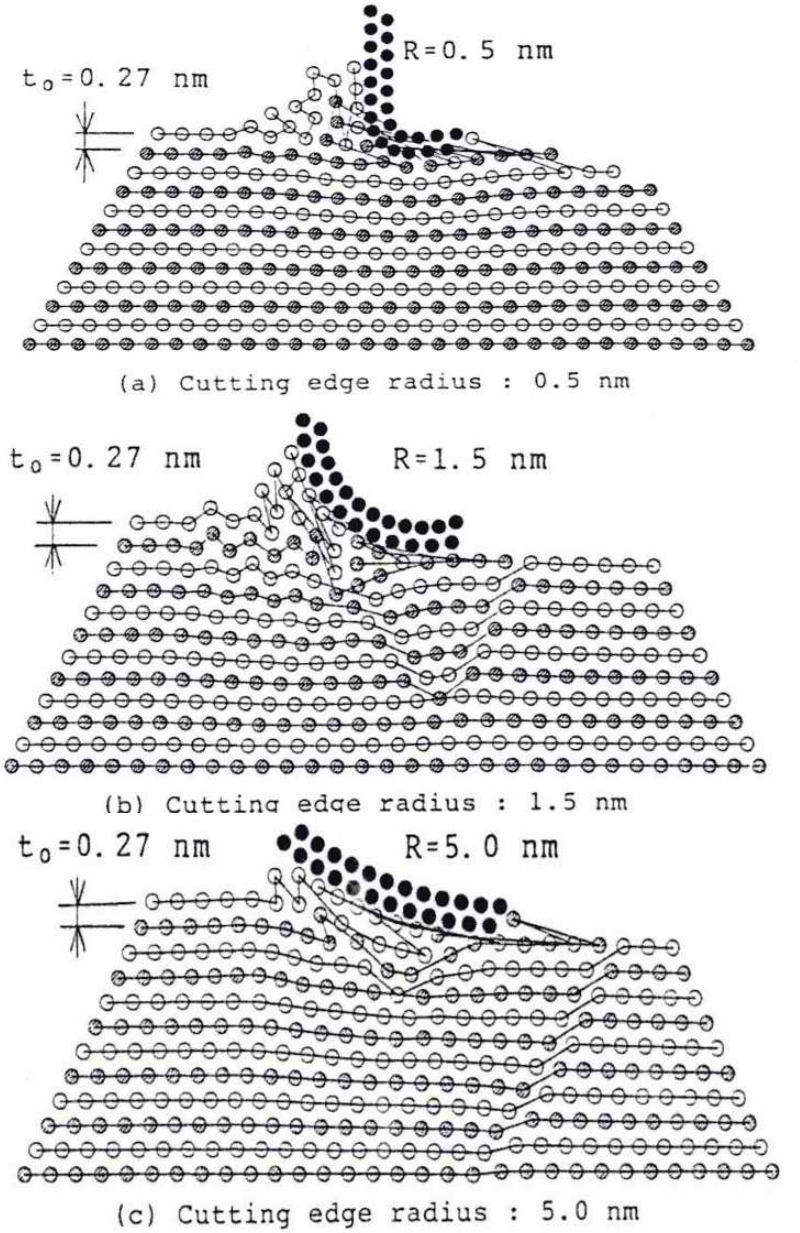

Figure 4.44. Chip Formation in Relation to the Depth of Cut and Cutting Edge Radius [80]

Usually silicon is brittle but if more electrons are available in the conduction band (usually at high temperatures) it can behave more like a metal. It has also been reported that there are no dislocations found in silicon substrates, this is an attributed effect of cutting at high speed. Significant differences were found between the machining characteristics of aluminum and silicon; most of these were attributed to the variation in ductility between the two materials. Aluminum chips form due to plastic deformation along their preferred crystallographic planes. The mechanism for plastic deformation of silicon is similar when it is being machined or extruded; this is due to the phase transformation from cubic to body centered tetragonal. This phase change also causes surface and subsurface material below the chip to become denser. The evidence for phase transformation is that silicon, which is usually brittle, acts in a more ductile manor; this is only made possible by a pressure induced phase change. Komanduri [89] also suggested subsurface damage, although very small, is inherent in micromachining, however the subsurface damage was found to decrease as the aspect ratio of the tool decreases. The subsurface densification was shown to decrease with an increase in rake angle and increase with an increasing aspect ratio. Side flow was predicted to decrease with increasing width of cut and increase with an increasing depth of cut. Low cutting forces are produced at the micro scale therefore smaller machine structures can achieve the damping and stiffness characteristics required for successful machining. The smaller footprint allows a greater number of machines per floor area yielding a greater throughput and making the technique suitable for mass production. Vogler, Liu, Kapoor, DeVor and Ehmann [90] have also examined the differences between macro and micro scale machining. Vogler [90] observes the tool edge and workpiece material grains become comparable in size. The tool edge radius becomes a similar size to the uncut chip thickness; this results in large ploughing forces. The tool's slenderness ratio reaches a point where tool stiffness is reduced. Vogler's force prediction model accounted for different grains such as pearlite and ferrite by examining their individual machining characteristics and incorporating them into his model, machining characteristics of the bulk material can then be predicted. It was found cutting edge conditions had a large effect on

machining forces. A worn tool edge can produce 300% more cutting force and results in poor surface roughness and increased burr formation. Cutting conditions of 120,000rpm, a feed per tooth of 4μm and a depth of cut of 100μm produced a peak cutting force of 3N. Separation between feed marks was 0.004mm and the associated waviness wavelength was 0.02mm. A molecular dynamics model was constructed and it was found when machining aluminum with a diamond tool chips can only form if the minimum depth of cut is approximately half the cutting tool radius. If the feed per tooth is less than the tools edge radius, the maximum uncut chip thickness does not coincide with the feed per tooth, indicating several rotations without the production of a chip. The chip forms when the critical depth of cut is reached.

4.7. Meso Machine Tool Design

If high speed machining is to be successful at the micro and nanoscale, high spindles speeds must be employed to ensure materials are processed at their recommended cutting speed. Popoli [91] has considered design problems of high-speed spindles and the limitations of adapting current spindle design. Conventionally belted or integral motors provide the power source for spindles. First consider a belt driven system, the belt is usually V-shaped or geared and the shaft holds the tool. Coupling efficiency between belt and motor determines the spindles performance. Advantages include, low cost because the spindle has few parts and the system is re-configurable because changing the motor and/or belt ratios can quickly and cheaply change the speed and torque available. However, there are disadvantages which include, low speed because of the limitations imposed by friction, belt deterioration due to stretching which leads to a loss of coupling efficiency and vibrations which increase with speed in geared systems making the machine unstable. At high speed the radial force exerted by the belt on the shaft becomes excessive. To stabilize the shaft large bearings are required, however such bearings are unable to reach high speed and belt driven systems are limited to around 15,000rpm. Thus they can be eliminated as a possible solution. An integral motor consists of a

shaft that holds the tool, and bearings that hold the shaft and a method of internally applying the power, e.g. windings on the shaft and a direct current. Smaller bearings can be used because there is no excessive source of radial force and higher speeds can be reached. For the case of an A.C. spindle speed is given by the following equation.

Speed (rpm) = (Frequency [Hz] x 120) / (number of motor poles)

(4.37)

Thus, a 4-pole motor with a top speed of 30,000rpm requires a frequency of 1000Hz. The next design issue to consider is the choice of bearings. The fastest rated bearings commercially available are precision bearings; their maximum speed is ultimately limited by friction and the use of non-contact solutions such as air bearings must be considered. Air bearings however, are sensitive to external debris such as dust but high positive pressures usually prevent this from being problematic. Frederickson and Grimes [92] highlight a problem of rating spindles by quoting the power, which is the product of torque and speed. A high power motor could be the result of low torque and high speed or high torque and low speed; maximum power may not be available at the maximum speed. Therefore, quoting power yields little information about the motor. Conventional wisdom dictates spindle design should focus on increasing torque to provide more cutting force. Current is applied to the windings, which briefly turn magnetic; permanent magnets repel the coil rotating the spindle. Larger windings and magnets produce more torque therefore torque is proportional to motor size. The bulk of a high torque motor can be reduced by careful design, for example a 100mm diameter stator has 3Nm of torque if its length is 40mm, but 15Nm for a length of 150mm. Elongating the spindle length can have a detrimental effect on machining performance. The effect of increasing distance between bearings is to lower the spindles natural frequency closer to its operating speed. The shaft then becomes susceptible to increased vibrations and bending. For example a 10mm elongation in motor length can alter the natural frequency from 51,000rpm to 44,445rpm, the operating speed of the

example motor is 40,000rpm, which is within 5000rpm of the natural frequency. A greater difference in rpm would be preferable reducing the risk of operating at the natural frequency. Spindles often run hot; there are two methods of reducing temperature, a liquid cooling jacket or cooling fins. Both techniques draw heat away from the spindle housing; the liquid method is more compact because fins are not required. Recommended micro scale cutting speeds can be approximately 500,000rpm, current dental drills can reach speeds up to 300,000rpm but have a run out of 10μm; a figure which is usually greater than the chip thickness. Tools with diameters of 25μm have been used to mill at 30,000rpm but can only achieve feeds of 5-14 inches per hour. Tool wear is different at the macro and micro scales. At the macro scale tools usually are considered worn due to edge wear, at the micro scale they fail because bending strength is exceeded. This occurs when the chip thickness ratio is larger than the tools edge radius and cutting forces are large. If chip thickness is smaller than edge radius the result is a negative rake angle (up to 50^{O}), thus increasing cutting forces required to form the chip and highlighting the need for smaller chips. Therefore, Zelinski [93] has concluded the only way to achieve a reasonable material removal rate is to rotate the tool faster. There are no established methods for concentrically holding the tool at the micro scale. Therefore the tool shaft is secured by a bearing and rotated by frictional contact with a large diameter fast turning wheel. High speeds are achieved through extremely large gearing ratios between the large diameter wheel and small diameter tool. Tool breakage can be detected if cutting forces are monitored throughout the machining cycle. The problem of high-speed bearings has also been encountered in the design of MEMS components. It has been shown rotating micro devices must have similar tip seeds to their macro scale counterparts. For example macro scale turbo machinery typically has tip speeds around 500m/s but current MEMS tip speeds are limited by MEMS bearings to approximately 2m/s. Frechette et al. [94] has considered this problem and designed a micro gas bearing. The rotor sits on a fluid film avoiding solid contact thereby minimizing friction. Gas bearings are used to support radial motion and gas thrust bearings support axial motion (Figure 4.45).

The device was designed to overcome viscous drag produced by the gas bearings and fluid membrane; at 500m/s this drag was computed to be 13W. The radial bearing (or journal bearing) separates the rotor and housing, it is 300μm deep and has an average separation of 15μm, which is maintained by a pressure differential. If the rotor becomes dislodged the pressure differential restores its center position, which was first demonstrated by Orr [95]. However, the hydrostatic journal bearing acts like a spring and a certain speed coincides with the natural frequency of the rotor producing unwanted oscillations. Diagnostic equipment can detect the onset of such oscillations and the pressure can be altered to change the rotors natural frequency thereby avoiding the problem. Rotating micro devices such as these have reached 1,400,000rpm before failure; this is equivalent to a tip speed of 300m/s. Failure occurs when the device becomes unstable and crashes, instabilities results from imperfect manufacture of the rotor and stator system. It is therefore critical to manufacture rotor and stator components accurately so stable conditions can established to prolonged operation of the device. It was also discovered that after surpassing a certain critical high speed the body rotates about its center of mass rather than its geometrical center.

4.8. Future Applications And Research Directions

The study of micro and nanomachining from a materials perspective has demonstrated a new outlook on the problems associated with machining with conventional cutting tools at these scales. The economies of scale can certainly be gained if a number of emerging problems can be solved. One dominant problem that occurs at the microscale is the bending of the cutting tool and the inability to cut chips at low speeds. Therefore, special attention must be applied to constructing stiffer tools and to prevent the rounding of the tool edge when the tool is initially straight. This may be overcome by coating small cutting tools with nanocrystalline diamond that has many cutting points, which are in contact with the workpiece even when tool bending takes place.

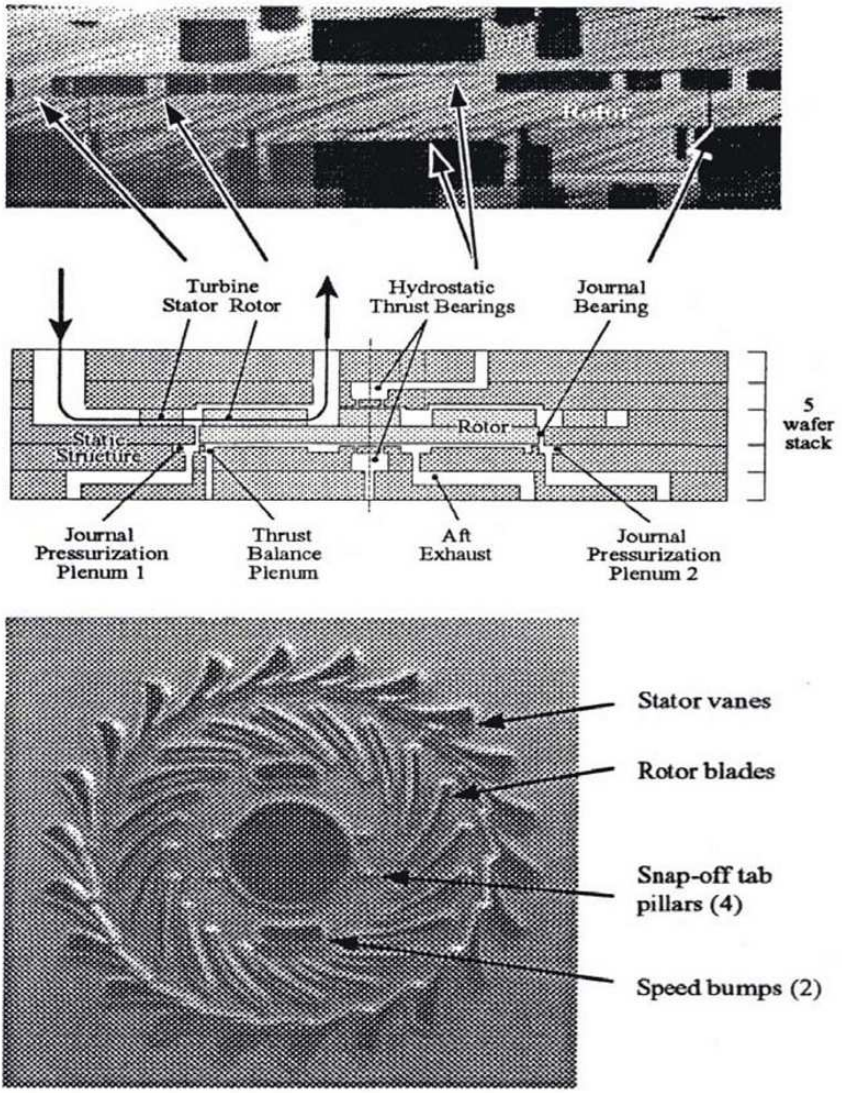

Figure 4.45. Gas Bearings Designed and Tested by Frechette [94]

The incompatibility between diamond and ferrous materials can be overcome by coating the nanocrystalline diamond with a thin coating of a compound that has the least thermodynamic potential for dissolution. This direction will give rise to using multilayered coatings that have beneficial advantages such as thermally conducting heat away from the zone of cutting and reducing the generation of frictional heat by using a carbon-based soft layer lubricating coating. In terms of the construction of meso machine tools, future research directions include designing spindles that rotate the cutting tool at extremely high speeds that use thin layer diamond coatings on bearing surfaces. Air turbine spindles with integrated gas bearings are the possible solution to achieving extremely high spindle speeds. In addition to using small-scale machine tools, machine tools must be axisymmetric in construction so that mechanical and thermal disturbances are minimized.

Acknowledgements

The chapter contributors wish to thank Inderscience publishers for granting permissions to reproduce work presented in this chapter.

References

[1] Ernst, H., & Merchant, M. E. Chip Formation, Friction and High Quality Machined Surfaces, *Surface Treatment of Metals* (Vol. 29, pp. 229-378). New York: American Society of Metals. (1941).

[2] Merchant, M., Mechanics of the Metal Cutting Process 1: Orthogonal Cutting and a Type 2 Chip, *Journal of Applied Physics, 16*(5), (1945) 267-275.

[3] Merchant, M., Mechanics of the Metal Cutting Process 2: Plasticity Conditions in Orthogonal Cutting, *Journal of Applied Physics, 16*(6), (1945) 318-324.

[4] Piispanen, V., Lastunmuodostumisen Teoriaa., *Teknillinen Aiakauslehti, 27*(9), (1937) 315-322.

[5] Shaw, M. C., Metal Cutting Principles – Second Edition, Oxford Series on Advanced Manufacturing, Oxford University Press, (2005)

[6] Merchant, M., & Zlatin, N., Nomographs for Analysis of Metal-Cutting Processes, *Mechanical Engineering, 67*(11), (1945) 737-742.

[7] Stabler, G. V., Fundamental Geometry of Cutting Tools, *Institution of Mechanical Engineers - Proceedings, 165*(63), (1951) 14-21.

[8] Lee, E. H., & Shaffer, B. W., Theory of Plasticity Applied to Problem of Machining, *Journal of Applied Mechanics, 73*, (1951) 405.

[9] Oxley, P. L. B., Strain Hardening Solution for 'Shear Angle' in Orthogonal Cutting. *Internationl Journal of Mechanical Sciences, 3*(1-2), (1961) 68-79.

[10] Shaw, M. C., The Size Effect in Metal Cutting, *Proceedings of the Indian Academy of Sciences – Sadhana, 28(5)*, (2003), 875-896.

[11] Shaw, M. C., & Jackson, M. J., The Size Effect of Micromachining, Published in 'Microfabrication and Nanomanufacturing', CRC Press (Taylor and Francis Publishers), Florida, USA, (2005).

[12] Schulz, H., State of the Art of High Speed Machining., In A. Molinari, D. Dudzinski & H. Schulz (Eds.), *High Speed Machining* (pp. 1-8), University of Metz, France, (1997).

[13] Usui, E., Hirota, A., & Masuko, M., Basic Cutting Model and Energy Approach., *Transactions of the ASME. Journal of Engineering for Industry, 100*(2), (1978) 222-228.

[14] Usui, E., & Hirota, A., Chip formation and Cutting Force With Conventional Single-Point Turning, *Transactions of the ASME. Journal of Engineering for Industry, 100*(2), (1978) 229-235.

[15] Usui, E., Shirakashi, T., & Kitagawa, T. Cutting Temperature and Crater Wear of Carbide Tools, *Transactions of the ASME. Journal of Engineering for Industry. 100*(2), (1978) 236-243.

[16] Kitagawa, T., Kubo, A., & Maekawa, K., Temperature and Wear of Cutting Tools in High Speed Machining of Inconel 718 and Ti-6Al-6V-2Sn, *Wear, 202*(2), (1997) 142-148.

[17] Ozel, T., & Altan, T., Process Simulation Using Finite Element Method - Prediction of Cutting Forces, Tool Stresses and Temperatures in High-Speed Flat end Milling. *International Journal of Machine Tools and Manufacutre, 40*(5), (2000) 713-738.

[18] Moufki, A., Modelling of Orthogonal Cutting. In A. Molinari, D. Dudzinski & H. Schulz (Eds.), *High Speed Machining* (1, Vol. 1, pp. 8-28). University of Metz, France (1997).

[19] Bailey, J. A., Friction in Metal Machining - Mechanical Aspects. *Wear, 31*(2), (1975) 243-275.

[20] Montgomery, R. S., Friction and Wear at High Sliding Speeds, *Wear, 36*(2), (1976) 275-298.

[21] Groover, M. P., & Kane, G. E., A Continuing Studyin the Determination of Temperatures in Metal Cutting Using Remote Thermocouples, *Transactions of the ASME, Series B, Journal of Engineering for Industry, 93*(2), (1971) 603-609.

[22] Wright, P. K., & Trent, E. M., Metallographic Methods of Determining Temperature Gradients in Cutting Tools, *Journal of the Iron and Steel Institute (London), 211*(5), (1973) 364-368.

[23] Fourment, L., Oudin, A., Massoni, E., Bittes, G., & Le Calvez, C. Numerical Simulation of Tool Wear in Orthogonal Cutting. *High Speed Machining* (1, Vol. 1, pp. 38-48). University of Metz. (1997).

[24] Kim, K. W., & Sin, H. C., Development of a Thermo-Viscoplastic Cutting Model Using Finite Element Method, *International Journal of Machine Tools and Manufacture, 36*(3), (1996) 379-397.

[25] Trent, E. M., & Wright, P. K., *Metal Cutting* (4th Edition). Woburn, MA, Butterworth-Heinemann (2000).

[26] Doyle, E. D., Horne, J. G., & Tabor, D., Frictional Interactions Between Chip and Rake Face in Continuous Chip Formation, *Proceedings of the Royal Socity of London, Series A (Mathematical and Physical Sciences), 366*(1725), (1979) 173-183.

[27] Gekonde, H. O., & Subramanian, S. V., Influence of Phase Transformation on Tool Crater Wear, In A. Molinari, D. Dudzinski & H. Schulz (Eds.), *High Speed Machining* (1, Vol. 1, pp. 49-62). University of Metz, France, (1997).

[28] Gygax, P. E., Cutting Dynamics and Process-Structure Interactions Applied to Milling, *Wear, 62*(1), (1980) 161-184.

[29] Rotberg, J., Cutting Force Prediction in High Speed Machining The Fast Evaluation Approach, In A. Molinari, D. Dudzinski & H. Schulz (Eds.), *High Speed Machining* (1, Vol. 1, pp. 63-74). University of Metz, France, (1997).

[30] Schmitt, I. T., High Speed Milling Machines, In A. Molinari, D. Dudzinski & H. Schulz (Eds.), *High Speed Machining* (1, Vol. 1, pp. 75-83). University of Metz, France, (1997).

[31] Weck, M., & Staimer, D., Parallel Kinematic Machine Tools - Current State and Future Potentials, *CIRP Annals - Manufacturing Technology, 51*(2), (2002) 671-683.

[32] Ibaraki, S., Okuda, T., Kakino, Y., Nakagawa, M., Matsushita, T., & Ando, T, Compensation of Gravity-Induced Errors on a Hexapod-Type Parallel Kinematic Machine Tool. *JSME International Journal, Series C (Mechanical Systems, Machine Elements and Manufacturing), 47*(1), (2004) 160-167.

[33] Moller, B., High Speed and Precision - Features of Motorised Spindles. In A. Molinari, D. Dudzinski & H. Schulz (Eds.), *High Speed Machining* (1, Vol. 1, pp. 116-128). University of Metz, France, (1997).

[34] Cohen, G., & Ronde, U, Use of Spindles With Hydrostatic Bearings in the Field of High Speed Cutting. In A. Molinari, D. Dudzinski & H. Schulz (Eds.), *High Speed Machining* (1, Vol. 1, (1997) pp.129-141). University of Metz, France, (1997).

[35] Tansel, I. N., Arkan, T. T., Bao, W. Y., Mahendrakar, N., Shisler, B., Smith, D., et al., Tool Wear Estimation in Micro-Machining. Part 1: Tool Usage-Cutting

Force Relationship, *International Journal of Machine Tools and Manufacture, 40*(4), (2000) 599-608.

[36] Ingle, S. S., Subramanian, S. V., & Kay, D. A. R., Micromechanisms of Crater Wear, *Proceedings of the Second Conference on the Behaviour of Materials in Machining* (pp. 112-124). London: Institute of Mateirals (1994).

[37] Bhattacharyya, A., & Ham, I., Analysis of Tool Wear Part 1: Theoretical Models of Flank Wear, *ASME-Paper 68-WA/Prod-5,* (1969) 9 Pages.

[38] Bhattacharyya, A., Ghosh, A., & Ham, I., Analysis of Tool Wear Part 2: Applications of Flank Wear Models, *ASME-Paper 69-WA/Prod-8,* (1969) 6 Pages.

[39] Subramanian, S. V., Ramanujachar, K., & Ingle, S. S., Micromechanisms of Tool Wear in High Speed Machining of Steel, *Proceedings of the First Conference on the Behaviour of Materials in Machining* (pp. 223-235). London: Institute of Materials (1989).

[40] Naerheim, Y., & Trent, E. M., Diffusion Wear Of Cemented Carbide Tools When Cutting Steel At High Speeds, *Metals Technology, 4*(12), (1977) 548-556.

[41] Hastings, W. F., Mathew, P., & Oxley, P. L., Machining Theory for Predicting Chip Geometry, Cutting Forces etc. From Work Material and Cutting Conditions, *Proceedings of the Royal Society of London, Series A: Mathematical and Physical Sciences, 371*(1747), (1980) 569-587.

[42] Boothroyd, G., Photographic Technique for Determination of Metal Cutting Temperature, *British Journal of Applied Physics, 12*(5), (1961) 238-242.

[43] Sherby, O. D., Orr, R. L., & Dorn, J. E., Creep Correlations of Metals at Elevated Temperatures, *Journal of Metals, 6*(1), (1954) 71-80.

[44] Sherby, O. D., Factors Affecting the High Temperature Strength of Polycrystalline Solids, *Acta Metallurgica, 10*(2), (1962) 135-147.

[45] Gregory, B., Diffusion Study of Titanium Carbide Effectivness in the Wear Resistance of Cemented Carbide Tools, *Metallurgia, 62*(490), (1970) 55-59.

[46] Suzuoka, T., Lattice and Grain Boundary Diffusion in Polycrystals, *Transactions of the Japan Institute of Metals, 2*(1), (1961) 25-33.

[47] Trent, E. M., Some Factors Affecting Wear on Cemented Carbide Tools, *Institution of Mechnanical Engineers - Proceedings, 166*(1), (1952) 64-70.

[48] Danneberg, W., Selbstdiffusionsuntersuchungen an Wolfram [Study of Self Diffusion of Tungsten], *Metall, 15*(10), (1961) 977-981.

[49] Nayak, P. N., & Cook, N. H., Evaluation of Some Models of Thermally Activated Tool Wear, *American Society of Mechancial Engineers - Papers, 67-Prod-15*, (1967) 11 Pages.

[50] Leymonie, C., & Lacombe, P., Mesure de l'energie d'activation d'autodiffusion Intergranulaire du fer [Measuring Activation Energy of Intergranular Self-Diffusion of Iron], *Memoires Scientifiques de la Revue de Metallurgie, 56*(1), (1959) 74-80.

[51] Davies, R., *A Tentative Model for the Mechancial Wear Process,* ASME Symposium on Friction and Wear, Detroit, USA, (1957).

[52] Faure, C., Hanni, W., Schmutz, C. J., & Gervanoni, M., Diamond-Coated Tool,. *Diamonds and Related Materials, 8*(2-5), (1999) 636-639.

[53] Jackson, M. J., Gill, M., Sein H., & Ahmed, W., Manufacture of Diamond Coated Cutting Tools for Micromachining Applications, *Proceedings of the Institution of Mechanical Engineers, Part L – Journal of Materials, 217,* (2003), 77-82.

[54] Bell, T., Surface Engineering: Its Current and Future Impact on Tribology, *Journal of Physics D: Applied Physics, 25*(1A), (1992) A297-306.

[55] Mills, B., Recent Developments in Cutting Tool Materials, *Journal of Materials Processing Technology, 56*(1-4), (1996) 16-23.

[56] Kubaschewski, O., & Alcock, C. B., *Metallurgical Thermochemistry* (5th), Oxford, Pergamon Press, (1979).

[57] Klocke, F., & Krieg, T., Coated Tools for Metal Cutting - Features and Applications, *CIRP Annals - Manufacturing Technology, 48*(2), (1999) 515-525.

[58] Quinto, D. T., Santhanam, A. T., & Jindal, P. C., Mechanical Properties, Structure and Performance of CVD and PVD Coated Carbide Tools, *International Journal of Refractory and Hard Metals, 8*(2), (1989) 95-101.

[59] Munz, W. D., Smith, I. J., Donohue, L. A., Deeming, A. P., & Goodwin, R, TiAlN Based PVD Coatings Tailored for Dry Cutting Operations, *Proceedings, Annual Technical Conference - Society of Vacuum Coaters* (pp. 83-93). Albuquerque, NM: Society of Vacuum Coaters (1997).

[60] Constable, C. P., Yarwood, J., & Munz, W. D., Raman Microscopic Studies of PVD Hard Coatings, *Surface Coatings and Technology, 116-119*, (1999) 155-159.

[61] Constable, C. P., Yarwood, J., Hovsepian, P., Donohue, L. A., & Munz, W. D., Structural Determination of Wear Debris Generated From Sliding Wear Tests on Ceramic Coatings Using Raman Microscopy, *Journal of Vacuum Science and Technology, Part A: Vacuum, Surfaces and Films, 18*(4 11), (2000) 1681-1689.

[62] Deeming, A. P., Munz, W. D., & Smith, I. J., *Dry High Performance Machining (HPM) of Die and Moulds Using PVD Coated Solid Cemented Carbide Tools,* Paper presented at the meeting of Sheffield P.V.D. Research Group. (2001).

[63] Creasey, S., Lewis, D. B., Smith, I. J., & Munz, W. D. (1997), SEM Image Analysis of Droplet Formation During Metal Ion Etching by a Steered Arc Discharge, *Surface and Coatings Technology, 97*(1-3), 163-175.

[64] Munz, W. D., Smith, I. J., Lewis, D. B., & Creasey, S., Droplet Formation on Steel Substrates During Cathodic Steered Arc Metal Ion Etching, *Vacuum, 48*(5), (1997) 473-481.

[65] Gahlin, R., Bromark, M., Hedenqvist, P., Hogmark, S., & Hakansson, G., Properties of TiN Coatings and CrN Coatings Deposited at low Temperature Using Reactive Arc-Evaporation, *Surface and Coatings Technology, 76*(1-3), (1995) 174-180.

[66] Wang, D. D., & Oki, T., The Morphology and Orientation of Cr-N Films Deposited by Reactive Ion Plating, *Thin Solid Films, 185*(2), (1990) 219-230.

[67] Hurkmans, T., Lewis, D. B., Brooks, J. S., & Munz, W. D., Chromium Nitride Coatings Grown by Unbalanced Magnetron (UBM) and Combined Arc/Unbalanced Magnetron (ABS) Deposition Techniques, *Surface and Coatings Technology, 86-87*(1-3), (1996) 192-199.

[68] Wadsworth, I., Smith, I. J., Donohue, L. A., & Munz, W. D., Thermal Stability and Oxidation Resistance of TiAlN/CrN Multilayer Coatings, *Surface and Coatings Technology, 94-95*(1-3), (1997) 315-321.

[69] Smith, I. J., Gillbrand, D., Brooks, J. S., Munz, W. D., Harvey, S., & Goodwin, R., Dry Cutting Performance of HSS Twist Drills Coated With Improved TiAlN, *Surface and Coatings Technology, 90*(1-2), (1997) 164-171.

[70] Petrov, I., Losbichler, P., Bergstrom, D., Greene, J. E., Munz, W. D., Hurkmans, T., et al., Ion Assisted Growth of Ti(1-x)AlxN/Ti(1-y)NbyN Multilayers by combined Cathodic-Arc/Magnetron-Sputter Deposition, *Thin Solid Films, 302*(1-2), (1997) 179-192.

[71] Salagean, E. E., Lewis, D. B., Brooks, J. S., Munz, W. D., Petrov, I., & Greene, J. E., Combined Steered Arc-Unbalanced Magnetron Grown Niobium Coatings for Decorative and Corrosion Resistance Applications, *Surface Coatings and Technology, 82*(1-2), (1996) 57-64.

[72] Donohue, L. A., Smith, I. J., Munz, W. D., Petrov, I., & Greene, J. E., Microstructure and Oxidation-Resistance of Ti(l-x-y-z)AlxCryYzN Layers Grown by Combined Steered-Arc/Unbalanced-Magnetron-Sputter Deposition, *Surface Coatings and Technology, 94-95*(1-3), (1997) 315-321.

[73] Inamura, T., Takezawa, N., & Kumaki, Y., Mechanics and Energy Dissipation in Nanoscale Cutting, *CIRP Annals, 42*(1), (1993) 79-82.

[74] Kim, J. D., & Moon, C. H., Study on the Cutting Mechanism of Microcutting Using Molecular Dynamics, *International Journal of Advanced Manufacturing Technology, 11*(5), (1996) 319-324.

[75] Gillespie, L. K., Deburring Precision Miniature Parts, *Precision Engineering, 1*(4), (1979) 189-198.

[76] Gilespie, L. K., & Blotter, P. T., Formations and Properties of Machining Burrs, *Journal of Engineering for Industry, Transactions of the ASME, 98 Ser B*(1), (1973) 66-74.

[77] Kim, J. S., Optimization and Control of Drilling Burr Formation in Metals (Doctoral dissertation, University of California at Berkeley), *Dissertation Abstracts International, 62*(01), (2000) 496B. (UMI No. 3001895)

[78] Ko, S. L., & Dornfield, D. A., American Society of Mechancial Engineers, Dynamics and Control Division DSC, *Study on Burr Formation Mechanism, 11*, (1988) 271-282.

[79] Lee, K., & Dornfeld, D. A., An Experimental Study of Burr Formation in Micro Milling Aluminum and Copper, *Technical Paper - Society of Manufacturing Engineers, MR*(MR02-202), (2002) 1-8.

[80] Ikawa, N., Shimada, S., & Tanaka, H., Minimum Thickness of Cut in Micromachining, *Nanotechnology, 3*(1), (1992) 6-9.

[81] Yuan, Z. J., Zhou, M., & Dong, S., Effect of Diamond Tool Sharpness on Minimum Cutting Thickness and Cutting Surface Integrity in Ultraprecision Machining, *Journal of Materials Processing Technology, 62*(4), (1996) 327-330.

[82] Kim, C. J., Bono, M., & Ni, J., Experimental Analysis of Chip Formation in Micro Milling, *Technical Paper - Society of Manufacturing Engineers, MR*(MR02-159), (2002) 1-8.

[83] Sutherland, J. W., & Babin, T. S., The Geometry of a Surface Generated by the Bottom of an End Mill, *Proceedings of NAMRC, 16*, (1988) 202-208.

[84] Ikawa, N., Shimada, S., Tanaka, H., & Ohmori, G., Atomistic Analysis of Nanometric Chip Removal as Affected by Tool-Work Interaction in Diamond Turning, *CIRP Annals, Manufacturing Technology, 40*(1), (1991) 551-554.

[85] Mizumoto, H., Arii, S., Yoshimoto, A., Shimizu, T., & Ikawa, N., Twist-Roller Friction Drive for Nanometer Positioning - Simplified Design Using Ball Bearings, *CIRP Annals - Manufacturing Technology, 45*(1), (1996) 501-504.

[86] Shimada, S., Ikawa, N., Tanaka, H., Ohmori, G., & Uchikoshi, J., Molecular Dynamics Analysis of Cutting Force and Chip Formation Processes in Microcutting, *Seimtsu Koaku Kaishi / Journal of the Japan Society for Precision Engineering, 59*(12), (1993) 2015-2021.

[87] Shimada, S., Molecular Dynamics Simulation of the Atomic Processes in Micromachining, In J. McGeough (Ed.), *Micromachining of Engineering Materials.* New York: Marcel Deckker (2002).

[88] Shimada, S., Inoue, R., Uchikoshi, J., & Ikawa, N., Molecular Dynamics Analysis on Microstructure of Diamond Turned Surfaces, *Proceedings of SPIE - The International Society for Optical Engineering, 2576*, (1995) 396-405.

[89] Komanduri, R., Chandrasekaran, I., & Raff, L. M., Molecular Dynamics Simulation of the Nanometric Cutting of Silicon, *Philosophical Magazine B (Physics of Condensed Matter. Statistical Mechanics, Electronic, Optical and Magnetic Properties, 81*(12), (2001) 1989-2019.

[90] Vogler, M. P., Liu, X., Kapoor, S. G., DeVor, R. E., & Ehmann, K. F., Development of Meso-Scale Machine Tool (mMT) Systems, *Technical Paper - Society of Manufacturing Engineers, MS*(MS02-181), (2002) 1-9.

[91] Popoli, W. F., High Speed Spindle Design and Construction, *Technical Paper - Society of Manufacturing Engineering, MR*(MR98-146), (1998) 23 Pages.

[92] Fredrickson, P., & Grimes, D., Optimizing Motor Technology for Spindle Applications, *Motion System Design, 46*(11), (2004) 24-32.

[93] Zelinski, P., Micro Milling at 1/2 Million RPM, *Modern Machine Shop,* 1 (2003). Retrieved 10 th March 2004, from www.mmsonline.com/articles/080306.html:

[94] Frechette, L. G., Jacobson, S. A., Breuer, K. S., Ehrich, F. F., Ghodssi, R., Khanna, R., et al., Demonstration of a Microfabricated High-Speed Turbine Supported on Gas Bearings, *Technical Digest. Solid-State Sensor and Actuator Workshop, TRF Cat No. 00TRF-0001*, (2000) 43-47.

[95] Orr, D. J., *Macro-Scale Investigation of High Speed Gas Bearings for MEMS Devices,* Doctoral dissertation, Massachusetts Institute of Technology (2000).

[94] Frechette, L. G., Jacobson, S. A., Breuer, K. S., Ehrich, F. F., Ghodssi, R., Khanna, R., et al., Demonstration of a Microfabricated High-Speed Turbine Supported on Gas Bearings, *Technical Digest. Solid-State Sensor and Actuator Workshop, TRF Cat No. 00TRF-0001*, (2000) 43-47.

[95] Orr, D. J., *Macro-Scale Investigation of High Speed Gas Bearings for MEMS Devices,* Doctoral dissertation, Massachusetts Institute of Technology (2000).

Chapter 5

Machining of Brittle Materials Using Nanostructured Diamond Tools

M. J. Jackson and W. Ahmed

5.1 Introduction

Recently, the demand for superhard tools for use in a range of industrial applications has been increasing rapidly [1]. The development of advanced materials with superior mechanical properties and iron-based components being replaced by new materials has made superhard tools an absolute necessity. The automotive and the mould making industries are two examples where superhard tools are essential. In addition, the use of aluminium-silicon alloys and graphite for electrical discharge machines (EDM) is increasing the demand for superior diamond tools. While hardness and wear resistance are major requirements for better machining of advanced materials, higher toughness is also a highly desirable property in order to reduce machining time and cost. The low fracture toughness of polycrystalline diamond (PCD) tools limits the cutting depth consequently increasing the machining time. Diamond itself has a very low fracture toughness, about half of actual PCD. Geometric restrictions also limit the tools that obtained from PCD and subsequently some specific practical machining problems cannot be solved using these tools. An attractive alternative is to employ thin diamond coatings on tougher substrates taking advantage of both high hardness and fracture toughness.

Initial finite element analyses of the machining of graphite was conducted to understand how using different tool materials contributed to the level of machining forces, machining temperatures, and the rate of heat generation at the shear zone. A

series of computations were generated that showed the effect of using uncoated tungsten carbide cutting tools and diamond cutting tools affected the magnitude of machining forces and temperatures generated during the machining process at two depths of cut, namely, 0.6 mm and 1.2mm, respectively.

In our laboratory, the performance of CVD diamond coatings has been compared with the commercial PCD, during dry machining of graphite used for electrical discharge machines (EMD electrodes) [2]. Our results indicate a clear increase in tool lifetime when compared to PCD and suggest that the diamond crystal's size influences the performance of the cutting tool. This study reports the influence of the coating grain size in the wear rate and chip flow during dry machining of graphite. In order to control the crystal grain size, the secondary nucleation of diamond was promoted during the film growth using the time modulated chemical vapour deposition (TMCVD) process [3,4]. Two coatings with different grain sizes and thickness between 5 and 6 μm were tested during high speed machining experiments machining graphite and were compared with commercial inserts of PCD.

5.2 Mechanisms of Tool Wear

The factors that lead to tool wear are mechanical, thermal, chemical, and abrasive. During chip formation a significant amount of heat is generated, particularly on the flank of the tool. Due to the cyclical nature of the cutting operation these thermal loads pulsate leading to thermal fatigue of the tool material. The typical wear zones on the cutting edge are shown in Figure 5.1. Figure 5.2 shows the effect these sources of wear have on a cutting insert. The high temperatures generated in the cutting zone make the tool particularly susceptible to diffusion wear.

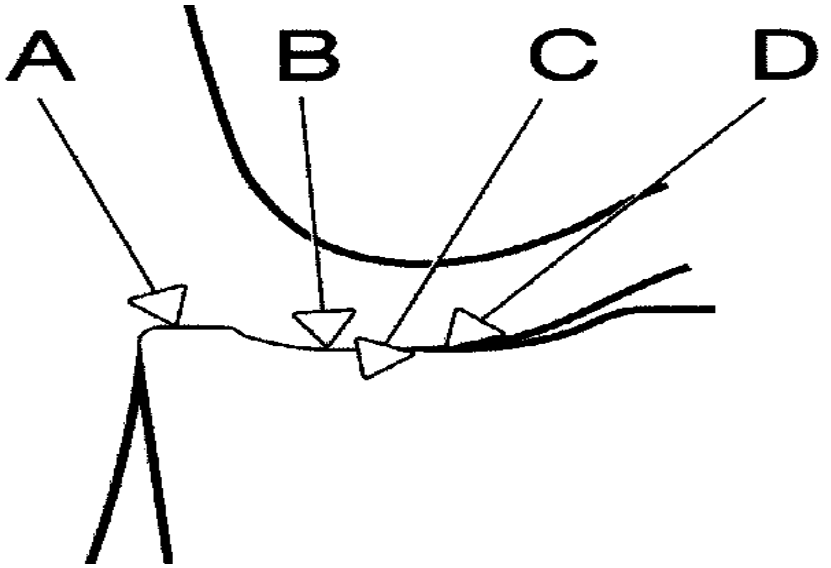

Figure 5.1. Wear zones on the cutting tool caused by chip formation

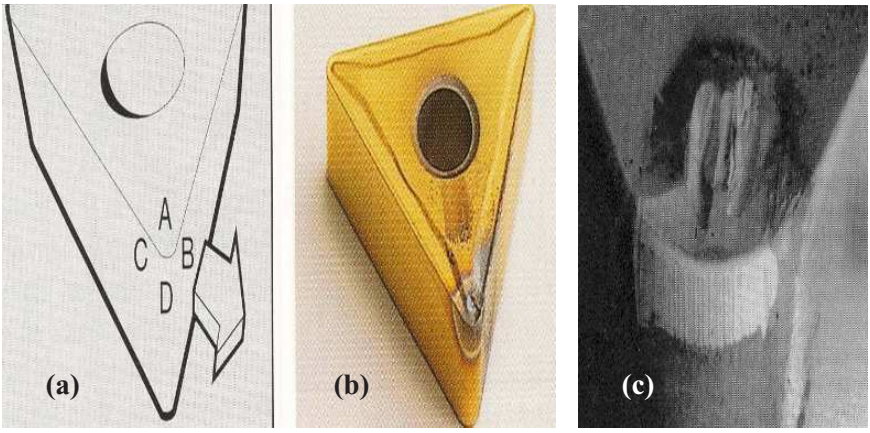

Figure 5.2. (a) Areas of wear on the cutting tool insert shown in Figure 5.1; (b) physical cutting tool insert showing worn edges described in (a); and (c) well developed flank and crater wear at the nose of the insert

As a result of load factors exerted on the cutting tool edge, a few basic mechanisms dominate metal cutting. These mechanisms are:

1. Diffusion wear – affected by chemical loading on the tool and is controlled by the metallurgical composition of the tool and coating material;

2. Abrasive wear – affected by the hardness of the tool material and is controlled by the carbide content of the cutting tool material;

3. Oxidation wear – causes gaps to occur in coated films and results in a loss of the coating at elevated temperatures;

4. Fatigue wear (static or dynamic) – this is a thermo-mechanical effect and leads to the break down of the edges of the cutting tool;

5. Adhesion wear – occurs at low machining temperatures on the chip face of the tool and leads to the formation of a built-up-edge, and the continual breakdown of the built-up edge and the tool edge itself.

The main categories of tool wear are summarized in Figure 5.3. The main wear characteristics of different wear processes are listed. Figure 5.4 shows the first three types of tool wear known as flank wear, crater wear, and plastic deformation. Flank wear is caused by the abrasive wear mechanism and is caused by the chip moving against the face of the cutting tool. Crater wear is caused by a combination of abrasive and diffusion wear mechanisms. Plastic deformation takes place as a function of high pressures and temperatures on the cutting tool.

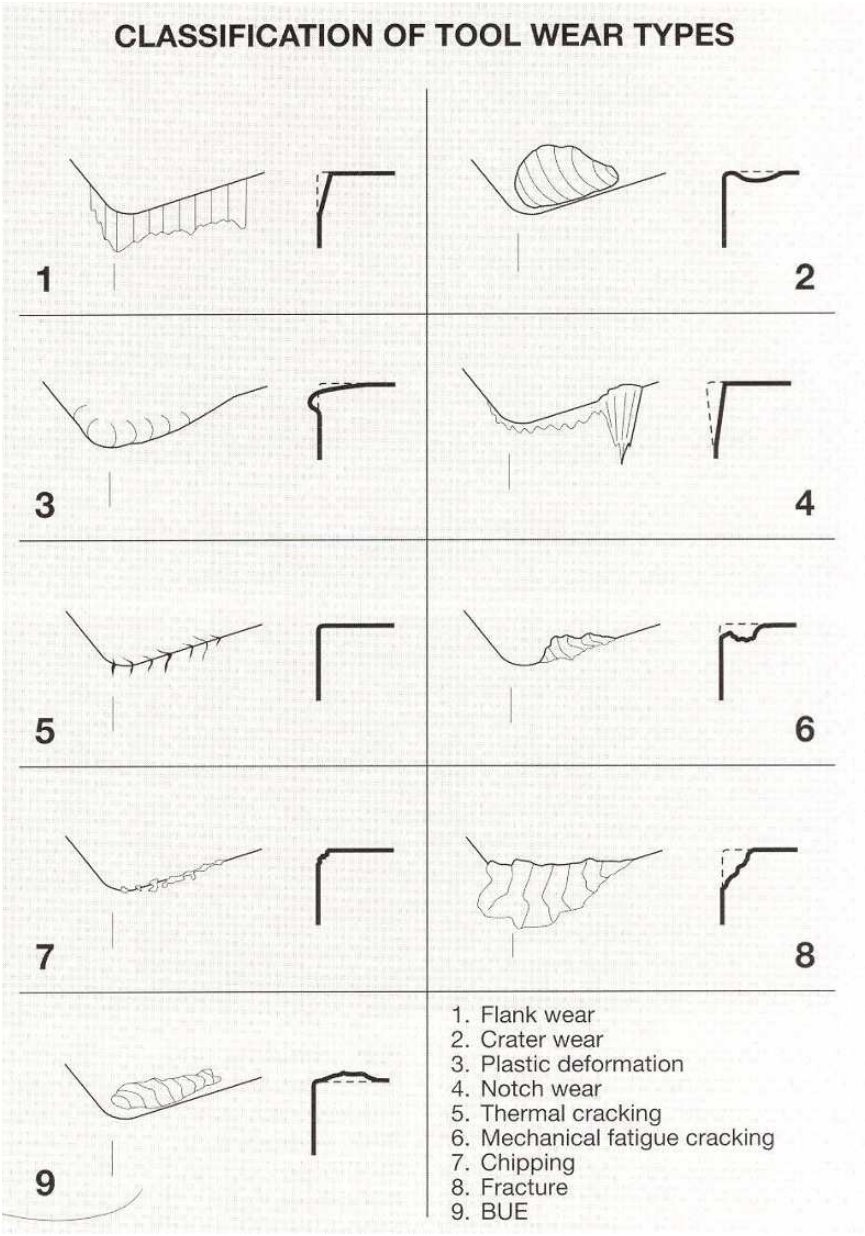

Figure 5.3. Classification of cutting tool wear caused by a combination of different tool wear mechanisms

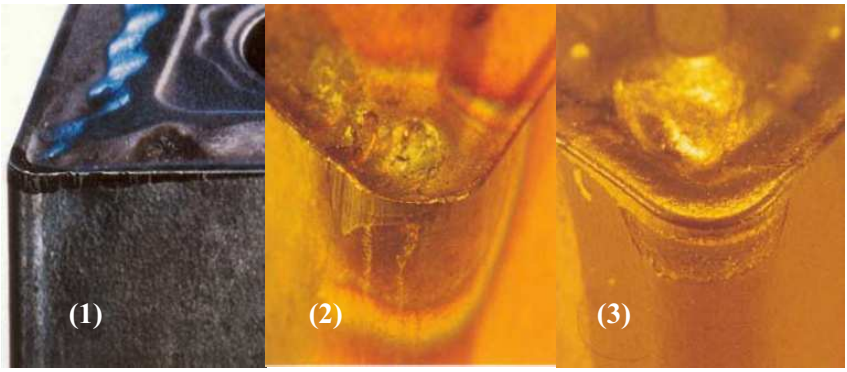

Figure 5.4. Cutting tool wear types: (1) flank wear; (2) crater wear; and (3) plastic deformation

Figure 5.5 shows notch wear, thermal cracking, and mechanical fatigue cracking of the cutting tool.

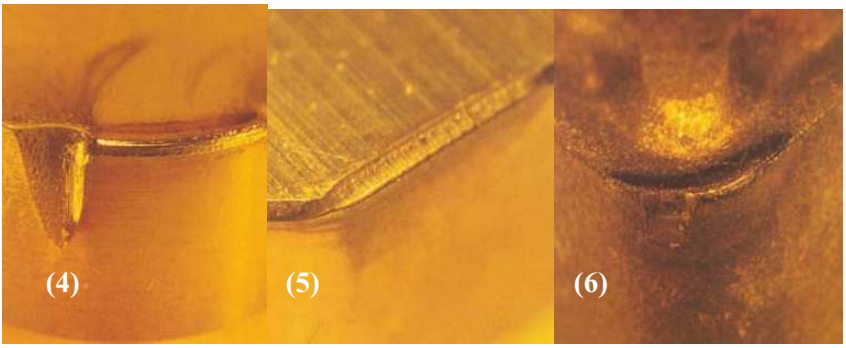

Figure 5.5. Cutting tool wear types: (4) notch wear; (5) thermal cracking; and (6) mechanical fatigue cracking

Notch wear on the trailing edge is a type of adhesion wear but can be caused by oxidation. The wear is localized at the end of the cut where air can penetrate the cutting zone. Notch wear on the leading edge is mechanical and weakens the cutting edge. Thermal cracking is a form of fatigue and is due to thermal cycling, cracks form in the tool material and the edge of the tool is lost through machining. Varying the chip thickness affects the cutting

temperature at the chip/tool interface, and can lead to the rapid breakdown of the tool material. Mechanical fatigue cracking takes place when cutting force shocks are excessive. Figure 5.6 shows the wear of the cutting edge caused by chipping, fracture, and the built-up edge.

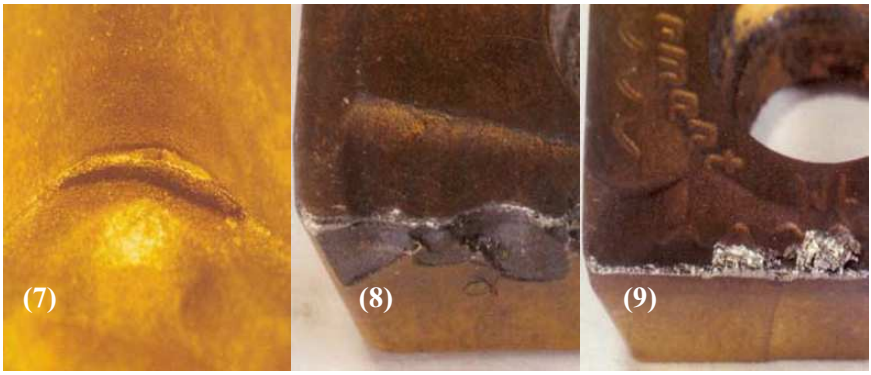

Figure 5.6. Cutting tool wear types: (7) chipping; (8) fracture; and (9) built-up edge

Chipping of the cutting edge is cyclic and is caused by the fatigue of the cutting tool due to intermittent cutting. Fracture is the catastrophic breakdown of the tool material and is caused by heavy cuts or very high cutting forces. Finally, the built-up edge changes the geometry of the cutting tool and leads to an increase in the level of cutting force. When the built-up edge breaks off, the cutting tool force reduces which leads to a cycling of the load. The tool edge eventually breaks off.

5.3 Machining Simulations

The initial simulations of the machining process were conducted using a proprietary finite element code. The initial modelling conditions were the same as those outlined in the experimental section of this paper. Figures 5.7-5.10 pertain to a 0.6mm depth of cut machining graphite with a tungsten carbide cutting tool. The cutting speed was 1200 mm/min and the graphite machined

possessed a bulk density of 1.3 g/cm^3, thermal conductivity of 25 W/m.K, and a specific heat capacity of 710 J/kg.K. The cutting tool had a rake angle of 7^O, a clearance angle of 10^O, and an edge radius of 0.02mm. It is shown in Figures 5.7 and 5.8 that the initial stages of machining produce an unsteady fluctuation in force in the X an Y directions, i.e. tangential and radial directions of the order of approximately 4 and 8N, respectively (Figures 5.7 and 5.8). The temperature of the tool relaxes to a steady temperature of approximately 550^{O}C at the tool tip (Figure 5.9). The rate of heat generation is concentrated at the tool tip and extends to the primary shear zone ahead of the tool (Figure 5.10).

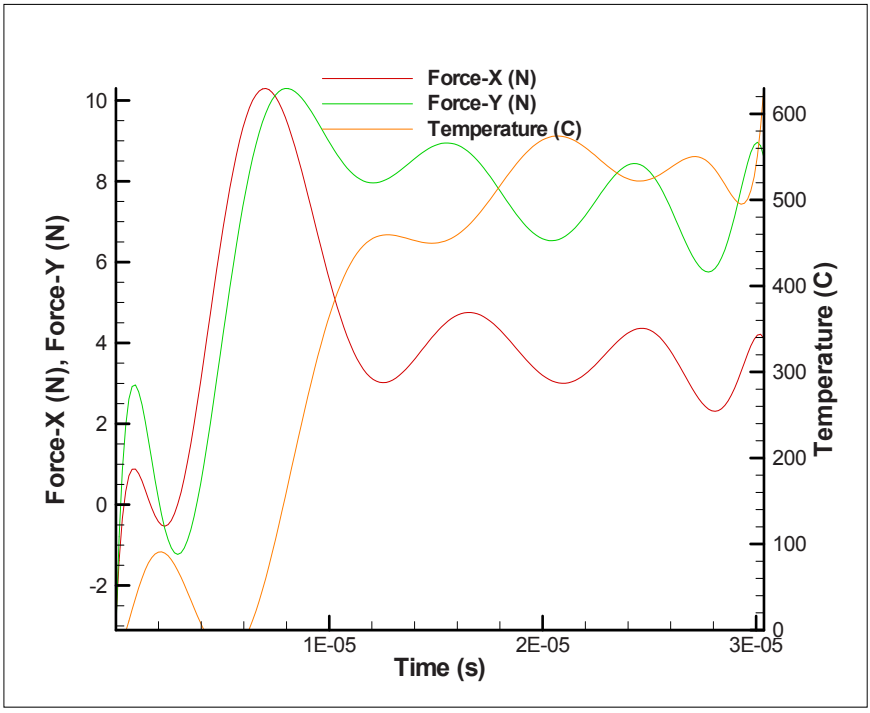

Figure 5.7. Force and temperature signatures as a function of time when machining graphite at a depth of cut of 0.6mm using a cobalt bonded tungsten carbide cutting tool

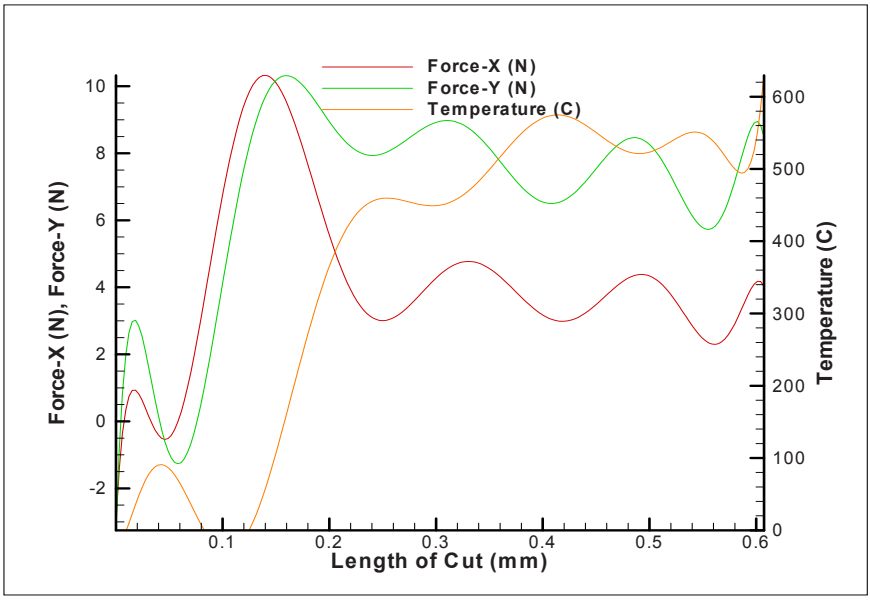

Figure 5.8. Force and temperature signatures as a function of the initial length of cut when machining graphite at a depth of cut of 0.6mm using a cobalt bonded tungsten carbide cutting tool

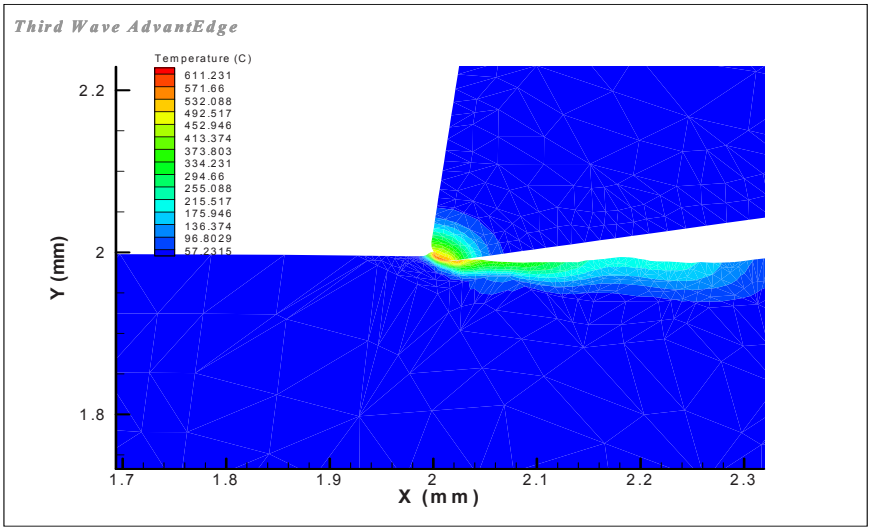

Figure 5.9. Temperature profile when machining graphite at a depth of cut of 0.6mm using a cobalt bonded tungsten carbide cutting tool

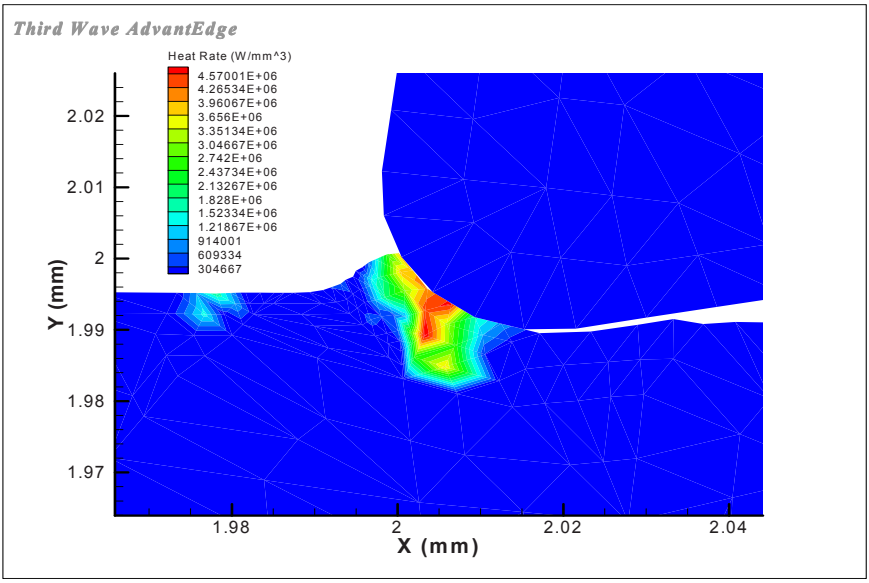

Figure 5.10. Rate of heat generated when machining graphite at a depth of cut of 0.6mm using a cobalt bonded tungsten carbide cutting tool

Figures 5.11-5.14 pertain to a 1.2mm depth of cut machining graphite with a tungsten carbide cutting tool. The cutting speed was 1200 mm/min and the graphite machined possessed a bulk density of 1.3 g/cm^3, thermal conductivity of 25 W/m.K, and a specific heat capacity of 710 J/kg.K. The cutting tool had a rake angle of 7^O, a clearance angle of 10^O, and an edge radius of 0.02mm. It is shown in Figures 18 and 19 that the initial stages of machining produce an unsteady fluctuation in force in the X an Y directions, i.e. tangential and radial directions of the order of approximately 8 and 15N, respectively. The temperature of the tool relaxes to a steady temperature of approximately 540^{O}C at the tool tip (Figure 5.13) and now shows a pronounced primary shear plane. The rate of heat generation is concentrated at the tool tip and extends to the clearance face away from the tool tip (Figure 5.14).

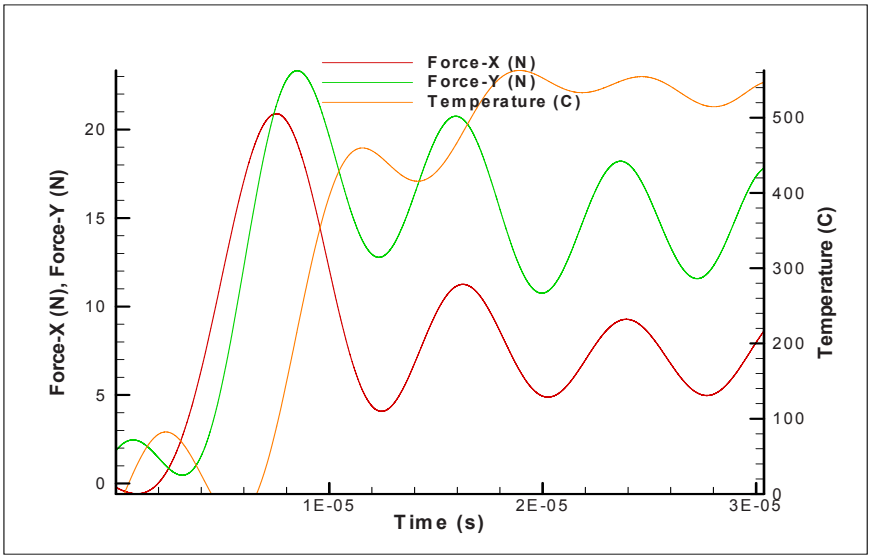

Figure 5.11. Force and temperature signatures as a function of time when machining graphite at a depth of cut of 1.2 mm using a cobalt bonded tungsten carbide cutting tool

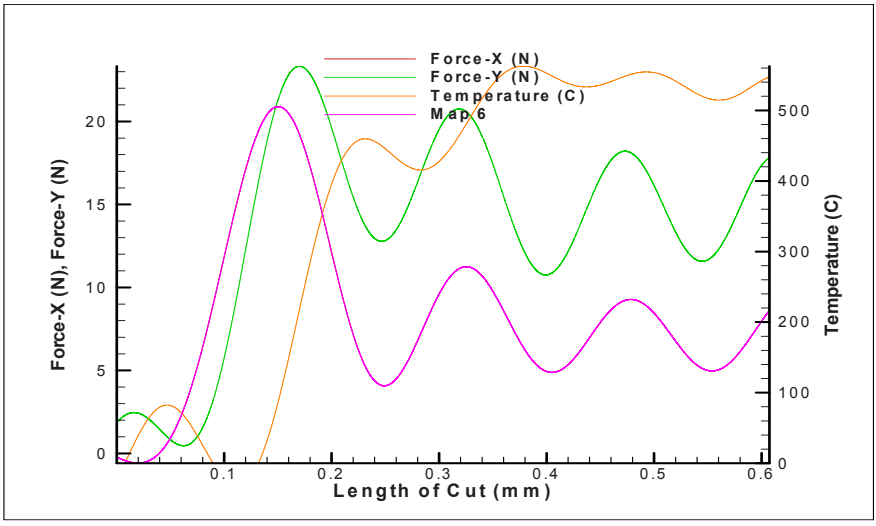

Figure 5.12. Force and temperature signatures as a function of the initial length of cut when machining graphite at a depth of cut of 1.2 mm using a cobalt bonded tungsten carbide cutting tool

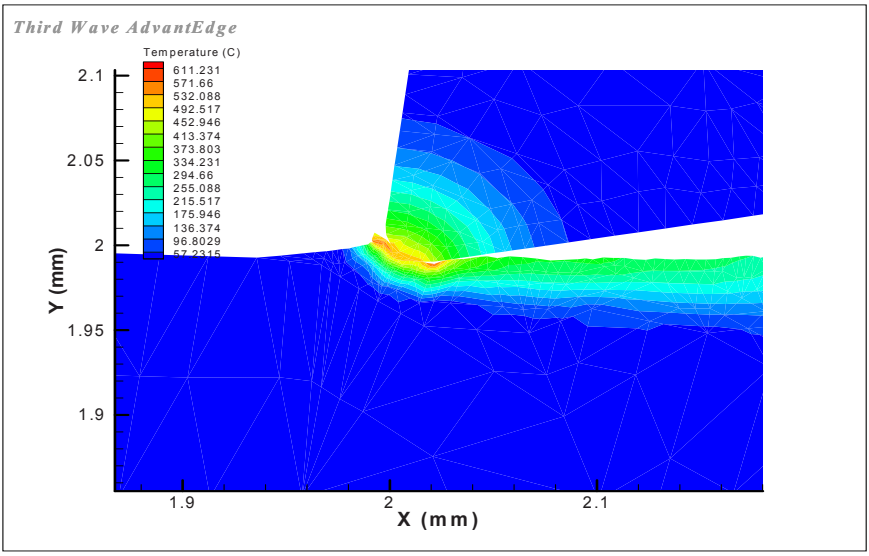

Figure 5.13. Temperature profile when machining graphite at a depth of cut of 1.2 mm using a cobalt bonded tungsten carbide cutting tool

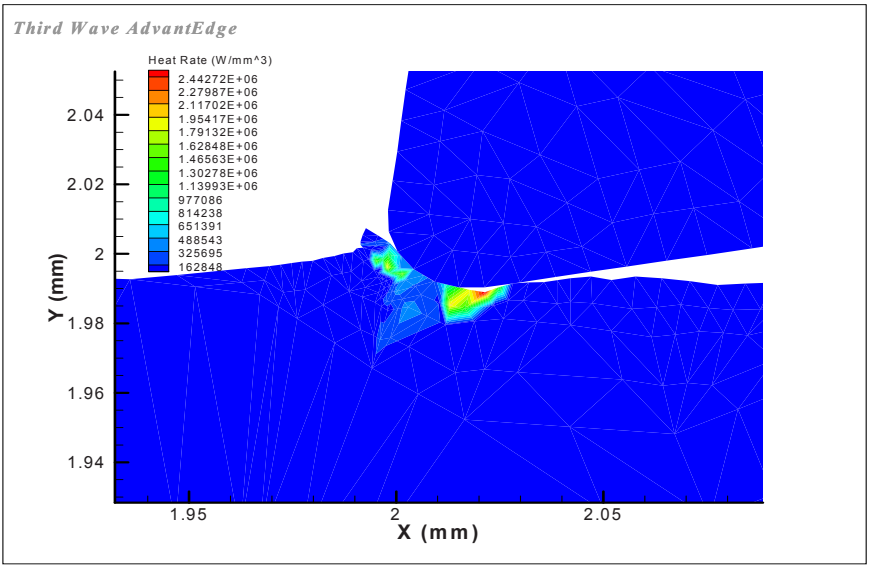

Figure 5.14. Rate of heat generated when machining graphite at a depth of cut of 1.2 mm using a cobalt bonded tungsten carbide cutting tool

Figures 5.15-5.18 pertain to a 0.6mm depth of cut machining graphite with a diamond coated tungsten cutting tool. The cutting speed was 1200 mm/min and the graphite machined possessed a bulk density of 1.3 g/cm^3, thermal conductivity of 25 W/m.K, and a specific heat capacity of 710 J/kg.K. The cutting tool had a rake angle of 7^O, a clearance angle of 10^O, and an edge radius of 0.02mm. It is shown in Figures 5.15 and 5.16 that the initial stages of machining produce an unsteady fluctuation in force in the X an Y directions, i.e. tangential and radial directions of the order of approximately 8.5 and 4.2N, respectively. The temperature of the tool relaxes to a steady temperature of approximately 380^{O}C at the tool tip (Figure 5.17) and now shows a pronounced primary shear plane. The rate of heat generation is concentrated at the primary shear plane (Figure 5.18).

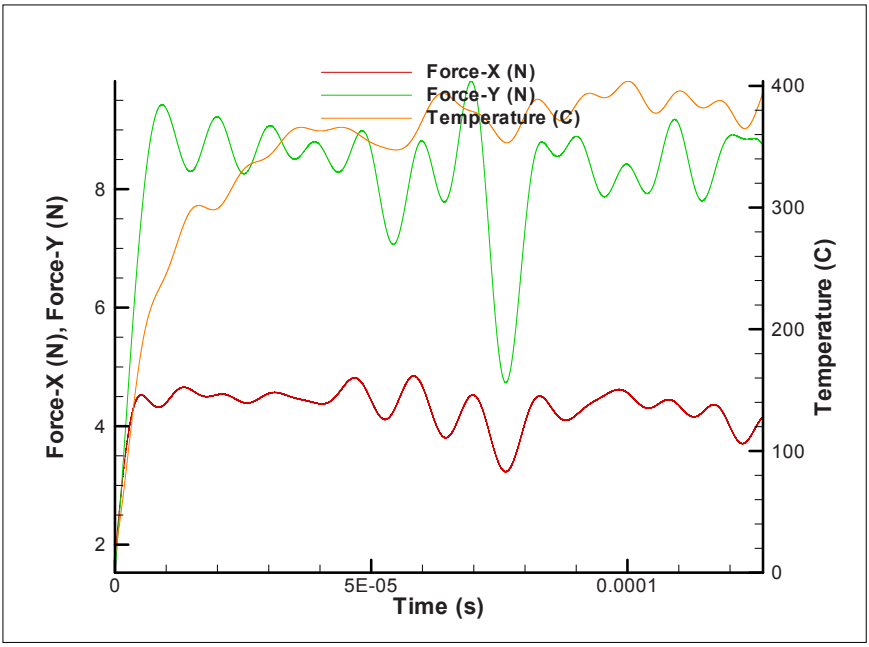

Figure 5.15. Force and temperature signatures as a function of time when machining graphite at a depth of cut of 0.6 mm using a diamond cutting tool

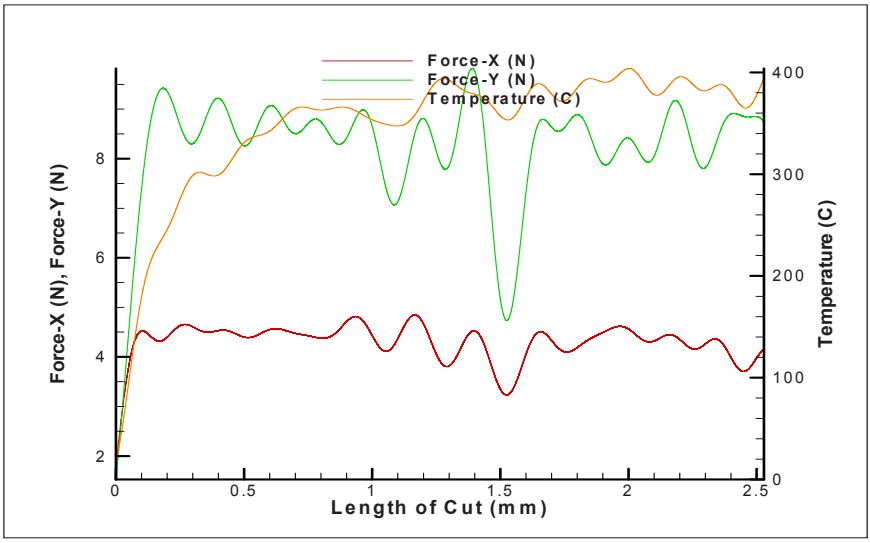

Figure 5.16. Force and temperature signatures as a function of length of cut when machining graphite at a depth of cut of 0.6 mm using a diamond cutting tool

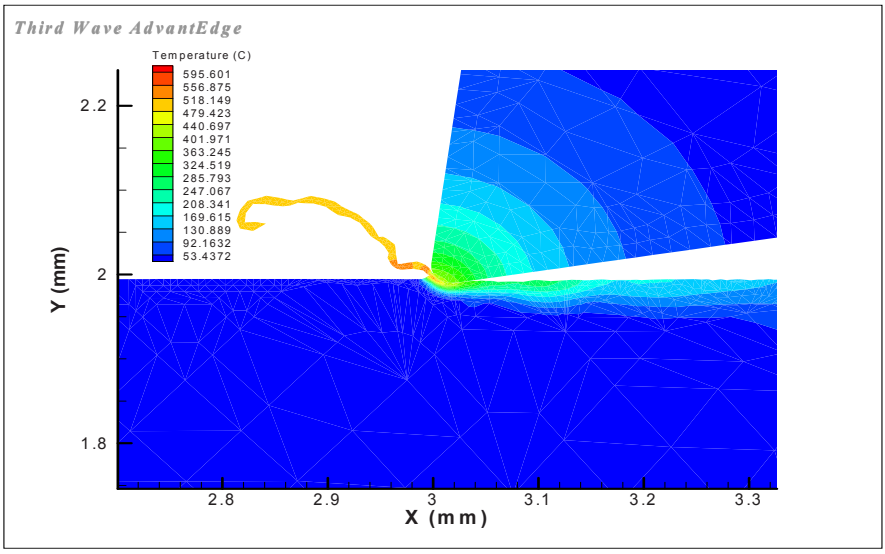

Figure 5.17. Temperature profile when machining graphite at a depth of cut of 0.6 mm using a diamond cutting tool

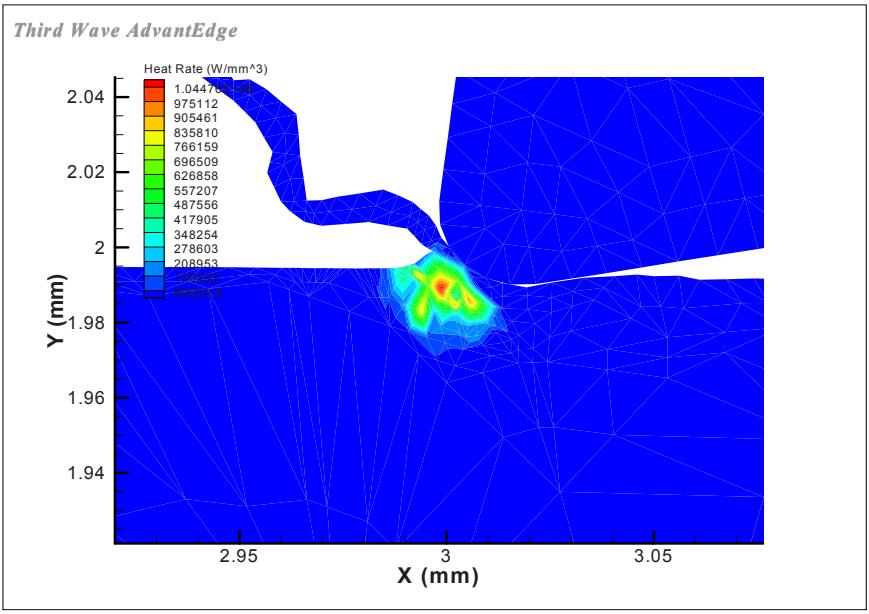

Figure 5.18. Rate of heat generated when machining graphite at a depth of cut of 0.6 mm using a diamond cutting tool

Figures 5.19-5.22 pertain to a 1.2mm depth of cut machining graphite with a diamond coated tungsten cutting tool. The cutting speed was 1200 mm/min and the graphite machined possessed a bulk density of 1.3 g/cm^3, thermal conductivity of 25 W/m.K, and a specific heat capacity of 710 J/kg.K. The cutting tool had a rake angle of 7^O, a clearance angle of 10^O, and an edge radius of 0.02mm. It is shown in Figures 5.19 and 5.20 that the initial stages of machining produce an unsteady fluctuation in force in the X an Y directions, i.e. tangential and radial directions of the order of approximately 17 and 8.5N, respectively. The temperature of the tool relaxes to a steady temperature of approximately 380^{O}C at the tool tip (Figure 5.21) and now shows a pronounced primary shear plane. The rate of heat generation is concentrated at the extremities of the primary shear plane (Figure 5.22).

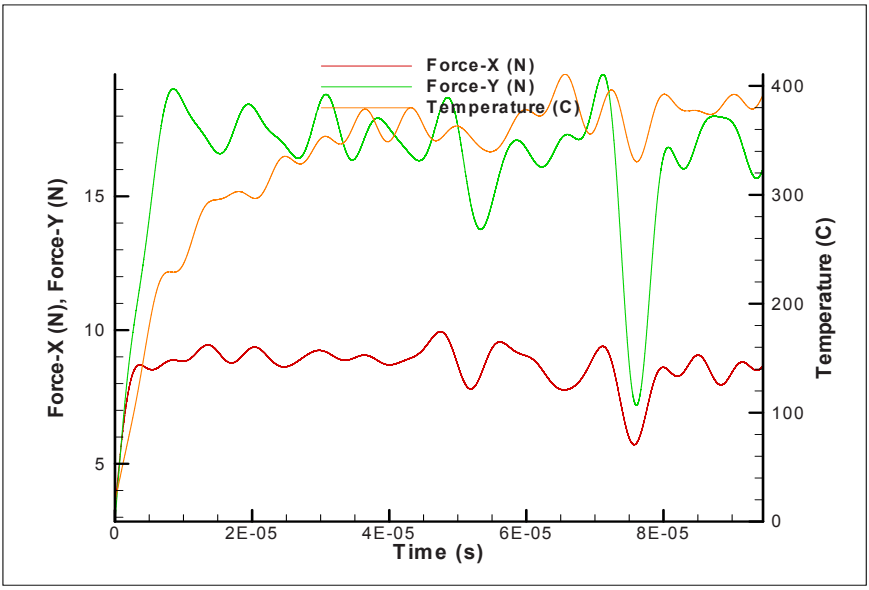

Figure 5.19. Force and temperature signatures as a function of time when machining graphite at a depth of cut of 1.2 mm using a diamond cutting tool

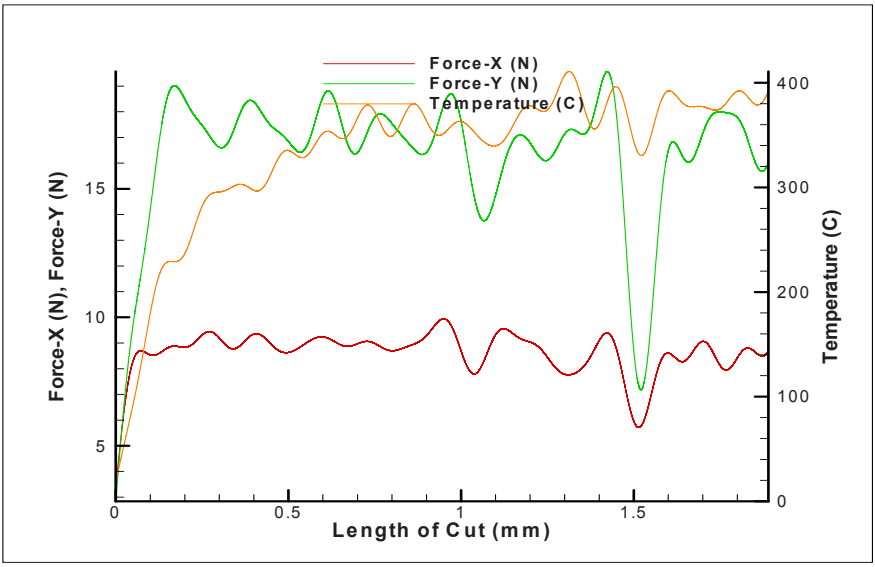

Figure 5.20. Force and temperature signatures as a function of length of cut when machining graphite at a depth of cut of 1.2 mm using a diamond cutting tool

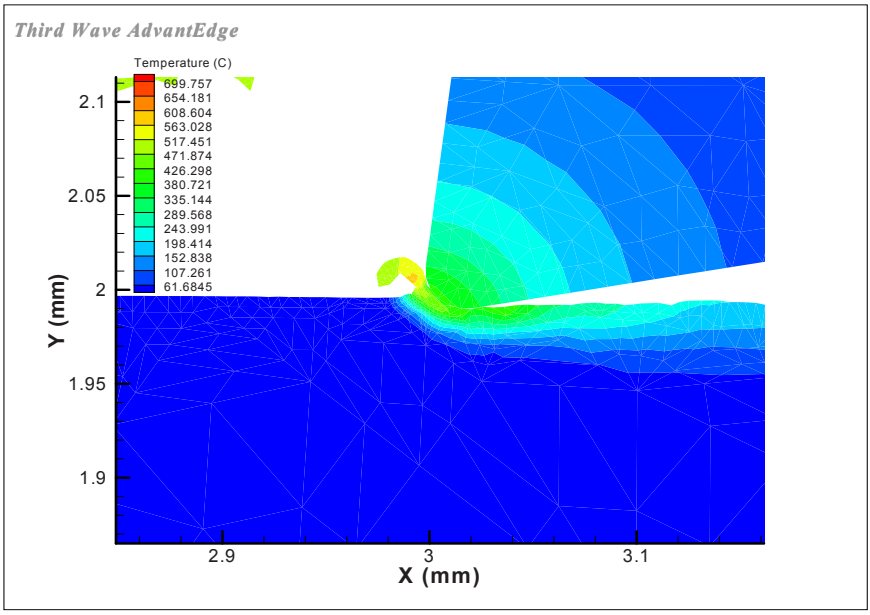

Figure 5.21. Temperature profile when machining graphite at a depth of cut of 1.2 mm using a diamond cutting tool

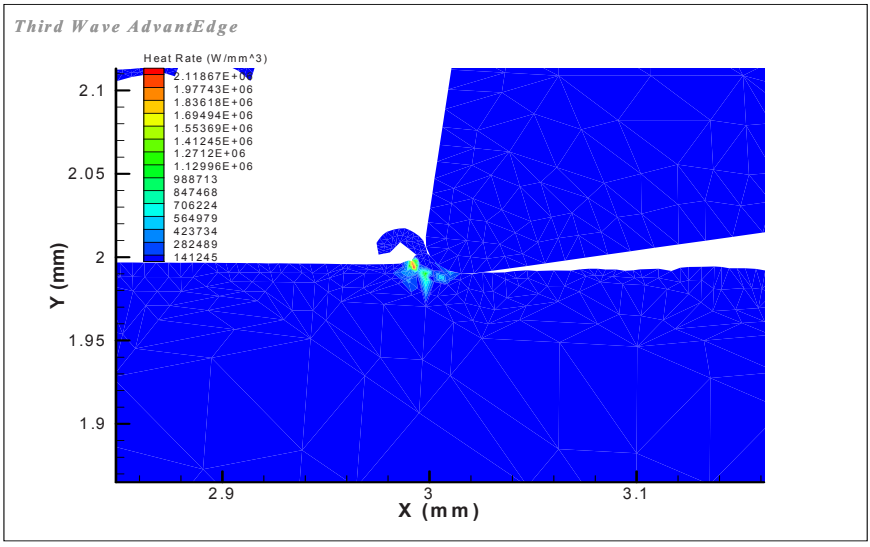

Figure 5.22. Rate of heat generated when machining graphite at a depth of cut of 1.2 mm using a diamond cutting tool

5.4 Experimental Methods

Diamond films were deposited onto fine-grained hard metal (WC-6wt.%Co) tool inserts (TPGN 110304) supplied by Palbit (Portugal). As-ground inserts were rinsed with acetone in an ultrasonic bath and then submitted to proper ex-situ pre-treatment described elsewhere [5-12]. Diamond depositions using the TMCVD process were carried out using a homemade stainless steel HFCVD system (TMCVD2 and TMCVD3). In order to get diamond films with same thickness (5-6 μm), two different TMCVD deposition cycles were employed. The CH_4 modulation in the gas flow rate leads to the step-modulation of the methane concentration between 0.5 and 2.5 mol.%, as shown in Figure 5.23a and Figure 5.23b, respectively. The substrate temperature was measured by a K-type thermocouple located near the insert surface. The temperature varied between 720ºC and 750ºC, depending on the CH_4/H_2 ratio. The pressure was set to a value of 4.0 kPa during all the deposition and automatically adjusted by a proportional and integration (PI) control.

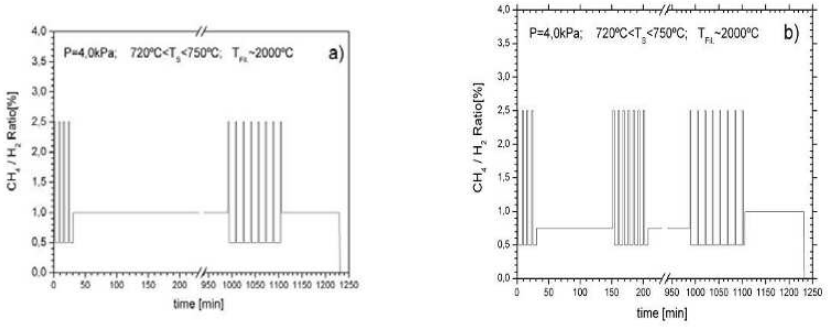

Fig. 5.23. Deposition cycles for TMCVD 2, panel (a), and TMCVD 3, panel (b)

The quality and the residual stress of diamond coatings were assessed by Raman spectroscopy at room temperature using a ISA JOBIN YVON-SPEX T64000 spectrometer equipped with an argon

ion laser ($\lambda = 514.5$ nm), in the 1100-1600 cm^{-1} range. PeakFit software was used to remove the baseline and fit the spectra. A second-order polynomial function was used for baseline subtraction. The diamond peak, the D and G bands were fitted with Lorentzian functions. The other bands were fitted with Gaussian functions. The diamond morphology and tool wear were evaluated by means of scanning electron microscopy (SEM/EDS, Hitachi 4100). The samples were also characterized by X-Ray diffraction. The diamond deposition was stopped after 60 minutes and the samples were characterized by X-Ray diffraction. XRD data were acquired in 20-90^o, 2θ range, using a grazing incident with ϕ=3^o to reduce the signal from the substrate and to enhance the signal from the coatings.

The cutting performance of the inserts was evaluated with dry turning of commercial graphite (ISEM8E). The feed rate was f=0.06 mm/rev, the depth of the cut was *DOC*=0.6 mm and *DOC*=1.2 mm and the cutting velocity was kept constant at 1200 m/min. The tests were performed on a total length of 330 mm on a CNC Kinsbury MHP 50 machine. The cutting forces were measured with a piezoelectric dynamometer with an acquisition data system (DynoWare software). The tests were periodically interrupted to measure the cutting tool wear with an optical microscope Mitutoyo TM-500 using 30X magnification and 1 μm resolution. SEM and Energy Disperse X-Ray Spectroscopy (EDS) were used as complementary techniques to optical microscopy, whenever crater formation or film delamination was observed.

The flank wear, film delamination, geometrical dimension of the piece and the surface defects/roughness of the piece machine were the criteria followed to evaluate the tool lifetime. Whenever one of these indicators reached the limit the test was finished. For the sake of comparison, the machining tests were carried out under identical conditions using commercial PCD inserts (TPUN 11 03 04 CD10) with a cutting velocity of 1200 m/min, a feed rate of 0.06 mm/rev and a depth of cut of 1.2 mm.

5.5 Experimental Results and Discussion

5.5.1 Film characterization

The two cycles of TMCVD allowed the growth of diamond coatings with different surface roughnesses. Figures 5.24 (a) and (b) shows TMCVD 2 coatings have a smother surface as the Raman spectra are shown in

Fig. 5.25. The first-order Raman band of diamond is present at 1338.0 and 1337.5 cm^{-1} in TMCVD 2 and TMCVD 3 coatings, respectively. The frequency shift of these peaks was 5.6 and 5.1 cm^{-1}, with respect to the value of natural diamond (1332.4 cm^{-1} at atmospheric pressure and 25 °C). These up-shifts indicate a residual compressive stress in the diamond coatings.

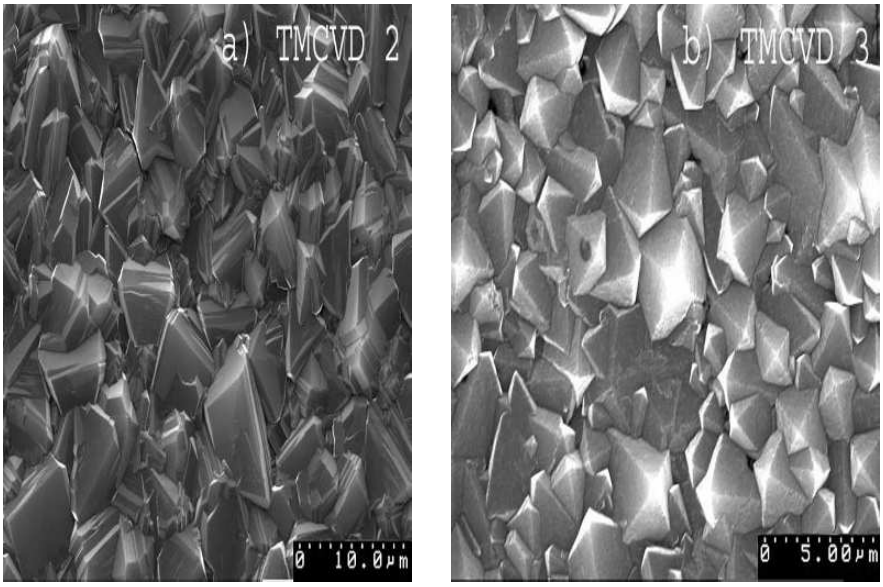

Fig. 5.24. Diamond morphology TMCVD 2, panel (a), and TMCVD 3 panel (b) morphology

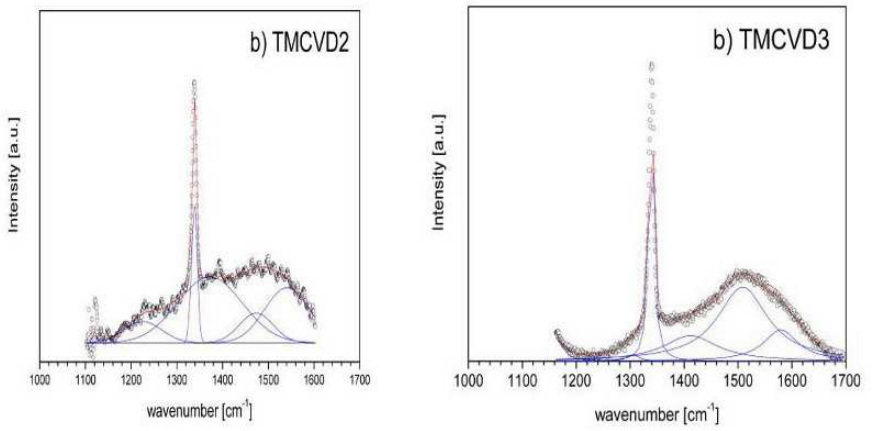

Fig. 5.25. Raman spectra of diamond coatings

In addition to the characteristic first-order diamond Raman band, the spectra displayed extra features centred at around 1140, 1200, 1360, 1470 and 1545 cm^{-1}. Ferrari and Robertson [13] assign the peaks centered at ~1140 cm^{-1} and ~1450 cm^{-1} to λ_1 (1140 cm^{-1}) and λ_3 (1450 cm^{-1}) modes of trans-polyacetylene. The π and empty π^* states give rise to bands that touch the Brillouin zone at K ~ 1200 cm^{-1}.

The disordered graphite displayed two fairly sharp modes in the Raman spectrum: the G-band centred at ~1545 cm^{-1} and the D-band centred at ~1350 cm^{-1}, usually assigned to zone centre of phonons of E_{2g} symmetry and K-point phonons of A_{1g} symmetry, respectively [14]. The existence of the peak centred at ~ 1350 cm^{-1} arises from finite crystallite size of graphitic regions [15]. Figure 5.26 shows the patterns of the WC-Co substrates after the nucleation step and after the diamond growth. The diffraction patterns showed WC and diamond peaks. No traces of cobalt were detected.

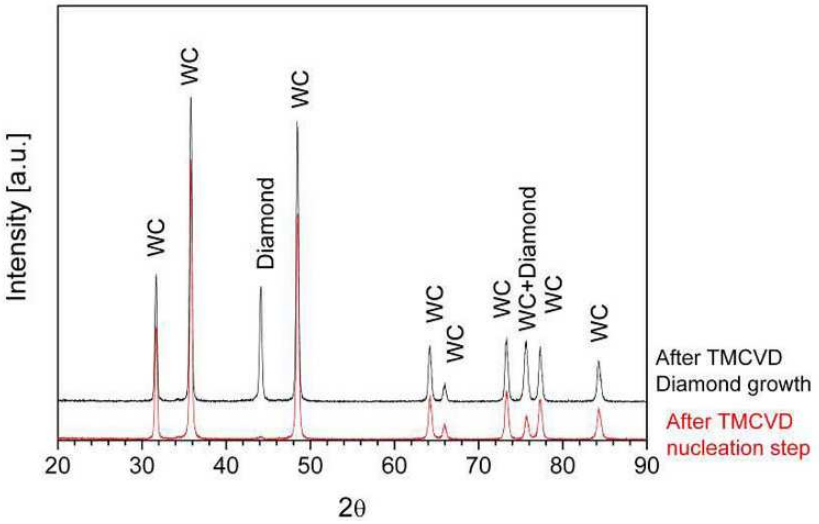

Fig. 5.26. XRD of WC-Co inserts submitted to TMCVD nucleation step and to subsequent deposition of 6 μm TMCVD 3 diamond film

5.5.2 Wear mechanisms

When the cutting tool becomes in contact with the graphite compression occurs. As more stress is applied to the brittle material by the cutting action, the graphite compresses until it reaches a point where rupture occurs and the chip separates from the unmachined portion. This cycle is repeated indefinitely during the cutting operation. During machining, the tool wear occurs gradually at two main locations, the rake face and the flank. Three main types of wear may be observed: (i) notching wear; (ii) crater wear; and (iii) flank wear.

5.5.2.1 Crater wear and notching wear

SEM evaluation showed the formation of a depth-of-cut notch on the relief face of the insert during the first minutes of cutting time. The dependence of the notch wear with the cutting time is shown in

Table 5.1. The localized notching formation happens at two specific points; the tool – work piece contact area is very small and the load concentrates in a small area, inducing high contact stresses. In the diamond-coated inserts, the localized stress exceeds the maximum critical value for the diamond/WC-Co system, causing a localized coating failure. The dimensions of this notching increase in depth with the cutting time; however, the experimental data showed that the quality of the machining only reflects this effect with longer cutting times.

Table 5.1. Notching formation against the cutting time

	TMCVD2	TMCVD3	PCD
Relief face notching	1 min	2 min	1 min
Tip notching	4 min	6 min	2 min

The interaction between the insert material and graphite originates the tool gradual wear. This wear leads not only to the formation of a crater but also to the lateral "channels" which work as alternative paths for the graphite powder flow from the cutting edge. By comparing panel (a) and (b) of Figure 5.27, it can be seen that after 15 min of cutting time both coatings shown a localized failure. The coating failure happened at the cutting edge for TMCVD2 and at the nose tip for TMCVD3. In both cases there is a sever damage in a working area of the insert, during the cutting operation. At this stage, the tests were considered finished.

The wear mechanism of PCD tools is different from the CVD diamond coated tools. PCD is a material made with a mix of diamond particles bonded by metallic cobalt, and the wear abrasion occurs in the binder phase, instead of being due to the graphite adhesion. On contrary, CVD diamond coatings have a single hard phase of diamond and its subsequent intrinsic properties, such as hardness and wear resistance. In this case, the beginning of the crater formation is located on the notching.

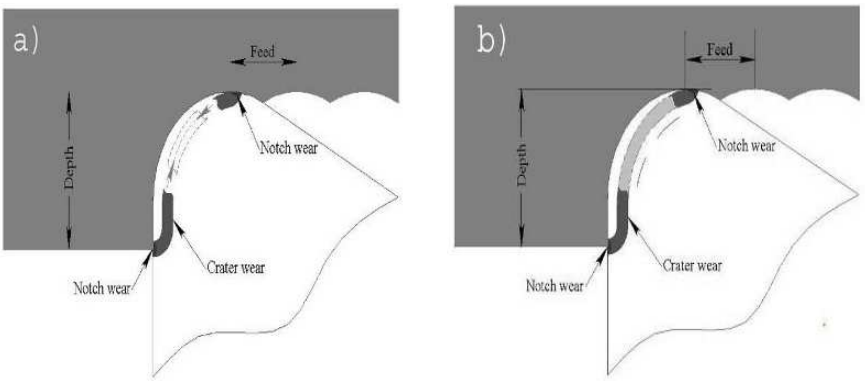

Fig. 5.27. Sequence of crater formation during dry machining of graphite

The combined effects of the graphite powder/chip flow towards the rake face and the abrasion wear of the WC-Co substrate located on the notching area are illustrated in Figure 5.27 (a). The growth of the crater wear from one notching towards the other notching by the localized peeling of the coating is apparent. At the same time, the crater depth increases, as a result of the abrasive wear of the WC-Co substrate, (Figure 5.27 (b)).

5.5.2.2 Flank wear

While crater wear is important because it changes the nominal cutting geometry, flank wear, V_B, is the more common method used to quantify the life of a cutting tool. The flank wear of the inserts is shown in Figure 5.28. The well defined band shown in Figure 5.28 (a) is mainly related to (i) graphite powder adhesion between the diamond crystals and (ii) groves on the coating and subsequent localized coating damages, identified as "***A***"**.** These groves originated in the motion of hard particles/grains, with micron sizes, at the interface of the graphite/tool during the turning. As a result, a few diamond grains are detached from the drag towards the flank face of the insert, damaging the coating even more.

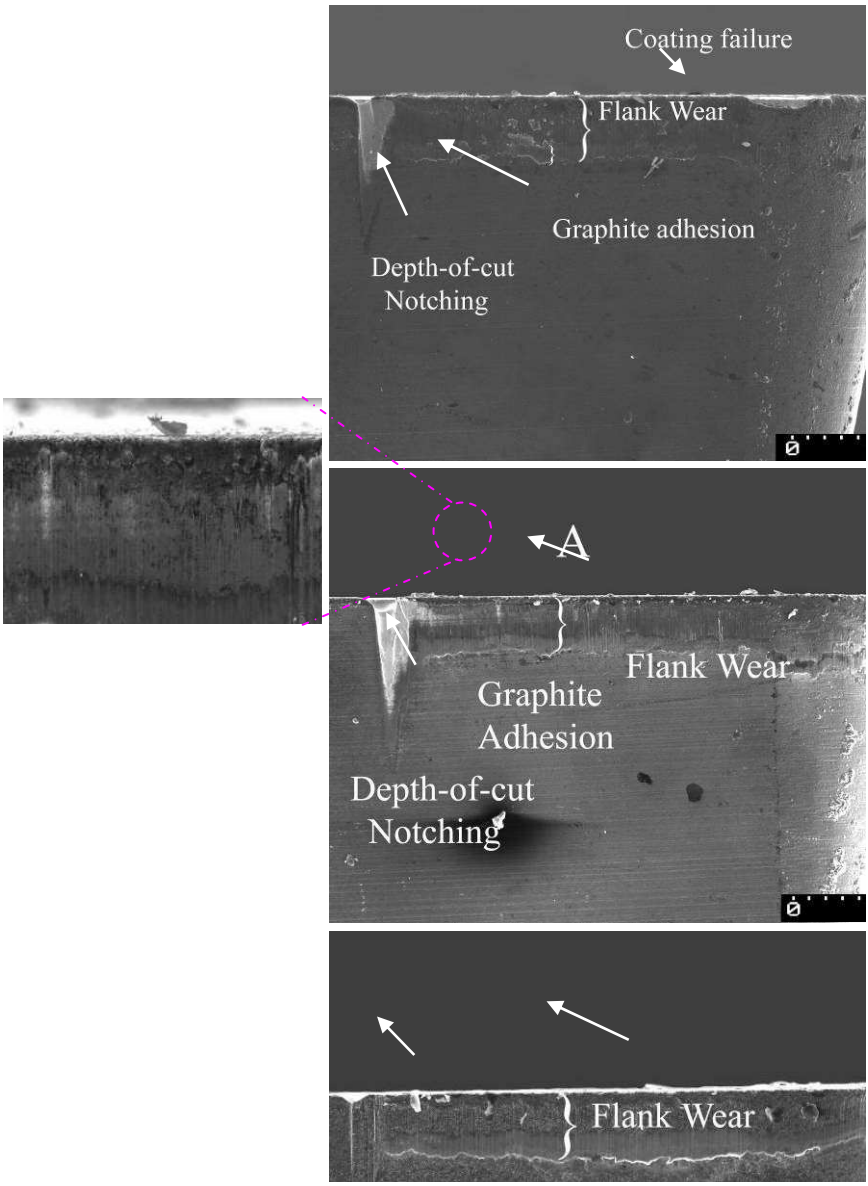

Fig. 5.28. Flank wear of tools tested at V_C=1200 m/min, DOC=1.2 mm and f=0.06 mm/rev: panel a) - TMCVD2 coating after 15 min of cutting time); panel b) - TMCVD3 after 15 min of cutting time; and panel c) - PCD after 12 min of cutting time

By comparing panel b with panel a, from Figure 5.29, it is notorious the higher amount of graphite adhered on the flank wear area of TMCVD2. The different graphite adherence is attributed to the higher surface roughness (larger diamond crystals size) of TMCVD2. Since there is no plastic deformation in graphite, the built up edge that appears during the machining of ductile metals does not appear. However, further in the flank wear region, a band of graphite powder adhered to the insert is clearly visible.

The dependence of the flank wear with the cutting time is shown in Figure 5.30 (a), for V_C=1200 m/min, f=0.06 mm/rev and DOC=1.2 mm. The flank wear of TMCVD 2 and TMCVD 3 coatings are lower than the flank wear of PCD. After 12 min of cutting time, the tests with PCD were completed, since traces began to appear in the machined surface, compromising the surface finishing. Interestingly, this type of surface defects were not present in the diamond coated inserts up to 15 min of cutting time.

For the CVD diamond coatings, two regions in the wear growth curves were identified. The first region occurs within the first few minutes of cutting. The break-in period is followed by wear that occurs at a fairly uniform rate (steady state region). The amount of adhered graphite is expected to be higher on TMCVD2, since this coating has a higher surface roughness, which makes it difficult for the powder/chip to flow. The adhesion of graphite changes the cutting surface with respect to the roughness and the number of cutting edges available to contribute to the cutting effort. Therefore, during the first minutes of cutting, the flank wear rate is higher for coatings with rougher surfaces.

When the depth of the cut was reduced to 0.6 mm, the existence of a third region of fast wear regime (Figure 5.30 panel (b)) appeared before the 15 min of cutting time. This marks the beginning of the failure region, in which the wear rate begins to accelerate. Further work is necessary to investigate the influence of different cutting parameters on tool life during graphite turning.

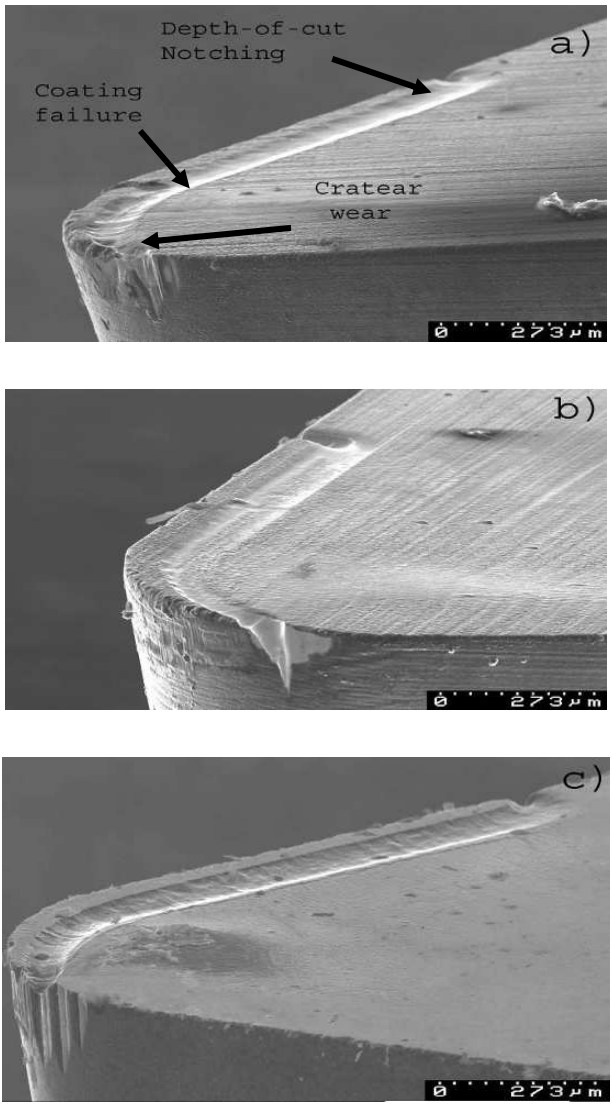

Fig. 5.29. Wear of tools tested at V_C=1200 m/min, DOC=1.2 mm and f=0.06 mm/rev: panel (a) - TMCVD2 coating after 15 min of cutting time); panel (b) - TMCVD3 after 15 min of cutting time; and panel (c) - PCD inserts after 12 min of cutting time

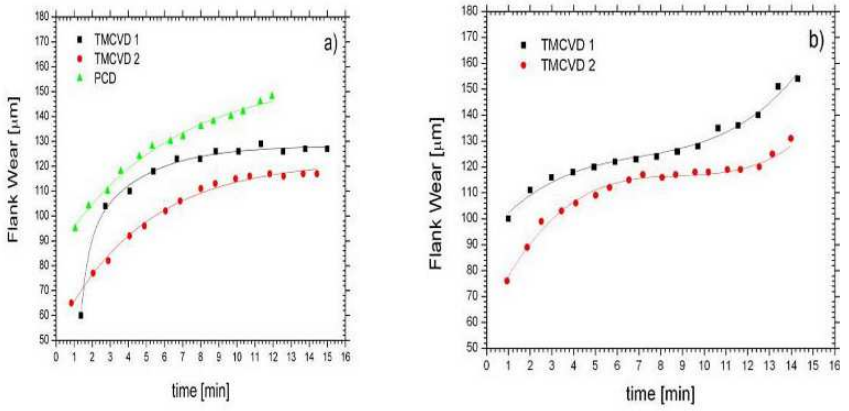

Fig. 5.30. Flank wear of tools tested at V_C=1200 m/min, DOC=1.2 mm, f=0.06 mm/rev (panel a) and V_C=1200 m/min, DOC=0.6 mm and f=0.06 mm/rev (panel b)

5.5.2.3 Cutting forces and friction coefficient

The cutting forces measured during the cutting operation revealed that before the formation of the depth-of-cut line, the cutting force of the tool reflected a higher value for the thrust force, F_t, than for the cutting force, F_c. After that, an inflection of the F_c trend with the cutting length was observed. The force between the tool and the chip is equal to the force between the workpiece and the chip. In the orthogonal cutting, the rake angle is zero (α=0º), thus the F_t/F_C ratio gives an indication of the cutting effort during machining. The F_t/F_C ratio for PCD is much higher than for the TMCVD 2 diamond coating, as can be seen in Figure 5.31. That may be due to the significant surface roughness change on the cutting edge of PCD induced by the high abrasion wear. The change of the rake angle to higher values also increases the shear plane [16], decreasing the F_t/F_C ratio.

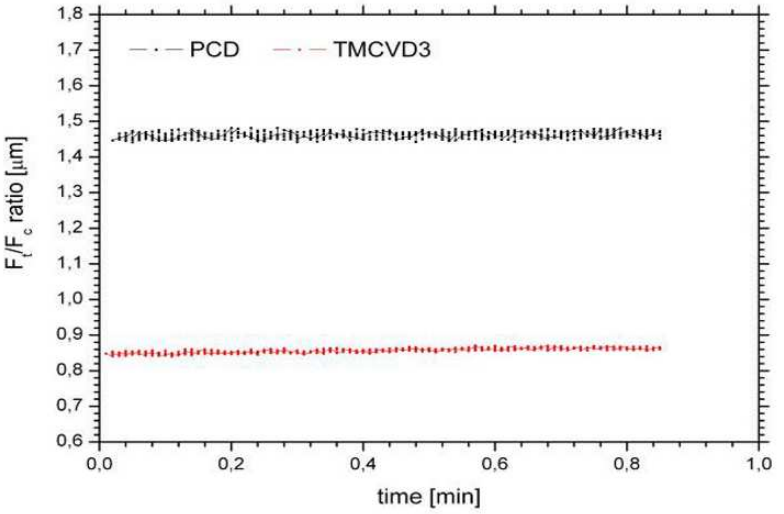

Fig. 5.31. F_t/F_c ratio for TMCVD 3 and PCD inserts

5.6 Conclusions

During the first few minutes of cutting, the flank wear rate is higher for coatings with surfaces rougher than the uncoated tools. Increasing the depth of cut requires higher forces to machine graphite, but displaces the point of heat generation from the tool tip to the primary shear plane. The change of the rake angle to higher values increases the shear plane, which tends to decrease the F_t/F_C ratio. Cutting tools wear by a combination of notching and flank wear when machining graphite.

Acknowledgements

The chapter contributors wish to thank Inderscience publishers for granting permissions to reproduce work presented in this chapter.

References

[1] A. Inspektor, C. E. Bauer and E. J. Oles, *Surf. Coat. Technol.*, **68/69,** (1994), 359.
[2] Gil Cabral, P. Reis, R. Polini, E. Titus, N. Ali, J. P. Davim and J.Grácio, *Diamond and Related Materials*, **15,** (2006), 1753.
[3] N. Ali, V. F. Neto, Sen Mei, G. Cabral, Y. Kousar, E. Titus, A. A. Ogwu, D. S. Misra and J. Gracio, *Thin Solid Films*, **469,** (2004), 154.
[4] Q. H. Fan, N. Ali, W. Ahmed, Y. Kousar and J. Gracio, *J. Mater. Res.*, **17,** (2002), 1563.
[5] Ernst, H., and Merchant, M. E., Chip Formation, Friction and High Quality Machined Surfaces, *Surface Treatment of Metals* (Vol. **29**, pp. 229-378). New York: American Society of Metals. (1941).
[6] Shaw, M. C., Metal Cutting Principles – Second Edition, Oxford Series on Advanced Manufacturing, Oxford University Press, (2005).
[7] Merchant, M., and Zlatin, N., Nomographs for Analysis of Metal-Cutting Processes, *Mechanical Engineering, **67***(11), (1945), 737-742.
[8] Stabler, G. V., Fundamental Geometry of Cutting Tools, *Institution of Mechanical Engineers - Proceedings, **165***(63), (1951), 14-21.
[9] Lee, E. H., and Shaffer, B. W., Theory of Plasticity Applied to Problem of Machining, *Journal of Applied Mechanics, **73***, (1951), 405.
[10] Oxley, P. L. B., Strain Hardening Solution for 'Shear Angle' in Orthogonal Cutting. *International Journal of Mechanical Sciences, **3***(1-2), (1961), 68-79.
[11] Shaw, M. C., The Size Effect in Metal Cutting, *Proceedings of the Indian Academy of Sciences – Sadhana, **28(5)***, (2003), 875-896.
[12] Shaw, M. C., and Jackson, M. J., The Size Effect of Micromachining, Published in 'Microfabrication and Nanomanufacturing', CRC Press (Taylor and Francis Publishers), Florida, USA, (2006).
[13] A.C. Ferrari and J. Robertson, *Physical Review*, **B63,** (2001), 12140.
[14] P. K. Bachmann and D. U. Wiechert, *Diamond and Related Materials,* **1,** (1992), 422.
[15] H. Seo, T.H. Lee, J.S. Park, *Diamond and Related Materials*, **12,** (2003), 1670.
[16] G. M. Robinson, M. J. Jackson, Micro and Nanomachining from a Materials Perspective, *Journal of Materials Processing Technology*, **167**, (2005), 316-337.

Chapter 6

Analysis of Contact Between Chip and Tool Using Nanostructured Coated Cutting Tools

M. J. Jackson, J. J. Evans, M. D. Whitfield and J. S. Morrell

6.1 Introduction

The stages of contact between a metal chip of AISI 1018 steel and a coated cutting tool creates significant opportunities for manufacturers of machined products to understand how dry machining and minimum quantity lubrication affects the economics of manufacturing. The present work not only compares various computational approaches to the solution of shear plane and tool face temperatures during dry machining with nanostructured coated milling tools, but also explains why there is a large discrepancy when calculating temperature generated during machining when using Loewen and Shaw's method for calculating shear plane and tool face temperatures. There has been a great deal of activity in understanding metal cutting mechanics. Traditional metal cutting theories are being challenged as a result of advances in computational mechanics. Astakhov and co-workers [1-4] are particularly critical of using theories developed in the 1940s that describe the mechanics of metal cutting. In response to Astakhov's [1-4] assertions that the previous theories do not readily apply to current machining practices, the authors have conducted a series of computational analyses of machining AISI 1018 steel in order to understand if the Loewen and Shaw's method can be applied to calculating shear plane and tool face temperatures by comparing with finite element models that were constructed using a commercial software package known as Third Wave Systems^{TM}. The following analysis allows one to test if Astakhov's statements apply to the primary stages of chip formation and the subsequent stages of chip

formation where a secondary shear zone is established that is caused by the formation of a built-up edge [5-14].

6.2 Computational Analysis of Machining Conditions

6.2.1 Loewen and Shaw's Method to Calculating Cutting Temperatures

There are several analytical approaches used to determine the cutting temperature. These methods are suitable for the analysis of soft materials, in particular low carbon steels containing a high percentage of ferrite. Of these methods, Stephenson [13] found that the most accurate model was Loewen and Shaw's because it accounted for the change in thermal properties of the tool and workpiece with temperature. Therefore, Loewen and Shaw's approach is used as demonstrated by Shaw [12] in order to explain the use of such formulae for the current experimental work. However, since there is no dynamometer currently available to measure cutting forces, the horizontal force can be closely approximated by the formula proposed by Isakov [8]. Once this quantity has been determined, Loewen and Shaw's approach can be used. Isakov's formula to find the tangential force or the force, in the horizontal orientation, F_{HO}, of a milling cutter is given by,

$$F_{HO} = \sigma_{UTS} A n_c C_m C_w \tag{6.1}$$

Where, σ_{UTS}, is the ultimate tensile strength (UTS) of the workpiece (for AISI 1018 steel, $\sigma = 4.18 \times 10^{10}$ MPa), A, is the uncut chip cross sectional area, n_c, is the number of teeth engaged in the workpiece, C_m, is a machinability adjustment factor, and C_w, is a tool wear adjustment factor. The feed per tooth, f_t, must be calculated, to do this the following quantities must be known, the feed, f = 0.381 m/min = 0.00635m/s, the spindle speed, N, = 2500rpm, or in radians the angular velocity, ω = 261.8 rad/s, the

number of cutting teeth, n = 4. The feed per tooth can now be calculated from the following equation,

$$f_t = \frac{f}{Nn} \tag{6.2}$$

$$f_t = \frac{0.381(m/min)}{2500(rpm)\times 4} \tag{6.3}$$

$f_t = 3.81\times10^{-5}m$

The rake angle is measured at $\alpha = 9°$, and the feed per tooth correction factor, f_{tc}, is given by,

$$f_{tc} = \frac{f_t}{Cos\alpha} \tag{6.4}$$

$$f_{tc} = \frac{3.81\times10^{-5}(m/min)}{Cos9^{\circ}} \tag{6.5}$$

$f_{tc} = 3.86\times10^{-5}m/min$

The method being followed is for orthogonal cutting, the case being considered is milling. Therefore, the orthogonal width of cut is replaced by the milling axial depth of cut, b, which is $1.27\times10^{-3}m$ and the uncut chip cross sectional, A, is given by,

$$A = f_{tc}b \tag{6.6}$$

$$A = 3.86\times10^{-5}(m)\times1.27\times10^{-3}(m) \tag{6.7}$$

$A = 4.9\times10^{-8}m^2$

The tool diameter, $d = 1.27\times10^{-2}m$, and the width of cut, W, is $0.635\times10^{-2}m$. The number of teeth engaged in the cut, n_c, can now be calculated by,

$$n_c = \frac{n(90 + \sin^{-1}((2W - d)/d)))}{360} \tag{6.8}$$

$$n_c = \frac{4(90 + \sin^{-1}((2x0.00635(m) - 0.0127(m))/0.0127(m)))}{360} \tag{6.9}$$

$n_c = 1$

The machinability adjustment factor taken from Isakov's [8] textbook and has a value of unity, and the tool wear adjustment factor is taken as 1.1, also from Isakov [8]. Therefore, F_{HO} can be calculated.

$$F_{HO} = \sigma A n_c C_m C_w \tag{6.10}$$

$$F_{HO} = 4.2\times10^{8} \times 4.9 \times10^{-8} \times 1 \times 1 \times 1.1 \tag{6.11}$$

$F_{HO} = 22.63N$

The chip thickness, t_c, was measured to be 1×10^{-4}m, thus, the chip thickness ratio, r, can be calculated from,

$$r = \frac{t_o}{t_c} \tag{6.12}$$

$$r = \frac{3.81\times10^{-5}(m)}{1\times10^{-4}(m)} \tag{6.13}$$

$r = 0.381$

This allows the shear plane angle, Φ, to be calculated from,

$$\Phi = \tan^{1}\left(\frac{r\mathrm{Cos}\alpha}{1 - r\mathrm{Sin}\alpha}\right) \tag{6.14}$$

$$\Phi = \tan^{1}\left(\frac{0.381\mathrm{Cos}9^{\circ}}{1 - 0.381\mathrm{Sin}9^{\circ}}\right) \tag{6.15}$$

$\Phi = 21.81°$

Based on the work of Bowden and Tabor [7] the coefficient of friction between tungsten carbide and a low carbon steel (in this case AISI 1018 steel) during dry rubbing conditions is, $\mu = 0.78$. This allows the calculation of the force in the vertical orientation F_{VO}, which is given by,

$$F_{VO} = \frac{\mu F_{HO} - F_{HO}\mathrm{Tan}\alpha}{1 + \mu\mathrm{Tan}\alpha} \tag{6.16}$$

$$F_{VO} = \frac{0.78 \times 22.63(\mathrm{N}) - 22.63(\mathrm{N})\mathrm{Tan}9^{\circ}}{1 + 0.78\mathrm{Tan}9^{\circ}} \tag{6.17}$$

$F_{VO} = 12.52\mathrm{N}$

The force along the tool face, F_{AT}, is given by,

$$F_{AT} = F_{HO}\mathrm{Sin}\alpha + F_{VO}\mathrm{Cos}\alpha \tag{6.18}$$

$$F_{AT} = 22.63(\mathrm{N})\mathrm{Sin}9° + 12.52(\mathrm{N})\mathrm{Cos}9° \tag{6.19}$$

$F_{AT} = 15.91\mathrm{N}$

The force normal to the tool face, $F_{NT,}$ can be calculated by,

$$F_{NT} = F_{HO}\mathrm{Cos}\alpha - F_{VO}\mathrm{Sin}\alpha \tag{6.20}$$

$$F_{NT} = 22.63(\mathrm{N})\mathrm{Cos}9° - 12.52(\mathrm{N})\mathrm{Sin}9° \tag{6.21}$$

$F_{NT} = 20.4N$

The force along the shear plane, $F_{AS,}$ is given by,

$$F_{AS} = F_{HO}Cos\Phi - F_{VO}Sin\Phi \quad (6.22)$$

$$F_{AS} = 22.63(N)Cos21.81° – 12.52(N)Sin21.81° \quad (6.23)$$

$F_{AS} = 16.36N$

The force normal to the shear plane, $F_{NS,}$ is given by,

$$F_{NS} = F_{VO}Cos\Phi + F_{HO}Sin\Phi \quad (6.24)$$

$$F_{NS} = 12.52(N)Cos21.81° + 22.63(N)Sin21.81° \quad (6.25)$$

$F_{NS} = 20.03N$

Since the milling process is being approximated by an orthogonal cutting operation, the milling axial depth of cut is equal to the orthogonal chip width, b. The maximum uncut chip thickness is equal to the feed per tooth t_o. The area of the shear plane A_s is given by,

$$A_s = \frac{bt_O}{Sin\Phi} \quad (6.26)$$

$$A_s = \frac{\left(1.27\times10^{-3}(m)\right)\left(3.81\times10^{-5}(m)\right)}{Sin21.81^{\circ}} \quad (6.27)$$

$A_s = 1.3\times10^{-7}m^2$

The shear stress, τ, is given by,

$$\tau = \frac{F_{AS}}{A_S} \tag{6.28}$$

$$\tau = 16.36(N) / 1.3\times10^{-7}(m^2) \tag{6.29}$$

$$\tau = 125.62\times10^{6}N/m^2$$

Similarly the normal stress, σ, is given by,

$$\sigma = \frac{F_{NS}}{A_S} \tag{6.30}$$

$$\sigma = 20.03(N) / 1.3\times10^{-7}(m^2) \tag{6.31}$$

$$\sigma = 153.82\times10^{6}N/m^2$$

The shear strain, γ, is given by,

$$\gamma = \frac{Cos\alpha}{Sin\Phi Cos(\Phi - \alpha)} \tag{6.32}$$

$$\gamma = \frac{Cos9^\circ}{Sin21.81^\circ Cos(21.81^\circ - 9^\circ)} \tag{6.33}$$

$$\gamma = 2.73$$

The cutting velocity, V, at the tool tip is given by,

$$V = r_t\omega$$

Where, r_t, is the tool radius and the units of, ω, are radians/s.

$$V = 0.00635(m)\left(\frac{2\pi}{60(s)}\times 2500(rpm)\right) \tag{6.34}$$

$$V = 1.66m/s$$

The chip velocity, V_C, is given by,

$$V_C = \frac{V\mathrm{Sin}\Phi}{\mathrm{Cos}(\Phi - \alpha)} \tag{6.35}$$

$$V_C = \frac{1.66(\mathrm{m/s})\mathrm{Sin}21.81^\circ}{\mathrm{Cos}(21.81^\circ - 9^\circ)} \tag{6.36}$$

$V_C = 0.632\mathrm{m/s}$

Similarly the shear velocity, V_S, is given by,

$$V_s = \frac{V\mathrm{Cos}\alpha}{\mathrm{Cos}(\Phi - \alpha)} \tag{6.37}$$

$$V_s = \frac{1.66(\mathrm{m/s})\mathrm{Cos}9^\circ}{\mathrm{Cos}(21.81^\circ - 9^\circ)} \tag{6.38}$$

$V_s = 1.68\mathrm{m/s}$

In order to determine the strain rate, $\dot{\gamma}$, the shear plane spacing, Δy, must be determined from chip images, in this case $\Delta y = 10\mu m$.

$$\dot{\gamma} = \frac{V\mathrm{Cos}\alpha}{\Delta y\mathrm{Cos}(\Phi - \alpha)} \tag{6.39}$$

$$\dot{\gamma} = \frac{1.66(\mathrm{m/s})\mathrm{Cos}9^\circ}{(1x10^{-5}(\mathrm{m}))\mathrm{Cos}(21.81^\circ - 9^\circ)} \tag{6.40}$$

$\dot{\gamma} = 168.39\times10^3 s^{-1}$

The theoretical scallop height, h, which reflects the surface roughness of the machined surface in an end milling operation is given by,

$$h = \frac{f_t^{\,2}}{4d} \tag{6.41}$$

$$h = \frac{\left(3.81\times10^{-5}(\mathrm{m})\right)^2}{4\left(0.0127(\mathrm{m})\right)} \tag{6.42}$$

$h = 2.86\text{x}10^{-8}\text{m}$

The energy per unit time, U, is given by,

$U = F_{HO}V$

$U = 22.63(\text{N})\times1.66(\text{m/s})$

$U = 37.63\text{Nms}^{-1}$, or 37.63Js^{-1}

The energy per unit volume, u, is given by,

$$u = \frac{F_{HO}}{bt_0} \tag{6.43}$$

$$u = \frac{22.63(\mathrm{N})}{\left(1.27\times10^{-3}(\mathrm{m})\right)\left(3.81\times10^{-5}(\mathrm{m})\right)} \tag{6.44}$$

$u = 467.76\times10^6\text{Nm/m}^3$ or $467.76\times10^6\text{J/m}^3$

The shear energy per unit volume, u_s, is given by,

$$u_s = \tau\gamma \tag{6.45}$$

$$u_s = 125622347(\text{N/m}^2)\times2.73(\text{m/m}) \tag{6.46}$$

$u_s = 342.49\times10^6 Nm/m^3$ or $342.49\times10^6 J/m^3$

The friction energy per unit volume, u_f, is given by,

$$u_f = \frac{F_{AT} r}{b t_0} \tag{6.47}$$

$$u_f = \frac{(15.91(N))(0.381)}{(1.27\times10^{-3}(m))(3.81\times10^{-6}(m))} \tag{6.48}$$

$u_f = 125.27\times10^6 Nm/m^3$ or $125.27\times10^6 J/m^3$

To determine the shear plane temperature, the method of Loewen and Shaw taken from Shaw [12] is used. The process involves several iterations, the final iteration is shown. The initial step is to estimate the shear plane temperature, θ_s = 70°C, and the ambient temperature is θ_o =25°C, then calculate the mean of these two temperatures, θ_{av}.

$$\theta_{AV} = \frac{\theta_s + \theta_o}{2} \tag{6.49}$$

$$\theta_{AV} = \frac{70^\circ C + 25^\circ C}{2} \tag{6.50}$$

θ_{AV} = 47.5°C

The thermal properties of the workpiece must be determined; in this case a low carbon steel. Shaw [12] displays these properties. At 47.5°C, the thermal diffusivity, $K_1 = 1.58x10^{-5} m^2/s$, and the volumetric specific heat is, $\rho_1 C_1 = 3.72\times10^6 J/m^3{}^\circ C$. Calculate the quantity R_1 from,

$$R_1 = \frac{1}{1 + 1.328\left(\frac{K_1\gamma}{Vt_0}\right)^{1/2}} \tag{6.51}$$

$$R_1 = \frac{1}{1 + 1.328\left(\frac{1.58\times10^{-5}(m^2/s)\times 2.73}{1.66(m/s)\times 3.81\times10^{-5}(m)}\right)^{1/2}} \tag{6.52}$$

$R_1 = 0.48$

Calculate the quantity θs - θo from,

$$\theta s - \theta o = \frac{R_1 u_s}{J\rho_1 C_1} \tag{6.53}$$

Where J is the mechanical equivalent of heat, the value used by Shaw (2005) of 9340 lbin/BTUs^2 for low carbon steel, or 0.99Nm/Js^2, will be used here,

$$\theta s - \theta o = \frac{0.48\left(342.49\times10^6(J/m^3)\right)}{\left(0.99(Nm/Js^2)\right)\left(371.88\times10^4(J/m3^\circ C)\right)} \tag{6.54}$$

θs - θo = 43.99°C

Therefore,

θs = 68.99°C

Shaw states the process is repeated until the initial estimate produces a shear plane temperature within 3.88°C of the initial estimate. Therefore, in this case the accepted shear plane temperature is 68.99°C.

To calculate the tool face temperature estimate the tool face temperature $\theta_T = 89.25°C$. Then determine the thermal properties of the workpiece at this temperature, in this case a low carbon steel, they are taken from Shaw [12]. At 89.25°C, $K_1 = 1.49x10^{-5}m^2/s$, $\rho_1 C_1 = 3.91\times10^6 J/m^3°C$. The chip contact length, a, is approximated as half the uncut chip length l, which is given by,

$$l = \left(dt_o\right)^{0.5} + \frac{f}{2nN} \tag{6.55}$$

$$l = \left(0.0127(m)\times3.81\times10^{-3}(m)\right)^{0.5} + \frac{0.381(m)}{2\times4\times2500(rpm)} \tag{6.56}$$

$l = 7.15x10^{-4}m$

Thus,

$$a = l/2 \tag{6.57}$$

$$a = 7.15\times10^{-4}(m)/2 \tag{6.58}$$

$a = 3.57\times10^{-4}m$

$$\frac{m}{l} = \frac{b}{2a} \tag{6.59}$$

$$\frac{m}{l} = \frac{1.27\times10^{-3}(m)}{2\left(3.57\times10^{-4}(m)\right)} \tag{6.60}$$

$$\frac{m}{l} = 8.89$$

Using Shaw's textbook [12] to find $\overline{A} = 2.1$, determine the thermal conductivity of the workpiece, k_S, at the previously calculated shear plane temperature of 68.99°C, in this case, $k_T = 6.12\times10^{-3}J/m^2s°C$. This allows C` to be calculated from,

$$C' = \frac{u_f V t_0 \overline{A}}{J k_T} \tag{6.61}$$

$$C' = \frac{\left(125.27\times10^{6}(J/m^{3})\right)\left(1.66(m/s)\right)\left(3.81\times10^{-5}(m)\right)\times 2.1}{\left(0.99(Nm/Js^{2})\right)\left(6.12\times10^{-3}(J/m^{2}s^{\circ}C)\right)} \tag{6.62}$$

C` = 27.24×10^{5}

Calculate B' from,

$$B' = \left(\frac{0.754u_f}{J\rho_S C_S}\right)\left(\frac{Vt_o^{\,2}}{arK_S}\right)^{1/2} \tag{6.63}$$

Where the subscript S denotes the thermal properties determined at the previously calculated shear plane temperature, $\rho_s c_s = 3.91\times10^{6}J/m^{3}{}^{\circ}C$ and $K_s = 1.49\times10^{-5}m^{2}/s$.

$$B' = \left(\frac{0.754\left(125.2\times10^{6}(J/m^{3})\right)}{\left(0.99(Nm/Js^{2})\right)\left(3.91\times10^{6}(J/m^{3\circ}C)\right)}\right)\left(\frac{\left(1.66(m/s)\right)\left(3.81\times10^{-5}(m)\right)^{2}}{\left(3.57\times10^{-4}(m)\right)\times 0.381\times\left(1.49\times10^{-5}(m^{2}/s)\right)}\right)^{1/2} \tag{6.64}$$

B` = 18.87

Calculate the quantity R_2 from,

$$R_2 = \frac{C' - \theta s + \theta o}{C' + B'} \tag{6.65}$$

$$R_2 = \frac{\left(2.72\times10^{6}\right) - \left(68.99(^{\circ}C)\right) + \left(25(^{\circ}C)\right)}{\left(2.72\times10^{6}(^{\circ}C)\right) + 18.87} \tag{6.66}$$

$R_2 = 0.99°C$

Calculate the temperature rise in the chip surface due to friction, $\Delta\theta_F$, from,

$$\Delta\theta_F = R_2 B' \tag{6.67}$$

$$\Delta\theta_F = 0.99(°C)\times 18.87 \tag{6.68}$$

$$\Delta\theta_F = 18.67°C$$

Finally the tool face temperature, θ_T, can be calculated from,

$$\theta_T = \theta_S + \Delta\theta_F \tag{6.69}$$

$$\theta_T = 68.99(°C) + 18.67(°C) \tag{6.70}$$

$$\theta_T = 87.66°C.$$

Shaw [12] states that the procedure for calculating the tool face temperature should be repeated until the initial estimate and the final calculated temperature are in agreement. In this case the difference of 1.59°C cannot be doubted since the material properties are determined from interpretation of line diagrams. Therefore, 89.25°C is the accepted tool face temperature. Tables 6.1 to 6.3 show the experimental parameters and equations that were used to calculate the shear plane and tool face temperatures. The tables include sample calculations to demonstrate the use of the equations and parameters shown above. Table 6.4 shows the shear plane approximation and calculation temperatures. It also includes the tool face approximations and calculations of the temperatures. The last column shows the percentage error between estimated and calculated temperatures. The coefficient of friction of 0.78 has been taken from Robinson [11] in order to compare with the calculations shown above. It is intended to be factual information based on the experimental work performed by Robinson [11]. The shear plane temperature and the tool face temperature have been calculated using different values of coefficient of friction in order to provide a

parametric analysis and to compare with the values for the different coatings. This ranges from 0.1 – 1.0 with 0.1 increments.

Cutting Speed - V	
(m/s)	1.662426113
Undeformed Chip Thickness - t_0	
(m)	0.0000381
Width of cut - b	
(m)	0.00635
Cutting Force - F_p	
(N)	22.63344932
Feed Force - F_q	
(N)	12.52230092
Chip Thick Ratio - r	0.381
Shear Strain - γ	2.726369114
Shear Energy / Unit Volume u_s	
(mN / m^3)	342492886.91
Friction Energy / Unit Volume - u_f	
(mN / m^3)	125266001.2
Mechanical Equivalent of Heat - J	
(Nm / Js^2)	0.998996696
Tool Diameter - d	
(m)	0.0127
Cutting Speed - V	
(m/min)	99.74556675
Number of Cutting Teeth - n	4
Cutting Speed - w	
(rpm)	2500

Table 6.1. Table of Computational Parameters Used for Machining Simulations

To Calculate Shear Plane Temperature - °C			
Step 1			
Estimate initial shear plane temperature θ_s		70.00	°C
Ambient Temperature θ_0		25.00	°C
Average temperature		47.50	°C
Find material properties from fig 12.25 at		47.50	°C
	K_1 - Thermal Diffusivity	1.5812E-05	m^2/s
	$C_1\rho_1$ - Volume Specific Heat	3718849.84	$J/m^3°C$
Calculate R_1	$R_1 = 1 / (1 + 1.328(K_1\gamma/Vt_0)^{1/2})$		
	R_1 =	0.477191655	
Step 2	$\theta_s - \theta_0 = R_1 u_s / JC_1\rho_1$		
	$\theta_s - \theta_0$ =	43.99179692	°C
Since θ_0 =		25.00	°C
θ_s =		68.99	°C
Step 3			
If initial guess is within 3.88°C use that temp, if not repeat.			
		-1.01	°C
	Feed Rate - f		
	(m/min)	0.381	
	Chip Contact Length - l		
	(m)	7.15E-04	
	Chip Contact Length - a (m)	0.000357329	
	(m)		

Table 6.2. Calculation of Shear Plane Temperature

To Calculate Tool Face Temperature - °C				
Step 4	Estimate initial shear plane temperature θ_T		89.25	°C
	Ambient Temperature θ'_0		25	°C
Material properties from fig 12.25 [12] at estimated tool temp of			89.25	°C
	K_2 . Thermal Conductivity	1.49E-05	m^2/s	
	$C_2\rho_2$ - Volume Specific Heat	3912751.678	$J/m^3°C$	
Calculate the ratio		m/l = b/2a		
	m/l =	8.89		
Use figure 12.17 [12] to find A		2.1		
Find k_3 from fig 12.25 at calculated shear plane temp of			68.99	
	k_3	6.12E-03	J/ms°C	
Step 5	Calculate the quantity	$C' = u_f V t_0 A / Jk_3$		
	C' =	2724338.49	°C	
Step 6	Calculate the quantity B'			
	$B' = (0.754u_f / J\rho_3 C_3)(Vt_0^2 / arK_2)^{1/2}$	18.66628618	°C	
Step 7	Determine R_2	$R_2 = (C' - \theta_s + \theta'_0) / (C' + B')$		
	R_2 =	0.999977001		
Step 8	Temp rise in chip due to friction, $\Delta\theta_F$	$\Delta\theta_F = R_2 B'$		
	$\Delta\theta_F$ =	18.66585687	°C	
Step 9	Calculate θ_T from	$\theta_T = \theta_s + \Delta\theta_F$		
	θ_T =	87.66	°C	
Repeat analysis until calculated value & estimate match				
	Diff =	1.59		

Table 6.3. Calculation of Tool Face Temperature

CoF	Shear Plane Approx. (°C)	Shear Plane Calc. (°C)	Error (°C)	Tool Face Approx.(° C)	Tool Face Calc. (°C)	Error (°C)
0.1	80	82.03	-2.03	85	87.4	-2.4
0.2	80	79.85	0.15	87	85.06	1.94
0.3	79	78	1	85	85.51	-0.51
0.4	76	75.45	0.55	84	85.32	-1.32
0.5	75	74.14	0.86	86	86.6	-0.6
0.6	74	72.71	1.29	87	87.44	-0.44
0.7	72	70.41	1.59	88	87.2	0.8
0.78	70	68.99	1.01	89.25	87.66	1.59
0.9	68	67.1	0.9	91	88.28	2.72
1	65	65.42	-0.42	92	88.58	3.42

Table 6.4. Approximate and Calculated Tool Face Temperatures and Shear Plane Temperatures

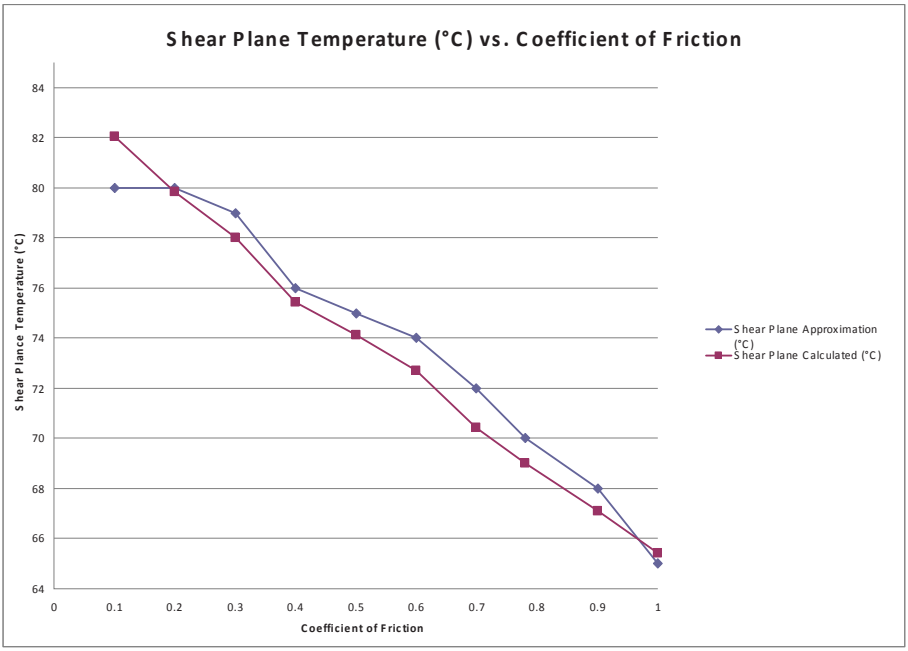

Figure 6.1. Shear Plane Temperature versus Coefficient of Friction

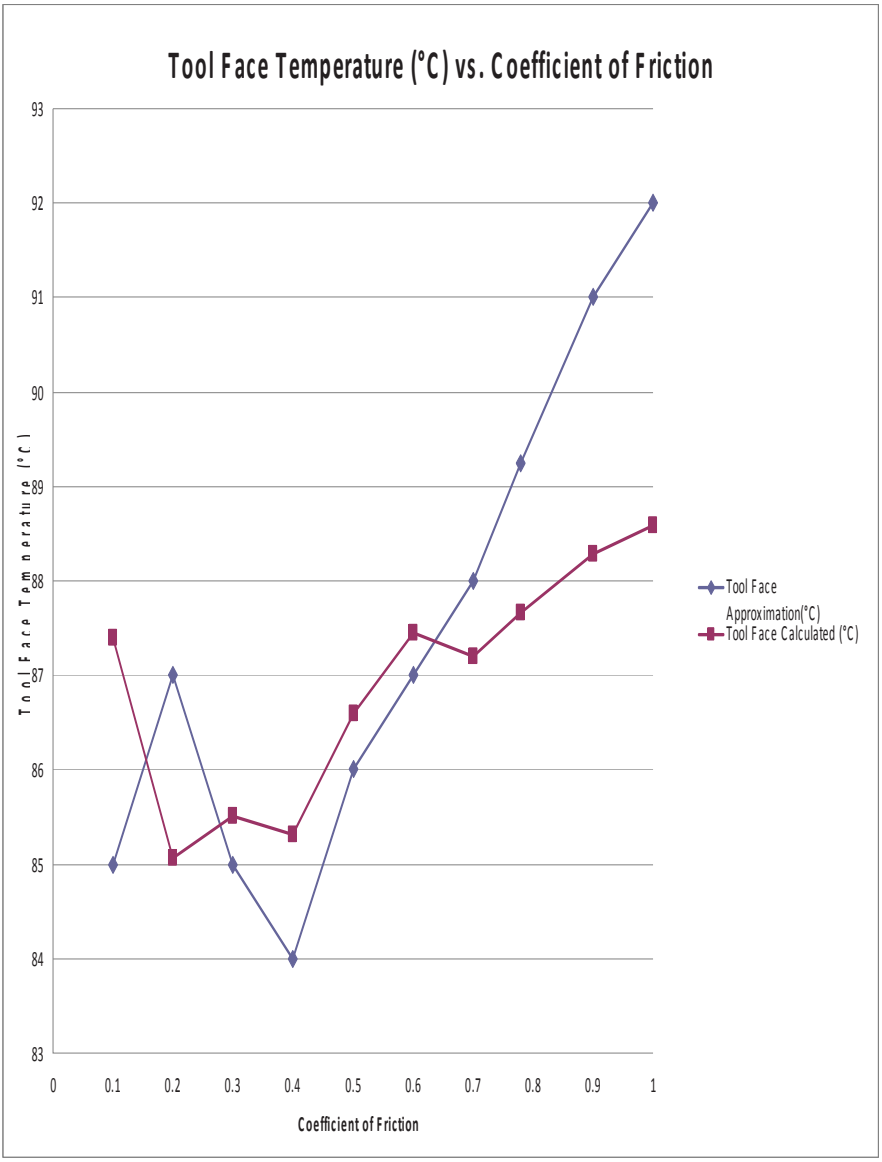

Figure 6.2. Tool Face Temperature versus Coefficient of Friction

This has then been compared to the approximate amounts of shear plane and tool face temperatures. The percentage error is then calculated for a comparison between the approximation and the calculation. The percentage of error is less than 3.5% for all calculations. From Figures 6.1 and 6.2, it can be seen that increasing the coefficient of friction lowers the shear plane temperature, but conversely the tool face temperature tends to increase.

6.3 Finite Element Studies of Machining Conditions

A metal cutting finite element software was chosen to simulate the metal cutting operation. The choice of the software is important because the output results may vary from software to software and with the input parameters also. Therefore, AdvantEdge^{TM} (provided by Third Wave Systems) was used in this study. The software uses adaptive meshing to improve the quality and precision of the output results and it also includes a wide range of workpiece material library. The simulations are replicas of what was done experimentally and the cutting parameters used were the same in both processes. Third Wave AdvantEdge^{TM} allows improving and optimizing of machining processes. To model the thermal-visco plastic behavior of the materials, the software employs a constitutive equation, the Johnson-Cook law, which can be represented by the following formula:

$$\sigma_{eq} = (A + B\varepsilon^{n})(1 + C\ln(\frac{\dot{\varepsilon}}{\dot{\varepsilon}_0}))(1 - (\frac{T - T_{room}}{T_m - T_{room}})^{m}) \qquad (6.71)$$

Where, ε, is the plastic strain, $\dot{\varepsilon}$, is the plastic strain rate (s^{-1}), , $\dot{\varepsilon}_0$ is the reference plastic strain rate (s^{-1}), T, is the temperature of the workpiece material (ºC), $T_{m,}$ is the melting temperature of the workpiece material (ºC), and, $T_{room,}$ is the room temperature (ºC).

Coefficient, A, is the yield strength (MPa), B, is the hardening modulus (MPa), and, C, is the strain rate sensitivity coefficient, n, is the hardening coefficient and, m, the thermal softening coefficient. The friction coefficient was obtained using the Coulomb model and was calculated with the following formula:

$$u = \frac{Ff + Fc \times tg\gamma}{Fc - Ff \times tg\gamma} \tag{6.72}$$

Where, Ff, the feed force, Fc, the cutting force, and, γ , is the rake angle.

The experiments were conducted using the following conditions: Cutting speed used was 300 meters per minute; the feed rate was kept constant at 0.15 mm per revolution; depth of cut was constant at 1 mm; length of cut was constant at 6 mm; the length of the work piece was 5 mm; the experimental specimen was 1018 steel; initial temperature was 20 degrees Celsius, and the coating thickness was constant at 4 microns' thickness. The coefficient of friction was varied between 0.1 and 1 in steps of 0.1 in order to compare results generated using Loewen and Shaw's method.

The finite element generated results (Figures 6.3 – 6.8) show the machining variables peak tool temperature and machining temperatures as a function of the coefficient of friction. In order to minimize computational effort, calculations for coefficient of friction of 0.1, 0.5, and 1.0 are shown in this paper. Figures 6.9 and 6.10 shows the comparison between calculated, approximate, and finite element generated shear plane and tool face temperatures. It is shown that as machining develops, shear plane and tool face temperatures increase rapidly after the initial frictional interactions between workpiece and cutting tool. Here, the method of Loewen and Shaw does not compare well. However, at the beginning of the cut, i.e., after the first 25mm is machined, it can be seen that Loewen and Shaw's method produces a very accurate estimate of shear plane and tool face temperature. This implies that their method is applicable at the first stages of intimate contact between chip and

tool. Clearly, it is noted that a secondary shear zone between chip and tool is not created at first contact. This implies that the secondary shear zone is somewhat responsible for frictional heating. This effect should be studied further using transparent sapphire tools in terms of understanding this effect on the generation of heat. The computational analysis leads us believe that intermittent contact caused by interrupted cuts and/or oscillating the cutting tool during machining is not only beneficial, but is well described by Loewen and Shaw's method.

Coefficient of Friction – 0.1

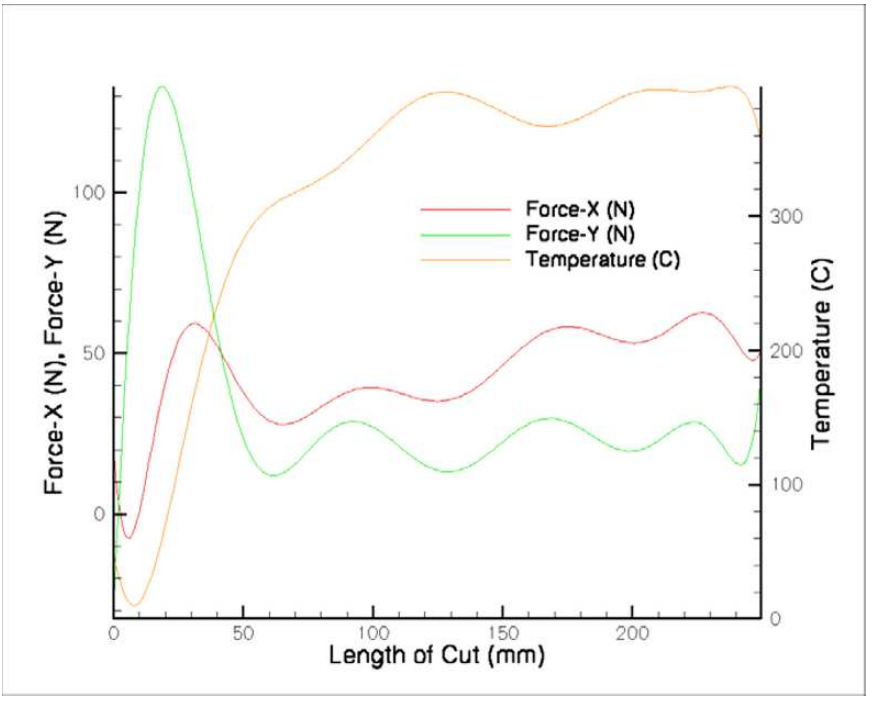

Figure 6.3. Peak tool temperature as a function of the length of cut for a coefficient of friction of 0.1 between tool and chip

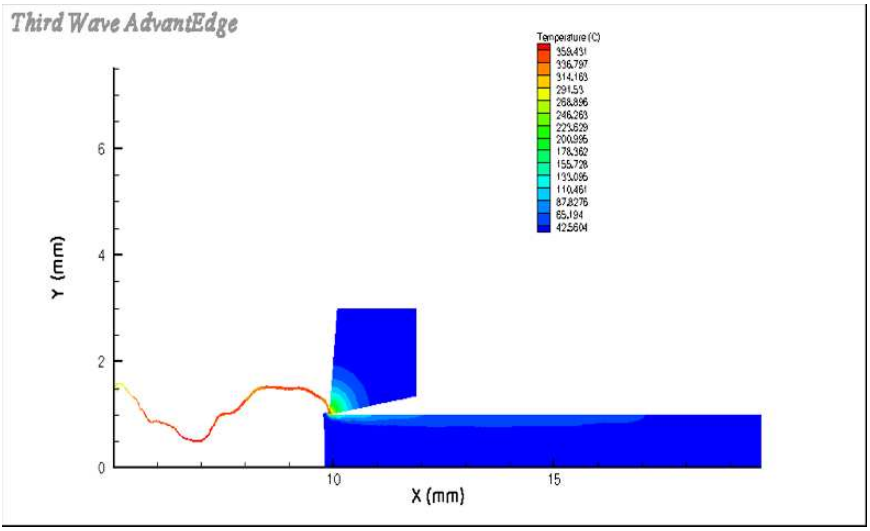

Figure 6.4. Temperature profile between chip and tool for a coefficient of friction of 0.1 between chip and tool

Coefficient of Friction – 0.5

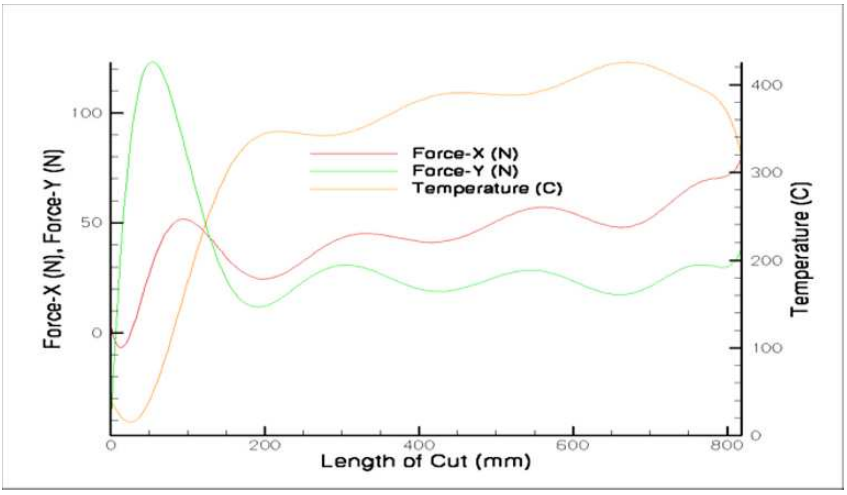

Figure 6.5. Peak tool temperature as a function of the length of cut for a coefficient of friction of 0.5 between tool and chip

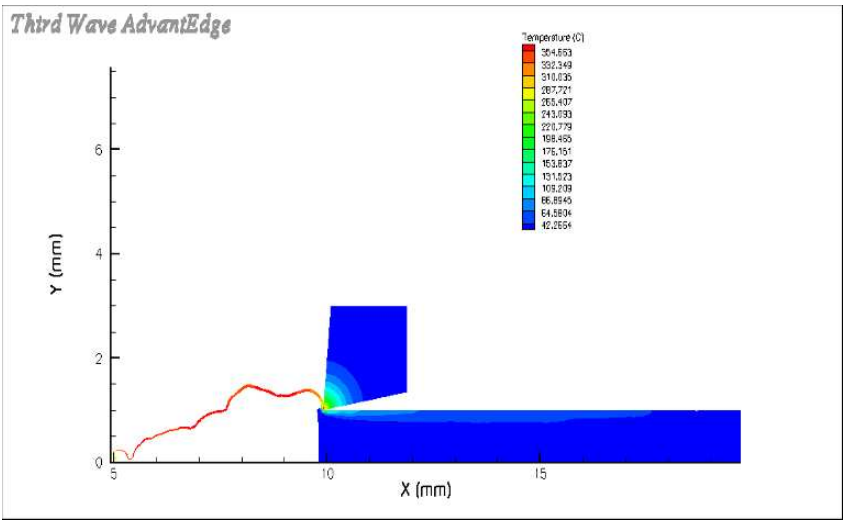

Figure 6.6. Temperature profile between chip and tool for a coefficient of friction of 0.5 between chip and tool

Coefficient of Friction – 1.0

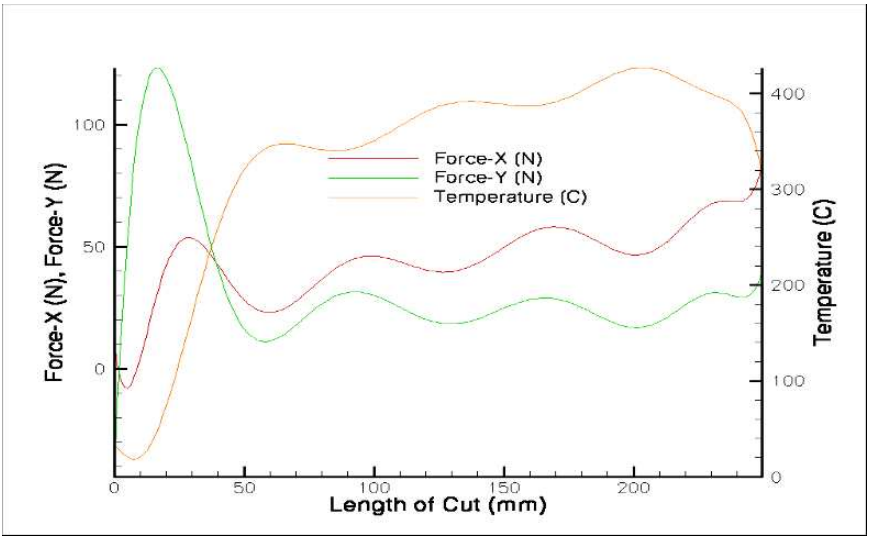

Figure 6.7. Peak tool temperature as a function of the length of cut for a coefficient of friction of 1.0 between tool and chip

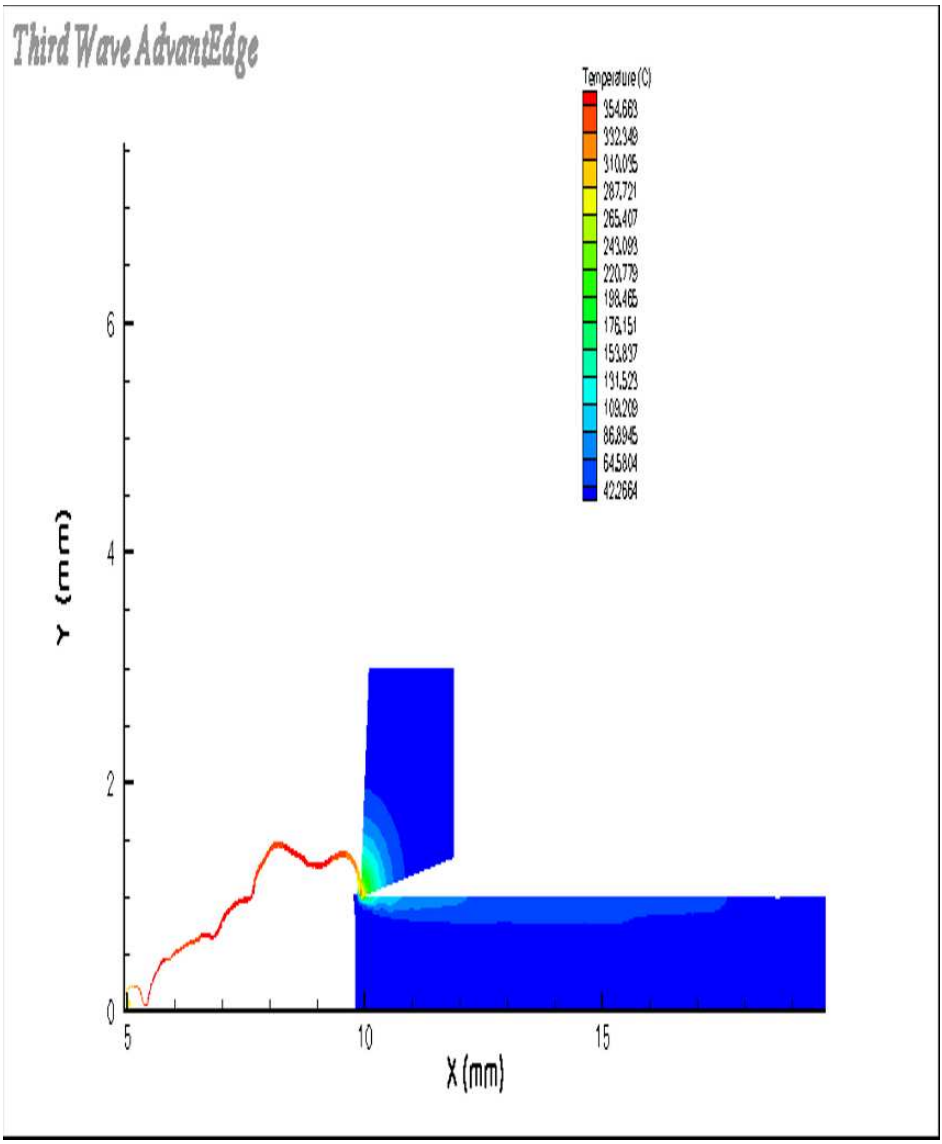

Figure 6.8. Temperature profile between chip and tool for a coefficient of friction of 1.0 between chip and cutting tool

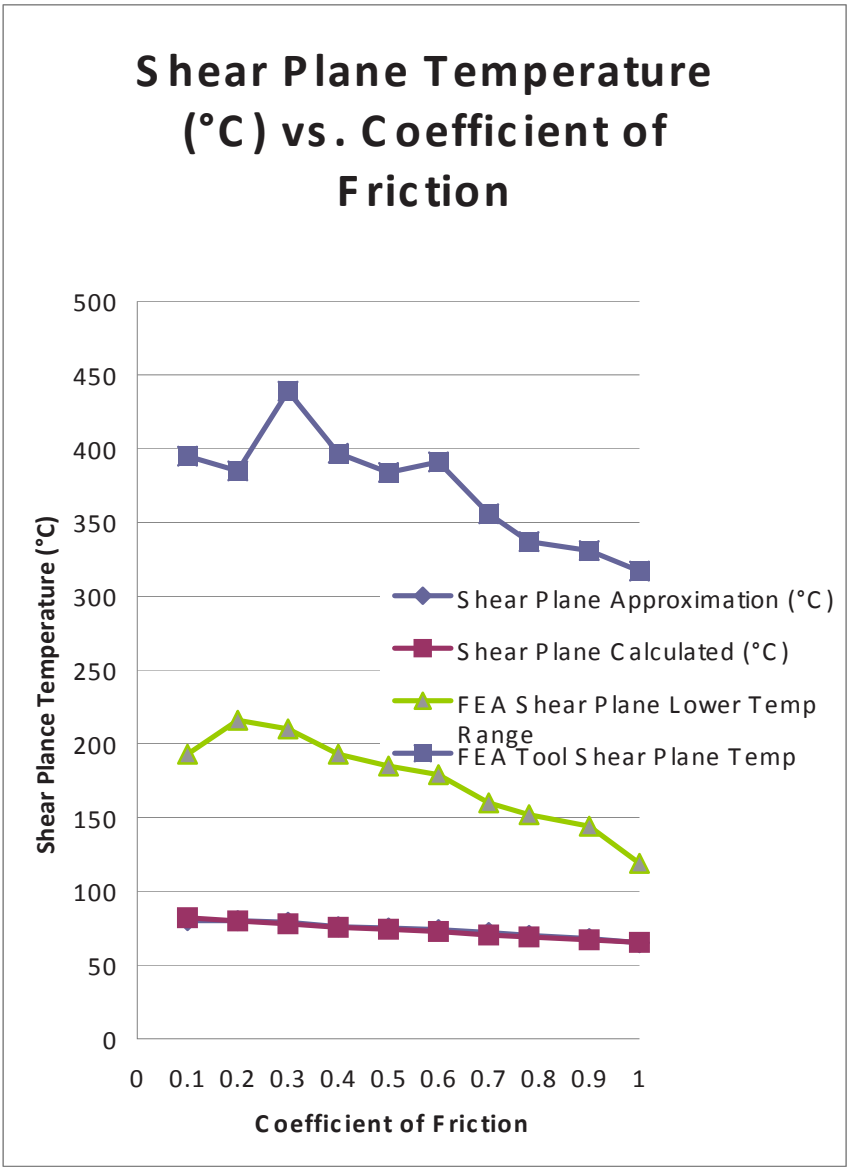

Figure 6.9. Comparison of approximate and calculated shear plane temperatures with finite element generated temperatures at the end of the machining pass (800 mm machined)

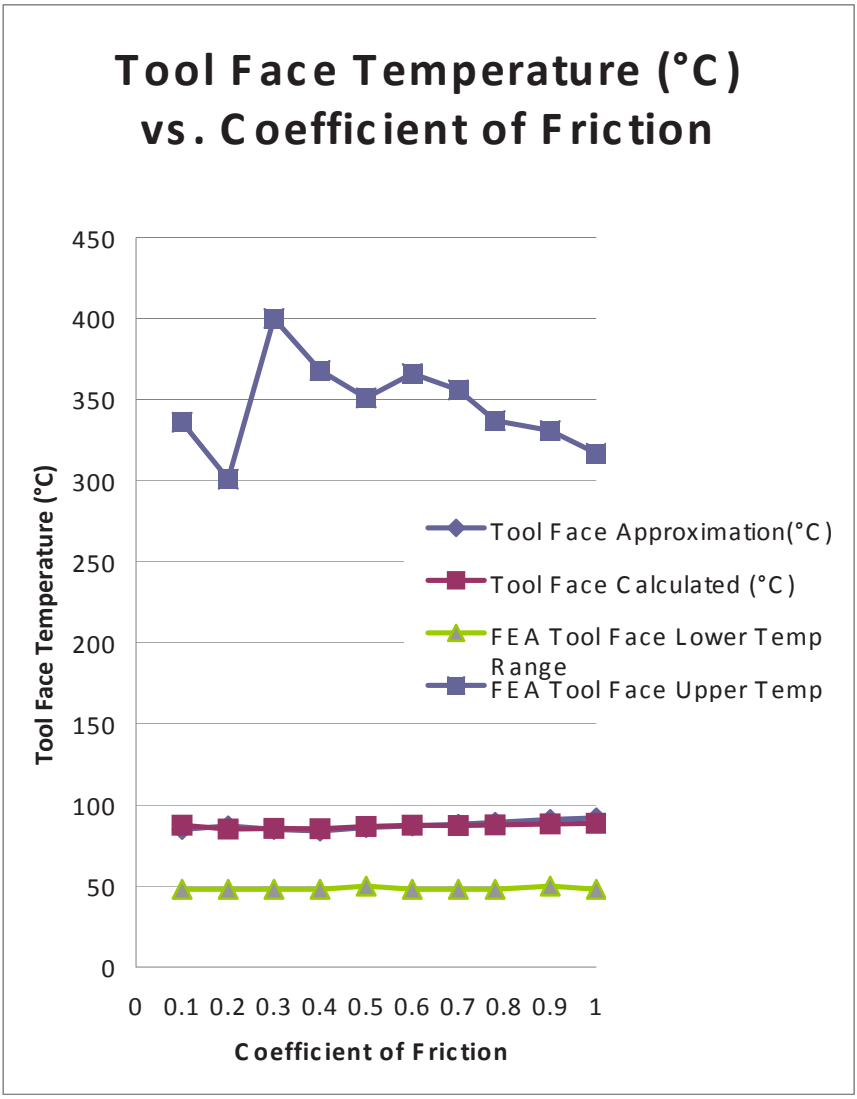

Figure 6.10. Comparison of approximate and calculated tool face temperatures with finite element generated temperatures at the end of the machining pass (800 mm machined)

6.4 Discussion

When one inspects the results of finite element modeling (Figures 6.3 - 6.8), it is observed that the change in the coefficient of friction tends to lower the shear plane temperature and increase the tool face temperature as it increases in value. In order to make the removal of the chip easier, it is advisable to focus the generation of heat towards the shear plane rather than toward the cutting tool. Therefore, during dry machining operations it is necessary to lower the coefficient of friction between chip and tool by providing a thin film coating to the tool in order to lower the coefficient of friction. It is also observed that the tool face temperature and the shear plane temperature increases rapidly as a large chip is cut. The initial stages of chip formation are usually confined to the point at which the chip does not stick to the tool, i.e. perfect sliding takes place between chip and tool. This appears to generate lower temperatures on the tool face. However, once the chip sticks to the tool a secondary shear zone is established and quickly heats up the tool face. It appears that the discrepancy between Loewen and Shaw's calculations and the finite element calculations occurs when adhesion of the chip to the tool takes place, i.e., after the first ten millimeters, or so, of chip formation depending on the coefficient of friction. The calculated peak tool temperature of the initial stage of chip formation is remarkably accurate to the finite element calculations, but not so when the secondary shear zone is established, i.e., when the chip sticks to the tool face. Figures 6.9 and 6.10 show the difference in values very well at the end of the machining stroke when 300 millimeters of chip has been cut. When one inspects Figures 6.3, 6.5, and 6.7, it is clear that Loewen and Shaw's method provides very good accuracy at the primary stages of chip formation. This statement implies that Astakhov's statements concerned with using the early forms of machining mechanics are both valid and invalid depending on how one describes the machining conditions, i.e., primary stages of chip formation where the secondary shear is non-existent, or steady-state machining conditions when the secondary shear zone is fully established.

6.5 Conclusions

The calculations of the change in coefficient of friction have shown that increasing the coefficient of friction will lower the shear plane temperature. Conversely, the tool face temperature will increase with the increase in coefficient of friction.

Loewen and Shaw's method of calculating shear plane and tool face temperature appears to be applicable at the first stages of intimate contact between chip and tool when the secondary shear zone is non-existent.

Loewen and Shaw's method of calculating shear plane and tool face temperature does not appear to be applicable under steady-state conditions when the secondary shear zone is firmly established.

Acknowledgements

The chapter contributors wish to thank Inderscience publishers for granting permissions to reproduce work presented in this chapter.

References

[1] Astakhov, V. P., Shvets, S. V., and Osman, M. O. M., (1997), 'Chip Structure Classification Based on Mechanisms and Their Formation, Journal of Materials Processing Technology, Vol. 71, pp. 247-257.
[2] Astakhov, V. P., (1999), Metal Cutting Mechanics, CRC Press, Florida, USA.
[3] Astakhov, V. P., (2004), 'The Assessment of Cutting Tool Wear', International Journal of Machine Tools and Manufacture, Vol. 44, pp. 637-647.
[4] Astakhov, V. P., (2005), 'On the Inadequacy of the Single Shear Plane Model of Chip Formation', International Journal of Mechanical Sciences, Vol. 47, pp. 1649-1672.
[5] Astakhov, V. P., (2006), Tribology of Metal Cutting, Elsevier, London, UK.
[6] Boothroyd, G., (1961), 'Photographic Technique for Determination of Metal Cutting Temperature.' British Journal of Applied Physics, Vol. 12 no. 5, pp. 238-242.
[7] Bowden, F.P. and Tabor, D., (1954), The Friction and Lubrication of Solids, Oxford, Clarendon Press.
[8] Isakov, E., (2004), Engineering Formulas for Metalcutting, New York: Industrial Press.

[9] ISO 8688-2 (1989), Tool Life Testing in Milling - Part 2: End Milling, Geneva : International Organization for Standardization
[10] Loewen, E.G. and Shaw, M.C. (1954) 'On the Analysis of Cutting Tool Temperatures.' Transactions of the American Society of Mechanical Engineers, Vol. 76, pp. 217-231
[11] Robinson, G. (2007), Wear of Nanostructured Coated Cutting Tools During Mixed Scale Machining, Ph. D. Dissertation, Purdue University.
[12] Shaw, M.C. (2005), Metal Cutting Principles, New York: Oxford University Press.
[13] Stephenson, D.A., (1991), 'Assessment of Steady-State Metal Cutting Temperature Models Based on Simultaneous Infrared and Thermocouple Data.' Journal of Engineering for Industry, Vol. 113, no. 2, pp.121-28.
[14] Wright, P.K. and Trent, E.M., (1973), 'Metallographic Methods of Determining Temperature Gradients in Cutting Tools.' Journal of the Iron and Steel Institute, Vol. 211, no. 5, pp. 364-368.

Chapter 7

Economic Analysis of Machining with Nanostructured Coatings

M. J. Jackson, M. D. Whitfield, J. S. Morrell, R. Handy and M. Whitt

7.1 Introduction

Nanostructured coated cutting tools are increasingly being used to machine diificult-to-cut materials. This is especially so in machining hardened tools, exotic alloys, and fissile materials. The paper describes the recent developments concerned with machining hardened M42 tool steel that is used to simulate the conditions that pertain to the unusually low speed machining of fissile materials. An experimental analysis of the wear of coated cutting tools and how the experimentally determined tool life is used to select the most appropriate coating according to the number of components to be machined is presented. The research shows that tools coated with a non-titanium based coating are superior to those already used for machining hardened tool steels at low cutting speeds. In environments where tools experience high wear forces and extreme pressure sintered tungsten carbide tools are used. However, ultra hard materials such as silicon alloys, abrasive materials, synthetic materials and composites can only be machined with diamond-coated tools. Faure, Hanni, Schmutz and Gerovanoni [1] discussed the main issues involving diamond coatings. Thin uncoated tool edges are susceptible to rounding and therefore must be protected. Coating the tool with a hard material such diamond does not offer sufficient protection because there is a sharp hardness gradient between the tool and its coating. Upon impact this gradient causes the coating to break therefore exposing tool material to the usual wear mechanisms. This effect can be reduced if an interlayer is

introduced with hardness between the tool material and diamond, e.g., TiC/TiN. Such an interlayer reduces the severity of the hardness gradient and enhances adhesion between the diamond and tool. Diamond is an ideal coating material; it has high hardness, high wear resistance and is chemically inert. However it is difficult to coat steels, Ni alloys, cemented carbides and alloys containing transition metals with diamond. It is possible to coat WC-Co, but the cobalt must be etched away or a diffusion barrier introduced [2].

Faure applied a $TiCl_4$ precursor to the tool before depositing an interlayer in a CVD reactor at a temperature between $900^{O}C$ and $1000^{O}C$. 1% methane in hydrogen gas is introduced at a flux of 2000 sccm at a pressure of 20mbar to a CVD chamber that has a tantalum filament, graphite work holders and a working surface area of $200cm^2$. These conditions allow a diamond film to grow on the tool. The tool material coated was a 6% Co tungsten carbide. A cobalt etch was undertaken before deposition of a TiN interlayer and a TiN/TiC multilayer. Seeding with a solution of diamond micro grains was performed prior to deposition of the diamond coating. The coating effectiveness was assessed by a 'Revetest' test device and drilling experiments. The 'Revetest' device applies a constant force to an indenter during constant velocity displacement of the sample and critical loads are identified by an acoustic signal. Drilling tests were performed at 69,000rpm at 3.5m/min with a 1mm diameter drill. The critical load causing coating failure is a function of the substrate hardness and the strength of adhesion between coating and tool. It is common for a soft substrate to deform plastically while its coating does not because it has a high Young's modulus. The coating alone bears the load and fails thus exposing tool material to wear mechanisms. Diamond coatings with a TiN interlayer can withstand 10 times more force compared to diamond coatings without the interlayer; adhesion is not necessarily better but toughness is improved. If a TiC/TiN/TiC multilayer is applied large forces, around 100N, are required to break the surface. It was found that thicker interlayers improved adhesion between the tool and diamond coating and interlayers with a Young's modulus between that of the tool and diamond coating produced better machining results. Uncoated tools were able to drill 10,000 holes and coated

tools drilled 20,000 holes before they were considered worn. Uncoated tools experienced rounding of the cutting edge.

Bell [3] categorized tool materials into three basic groups, high-speed steels, cemented carbides and ceramic and super hard materials including alumina based composites, sialons, diamond and cubic boron nitride. In addition the surface properties of these materials can be modified. Tool wear can be defined by the following description, 'A cutting tool is considered to have failed when it has worn sufficiently that dimensional tolerance or surface roughness are impaired, or when there is catastrophic tool failure or impending catastrophic tool failure'. To prevent failure Mills [4] suggests surface modification techniques such as coating should be employed to improve tool performance. PVD has the capability to deposit wear resistant ceramic layers on high-speed tool steels. Although CVD can be used PVD appears to be advantageous in terms of coating adhesion and producing coatings with compressive stresses. It is increasingly being discovered that cubic boron nitride is an effective tool coating. Different machining processes are characterized by different wear mechanisms and the choice of tool coating should be selected to offer the best protection for a particular set of machining conditions. Tool coatings can modify contact conditions which alters the coefficient of friction, in turn this alters heat generation and heat flow; there are four main types of coating. The first category is titanium-based coatings such as TiAlN; other elements are added to improve hardness and oxidation resistance. Titanium based coatings are popular because they provide a wide range of average protection properties, have good adhesion and are relatively easy and quick to coat. The second category is ceramic-based coatings, e.g., Al_2O_3, where ceramics have good thermal properties and excellent resistance to wear but are difficult to deposit. The third category is super hard coatings such as CVD diamond. The fourth category is solid lubricant coatings such as amorphous metal carbon, Me-C:H. Combinations of these coatings can give the best wear resistance; for example a recent development has been to take super hard coatings and deposit low friction MoS_2 or pure carbon on their surfaces. Kubaschewski and Alcock [5] concluded that to prevent the onset of diffusion the enthalpy of the

coating must be as negative as possible to increase the temperature at which diffusion is triggered. From this point of view most carbide coating materials such as TiC, HfC, ZrC are more suitable for cutting steel than tungsten carbide, similarly for the nitrides except CrN up to a temperature of $1500^{O}C$. The technique used to coat the tool can affect its performance; CVD requires high temperatures that can have an annealing effect on the tool. This changes the tool's toughness and rupture strength because a brittle η phase $(Co_XW_YC_Z)^2$ forms. A standard CVD process operating at $1100^{O}C$ can reduce the materials strength by 30%. PVD techniques such as evaporation, sputtering and ion plating usually take place between $200\text{-}500^{O}C$ avoiding such problems.

Eventually, multilayer coatings were developed. Klocke and Krieg [6] summarized their three main advantages: (1) Multilayer coatings have better adhesion to the tool. This is because the adhesion between the tool, intermediate layer and coating is better than the adhesion between the tool and coating alone; for example the presence of TiC in a CVD TiC-Al_2O_3-TiN coating system; (2) Multilayer coatings have improved mechanical properties such as hardness and toughness. For example, the advantages of a (Ti,Al)N layer can be combined with advantages of a TiN layer (good bonding and high toughness) by building up alternate layers of each coating. Layering is also thought to provide a barrier to resist crack propagation; and (3) Each level of a multilayer coating can provide a different function. For example, a coating could consist of a mid-layer with high thermal stability and a top layer with high hardness to produce a coating that maintains its hardness at high temperatures. It is possible for coatings to protect the substrate from heat if they are good insulators, have low thermal conductivity and a low coefficient of heat transfer. An example of such an improvement is a TiN-NaCl multilayer, which has hardness that is 1.6 times greater than a single TiN layer. (Al,Ti)N coated tools have been compared to TiN and uncoated tools when milling at 600m/min. The (Al,Ti)N coated tools exhibit much less flank wear, which correlates to a higher hardness, 2720HV for (Al,Ti)N vs 1930HV for TiN and an improved oxidation temperature, $840^{O}C$ for (Al,Ti)N v $620^{O}C$ for

TiN. The improved performance of (Al,Ti)N coated tools is due to their ability to maintain a higher hardness at elevated temperatures.

It has been noted that in some extreme cases of machining highly abrasive materials, e.g. hypereutectic Al-Si alloys where the Si particles are highly abrasive, variations of Ti based coatings do not improve the tool life. In such cases only the hardness of diamond coatings can improve the abrasion resistance and therefore prolong tool life. Quinto, Santhanam and Jindal [7] investigated coatings deposited by CVD and PVD techniques. Coatings with an Al content tend to perform better regardless of the application, coating process or chemical content of other the coating constituents. This is because abrasive resistance, oxidation resistance and hardness are all improved. Thermal relief experienced by the substrate is of special interest in terms of volume effects like fatigue and diffusion. Examples of coatings offering this relief are PVD (Ti,Al)N and CVD TiC-Al_2O_3-TiN.

Dry machining of steels in the range of 55-62HRC at 15,000-25,000 rpm generates cutting temperatures of 1000^{O}C and the tool must be protected from oxidation wear. Previous work by Munz, Smith, Donohue, Deeming and Goodwin [8] has shown that above 800^{O}C diffusion of stainless steel is triggered and cavities begin to form between the substrate and coating, although this can be prevented by adding 1% yttrium. One method used by Constable, Yarwood and Munz [9] to analyze the integrity of coatings is Raman microscopy. It has been used to study wear, wear debris, stress, oxidation, and the structure of single layer PVD coatings; it is now being used to study multilayer PVD coatings. Raman microscopy works by analyzing photon interactions with the lattice to determine the characteristic vibrations of the molecules. Thus, the process is sensitive to lattice re-arrangement that can occur as a result of local changes in material properties due to high cutting temperatures. Constable, Yarwood, Hovsepian, Donohue and Lewis [10] demonstrated the usefulness of Raman microscopy when a PVD combined cathodic arc/unbalanced magnetron deposition system was used to coat high-speed steel and stainless steel for abrasion tests. The coatings had a thickness between 2.5-4μm with a surface

roughness of 0.02-0.03μm Ra (roughness average). Polycrystalline corundum with a hardness of 1900HV and Ra of 0.2μm was brought into contact with the PVD coating. A constant load of 5N was applied and the relative sliding speed between the two surfaces was 10cm/s. A 25mW HeNe laser with an excitation wavelength of 632.8nm was used to obtain Raman results. The PVD coating consisted of a 1.5μm thick TiN base layer with alternating layers of TiCN, 0.4μm thick and TiN, 0.6μm thick; the total thickness was 3.9μm. The expected wear debris was rutile, TiO_2, which yields a peak at 426cm^{-1}; however peaks were also detected at 512 and 602cm^{-1} indicating anatase debris. This would suggest the contact temperature was lower than expected, indicating the coefficient of friction was also lower than expected. Deeming, Munz and Smith [11] investigated the effect different coatings have on delaying the onset of oxidation. During high speed machining, temperatures regularly exceed 900^0C. Deeming found a TiN coating delayed oxidation until 500^0C, a TiAlN coating delayed oxidation until 700^0C and a multilayered system delayed oxidation formation until 950^0C. The final coating tested was TiAlCrYN, prior to deposition Cr is added to etch the tool thereby achieving the smoothest, most strongly adhered, dense coatings possible. The addition of Y increases wear of the tool at low temperatures, however at higher temperatures Y causes maximum wear to occur at 600^0C and minimal wear to occur at 900^0C. Without the addition of Y the wear rate continually increases with temperature. Deeming [11] suggests Y diffuses into the grain boundaries and at high temperatures there is some stress relaxation. Heat-treated TiAlCrYN therefore has lower internal compressive stresses than regular TiAlCrYN. TiAlCrYN also has a lower coefficient of friction with increasing temperature compared to TiN. Recent developments in tool coatings have generated improved results by using a non-titanium based coating such as AlCrN [12].

Highly alloyed fissile materials contain numerous carbides that make it difficult to machine. An alloy that simulates the machining characteristics of highly alloyed fissile material is M42 tool steel that contains numerous types of carbides that chips away the edges of cutting tools. Therefore, tool life equations pertaining to M42 tool

steels are intended to simulate the machining characteristics of highly alloyed fissile materials.

7.2 Experimental Apparatus

Machining experiments were conducted using a Hurco TM8 centre lathe. The experiments were conducted using the following conditions. Spindle speeds used were 121, 158, and 200 revolutions per minute; cutting speed was kept constant at 0.0026 inches per revolution; and depth of cut was constant at 0.0025 inch. The specimen tested was M42 high-speed steel. The specimen was heat treated to Rockwell "C" 65. Plain cutting tool inserts supplied by Kennametal (type TPG322/TPGN160308/K313) were coated with a variety of coatings, such as TiN, TiAlN, TiCN, CrN, WC/C, and AlCrN, supplied by Oerlikon Balzers. The tool inserts were held in a specially designed tool holder. After each 0.200" length of cut, the tool edge was photographed using an optical microscope to record wear on the top face and flank of the tool. The tool was considered worn when the length-of-flank wear reached 500 μm, in accordance with international standards.

7.3 Experimental Results

7.3.1 Cutting tool wear

Figures **7.**1 – **7.**10 show the wear of the cutting tools during the experimental work for tools coated with TiCN and AlCrN. The images shown are of the top face and the flank face of the tool inserts. Figure 7.1 shows the initial generation of wear from using a virgin tool insert. The progressive wear appears to be associated with chipping on the nose radius of the insert, this case being cutting edge number 6. It appears that there is a form of delamination occurring on the edge of the tool. Figure 7.2 shows the effect of machining M42 tool steels at low speed using a TiCN coated insert. At 121 rpm and with a very small volume of the workpiece removed, there are signs of coating delamination and flaking at the nose of the cutting tool insert edge number 6.

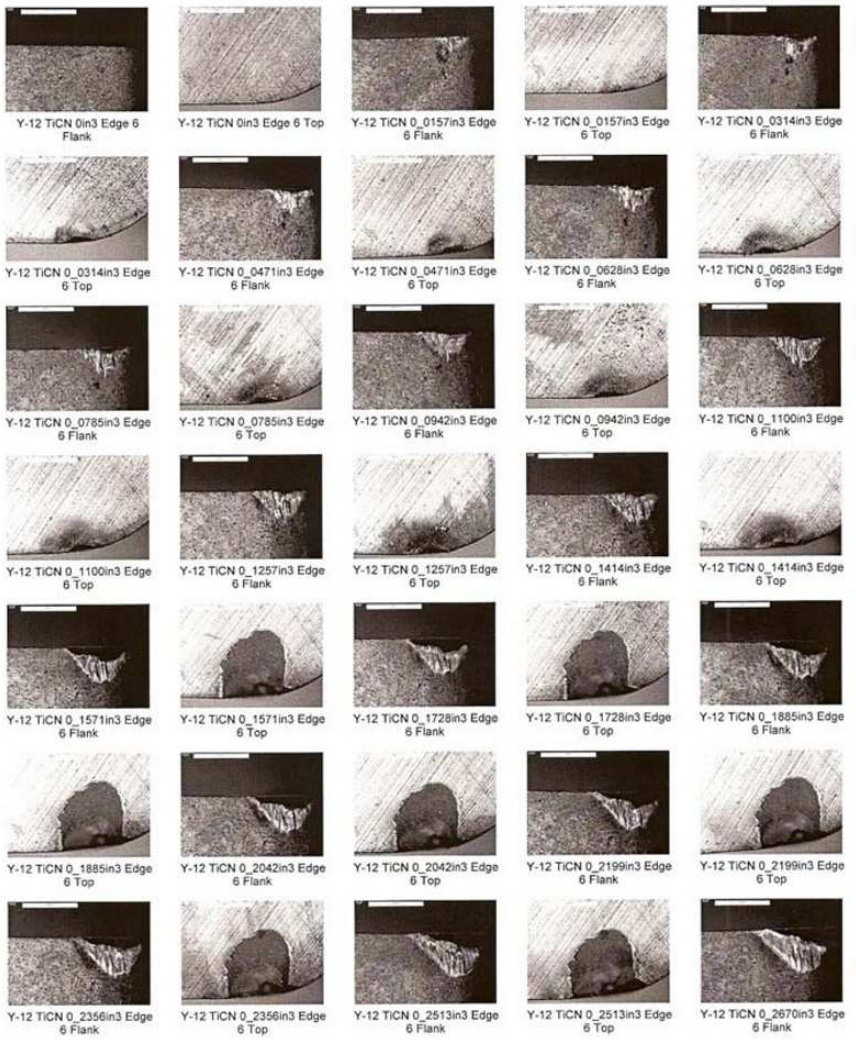

Figure 7.1. TiCN Tool Cutting Edge 6 machined at 121 RPM. 0 – 0.2513 in^3 of workpiece removed

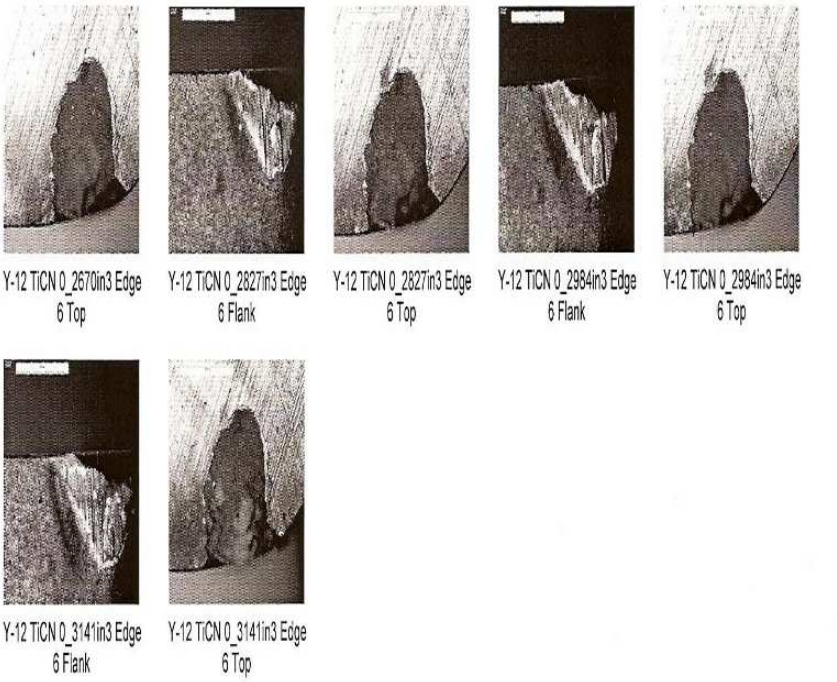

Figure 7.2. TiCN Tool Cutting Edge 6 machined at 121 RPM. 0.2670–0.3141 in^3 of workpiece removed

At higher speeds, Figure 7.3 shows the effect of increasing speed to 158 rpm. Figure 7.3 shows the progression of wear from using a virgin insert until 0.2356 in^3 of workpiece material is removed, this time using cutting tool edge number 5. A pronounced form of nose wear is shown as a function of gross fracture along the flank face until delamination of the coating occurs. Figure 4 shows the mode of failure at a speed of 200 rpm. At this speed, the damage appears to be less acute than at the median range speed of 158 rpm. This may be due to reduced forces, or significant improvements in the retention of the coating preventing it from being delaminated.

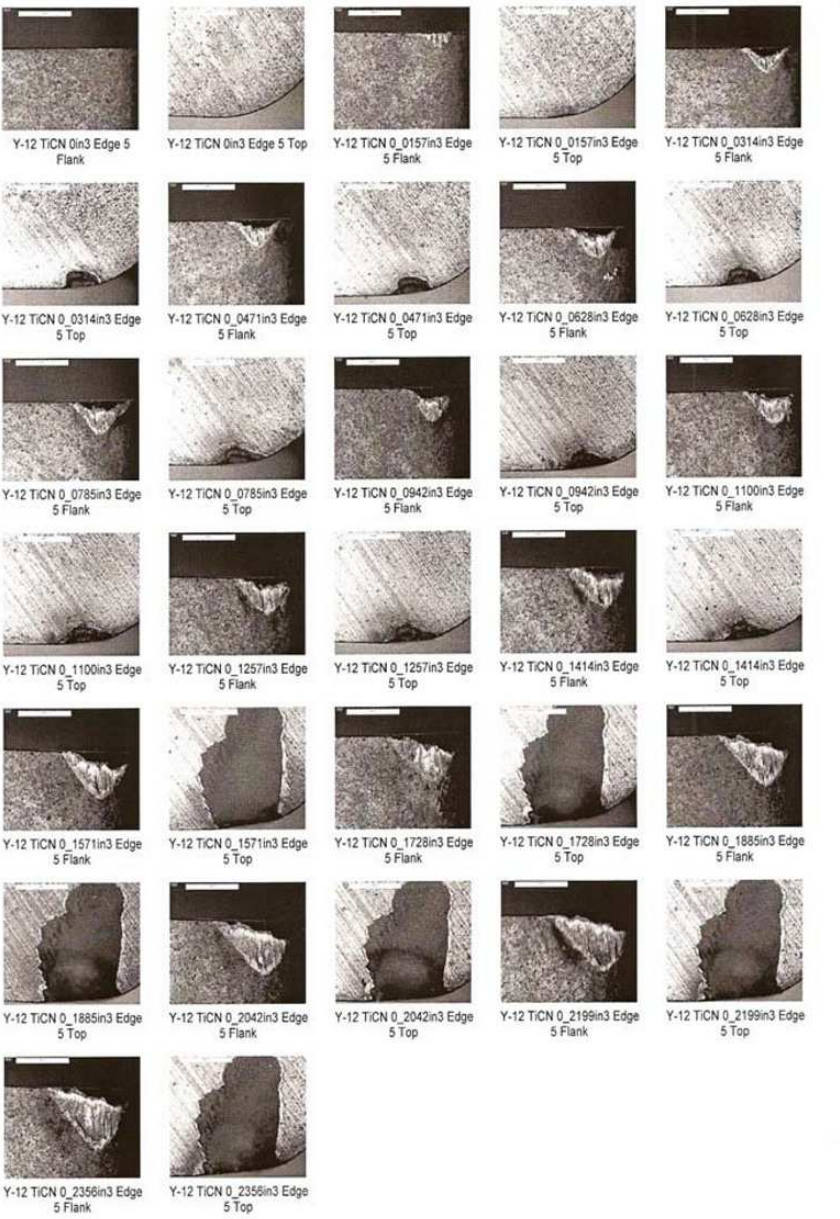

Figure 7.3. TiCN Tool Cutting Edge 5 machined at 158 RPM. 0 – 0.2356 in^3 workpiece removed

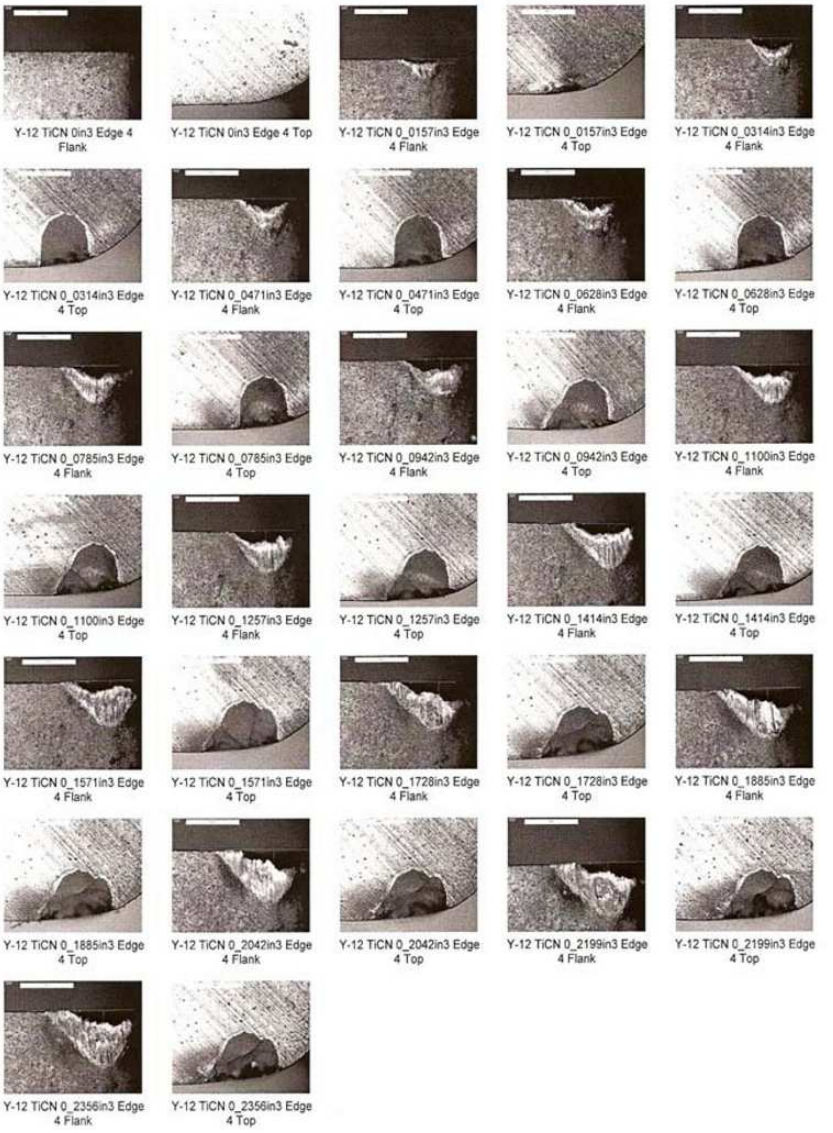

Figure 7.4. TiCN Tool Cutting Edge 4 machined at 200 RPM. 0 – 0.2356 in^3 workpiece removed

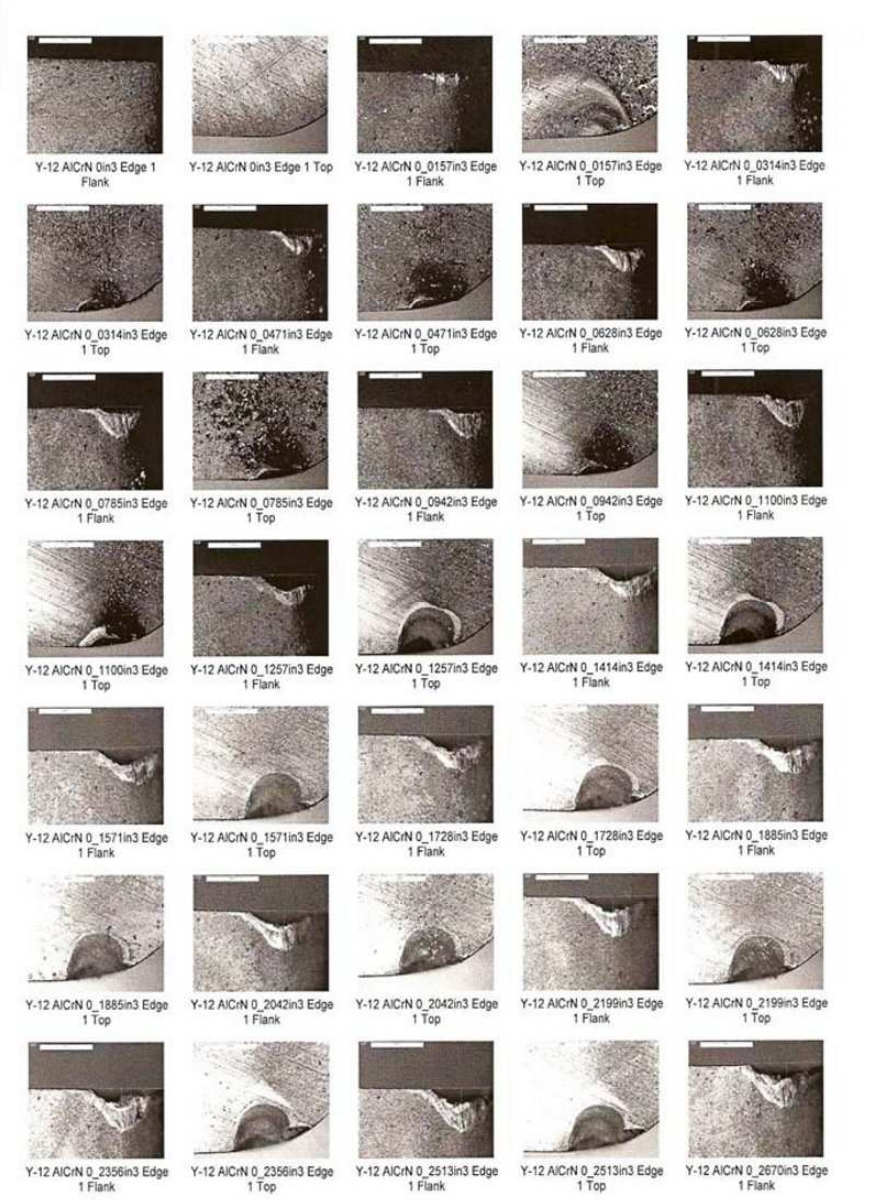

Figure 7.5. AlCrN Tool Cutting Edge 1 machined at 121 RPM. 0 - 0.2513 in^3 workpiece removed

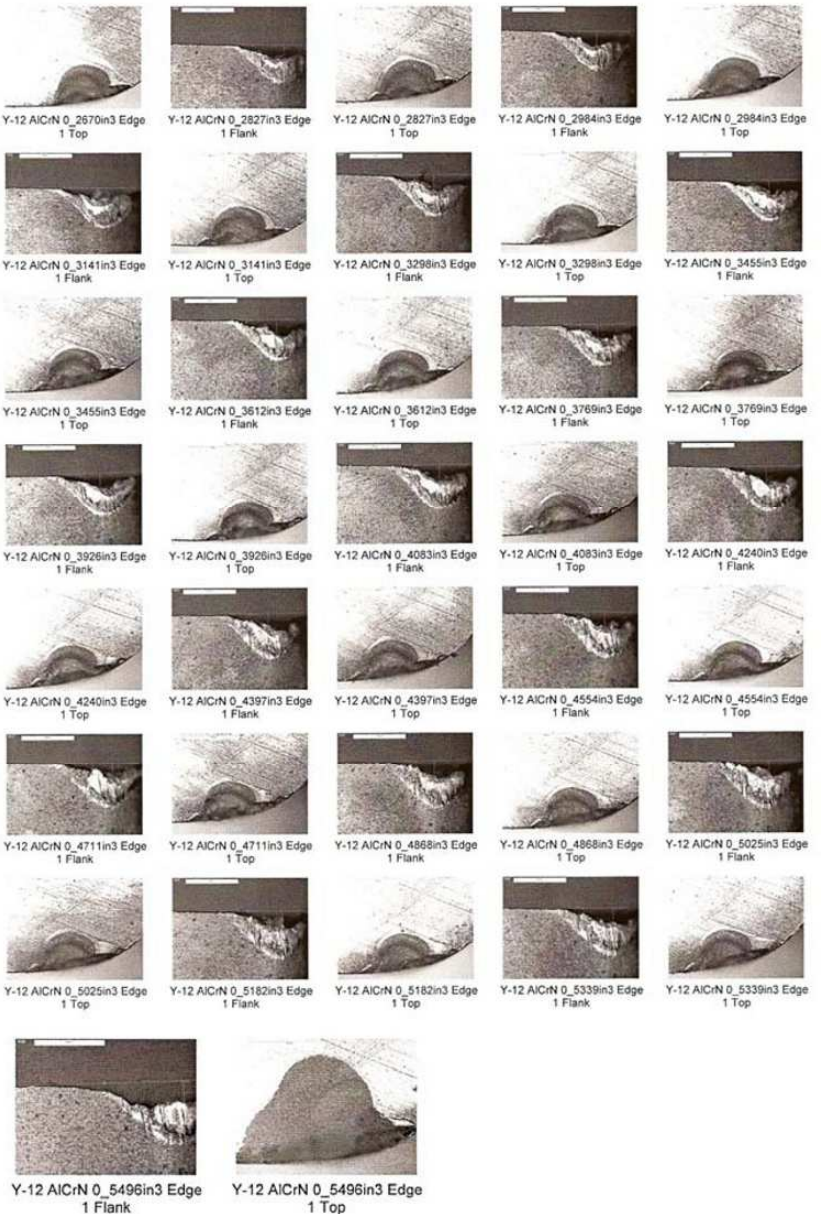

Figure 7.6. AlCrN Tool Cutting Edge 1 machined at 121 RPM. 0.2670 - 0.5496 in^3 workpiece removed

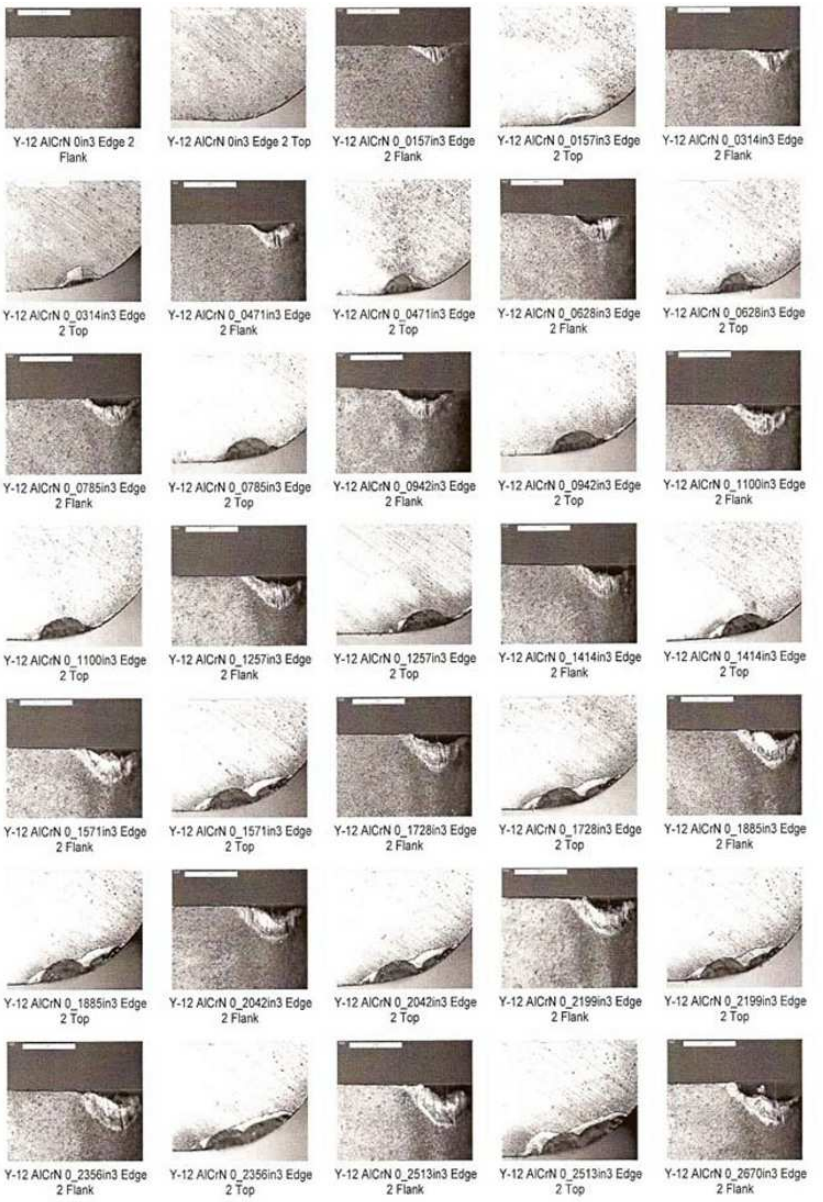

Figure 7.7. AlCrN Tool Cutting Edge 2 machined at 158 RPM. 0 - 0.2513 in^3 wokpiece removed

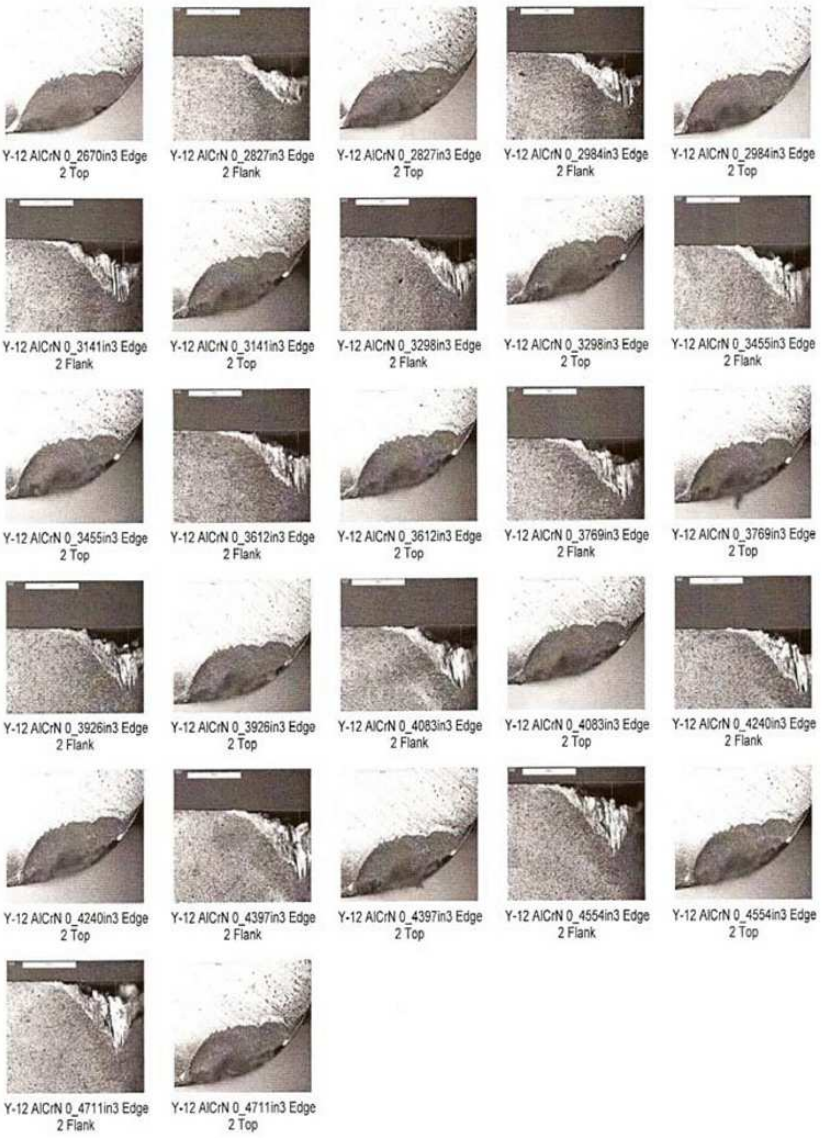

Figure 7.8. AlCrN Tool Cutting Edge 2 machined at 158 RPM. 0.2670 - 0.4711 in^3 workpiece removed

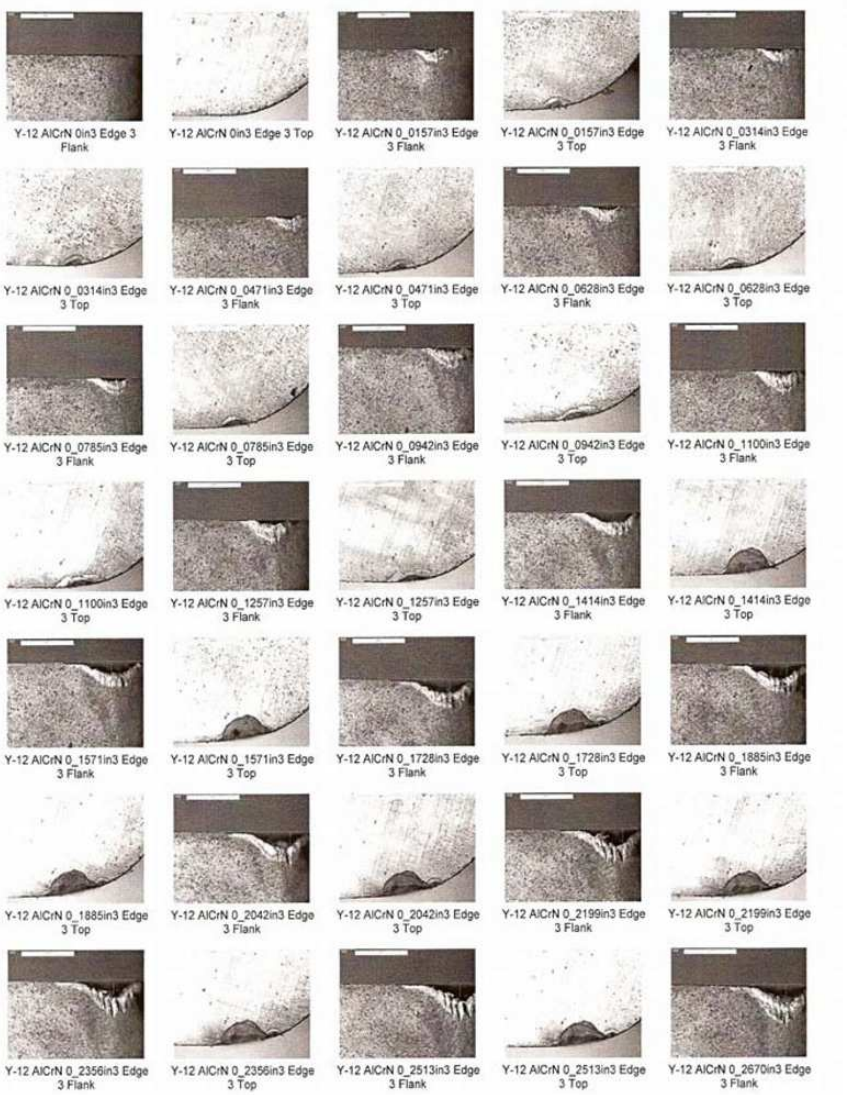

Figure 7.9. AlCrN Tool Cutting Edge 3 machined at 200 RPM. 0 - 0.2513 in^3 workpiece removed

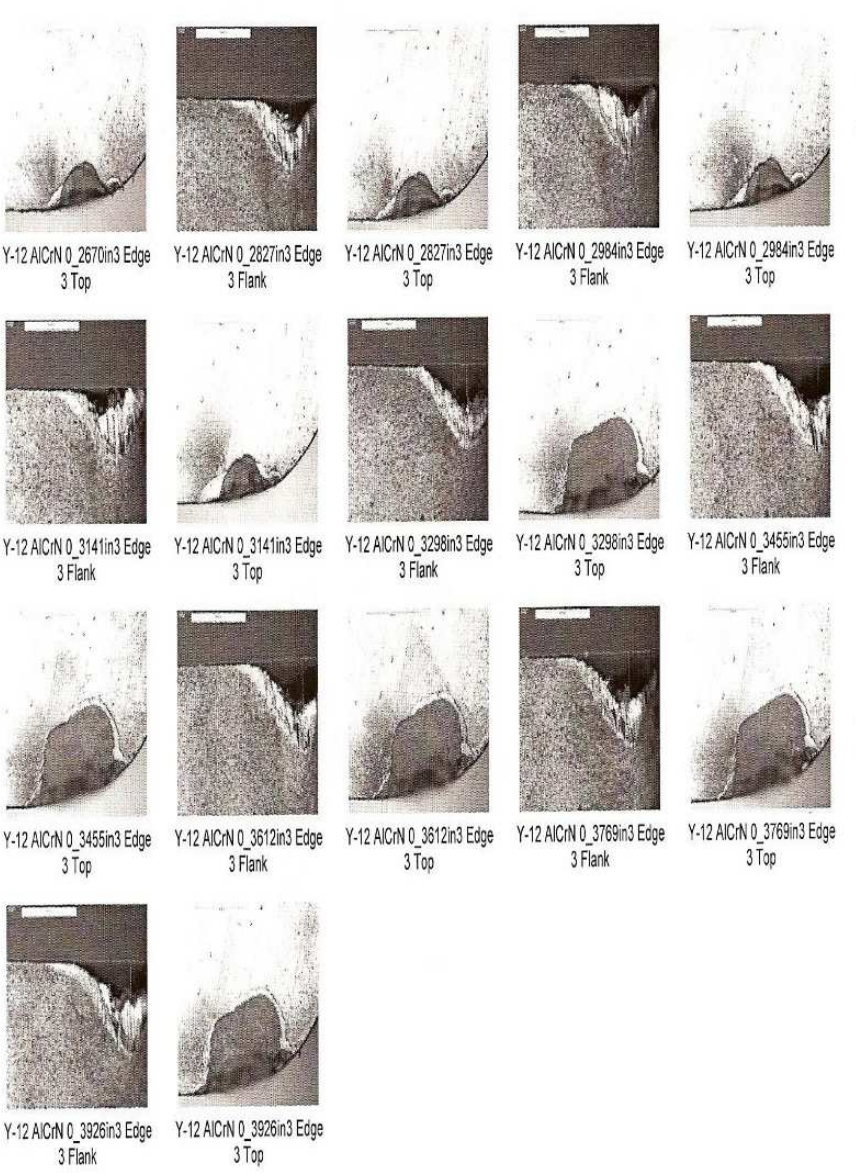

Figure 7.10. AlCrN Tool Cutting Edge 3 machined at 200 RPM. 0.2670 - 0.3926 in^3 workpiece removed

Figure 7.5 shows the initial generation of wear from using a virgin tool insert coated with AlCrN. The progressive wear appears to be associated with chipping on the nose radius of the insert, this case being cutting edge number 1. It appears that there is a form of delamination occurring on the edge of the tool, but is not so pronounced as it is when using the TiCN coating. Figure 7.6 shows the effect of machining M42 tool steels at low speed. At 121 rpm and with a very small volume of the workpiece removed, there are signs of coating delamination and flaking at the nose of the cutting tool insert edge number 6. At higher speeds, Figure 7.7 shows the effect of increasing speed to 158 rpm. Figure 7.8 shows the progression of wear from using a virgin insert until 0.2356 in^3 of workpiece material is removed, this time using cutting tool edge number 2. A pronounced form of nose wear is shown as a function of gross fracture along the flank face until delamination of the coating occurs. Figures 7.9 and 7.10 shows the mode of failure at a speed of 200 rpm. Again at this speed, the damage appears to be less acute than at the median range speed of 158 rpm. This may be due to reduced forces, or significant improvements in the retention of the coating preventing it from being delaminated.

7.3.2 Volume removed as a function of flank wear

Figures 7.11 – 7.13 show the volume removed versus the flank wear for the three spindle speeds used during the experimental work. The graphs show that AlCrN coated tools have similar results of increased tool life compared with TiAlN coated tools. At 121 rpm, TiAlN coated tools appear to provide the best resistance against wear. At 158 rpm, AlCrN coated tools perform slightly better, whereas at 200 rpm the AlCrN coated tool clearly performs better than all other cutting tool coatings.

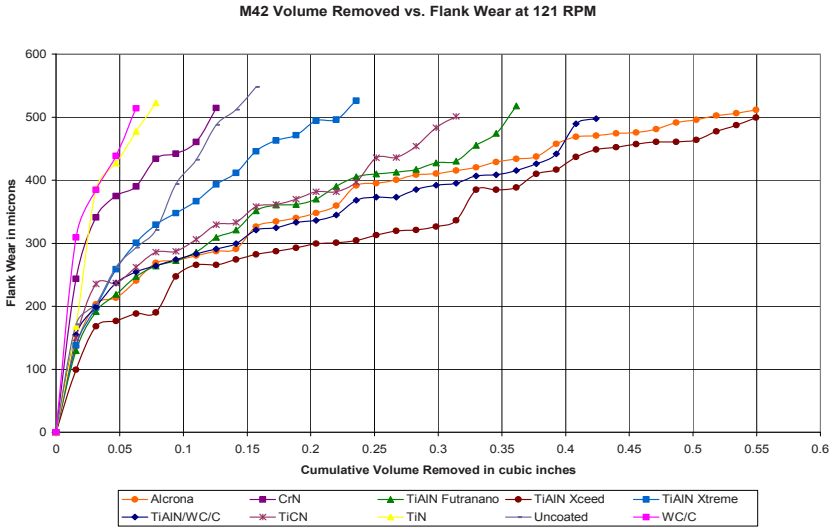

Figure 7.11. Volume Removed versus Flank Wear at a spindle speed of 121 RPM

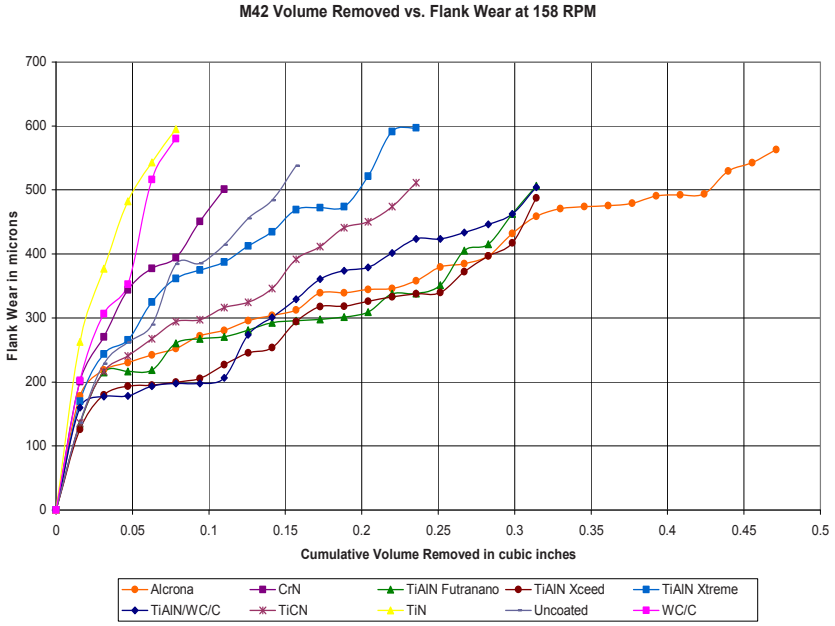

Figure 7.12. Volume Removed vs. Flank Wear at a spindle speed of 158 RPM

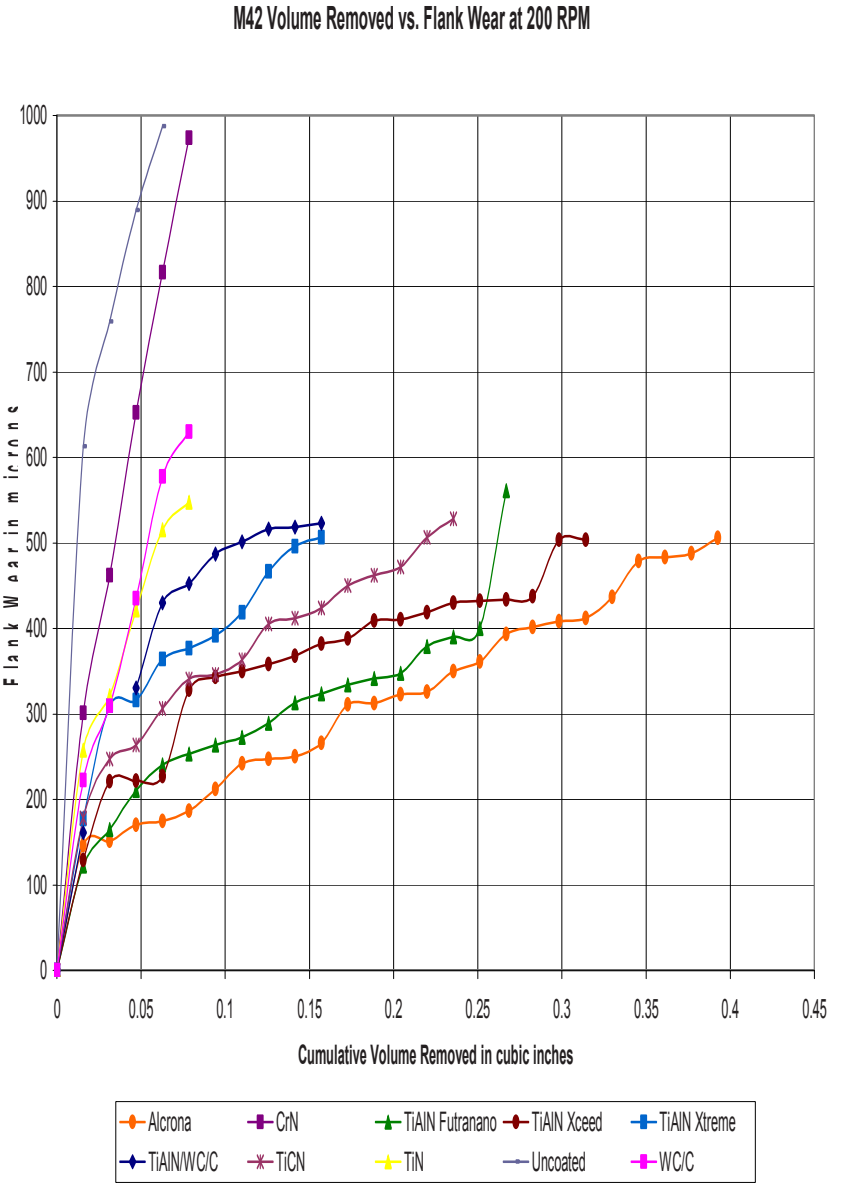

Figure 7.13. Volume Removed vs. Flank Wear at a spindle speed of 200 RPM

7.3.3 Summary of experimental results

Table 7.1 shows the results of cutting speed as a function of tool life. The results are given for three spindle speeds and the life of the tool inserts are in seconds. The uncoated and all coated tools are shown in Table 7.1.

		Tool Life (s)									
		TiCN	TiAlN (50% Ti:50 %Al)	TiN	Uncoated	CrN	TiAlN (30%Ti:70%Al)	TiAlN (40%Ti:60%Al)	WC/C	TiAlN/WC/C	AlCrN
Cutting Speed (m/s)	1.61	762.9	877.3	190.7	343.3	305.1	572.2	1335.0	152.6	1029.9	1258.7
	2.1	438.2	584.2	116.8	292.1	204.5	409.0	584.2	116.8	584.2	817.9
	2.66	323.1	392.3	92.3	23.1	69.2	230.8	438.5	92.3	161.5	576.9

Table 7.1. Tool life data of coated cutting tools

7.4 Cutting Tool Life

Taylor's tool life equation can be used to predict the tool life at a given cutting speed. Taylor's tool life is used in the economic analysis of the tools. It is given by:

$$VT^n = C \tag{7.1}$$

Where, V = cutting speed – m/s, T = tool life – s, n = tool life exponent constant, C = tool life constant. To determine n and C, experiments much be conducted. The constant n is determined using a log-log plot of the cutting speed versus the tool life. The gradient of the regression line is n. The constant C can then be determined.

7.4.1 Determination of exponents

From these experiments, the cutting speed was the only variable known. The cutting speed was used to determine the tool life experimentally. After the experiments were conducted, a log-log plot of cutting speed versus tool life was made. Figures 7.14 – 7.16 show the plots of the cutting speed versus tool life. The regression function was calculated for each graph and was used to determine the exponent, n. Table 7.2 shows the value of, n, for all tools used in the experiments.

$$n = -\frac{\log V_{c2} - \log V_{c1}}{\log T_{c2} - \log T_{c1}} \tag{7.2}$$

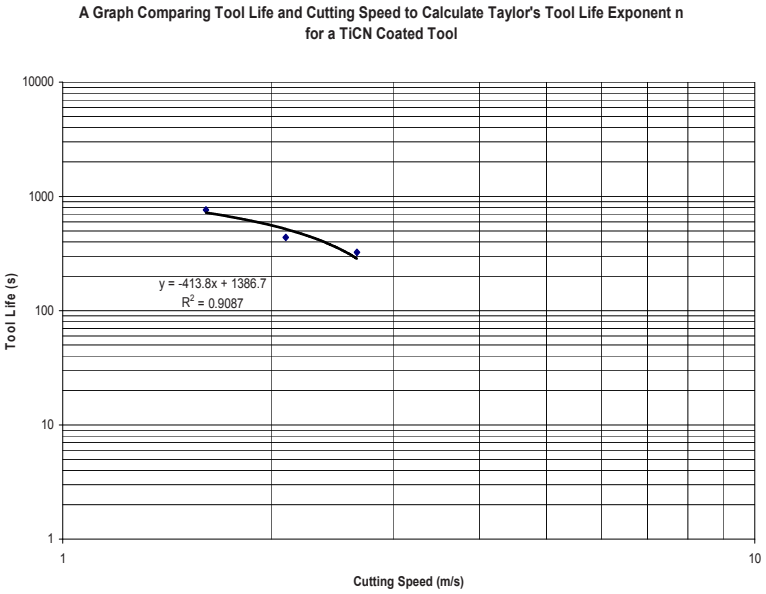

Figure 7.14. Tool Life versus Cutting Speed for TiCN coated tool

Where, Vc_1 is the first cutting speed point on the plot, i.e., 1.61 m/s, Vc_2 is the second cutting speed point on the plot, i.e., 2.66 m/s, Tc_1 is determined using Vc_1 in the best fit regression line, Tc_2 is determined using Vc_2 in the best fit regression line, and R^2 is the correlation coefficient.

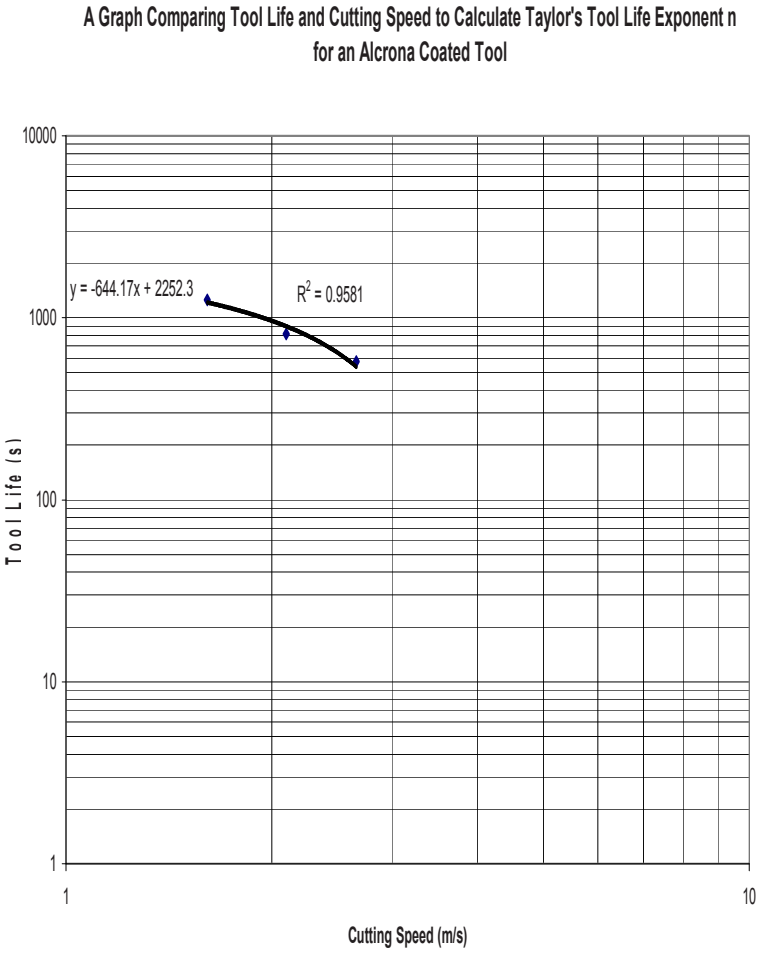

Figure 7.15. Tool Life versus Cutting Speed for AlCrN coated tool

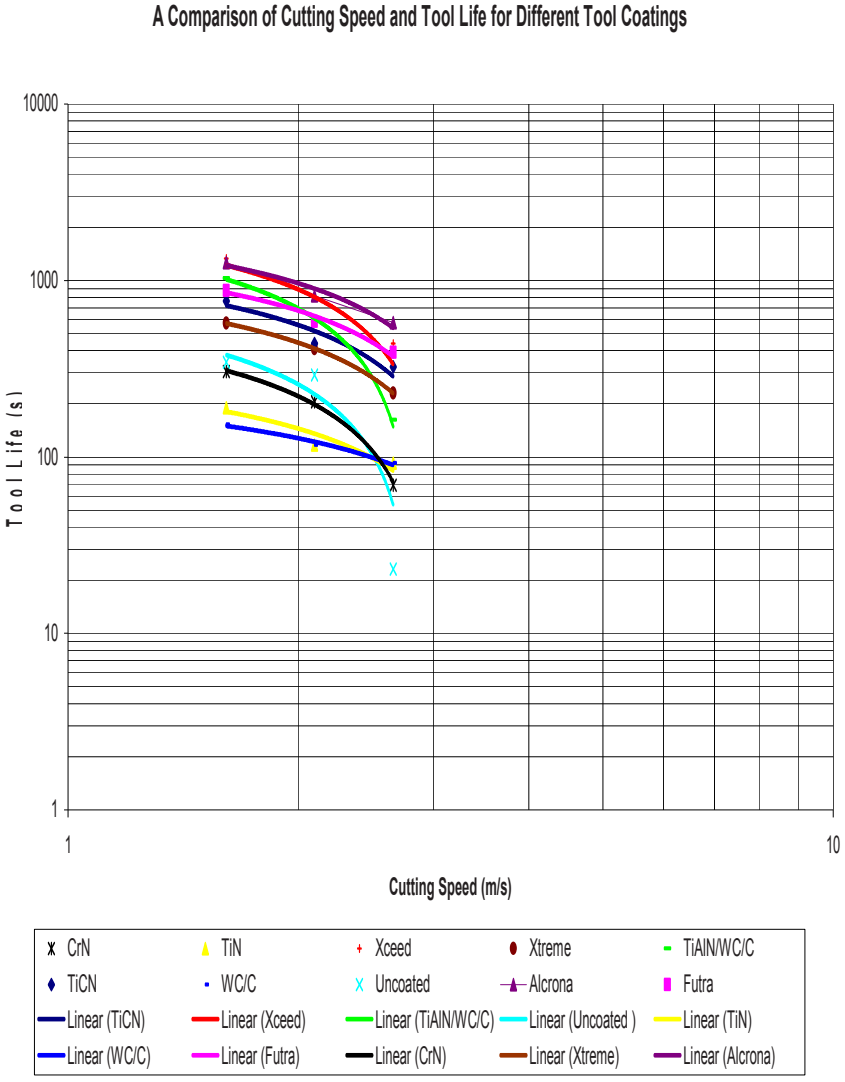

Figure 7.16. Tool Life versus Cutting Speed for the coated cutting tools

Coating	n
CrN	0.346
TiAlN (Ti%50:Al%50)	0.604
TiAlN-WC-C	0.262
TiCN	0.543
TiN	0.651
Uncoated	0.257
WC-C	0.983
TiAlN (Ti%40:Al%60)	0.389
TiAlN (Ti%30:Al%70)	0.551
AlCrN	0.617

Table 7.2. Values of the exponent, n, for the coated tools

7.4.2 Determination of the constant

With the variables, V, T, and, n, C can be calculated using Taylor's tool life. After C is found for all spindle speeds, the average is then calculated. This is valid for interpolation only, i.e., 1.61 – 2.66 m/s. Table 7.3 shows the average of the constant, C, values for all tools. Equation 2 can be solved for T, thus,

$$T = e^{(\frac{1}{n}\ln\frac{C}{V})} \tag{7.3}$$

Tables 7.2 and 7.3 can be used to determine tool life, T, for a given cutting speed. This has been used to predict the theoretical tool life in the economical analysis, tp.

Coating	C
CrN	12.14
TiAlN (Ti%50:Al%50)	97.66
TiAlN-WC-C	10.38
TiCN	133.89
TiN	48.78
Uncoated	7.4
WC-C	226.39
TiAlN (Ti%40:Al%60)	26.61
TiAlN (Ti%30:Al%70)	54.76
AlCrN	132.58

Table 7.3. Average values of C for coated cutting tools

7.5 Economic Analysis

The economic analysis was calculated using Equation 7.4. The reference time variable is based on the experimental data collected for the tool life. The other variables are based on data from machining handbooks. These variables are relative in each equation. This will allow for the only change in the calculations to be the tool life. Table 7.4 shows the cost per component of each tool.

$$C_{pr} = Mt_l + Mt_R + \frac{t_R}{t_P}\left(Mt_{ct} + C_t\right) \tag{7.4}$$

Where, C_{pr} is cost of tooling per component ($), M is total machine and operator rate including overhead ($/min), t_l is load time (min),

t_R is reference time (min), t_P is time predicted by Taylor's tool life (min), t_{ct} is tool changing time (min), and C_t is the new tool cost ($).

Coating	Cc ($)	Ct ($)	tp (s)	Cpr ($)	%
AlCrN	7.22	14.22	776.00	6.45	49.76
TiAlN (Al70:Ti30)	4.87	11.87	625.00	6.71	47.72
TiAlN (Al50:Ti50)	4.87	11.87	450.00	8.22	35.96
TiCN	10.28	17.28	536.00	9.00	29.87
TiAlN+WC/C	5.41	12.41	406.00	9.02	29.72
TiAlN (Al60:Ti40)	0.00	7.00	163.00	12.83	0.00
CrN	5.05	12.05	183.00	16.24	-26.54
TiN	3.61	10.61	135.00	19.26	-50.09
WC/C	5.41	12.41	123.00	23.25	-81.23

Table 7.4. Cost per component of coated tools

7.6 Discussion

From Table 7.4, the tool cost per component is least for the AlCrN tools. The TiAlN (Ti%70:Al%30) is the second lowest cost per tool component. The WC/C tool is the highest cost per component tool owing to the fact that it delaminates almost instantaneously when machining M42 tool steel. The TiAlN coatings performed well. These coatings have a high microhardness and a low coefficient of friction. The WC/C coating is a multilayer coating with a hard layer and a soft, lubricating layer. This coating did not perform well. The tungsten carbide layer is very hard. The hardness gradient between the two layers is drastic and could account for the poor performance of the tool insert. AlCrN coating has the highest oxidation temperature, which might account for the extended tool life. This coating performs well with a high hardness material, i.e., hardened M42 tool steel. The composition of AlCrN is $Al_{0.7}Cr_{0.3}N$. This is a similar composition to the TiAlN (Al%60:Ti%40) coating

that has a composition of $Al_{0.66}Ti_{0.34}N$. The addition of chromium instead of titanium apparently increases the oxidation temperature significantly. It is noted that replacing titanium in the coating has a significant effect on cutting tool life. Cutting tool coatings appear to fail by delamination. This was significant when using titanium-based coatings. The hard abrasive carbide particles appear to be the cause of the loss of coating on the nose of the coated insert. It is not clear if thermal and/or mechanical effects dominate the failure of coatings when machining at such low speeds. This should be an area of investigation for future work in the field of low speed machining.

Conclusions

The best performing coatings were the AlCrN coating and the TiAlN (Al%70:Ti%30) coating. The R^2 value of TiCN tool was 0.6654 for the first experiment. The second experiment yielded a value of 0.9087. This value is relatively close to the R^2 values of the other coatings. Values of exponent, n, do not correlate with the cost per component.

Acknowledgements

The chapter contributors wish to thank Inderscience publishers for granting permissions to reproduce work presented in this chapter.

References

[1] Faure, C., Hanni, W., Schmutz, C. J., & Gervanoni, M., Diamond-Coated Tool,. Diamonds and Related Materials, **8**(2-5), (1999) 636-639.

[2] Jackson, M. J., Gill, M., Sein H., & Ahmed, W., Manufacture of Diamond Coated Cutting Tools for Micromachining Applications, Proceedings of the Institution of Mechanical Engineers, Part L – Journal of Materials, **217**, (2003), 77-82.

[3] Bell, T., Surface Engineering: Its Current and Future Impact on Tribology, Journal of Physics D: Applied Physics, **25**(1A), (1992) A297-306.

[4] Mills, B., Recent Developments in Cutting Tool Materials, Journal of Materials Processing Technology, **56**(1-4), (1996) 16-23.

[5] Kubaschewski, O., & Alcock, C. B., Metallurgical Thermochemistry (5th), Oxford, Pergamon Press, (1979).

[6] Klocke, F., & Krieg, T., Coated Tools for Metal Cutting - Features and Applications, CIRP Annals - Manufacturing Technology, **48**(2), (1999) 515-525.

[7] Quinto, D. T., Santhanam, A. T., & Jindal, P. C., Mechanical Properties, Structure and Performance of CVD and PVD Coated Carbide Tools, International Journal of Refractory and Hard Metals, **8**(2), (1989) 95-101.

[8] Munz, W. D., Smith, I. J., Donohue, L. A., Deeming, A. P., & Goodwin, R, TiAlN Based PVD Coatings Tailored for Dry Cutting Operations, Proceedings, Annual Technical Conference - Society of Vacuum Coaters (pp. 83-93). Albuquerque, NM: Society of Vacuum Coaters (1997).

[9] Constable, C. P., Yarwood, J., & Munz, W. D., Raman Microscopic Studies of PVD Hard Coatings, Surface Coatings and Technology, **116-119**, (1999) 155-159.

[10] Constable, C. P., Yarwood, J., Hovsepian, P., Donohue, L. A., & Munz, W. D., Structural Determination of Wear Debris Generated From Sliding Wear Tests on Ceramic Coatings Using Raman Microscopy, Journal of Vacuum Science and Technology, Part A: Vacuum, Surfaces and Films, **18**(4), (2000) 1681-1689.

[11] Deeming, A. P., Munz, W. D., & Smith, I. J., Dry High Performance Machining (HPM) of Die and Moulds Using PVD Coated Solid Cemented Carbide Tools, Paper presented at the meeting of Sheffield P.V.D. Research Group. (2001).

[12] R. T. Coelho, E-G Ng, & M. Elbestawi, A Study of Wear on Coated PCBN Tools When Turning Highly Hardened AISI 4340 Using FEM Simulation, Industrial Diamond Review, **4**, (2006), 60-67.

Chapter 8

Analysis of Machining Hardened Steels Using Coated Cutting Tools

M. J. Jackson, R. Handy, M. Whitt, M. D. Whitfield and J. S. Morrell

8.1 Introduction

Laser heat-treated tool steels provide a challenge to process, especially machining and grinding. After hardening, the material becomes very abrasive. It can be a difficult material to grind let alone process in a single point operation. During laser hardening operations, carbon, chromium, and molybdenum atoms enrich austenite grains in the structure of the steel. This directly affects the hardness of the specimen. There is a large amount of molybdenum carbides that contributes to the excellent wear resistance of this material. The result is a low toughness that is acceptable for a number of applications. Laser-hardened D2 tool steel is generally used for cold working operations such as stamping and forming. The characteristics are high resistance to wear and cracking. Traditional metal cutting theories are being challenged as a result of advances in computational mechanics and analysis. Astakhov and co-workers [1-3] are critical of using theories developed in the 1940s that describe the mechanics of metal cutting at the macroscale. In response to Astakhov's [1-5] assertions that the previous theories do not readily apply to current machining practices, the authors of this paper have conducted a series of computational analyses of machining D2 tool steel in order to understand if Loewen and Shaw's method [5-13] can be applied to calculating shear plane and tool face temperatures by comparing with current finite element models that were constructed using a commercial software package. The following analysis allows one to understand if the primary stages of chip formation when machining laser hardened D2 tool

steel contribute to the applicability of using Loewen and Shaw's methods to calculate various machining variables.

8.2 Computational Understanding of Various Machining Conditions

8.2.1 Properties of D2 Tool Steel

Table 8.1 shows the chemical composition of D2 tool steel. The steel has a high content of chromium so that chromium carbides are generated after a significant amount of heat treatment. Table 8.2 shows the mechanical properties of D2.

Carbon	1.4-1.6%
Chromium	11-13%
Iron	81.6-86.9%
Manganese	0-0.6%
Molybdenum	0.7-1.2%
Nickel	0-0.3%
Silicon	0-0.6%
Vanadium	0-1.1%

Table 8.1. Chemical Composition of D2 Tool Steel

Bulk Modulus	23.64-24.8 x 10^6 psi
Compressive Strength	270.4-332 ksi
Elongation	1.37-1.52 %
Elastic Limit	270.4-332 ksi
Modulus of Rupture	270.4-332 ksi
Poisson's Ratio	0.285-0.295
Shape Factor	11
Shear Modulus	11.46-12.18 10^6 psi
Tensile Strength	304.6-362.9 ksi
Young's Modulus	29.73-31.18 10^6 psi

Table 8.2. Mechanical Properties of D2 Tool Steel

Table 8.3 provides the essential thermal properties that are necessary to provide data for finite element analysis.

Maximum Service Temperature	1042-1101 °F
Melting Point	2606-2696 °F
Minimum Service Temperature	-99.4 to -63.4 °F
Specific Heat	0.1137-0.1146 BTU/lb.F
Thermal Conductivity	16.93-18.34 BTU.ft/h.ft^2.F
Thermal Expansion	5.772-6.667 µstrain/°F

Table 8.3. Thermal Properties of D2 Tool Steel

The following figures are for thermal properties of D2 tool steel based on data from Crucible Specialty Metals. The following data shows the thermal conductivity (Table 8.4, Figure 8.1), specific heat (Table 8.5, Figure 8.2), and thermal diffusivity properties (Table 8.6, Figure 8.3) for D2 tool steel.

Temp (^{o}C)	Thermal Conductivity (W/cm.K)
22	0.19454
100	0.209
200	0.22453
300	0.24092
400	0.25133
500	0.25592
550	0.25736

Table 8.4. Thermal Conductivity for D2 tool steel

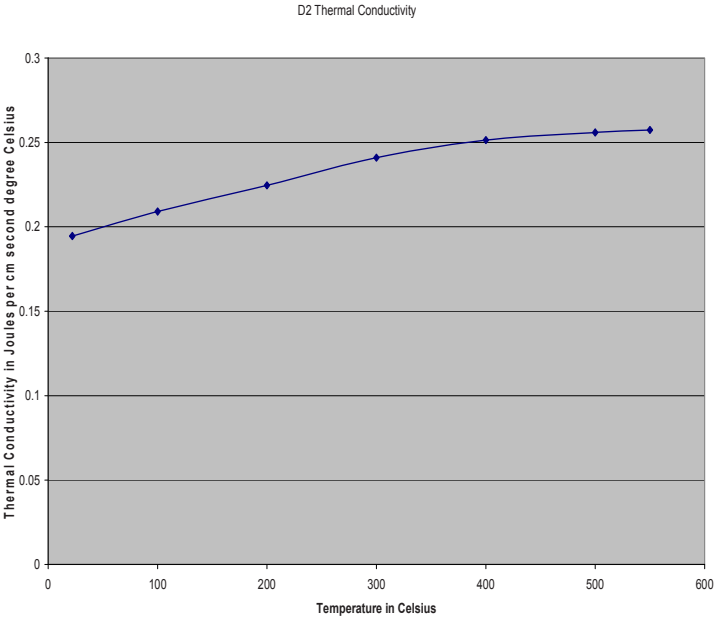

Figure 8.1. Thermal Conductivity for D2 Tool Steel

Temp (^{o}C)	Volume Specific Heat (J/cm^{3}.C)
22	3.556512
100	3.793104
200	4.060224
300	4.3884
400	4.724208
500	5.067648
550	5.220288

Table 8.5. Volume Specific Heat for D2 Tool Steel

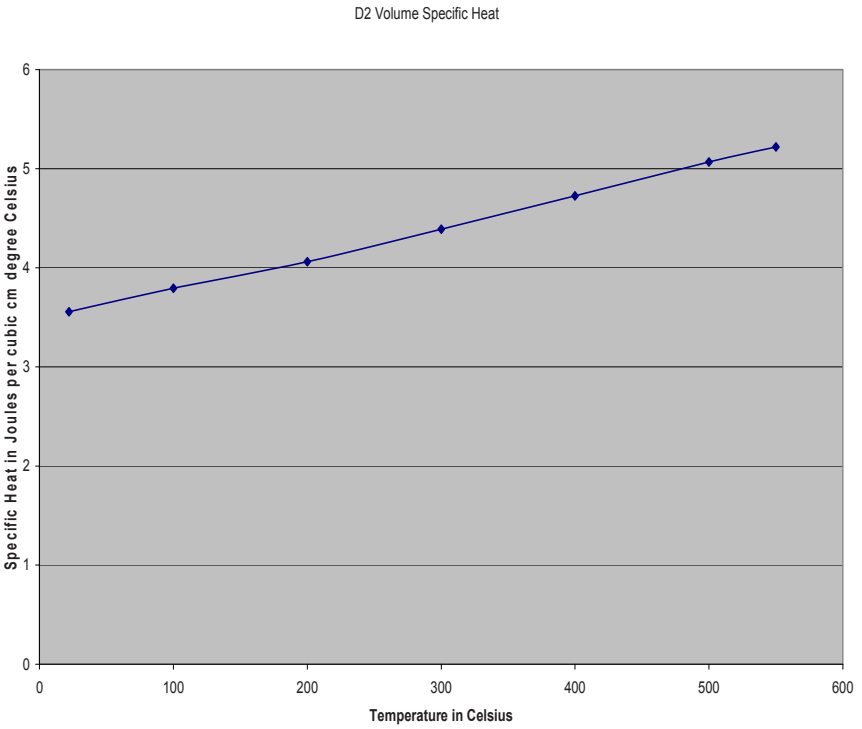

Figure 8.2. Volume Specific Heat for D2 Tool Steel

Temp (^{o}C)	Thermal Diffusivity (cm^2/s)
22	0.0547
100	0.0551
200	0.0553
300	0.0549
400	0.0532
500	0.0505
550	0.0493

Table 8.6. Thermal Diffusivity for D2 Tool Steel

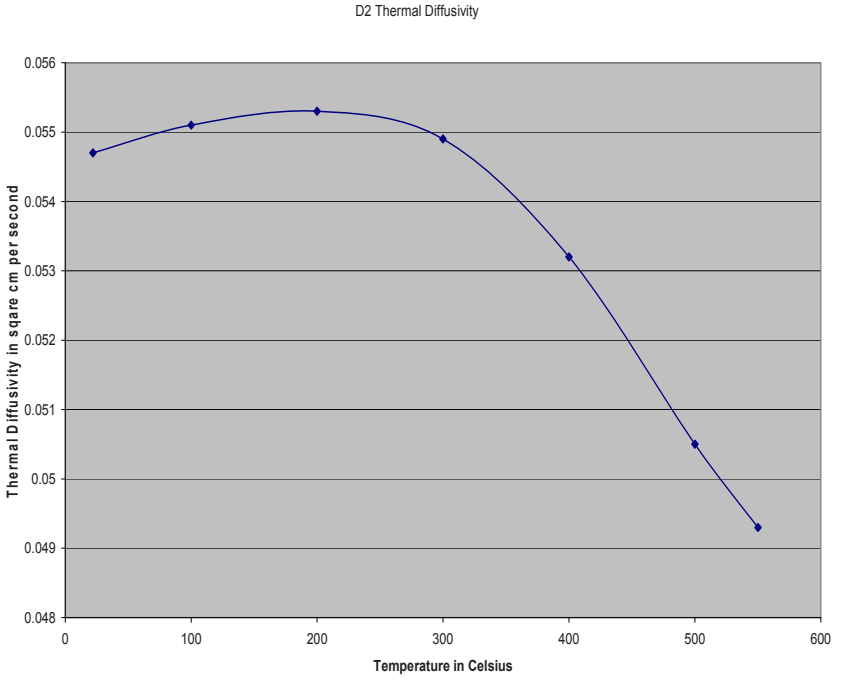

Figure 8.3. Thermal Diffusivity for D2 Tool Steel

8.2.2 Loewen and Shaw's Method Applied to Calculating Temperature

There are several analytical approaches used to determine the cutting temperature, which include: Boothroyd [6]; Wright and Trent [13]; and Loewen and Shaw [9]. These methods are suitable for the analysis of soft materials, in particular low carbon steels containing a high percentage of ferrite. Of these methods, Stephenson [12] found that the most accurate model used was Loewen and Shaw's because it accounted for the change in thermal properties of the tool and workpiece with increasing temperature. Therefore, Loewen and Shaw's approach is used as demonstrated by Shaw [11] in order to explain the use of such formulae for the experimental work. However, since there is no dynamometer currently available to measure cutting forces, the horizontal force can be closely

approximated by the formula proposed by Isakov [8]. Once this quantity has been determined, Loewen and Shaw's approach can be used. Isakov's formula to find the tangential force or the force, in the horizontal orientation, F_{HO}, of a milling cutter is given by,

$$F_{HO} = \sigma_{UTS} A n_c C_m C_w \tag{8.1}$$

Where, σ_{UTS}, is the ultimate tensile strength (UTS) of the workpiece (for D2 tool steel, $\sigma = 2.344 \times 10^9$ MPa), A, is the uncut chip cross sectional area, n_c, is the number of teeth engaged in the workpiece, C_m, is a machinability adjustment factor, and C_w, is a tool wear adjustment factor.

The feed per tooth, f_t, must be calculated, to do this the following quantities must be known, the feed, f = 0.0508 m/min = 0.000847m/s, the spindle speed, N, = 300rpm, or in radians the angular velocity, $\omega = 31.42$ rad/s, the number of cutting teeth, n = 4. The feed per tooth can now be calculated from the following equation,

$$f_t = \frac{f}{Nn} \tag{8.2}$$

$f_t = 4.23 \times 10^{-5}$m

The rake angle is measured at $\alpha = 9°$, and the feed per tooth correction factor, f_{tc}, is given by,

$$f_{tc} = \frac{f_t}{\cos\alpha} \tag{8.3}$$

$f_{tc} = 4.286 \times 10^{-5}$m/min

The method being followed is for orthogonal cutting, the case being considered is milling. Therefore, the orthogonal width of cut is replaced by the milling axial depth of cut, b, which is 1.27×10^{-3}m and the uncut chip cross sectional, A, is given by,

$$A = f_{tc}b \tag{8.4}$$

$A = 5.44\times10^{-8}m^2$

The tool diameter, $d = 1.27\times10^{-2}m$, and the width of cut, W, is $0.635\times10^{-2}m$. The number of teeth engaged in the cut, n_c, can now be calculated by,

$$n_c = \frac{n(90 + \sin^{-1}((2W - d)/d)))}{360} \tag{8.5}$$

$n_c = 1$

The machinability adjustment factor taken from Isakov's [8] textbook and has a value of unity, and the tool wear adjustment factor is taken as 1.1, also from Isakov [8]. Therefore, F_{HO} can be calculated.

$$F_{HO} = \sigma A n_c C_m C_w \tag{8.6}$$

$F_{HO} = 140.35N$

The chip thickness, t_c, was measured to be $1\times10^{-4}m$, thus, the chip thickness ratio, r, can be calculated from,

$$r = \frac{t_o}{t_c} \tag{8.7}$$

$r = 0.423$

This allows the shear plane angle, Φ, to be calculated from,

$$\Phi = \tan^{1}\left(\frac{r\text{Cos}\alpha}{1 - r\text{Sin}\alpha}\right) \tag{8.8}$$

$\Phi = 24.12°$

Based on the work of Bowden and Tabor [7] the coefficient of friction between tungsten carbide and a low carbon steel during dry rubbing conditions is, $\mu = 0.78$. However, during our simulations the coefficient of friction was varied between 0.1 and 1 in increments of 0.1. For the purpose of the sample calculation, the coefficient of friction is set to 0.1. This allows the calculation of the force in the vertical orientation F_{VO}, which is given by,

$$F_{VO} = \frac{\mu F_{HO} - F_{HO} Tan\alpha}{1 + \mu Tan\alpha} \tag{8.9}$$

$F_{VO} = 8.067N$

The force along the tool face, F_{AT}, is given by,

$$F_{AT} = F_{HO}Sin\alpha + F_{VO}Cos\alpha \tag{8.10}$$

$F_{AT} = 13.99N$

The force normal to the tool face, $F_{NT,}$ can be calculated by,

$$F_{NT} = F_{HO}Cos\alpha - F_{VO}Sin\alpha \tag{8.11}$$

$F_{NT} = 139.88N$

The force along the shear plane, $F_{AS,}$ is given by,

$$F_{AS} = F_{HO}Cos\Phi - F_{VO}Sin\Phi \tag{8.12}$$

$F_{AS} = 131.39N$

The force normal to the shear plane, $F_{NS,}$ is given by,

$$F_{NS} = F_{VO}Cos\Phi + F_{HO}Sin\Phi \tag{8.13}$$

$F_{NS} = 49.995N$

Since the milling process is being approximated by an orthogonal cutting operation, the milling axial depth of cut is equal to the orthogonal chip width, b. The maximum uncut chip thickness is equal to the feed per tooth t_o. The area of the shear plane A_s is given by,

$$A_s = \frac{bt_O}{Sin\Phi} \tag{8.14}$$

$A_s = 1.31\times10^{-7}m^2$

The shear stress, τ, is given by,

$$\tau = \frac{F_{AS}}{A_S} \tag{8.15}$$

$\tau = 998.72\times10^{6}N/m^2$

Similarly the normal stress, σ, is given by,

$$\sigma = \frac{F_{NS}}{A_S} \tag{8.16}$$

$\sigma = 380.04\times10^{6}N/m^2$

The shear strain, γ, is given by,

$$\gamma = \frac{Cos\alpha}{Sin\Phi Cos(\Phi - \alpha)} \tag{8.17}$$

$\gamma = 2.5$

The cutting velocity, V, at the tool tip is given by,

$$V = r_t\omega \tag{8.18}$$

Where, r_t, is the tool radius and the units of, ω, are radians/s.

$V = 0.2m/s$

The chip velocity, V_C, is given by,

$$V_C = \frac{V\mathrm{Sin}\Phi}{\mathrm{Cos}(\Phi - \alpha)} \tag{8.19}$$

$V_C = 0.084m/s$

Similarly the shear velocity, V_S, is given by,

$$V_s = \frac{V\mathrm{Cos}\alpha}{\mathrm{Cos}(\Phi - \alpha)} \tag{8.20}$$

$V_s = 0.204m/s$

In order to determine the strain rate, $\dot{\gamma}$, the shear plane spacing, Δy, must be determined from chip images, in this case $\Delta y = 10\mu m$.

$$\dot{\gamma} = \frac{V\mathrm{Cos}\alpha}{\Delta y\mathrm{Cos}(\Phi - \alpha)} \tag{8.21}$$

$\dot{\gamma} = 20.4\times10^3 s^{-1}$

The theoretical scallop height, h, which reflects the surface roughness of the machined surface in an end milling operation is given by,

$$h = \frac{f_t^{\,2}}{4d} \tag{8.22}$$

$h = 3.53x10^{-8}m$

The energy per unit time, U, is given by,

$$U = F_{HO}V \tag{8.23}$$

$U = 27.99Nms^{-1}$, or $27.99Js^{-1}$

The energy per unit volume, u, is given by,

$$u = \frac{F_{HO}}{bt_0} \tag{8.24}$$

$u = 2610.54\times10^{6}Nm/m^3$ or $2610.54\times10^{6}J/m^3$

The shear energy per unit volume, u_s, is given by,

$$u_s = \tau\gamma \tag{8.25}$$

$u_s = 2500.4\times10^{6}Nm/m^3$ or $2500.4\times10^{6}J/m^3$

The friction energy per unit volume, u_f, is given by,

$$u_f = \frac{F_{AT}r}{bt_0} \tag{8.26}$$

$u_f = 110.14\times10^{6}Nm/m^3$ or $110.14\times10^{6}J/m^3$

To determine the shear plane temperature, the method of Loewen and Shaw taken from Shaw [11] is used. The process involves several iterations, the final iteration is shown. The initial step is to estimate the shear plane temperature, $\theta_s = 265.83°C$, and the ambient temperature is $\theta_o = 25°C$, then calculate the mean of these two temperatures, θ_{av}.

$$\theta_{AV} = \frac{\theta_s + \theta_o}{2} \tag{8.27}$$

$\theta_{AV} = 145.41°C$

The thermal properties of the workpiece must be determined; in this case a low carbon steel. Shaw [11] displays these properties. At 145.41°C, the thermal diffusivity, $K_1 = 0.552x10^{-5}m^2/s$, and the volumetric specific heat is, $\rho_1 C_1 = 3.85\times10^6 J/m^3°C$. Calculate the quantity R_1 from,

$$R_1 = \frac{1}{1 + 1.328\left(\frac{K_1\gamma}{Vt_0}\right)^{1/2}} \tag{8.28}$$

$R_1 = 0.37$

Calculate the quantity θs - θo from,

$$\theta s - \theta o = \frac{R_1 u_s}{J\rho_1 C_1} \tag{8.29}$$

Where, J is the mechanical equivalent of heat, the value used by Shaw [11] of 9340 lbin/BTUs^2 for low carbon steel, or 0.998Nm/Js^2, will be used here,

θs - θo = 240.83°C

Therefore,

θs = 265.83°C

Shaw states the process is repeated until the initial estimate produces a shear plane temperature within 3.88°C of the initial

estimate. Therefore, in this case the accepted shear plane temperature is 265.83°C.

To calculate the tool face temperature, estimate the tool face temperature as $\theta_T = 275°C$. Then determine the thermal properties of the workpiece at this temperature from the figures in section 8.2.1. At 275°C, $K_1 = 1.5x10^{-5}m^2/s$, $\rho_1 C_1 = 3.9\times10^6 J/m^3°C$. The chip contact length, a, is approximated as half the uncut chip length l, which is given by,

$$l = \left(dt_o\right)^{0.5} + \frac{f}{2nN} \tag{8.30}$$

$l = 7.54x10^{-4}m$

Thus,

$$a = l/2 \tag{8.31}$$

$a = 3.77\times10^{-4}m$

$$\frac{m}{l} = \frac{b}{2a} \tag{8.32}$$

$m/l = 8.42$

Using Shaw's textbook [11] to find $\overline{A} = 2.1$, determine the thermal conductivity of the workpiece, k_S, at the previously calculated shear plane temperature of 265.83°C, in this case, $k_T = 6.12\times10^{-3}J/m^2s°C$. This allows C` to be calculated from,

$$C' = \frac{u_f V t_0 \overline{A}}{J k_T} \tag{8.33}$$

$C` = 8.28\times10^5$

Calculate B' from,

$$B' = \left(\frac{0.754 u_f}{J \rho_S C_S} \right) \left(\frac{V t_o^{\,2}}{a r K_S} \right)^{1/2} \tag{8.34}$$

Where the subscript S denotes the thermal properties determined at the previously calculated shear plane temperature, $\rho_s c_s = 3.9 \times 10^6 J/m^3 °C$ and $K_s = 1.49 \times 10^{-5} m^2/s$.

B` = 18.87

Calculate the quantity R_2 from,

$$R_2 = \frac{C' - \theta s + \theta o}{C' + B'} \tag{8.35}$$

$R_2 = 0.99°C$

Calculate the temperature rise in the chip surface due to friction, $\Delta\theta_F$, from,

$$\Delta\theta_F = R_2 B' \tag{8.36}$$

$\Delta\theta_F = 8.71°C$

Finally the tool face temperature, θ_T, can be calculated from,

$$\theta_T = \theta_S + \Delta\theta_F \tag{8.37}$$

$\theta_T = 274.55°C$.

Shaw states that the procedure for calculating the tool face temperature should be repeated until the initial estimate and the final calculated temperature are in agreement. In this case the difference of 0.45°C cannot be doubted since the material properties are determined from interpretation of line diagrams. Therefore, 275°C is

the accepted tool face temperature. The data shown in Tables 8.7 and 8.8 are calculated using the mathematical analysis of Loewen and Shaw to determine shear plane and tool face temperatures.

CoF	Shear Plane Approximation (°C)	Shear Plane Calculated (°C)	FEA Shear PlaneTemp Range (°C)	Tool Face Approximation (°C)	Tool Face Calculated (°C)	FEA Tool Face Temp Range (°C)
0.1	266	265.8	84-215	275	274.5	48-183
0.2	255	256.2	87-222	273	273.4	48-201
0.3	246	246.2	91-234	272	271.6	48-219
0.4	237	236.5	93-237	270	269.8	48-221
0.5	227	227.6	96-249	268	268.6	48-219
0.6	219	218.6	101-264	267	267.7	48-216
0.7	210	209.9	104-272	266	266.0	48-221
0.78	203	203.1	109-279	265	264.8	48-228
0.9	193	193.0	114-284	263	263.9	50-233
1	185	185.5	119-290	263	263.1	48-241

Table 8.7. Shear plane and tool face temperatures and approximations

The cells that are highlighted red are an approximation based on the data collected for the lower coefficients of friction. An observation during the experiments was noted when cutting D2 tool steel; higher coefficients of friction lower the shear plane and tool face temperatures. The increase in the coefficient of friction appears to decrease the shear plane temperature but increases the tool face temperature.

	FEA Shear Plane Temp		FEA Tool Face Range	
	Low	High	Low	High
0.1	84	215	48	183
0.2	87	222	48	201
0.3	91	234	48	219
0.4	93	237	48	221
0.5	96	249	48	219
0.6	101	264	48	216
0.7	104	272	48	221
0.8	109	279	48	228
0.9	114	284	48	233
1	119	290	48	241

Table 8.8. Computational shear plane temperatures and computational tool face temperatures. The red cells are approximations

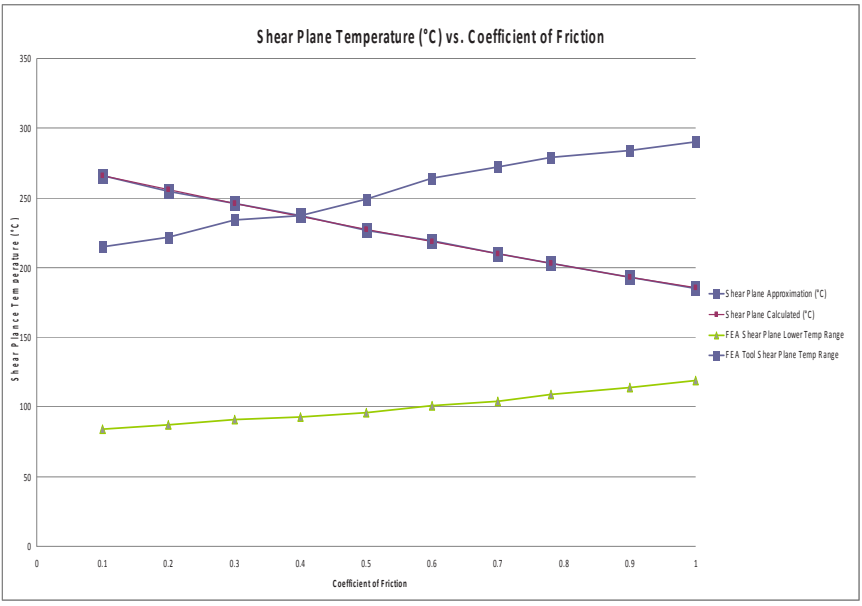

Figure 8.4. Shear plane temperature versus coefficient of friction

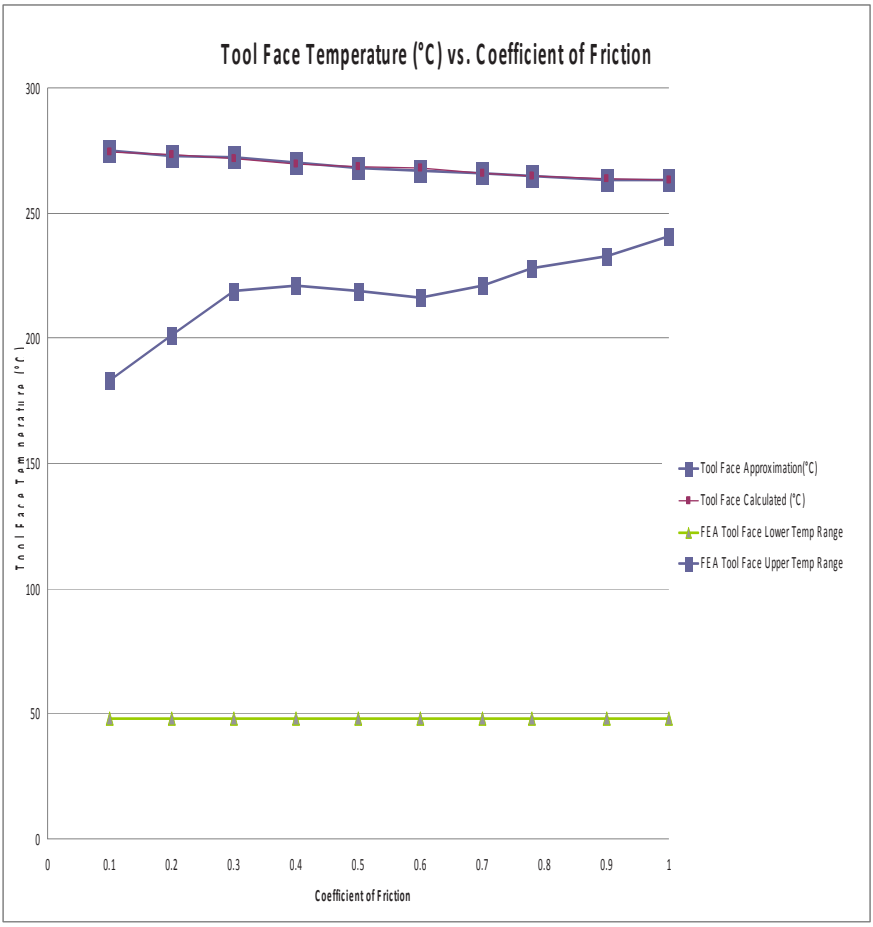

Figure 8.5. Tool face temperature versus coefficient of friction

As shown in Figure 8.4, the calculated and approximated shear plane temperatures are in agreement. The calculated and approximate temperatures are between the lower and upper temperature ranges for the computational analysis. The approximate and calculated tool face temperatures are in complete agreement (Figure 8.5). These temperatures are in between the upper and lower bounds of the tool face temperature range. Table 8.9 shows the effect of changing the coefficient of friction on the machining parameters.

Coefficient of Friction - μ_f	Force along Shear Plane - F_s (N)	Friction Energy/Unit Volume (Nm/m^3)	Force Normal to Shear - N_s (N)	Force in Vertical Orientation - F_{vo} (N)	Deformation Power - U_s	Force along Tool Face - F_c (N)	Shear Stress - τ (Pa)	Force Normal to Tool Face - N_c (N)	Normal Stress - σ (Pa)	Shear Energy/Volume - u_s (Nm/m^3)
0.1	131.4	110145880.8	50.0	-8.1	26.8	14.0	998762903.7	139.9	380037381.7	2500394199.6
0.2	125.8	216909812.4	62.5	5.7	25.7	27.5	956116886.3	137.7	475277259.4	2393630267.9
0.3	120.3	320445200.3	74.7	19.0	24.6	40.7	914760485.6	135.7	567637080.9	2290094880.0
0.4	115.1	420896310.0	86.5	31.9	23.5	53.5	874636075.6	133.6	657245539.9	2189643770.4
0.5	109.9	518398937.9	97.9	44.4	22.4	65.8	835689413.6	131.7	744223775.1	2092141142.4
0.6	105.0	613081024.0	109.0	56.6	21.4	77.9	797869395.0	129.8	828685916.5	1997459056.4
0.7	100.1	705063211.5	119.8	68.4	20.4	89.5	761127829.7	127.9	910739585.3	1905476868.8
0.78	96.4	776781764.1	128.2	77.7	19.7	98.7	732480414.9	126.5	974716867.4	1833758316.3
0.9	90.9	881377016.4	140.5	91.1	18.5	111.9	690700659.5	124.4	106802152.1	1729163063.9
1.0	86.4	965917844.3	150.4	102.0	17.6	122.7	656931487.1	122.7	114343678.5	1644622236.1

Table 8.9. Machining parameters as a function of the change in the coefficient of friction

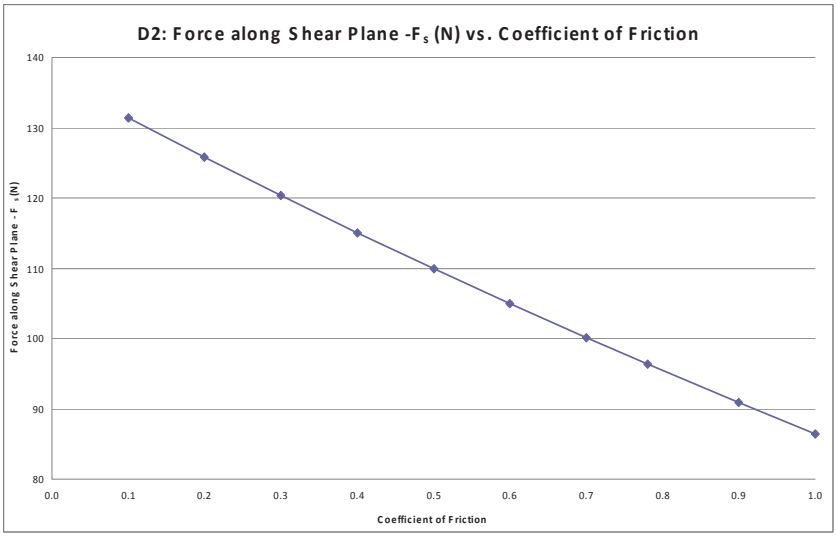

Figure 8.6. Force along Shear Plane versus coefficient of friction

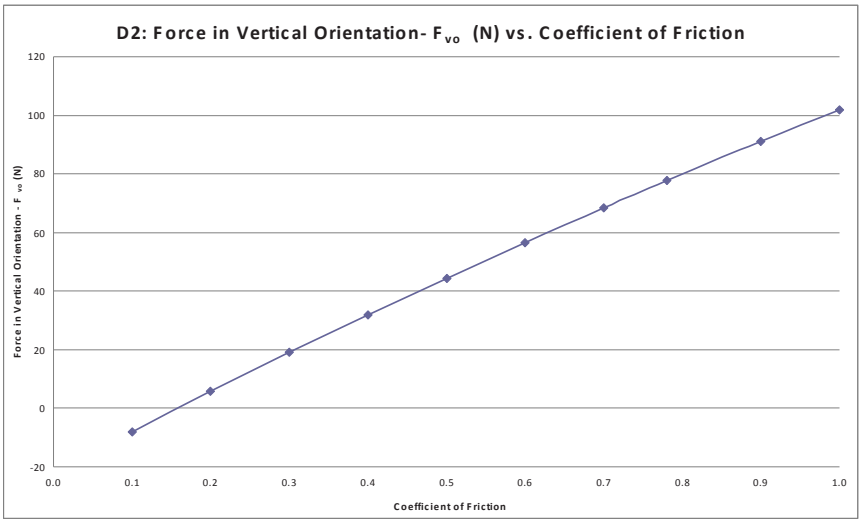

Figure 8.7. Force in Vertical Orientation versus coefficient of friction

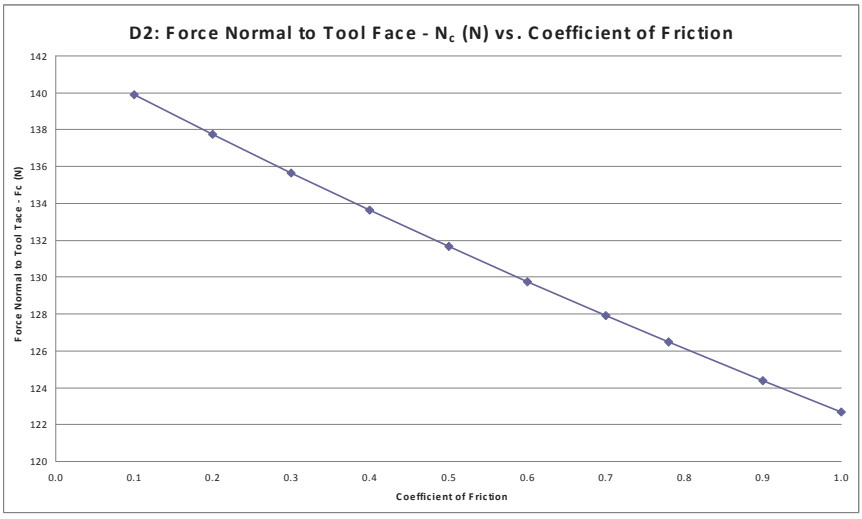

Figure 8.8. Force Normal to Tool Face versus coefficient of friction

Figure 8.9. Shear Stress versus coefficient of friction

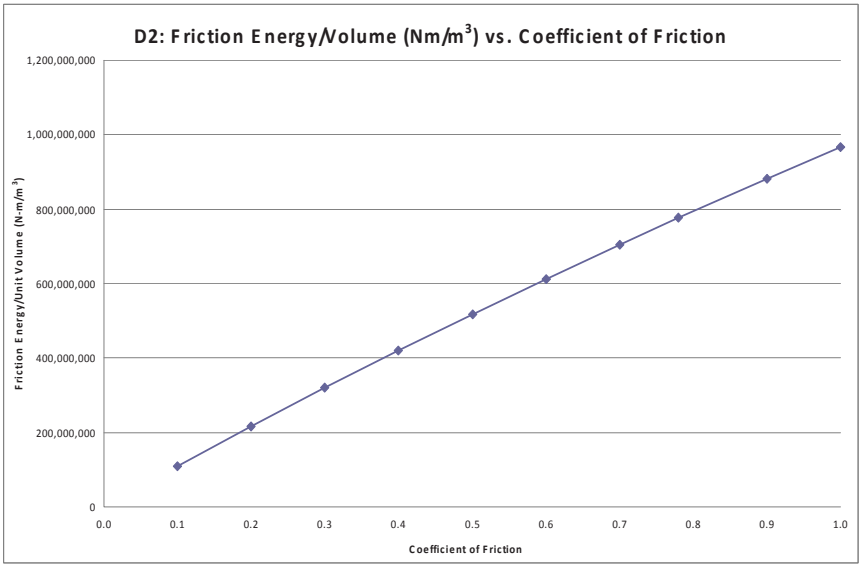

Figure 8.10. Friction Energy/Volume versus coefficient of friction

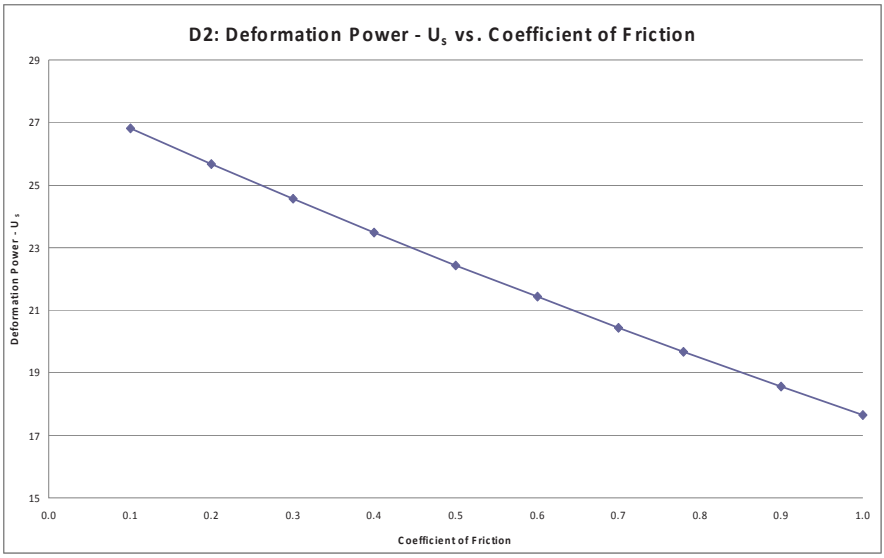

Figure 8.11. Deformation Power versus coefficient of friction

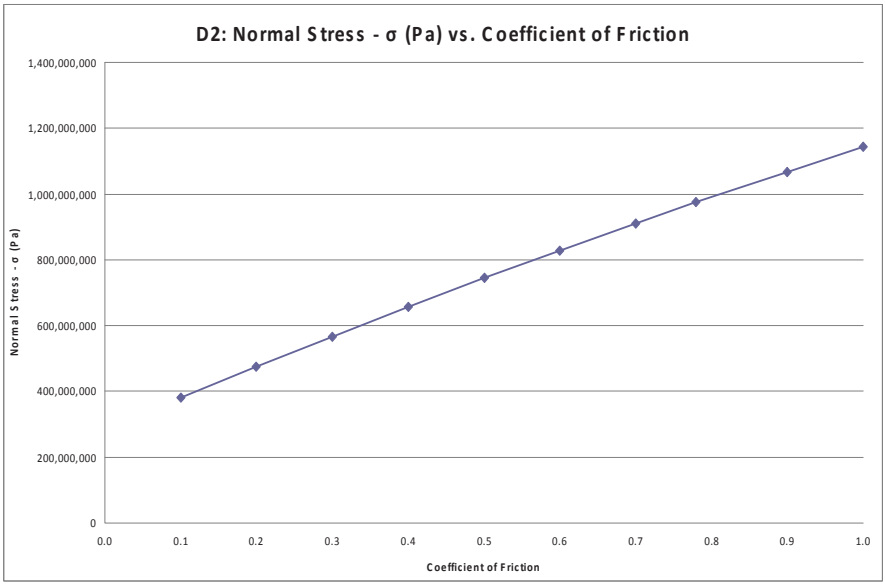

Figure 8.12. Normal Stress versus coefficient of friction

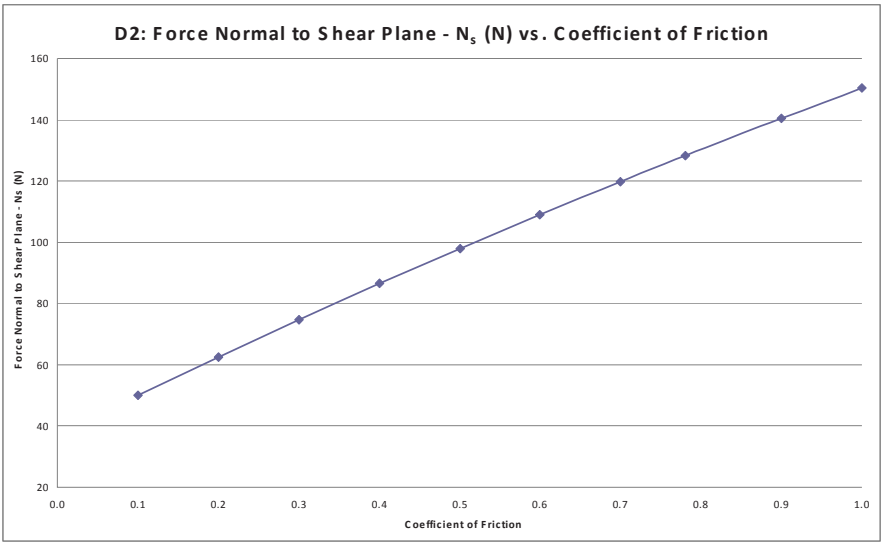

Figure 8.13. Force Normal to Shear Plane versus coefficient of friction

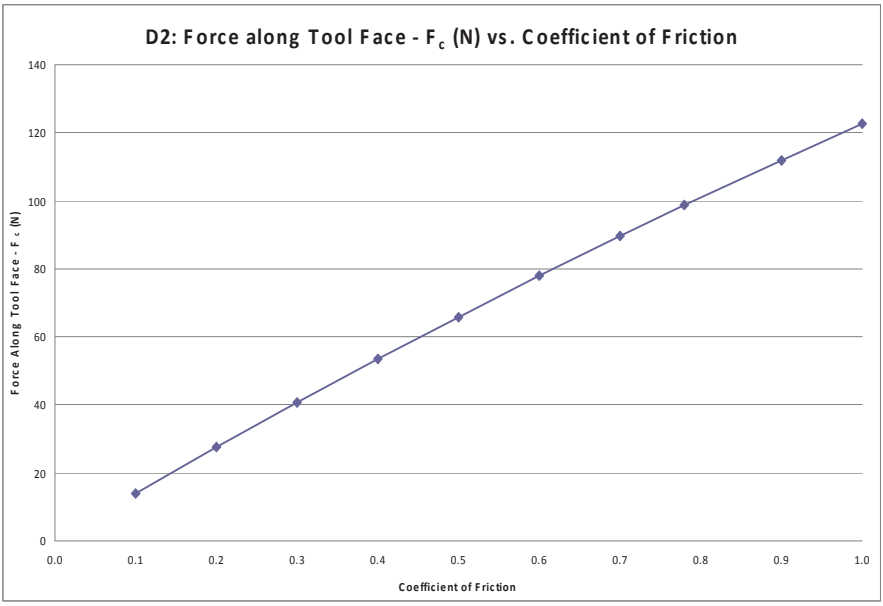

Figure 8.14. Force along tool face versus coefficient of friction

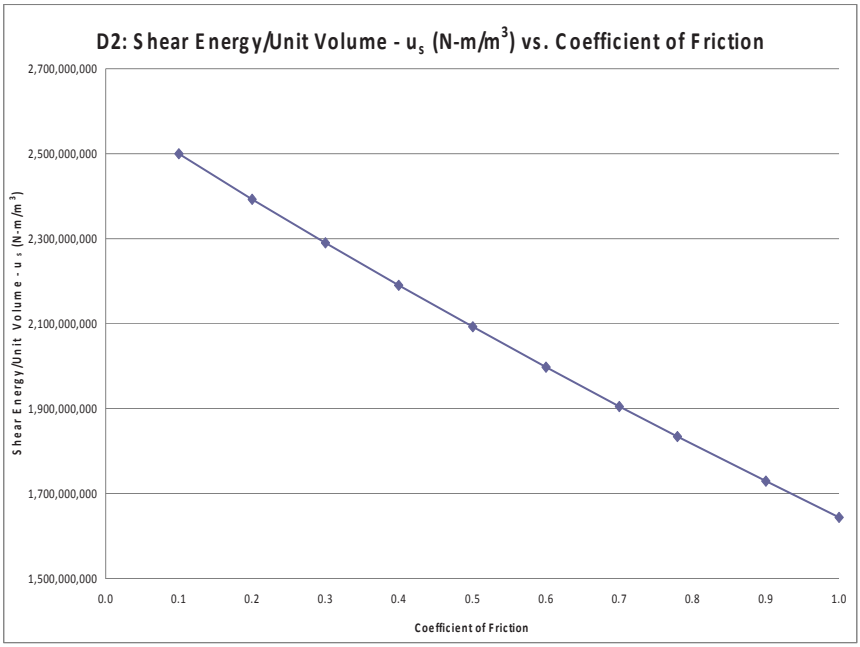

Figure 8.15. Shear Energy/Unit Volume versus coefficient of friction

Figures 8.6 to 8.15 show various machining parameters such as forces, power, energy, and stress versus coefficient of friction. Figure 8.6 shows the tool force along the shear plane decreases with an increase in coefficient of friction. Figure 8.7 displays an opposite pattern with an increase of force in the vertical orientation with an increase in coefficient of friction. The force normal to the face and the shear stress decrease when compared to the coefficient of friction (Figures 8.8 and 8.9). Conversely, in Figure 8.10, the friction energy/volume increases with an increase in coefficient of friction. Deformation power decreases in Figure 8.11 while the normal stress increases in Figure 8.12. The force normal to tool face increases in Figure 8.13. The force along the tool face is featured in Figure 8.14 and shows the force increases with the coefficient of friction. Figure 8.15 shows shear energy/unit volume decreasing as coefficient of friction increases.

8.3 Finite Element Studies of Machining Conditions

A metal cutting finite element software was chosen to simulate the metal cutting operation. AdvantEdge^{TM} (provided by Third Wave Systems) was used in this study. The software uses adaptive meshing to improve the quality and precision of the output results and it also includes a wide range of workpiece material library. Third Wave AdvantEdge^{TM} allows improving and optimizing of machining processes. To model the thermal-visco plastic behavior of the materials, the software employs a constitutive equation, the Johnson-Cook law.

The experiments were conducted using the following conditions: Cutting speed used was 300 meters per minute; the feed rate was kept constant at 0.15 mm per revolution; depth of cut was constant at 1 mm; length of cut was constant at 6 mm; the length of the work piece was 5 mm; the experimental specimen was D2 tool steel; initial temperature was 20 degrees Celsius, and the coating thickness was constant at 4 microns' thickness. The coefficient of friction was varied between 0.1 and 1 in steps of 0.1 in order to compare results generated using Loewen and Shaw's method.

The finite element generated results (Figures 8.16 – 8.29) show the machining variable as a function of the coefficient of friction. Calculations for a coefficient of friction of 0.1 are shown in this paper. Figures 8.30 and 8.31 shows the comparison between calculated, approximate, and finite element generated shear plane and tool face temperatures. It is shown that as machining develops, shear plane and tool face temperatures increase rapidly after the initial frictional interactions between workpiece and cutting tool. Here, the method of Loewen and Shaw does not appear to be accurate. However, at the beginning of the cut, i.e., after the first 25mm is machined, it can be seen that Loewen and Shaw's method produces a very good estimate of shear plane and tool face temperature. This implies that their method is applicable at the first stages of intimate contact between chip and tool. Clearly, it is noted

that a secondary shear zone between chip and tool is not created at first contact. This implies that the secondary shear zone is somewhat responsible for frictional heating. This effect should be studied further using transparent sapphire tools in terms of understanding this effect on the generation of heat. The computational analysis leads us believe that intermittent contact caused by interrupted cuts and/or oscillating the cutting tool during machining is well described by Loewen and Shaw's method.

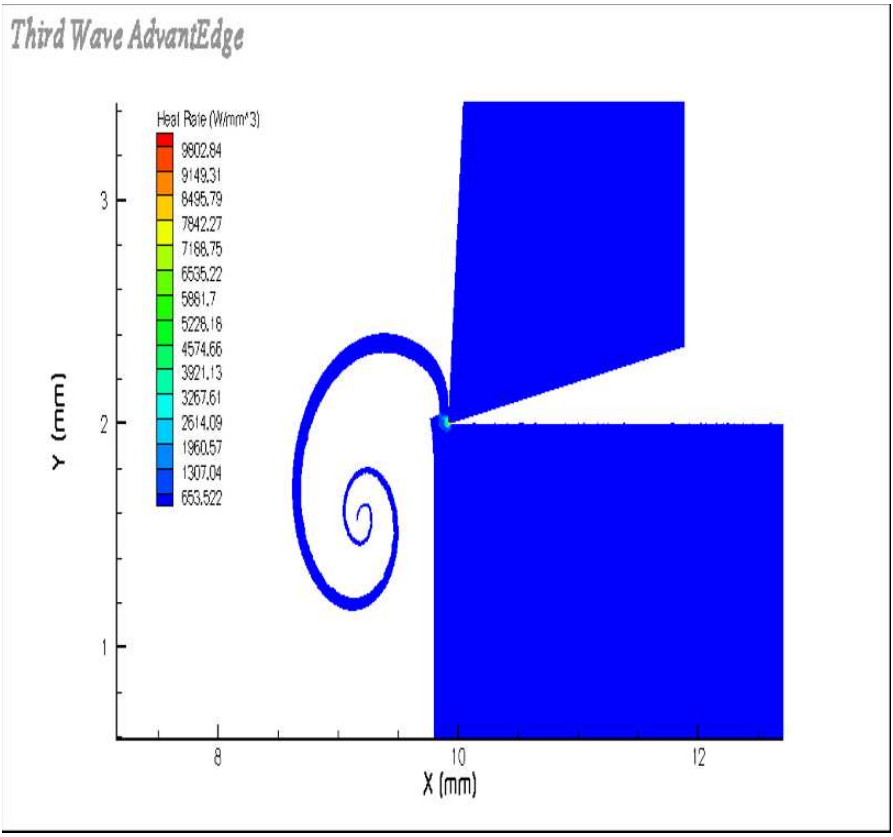

Figure 8.16. Rate of heat generated at the end of cut for laser-hardened D2 tool steel

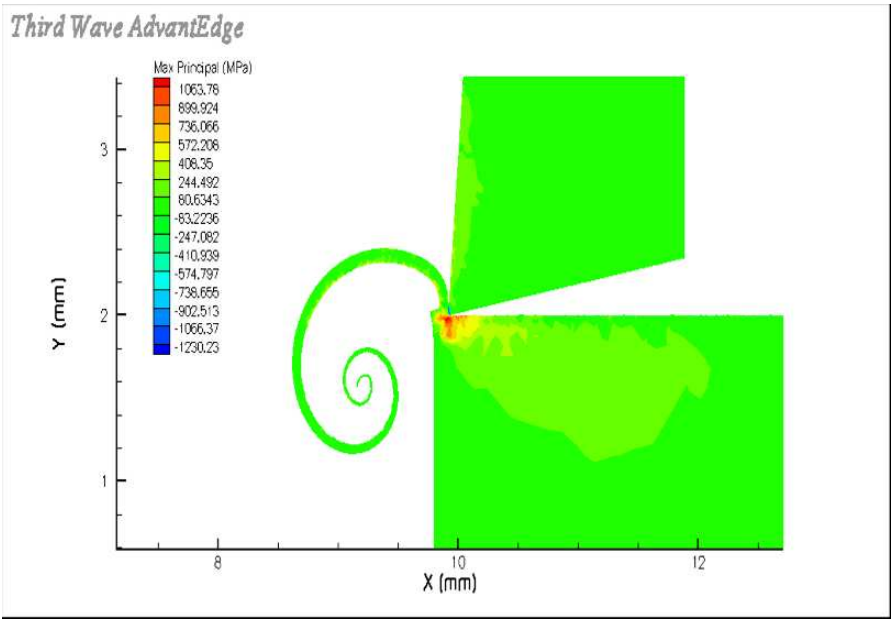

Figure 8.17. Maximum principal stress generated at the end of cut for laser-hardened D2 tool steel

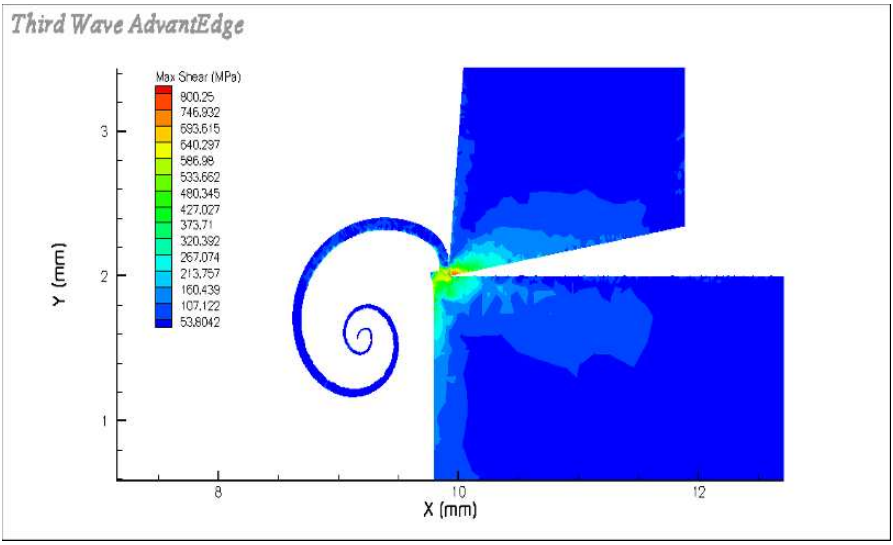

Figure 8.18. Maximum shear stress generated at the end of cut for laser-hardened D2 tool steel

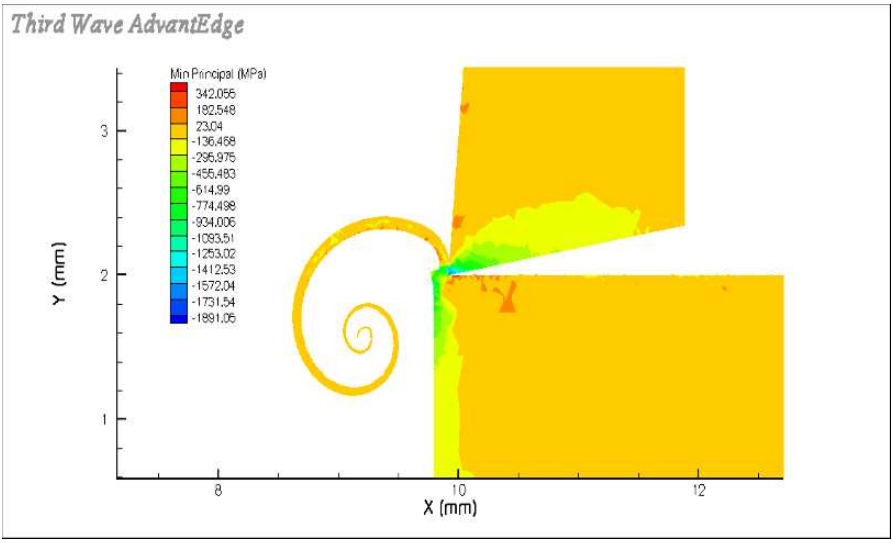

Figure 8.19. Minimum principal stress generated at the end of cut for laser-hardened D2 tool steel

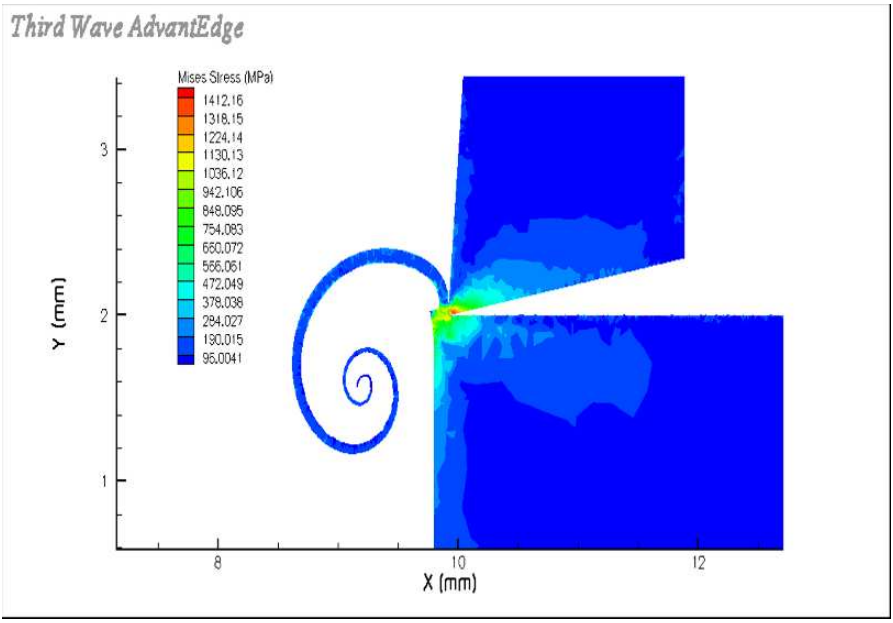

Figure 8.20. Von Mises stress generated at the end of cut for laser-hardened D2 tool steel

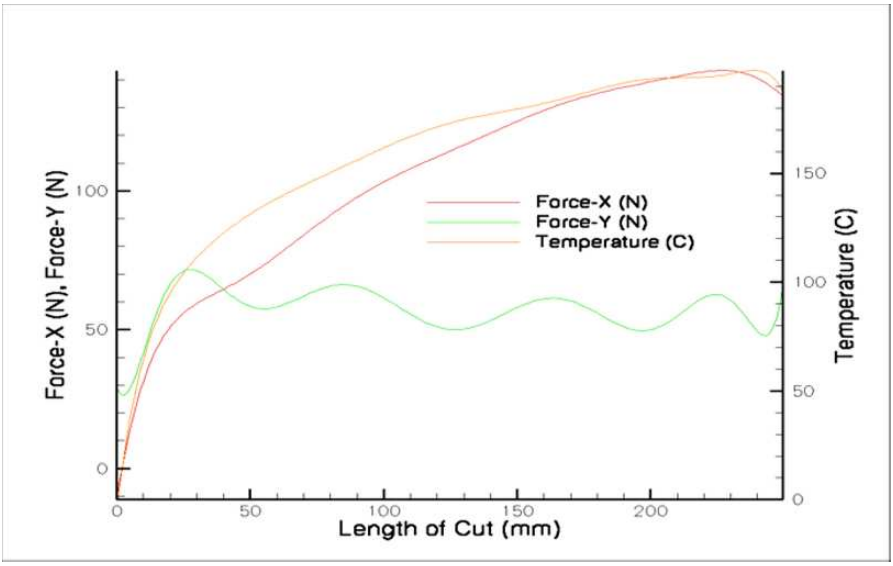

Figure 8.21. Cutting forces and temperatures generated over the complete length of cut for laser-hardened D2 tool steel

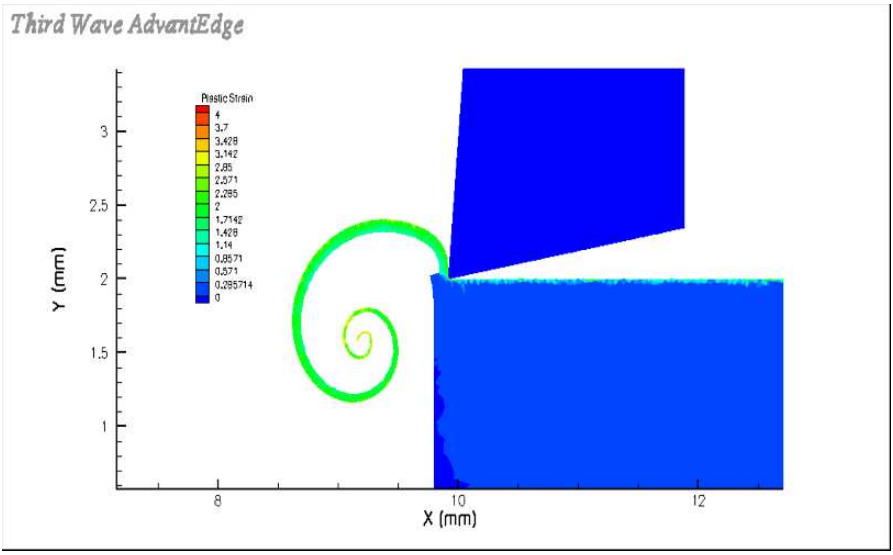

Figure 8.22. Plastic shear strain generated at the end of cut for laser-hardened D2 tool steel

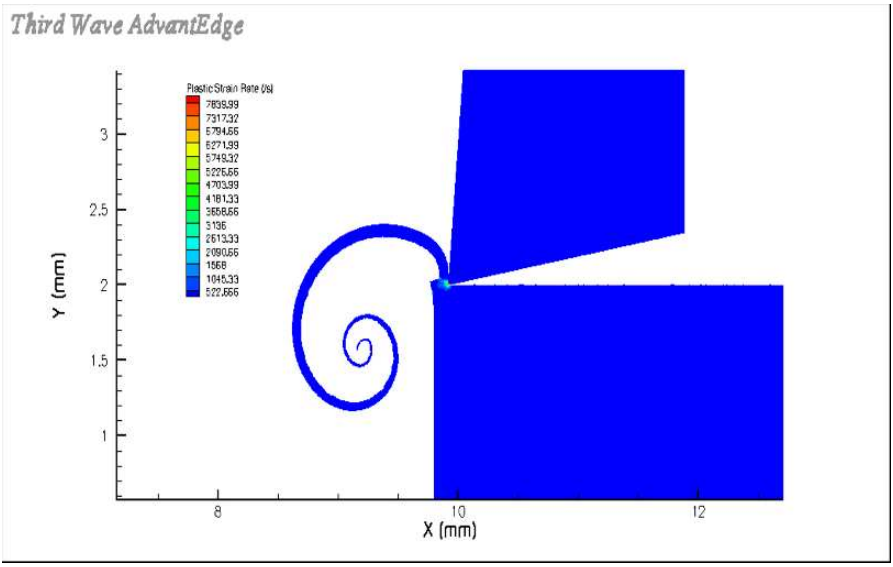

Figure 8.23. Plastic shear strain rate generated at the end of cut for laser-hardened D2 tool steel

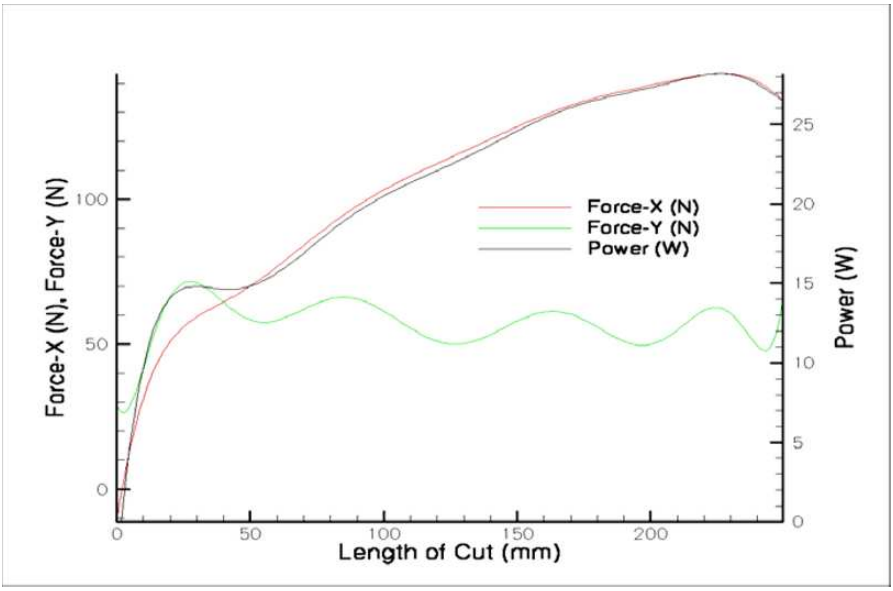

Figure 8.24. Cutting forces and machining power generated over the complete length of cut for laser-hardened D2 tool steel

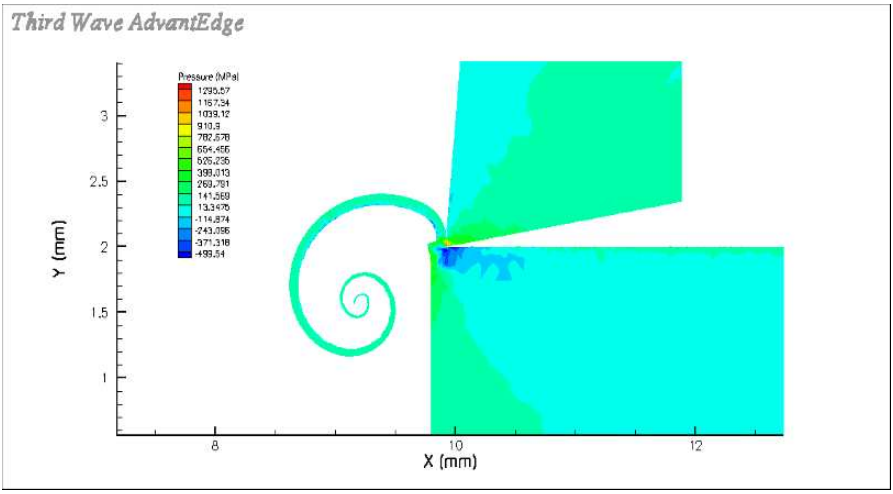

Figure 8.25. Machining pressure generated at the end of cut for laser-hardened D2 tool steel

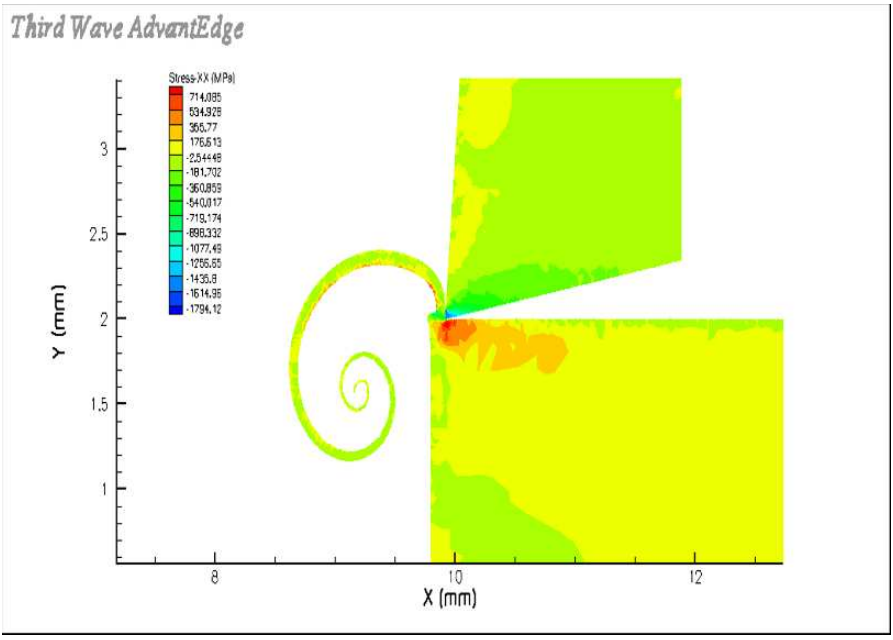

Figure 8.26. Stress σ_{xx} generated at the end of cut for laser-hardened D2 tool steel

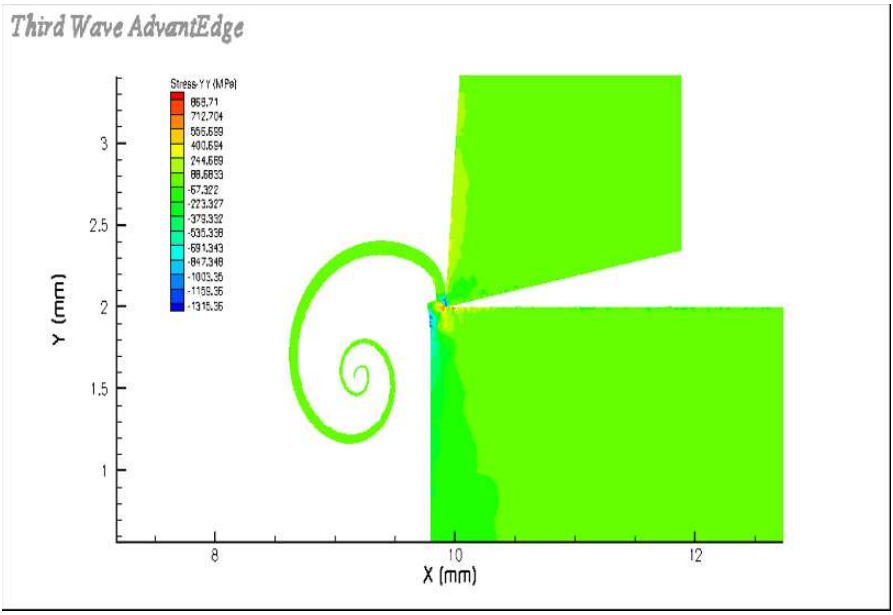

Figure 8.27. Stress σ_{yy} generated at the end of cut for laser-hardened D2 tool steel

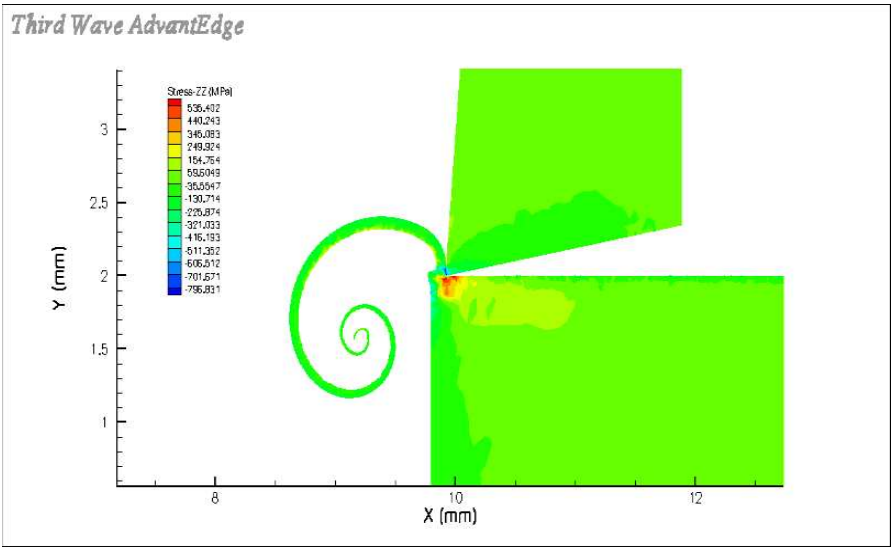

Figure 8.28. Stress σ_{zz} generated at the end of cut for laser-hardened D2 tool steel

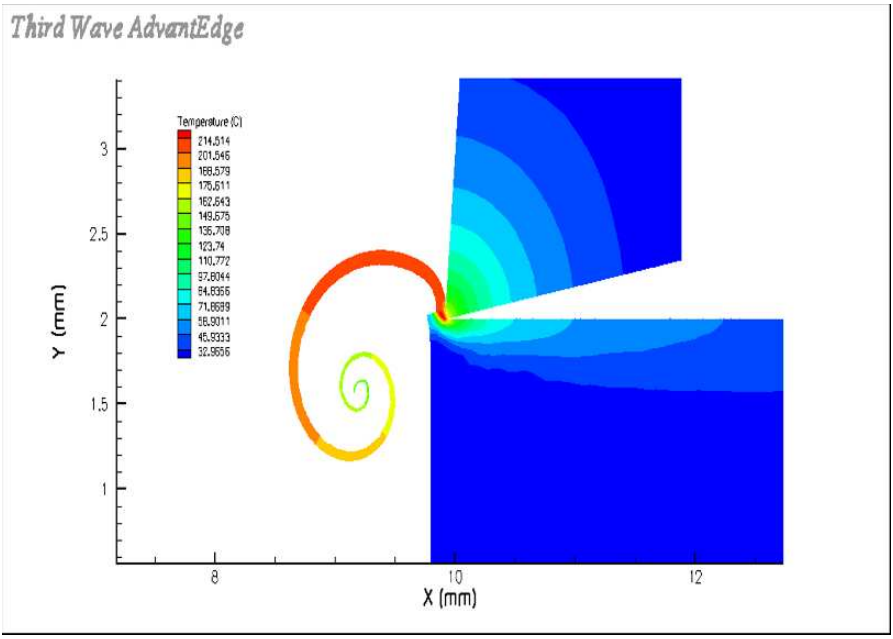

Figure 8.29. Temperature generated at the end of cut for laser-hardened D2 tool steel

8.4 Discussion

When one inspects the results of finite element modeling (Figures 8.16-8.29), it is observed that the change in the coefficient of friction tends to lower the shear plane temperature and increase the tool face temperature as it increases in value. Therefore, during dry machining operations it is necessary to lower the coefficient of friction between chip and tool by providing a thin film coating to the tool in order to lower the coefficient of friction. It is also observed that the tool face temperature and the shear plane temperature increases rapidly as a large chip is cut. The initial stages of chip formation are usually confined to the point at which the chip does not stick to the tool, i.e. perfect sliding takes place between chip and tool. This appears to generate lower temperatures on the tool face. However, once the chip sticks to the tool a secondary shear zone is established and quickly heats up the tool face.

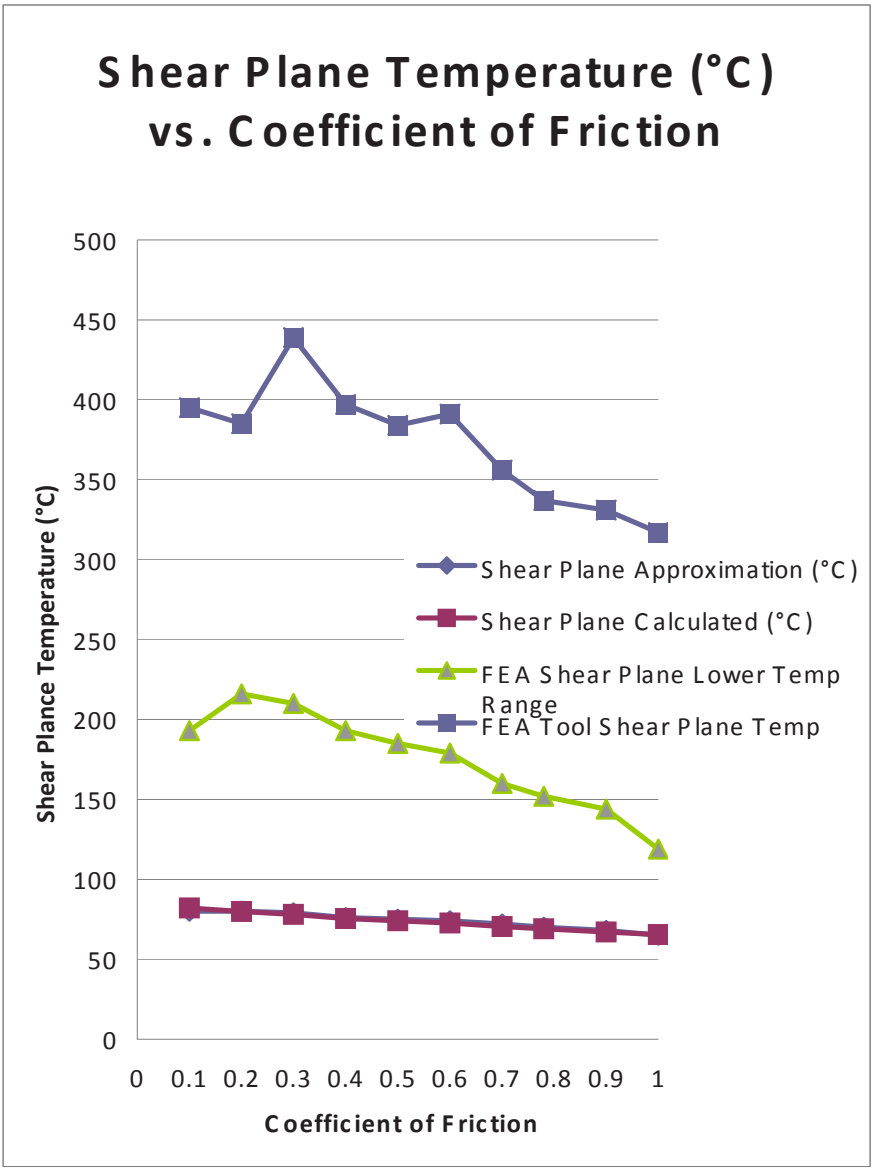

Figure 8.30. Comparison of approximate and calculated shear plane temperatures with finite element generated temperatures at the end of the machining pass (300 mm machined)

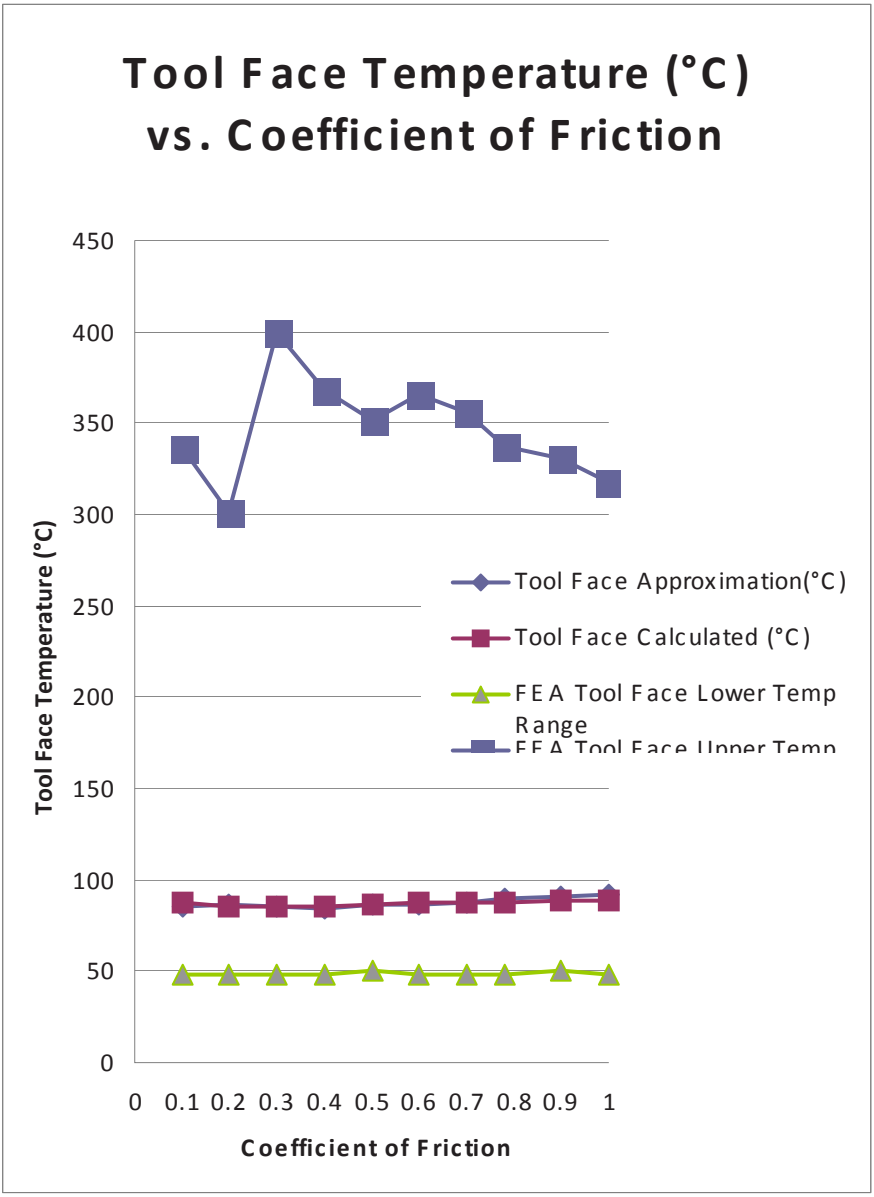

Figure 8.31. Comparison of approximate and calculated tool face temperatures with finite element generated temperatures at the end of the machining pass (300 mm machined)

It appears that the discrepancy between Loewen and Shaw's calculations and the finite element calculations occurs when adhesion of the chip to the tool takes place, i.e., after the first ten millimeters, or so, of chip formation depending on the coefficient of friction. The calculated peak tool temperature of the initial stage of chip formation is remarkably accurate to the finite element calculations, but not so when the secondary shear zone is established. Figures 8.30 and 8.31 show the difference in values very well at the end of the machining stroke when 300 millimeters of chip has been cut. It is clear that Loewen and Shaw's method provides very good accuracy at the primary stages of chip formation when machining D2 tool steel. This statement implies that statements concerned with using the early forms of machining mechanics are both valid and invalid depending on how one describes the machining conditions, i.e., primary stages of chip formation where the secondary shear is non-existent, or steady-state machining conditions when the secondary shear zone is fully established.

8.5 Conclusions

The calculations of the change in coefficient of friction have shown that increasing the coefficient of friction will lower the shear plane temperature. Loewen and Shaw's method of calculating shear plane and tool face temperature appears to be applicable at the first stages of intimate contact between chip and tool. Loewen and Shaw's method of calculating shear plane and tool face temperature does not appear to be applicable under steady-state conditions when the secondary shear zone is firmly established. This is confirmed by the finite element generated calculations.

Acknowledgements

The chapter contributors wish to thank Inderscience publishers for granting permissions to reproduce work presented in this chapter.

References

[1] Astakhov, V. P., Shvets, S. V., and Osman, M. O. M., (1997), 'Chip Structure Classification Based on Mechanisms and Their Formation, Journal of Materials Processing Technology, Vol. 71, pp. 247-257.
[2] Astakhov, V. P., (1999), Metal Cutting Mechanics, CRC Press, Florida, USA.
[3] Astakhov, V. P., (2004), 'The Assessment of Cutting Tool Wear', International Journal of Machine Tools and Manufacture, Vol. 44, pp. 637-647.
[4] Astakhov, V. P., (2005), 'On the Inadequacy of the Single Shear Plane Model of Chip Formation', International Journal of Mechanical Sciences, Vol. 47, pp. 1649-1672.
[5] Astakhov, V. P., (2006), Tribology of Metal Cutting, Elsevier, London, UK.
[6] Boothroyd, G., (1961), 'Photographic Technique for Determination of Metal Cutting Temperature.' British Journal of Applied Physics, Vol. 12 no. 5, pp. 238-242.
[7] Bowden, F.P. and Tabor, D., (1954), The Friction and Lubrication of Solids, Oxford, Clarendon Press.
[8] Isakov, E., (2004), Engineering Formulas for Metalcutting, New York: Industrial Press.
[9] Loewen, E.G. and Shaw, M.C. (1954) 'On the Analysis of Cutting Tool Temperatures.' Transactions of the American Society of Mechanical Engineers, Vol. 76, pp. 217-231
[10] Robinson, G. (2007), Wear of Nanostructured Coated Cutting Tools During Mixed Scale Machining, Ph. D. Dissertation, Purdue University.
[11] Shaw, M.C. (2005), Metal Cutting Principles, New York: Oxford University Press.
[12] Stephenson, D.A., (1991), 'Assessment of Steady-State Metal Cutting Temperature Models Based on Simultaneous Infrared and Thermocouple Data.' Journal of Engineering for Industry, Vol. 113, no. 2, pp.121-28.
[13] Wright, P.K. and Trent, E.M., (1973), 'Metallographic Methods of Determining Temperature Gradients in Cutting Tools.' Journal of the Iron and Steel Institute, Vol. 211, no. 5, pp. 364-368.

Chapter 9

Formation of Nanostructured Metals by Machining

M. J. Jackson, J. J. Evans, C. Xu and W. Ahmed

9.1 Introduction

The interaction between a newly formed metal chip and the rake face of a cutting tool reveal the complicated nature of initial chip formation and plastic shear strains during the first few seconds of intimate contact. The loading placed on the metal chip during the first encounter with the cutting tool manifest themselves as an unpredictable curl that forces the chip to move away from the surface of the rake face and produce uneven plastic shear strains throughout the chip. The variation of the load causes instabilities on the shear plane that is directly observed using a high-speed camera. As the variation of load progresses, the chip tends to curl away from the tool with varying radii until the apparently curved shear plane becomes linear. The results of initial chip formation demonstrate a very complex interaction between metal chip and rake face of the tool and the resulting development of the shear plane and its effect on plastic shear strains within the metal chip.

Chip formation is of fundamental importance during high-speed metal cutting [1-14]. Poor chip control leads to chip build-up and an uncontrollable surface roughness. The use of chip breaking is arbitrary because of the mechanics of chip curl is not well understood. The causes of chip curl and chip flow are still the subject of intense discussion and research among plasticity researchers. The subject originally focused on cutting forces and on the conditions at the chip-tool interface using soft plastic metals.

The increasing speed of cutting has focused researchers to look at chip breaking after the chip has been cut. In the first instance, chips were considered to be continuous, discontinuous, and continuous with a built-up edge. The theories of metal cutting allow one to predict the forces and stresses in the chip during formation but do not tell us anything about the strain within the chip, unless a computational approach is used. Astakhov [1] gives a frank and lucid explanation of the different theories surrounding metal cutting theory and its non-applicability to the problem of chip curl and chip condition. Timme [2] described chip formation as a process where the tool penetrates the workpiece with an increasing force until a small portion of the workpiece fractures and moves along a sliding plane. At this point the penetration force dramatically decreases and then begins to rise again as a new chip is formed. Lee and Shafer's [3] approach was to apply slip-line field theory to the cutting of perfectly plastic materials. It is assumed a slip-line field exists in a triangle beginning at the tool tip and extending to the shortest distance of the chip's free surface. From that point the area extends to the final point of where the tool and chip are in contact and finally back to the tool tip. The area contained by these boundaries is composed of two sets of parallel lines. The uniform stress concentration takes place in the plastic region and the maximum stress extends from the tool tip to the shortest distance on the free surface of the chip. However, most materials are elasto-plastic so the practical applications are limited. Shaw, Cook, and Finnie [4] related shear and frictional interactions in metal cutting. The slip-line field solution was combined with the assumption that the shear plane is not in the direction of maximum shear. The approach highlighted the importance of accounting for shear and friction during the final steady-state. However, pure shearing is assumed and a perfectly plastic material is required. Zorev [5] considered machining of ductile materials; the shear plane is replaced with a triangle whose apex is the tool tip. The lower boundary of the triangle is the shear line where a particle in the chip is first deformed. The upper boundary of the triangle occurs where the shear line causes the least deformation. Deformation is zero just below the lower boundary and at a maximum at the upper boundary. However, the model cannot explain the mechanisms by which these

boundaries form, but the model is in good agreement with the theory of plasticity. It can be seen from the discussion of cutting theories that individual cutting cases can be well explained but no unifying theory has yet accounted for all conditions of chip formation that are likely to be encountered.

9.2 Chip Formation

According to Astakhov [1], methods of chip formation are described in terms of certain material characteristics such as brittle, elastoplastic, and plastic properties. When considering plastic properties, chip formation is characterized by a lack of a bending moment capable of breaking the chip due to the low rigidity of the chip material. Therefore, chip formation takes place along a shear plane with successive shearing determining the shape and length of the chip. The bending moment affects the fracture of the chip and it occurs in the deformation zone from the chip side. As the free end of the chip curls, the bending moment is a decisive factor in chip breaking in addition to the elasticity of the material.

However, if a soft plastic material re-crystallizes before the chip has time to fracture, then fracture may be inhibited. In addition to the bending moment, chip fracture is dependent upon the movement of dislocations towards the grain boundaries so that microcracks can form and eventually form a macrocrack of such magnitude that the chip breaks away from its original starting point. The purpose of the paper is to demonstrate initial chip formation using microtool with a negative rake angle machining a soft, plastic, re-crystallizing material such as lead and tin, and to understand the condition of rake face contact and how it affects the magnitude of shear strain.

9.2.1 Chip Curl Modeling and Shear Strains

Chip curvature is a highly significant parameter in machining operations from which a continuous chip is produced. There is a great deal of uncertainty regarding the mechanism of curly chip formation and the factors determining the chip radius. In this paper, observations are made on initial chip curl in the simplified case of orthogonal cutting at the micro and nanoscale. The cutting process may be modeled using a simple primary shear plane and frictional sliding of the chip along the rake face. When the region of chip and tool interaction at the rake face is treated as a secondary shear zone and the shear zones are analysed by means of slip-line field theory, it is predicted that the chip will curl. Thus chip curvature may be interpreted as the consequence of secondary shear. Tight chip curl is usually associated with conditions of good rake face lubrication [6].

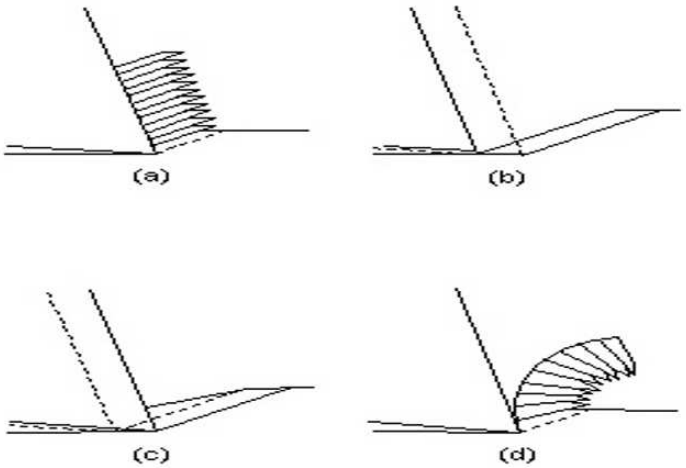

Figure 9.1. Instability during the formation of a chip during micromachining: (a) segmented, continuous chip; (b) chip forming instability due to built-up edge; (c) movement of a built-up edge to form a chip; (d) serrated, continuous chip curl

At the beginning of the cut, a transient tight curl is often observed, the chip radius increasing as the contact area on the rake face grows to an equilibrium value. Thus, it might be suggested that tight curl is an integral part of the initial deformation. It has been suggested that the process of continuous chip formation is not uniquely defined by the boundary conditions in the steady state and that the radius of curl may depend on the build-up of deformation at the beginning of the cut. A treatment of initial chip curl at the micro scale curl is now presented, which considers chip curl as a series of heterogeneous elements in continuous chip formation at the micro scale. The free surface of the chip always displays fine striations, or 'lamellae', parallel to the cutting edge. The chip is usually considered to form by a regular series of discrete shear events giving a straight chip made up of small parallel segments. However, no account is taken of the workpiece material that moves passed the tool between shear events. The following observations follow on from Doyle, Horne, and Tabor's [6] analysis of initial chip formation.

Figure 9.1 shows the instabilities during chip formation that gives rise to initial chip curl. Figure 9.1b shows the consequence of a built-up edge that very quickly becomes part of the segmented chips shown in Figure 9.2d. This 'material' provides the means to curl the chip and as a consequence of this event, the following model is presented. Previous treatments of chip curl analysis (Jackson et al. [7,8]) have focused on chip formation with a very stiff cutting tool. However, during micromachining the cutting tool bends as it machines the workpiece material. This means that primary chip curl models must account for deflection of the cutting tool by bending during an orthogonal micromachining operation. Computational approaches to modeling chip formation at the micro and nanoscales have been attempted in recent years by a number of researchers [9 – 14], who have used a molecular dynamics simulation approach using stiff cutting tools.

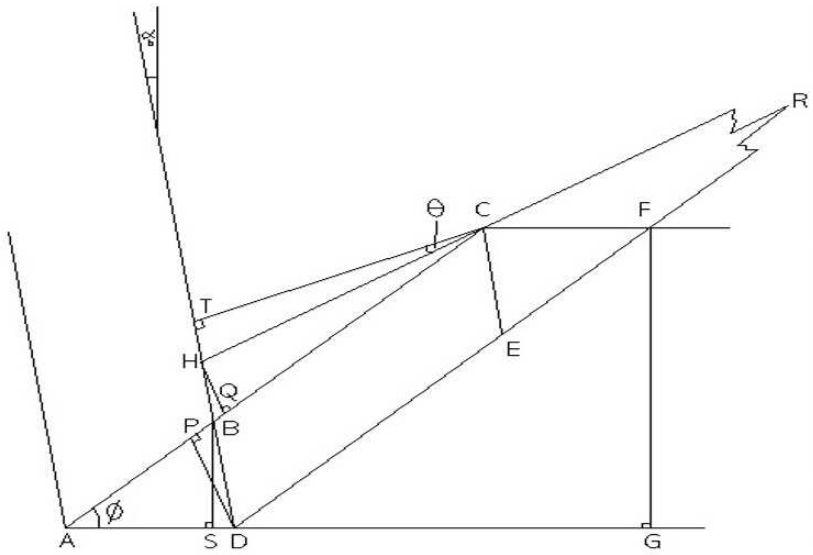

Figure 9.2. Schematic diagram of the geometry of the primary chip that forms a curled chip

The generation of a transient built-up edge ahead of the cutting tool between shearing events in a bulging-type of motion generates the shape of the segment of the metal chip. This is shown in Figure 9.1c, with the built-up edge forming the 'shaded triangle' above the shear plane. If it is assumed that the built-up edge does not 'escape' under the tool edge, then the areas of the shaded triangles in Figures 9.1b and 9.1c will be equal. The chip moves away from the rake force in a manner shown in Figure 9.1d. The radius of chip curl can be calculated by assuming that the built-up edge in transient and that the element of the 'bulged' material contains a small angle relative to the tool and workpiece. This angle will inevitably change during the bending action of the cutting tool. With reference to Figure 9.2, if we assume that the cutting tool moves from point A to point D then the shear plane AC rotates to position HC as the built-up edge from triangle ABD is pushed into the segment of the chip. At point D, the shear along DF begins and segment DHCF is completed. HC and DF meet at R, the centre of the circle of the chip segment. Since the angle HRD is small, RD may be referred to as the radius of the chip. The clearance angle is θ. Triangles ABD and HBC are equal

in area and the depth of cut FG is equal to d. The spacing between the segments, i.e., the lamellae, is CE, which is equal to BD, which is equal to s. The chip thickness between lamellae, TC, is equal to t, whilst the rake angle SBD is equal to α. The cutting tool bends when machining at the microscale, which reduces the effective rake angle to α_b. We know that the chip radius r can be taken as RD, whilst the shear angle subtended is BÂD, or ϕ. The calculation of the chip radius is provided by Jackson [7], and was shown to be,

$$r = \frac{d^2}{s.\cos\alpha_b.\sin\phi} \tag{9.1}$$

Equation 9.1 predicts a positive chip radius even at negative rake angles. The approximations considered in this model are appropriate when one considers that the model assumes that a secondary shear plane exists. However, the grain structure of the formed chip is highly variable and the formation of nanostructured grains can exist but is highly dependent upon the magnitude of plastic shear strain within the chip. The shear strain imposed during the machining operation in the deformation zone is given by the following equation:

$$\gamma = \frac{\cos\alpha}{\sin\phi\cos(\phi-\alpha)} \tag{9.2}$$

This equation assumes that the shear plane is linear and that the shear strain can be measured by knowing the shear plane angle, ϕ, and the rake angle of the cutting tool, α, which also remains constant during shearing. These simple equations provide a false sense of security when calculating shear strain, in that the magnitude of shear strain is dependent upon the amount of chip curl and, consequently, the nature the frictional interaction between chip and tool. One way of preventing chip contact conditions from dominating such a situation is to oscillate the cutting tool with known modulation frequencies.

9.2.2 Chip Formation with Modulation

Nanostructured materials that are composed of sub micron-sized grains have attributes not normally seen in conventional materials. These include novel magnetic and electrical properties and have high ductility, hardness, and strength. Methods for manufacturing nanostructured metals include severe plastic deformation, rolling, drawing, equal channel angular extrusion, and high pressure torsional straining. The most economic way of producing nanocrystalline metals is to use extreme plastic machining processes. The way to do this is to machine a material such that its microstructure becomes nanocrystalline.

Machining involves creating nanocrystalline feedstock by extreme plastic straining where a wedge tool removes material from the surface of a workpiece by very large strain deformation. Chip formation occurs by concentrated shear deformation along a narrow zone known as the shear plane. The geometry is determined by the shear plane angle and shear strains of 2-10 are normally used. Strain rates are typically 10^6/s and shear plane temperatures of up to $0.7T_m$ are quite common in chip formation processes. Figure 9.3 shows partially formed chip showing the variation in Vickers' hardness values indicative of the improvement in mechanical properties when applying the extreme plastic deformation process to metals such as oxygen free high conductivity copper. The sudden change in microstructure occurs over a narrow zone between the chip and the bulk microstructure [10].

The resulting microstructures revealed in the chips show a variety of geometry and particle size. Figure 9.4 shows a collage of high-resolution transmission electron micrographs (HRTEM) of a variety of engineering metals. The collage shows the selected area diffraction patterns of various metals and alloys showing a largely polycrystalline network of elongated nanocrystalline sized grains. Furthermore, the grains appear to be severely deformed with a high density of dislocations in various degrees of aspect ratios according to shearing direction and the original crystallographic orientation of the parent metal. The grains are nanocrystalline with a mixture of

small and high-angle grain boundaries. The characteristics of these grains have been qualified and analysed by Brown et al. [10].

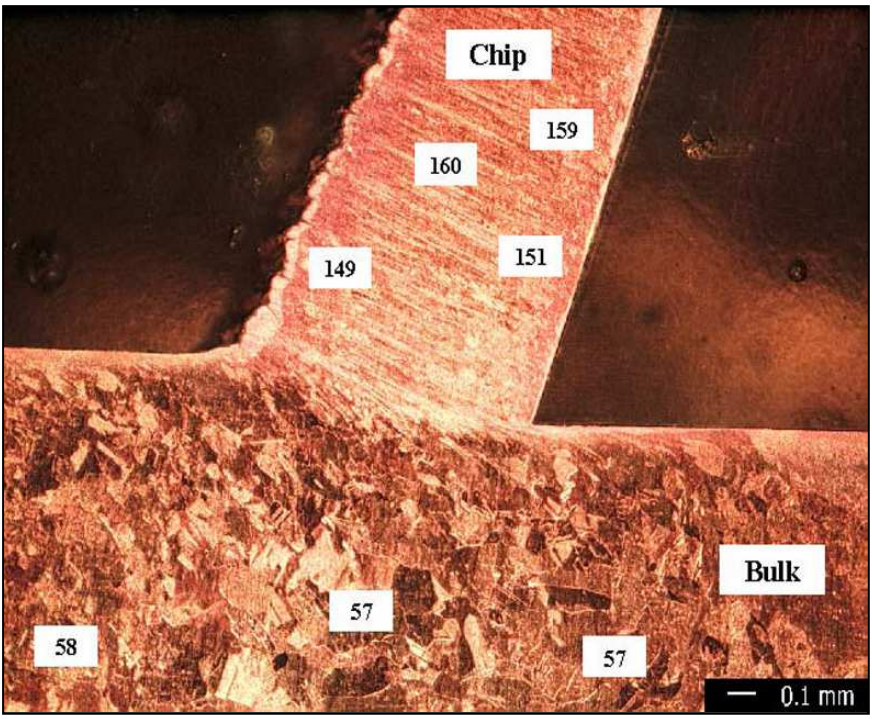

Figure 9.3. Schematic diagram of extreme plastic straining of OFHC copper showing Vickers' hardness values in kg/mm^2 [10]

The improvement in mechanical properties is described in much detail in Figure 9.5. Here, the figure shows how the hardness has increased in the chip compared to the bulk of the material for aluminium alloy 6061-T6, OFHC H4 copper, and 360-H4 brass. The properties vary depending upon initial material condition and the nature of contact between chip and rake face of the cutting tool.

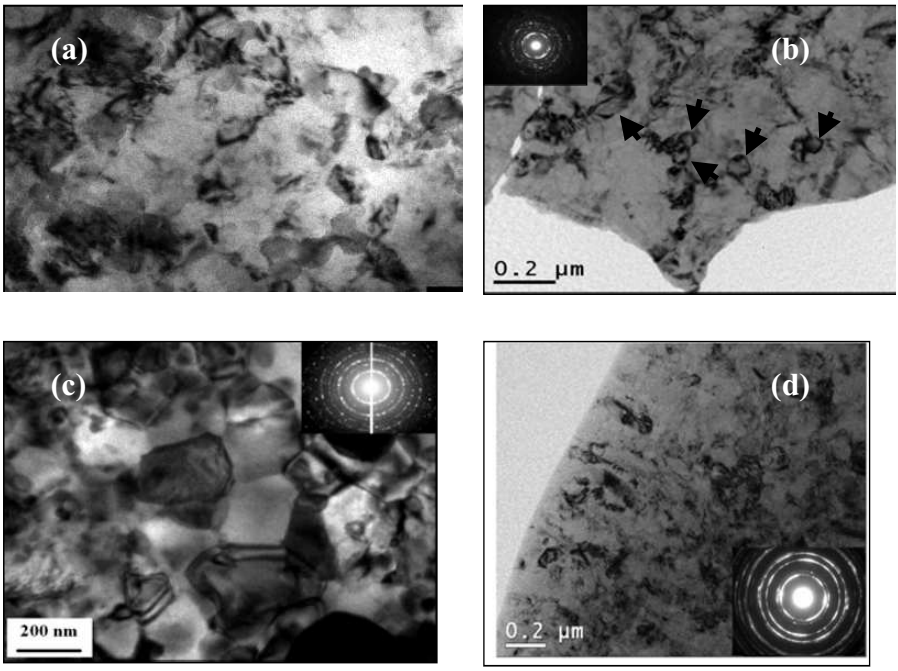

Figure 9.4. Collage of HRTEM images of metals such as: (a) Al6061-T6; (b) titanium; (c) 52100 steel, and (d) Inconel 718 showing grains sizes between 75 and 90nm [10]

Brown et al. [10] have shown that very large strains can change the shape and sizes of the individual grains even though controlling their size appears to be more complicated than explained. The change in mechanical properties, such as hardness, is very impressive even though plastic shear strains are highly variable across the shear plane during chip formations where the loading is complex and unsteady during the initial formation of the chip.

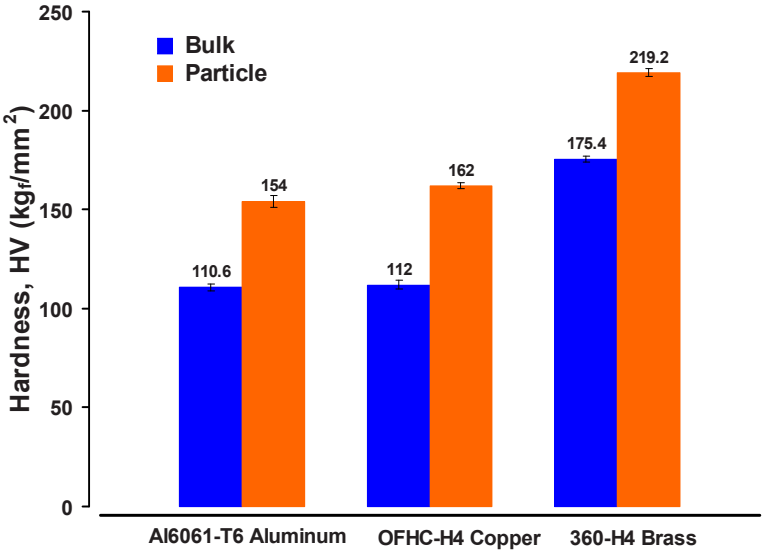

Figure 9.5. Comparison of hardness for chip and bulk material for materials Al6061-T6, OFHC copper, and H4 brass [10]

The production of feedstock is produced by oscillating the cutting tool about the workpiece by a specially developed modulating tool that produces small sized chips that do not require further comminution. The tool is shown in Figure 9.6 and the resultant chips are shown in Figure 9.7. Experiments have been conducted with both positive and negative rake angles.

9.2.3 Computational Analysis

AdvantEdge™ is a commercial finite element model software developed by Third Wave Systems that is used for metal-cutting processes based on a Lagrangian finite element model that applies adaptive meshing and continuous re-meshing. The software has a user-friendly interface with simple input screens to supply the tool and workpiece geometry as well as process parameters, which make it an easy programme to use for performing machining simulations.

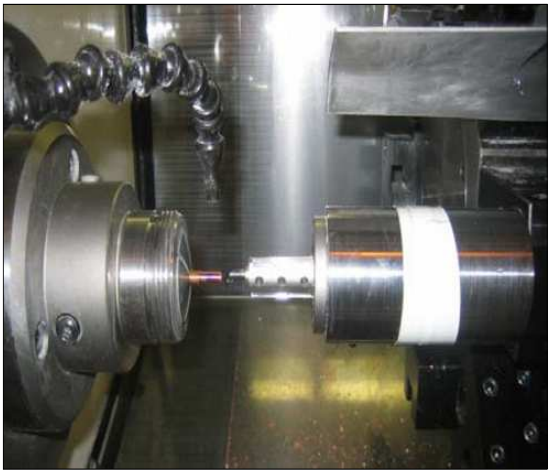

Figure 9.6. Specially developed oscillating tool attached to the piezoelectric oscillator located within the machining center

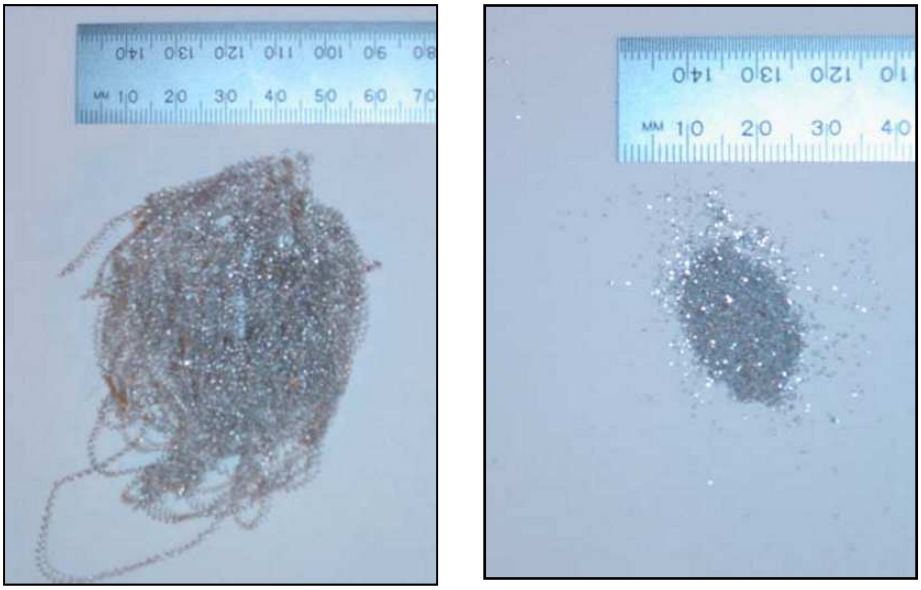

Figure 9.7. Nanocrystalline feedstock produced with and without modulation [10]

AdvantEdge™ has pre-programmed modules for 2D and 3D machining operations and a material library with models of engineering metals and alloys. AdvantEdge™ simulation software provides detailed analysis of conventional cutting processes, which allows one to improve material removal rates and tool performance while decreasing the need for physical testing. In addition to force and temperature prediction, AdvantEdge™ features tool wear prediction capabilities, 3D residual stress analysis, 3D tool thermal boundary conditions, and enhanced rake face data extraction capabilities. The formulation is discretized by six-noded quadratic triangular elements that provide quadratic interpolation of the degree of freedom and linear pressure distribution within the element. The cutting tool is parameterized by rake and clearance angles and a cutting edge radius, but can also accommodate general chip breaker geometries and the workpiece-by-workpiece length and height. The software uses an explicit dynamic, thermo-mechanically coupled finite element method and employs adaptive re-meshing to resolve highly distorted meshes. Where necessary, it refines large elements, re-meshes distorted elements, and coarsens small elements. The friction model is based on Coulomb's law of friction.

9.3. Experimental Procedure

To observe initial chip formation and shear strain instability, machining experiments were conducted at the microscale using a negative rake angle wedge made from tungsten carbide bonded with cobalt. The linear machine tool was constructed to incorporate the wedge shaped tool that interacted with the workpiece using a linear slide. The table of the machine tool was configured to move in the x co-ordinate by attaching a slide powered by a d.c. motor. The cutting tool used were uncoated tungsten carbide bonded with cobalt. During machining, the machining event was captured using a high-speed camera. The cutting tool was inspected at the end of all machining experiments using a scanning electron microscope. The

depth of cut was 200 μm for all machining experiments. The machining feed rate was conducted at 5 mm/s (0.3 m/min). The microscale cutting tool used was 950 μm in diameter (microscale) and was associated with a cutting speed of 117 m/min and a machining feed rate of 0.3 m/min. Commercially pure lead and tin were machined at the microscale in air. The experimental results are shown in Table 9.1. The machined chips were examined in an environmental scanning electron microscope where the lamellar spacing on each chip was determined. Transient chip curl was measured at the first 90^{o} of tight chip curl. The curl radii was then compared with the calculated value derived using the idealized model, taking into account the degree of bending of the cutting tool.

9.4. Experimental Results

9.4.1 Finite Element Analysis

Figures 9.8 – 9.13 show the results for the magnitude of plastic shear strain during the initial stages of chip formation. Figure 9.8 shows the magnitude of plastic shear strain during the initial ploughing contact between wedge and workpiece. Figure 9.9 shows that plastic shear strain is approximately 4 at the apex of the grinding wedge. The magnitude of shear strain moves outwards towards the primary shear plane.

Figure 9.10 shows the magnitude of plastic shear strain during the formation of the initial chip showing intense shear strain at the root of the chip and developing along the primary shear plane. The extent of plastic shear strain moves beyond the primary shear plane towards the interior of the chip and towards its free surface. The resulting plastic shear is shown in the surface of the machined workpiece.

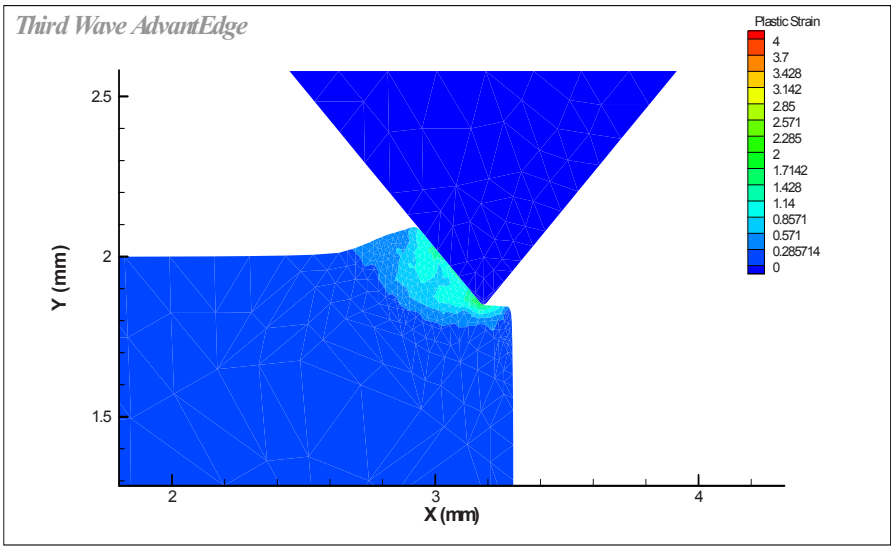

Figure 9.8. Magnitude of plastic shear strain during the initial ploughing contact between wedge and workpiece

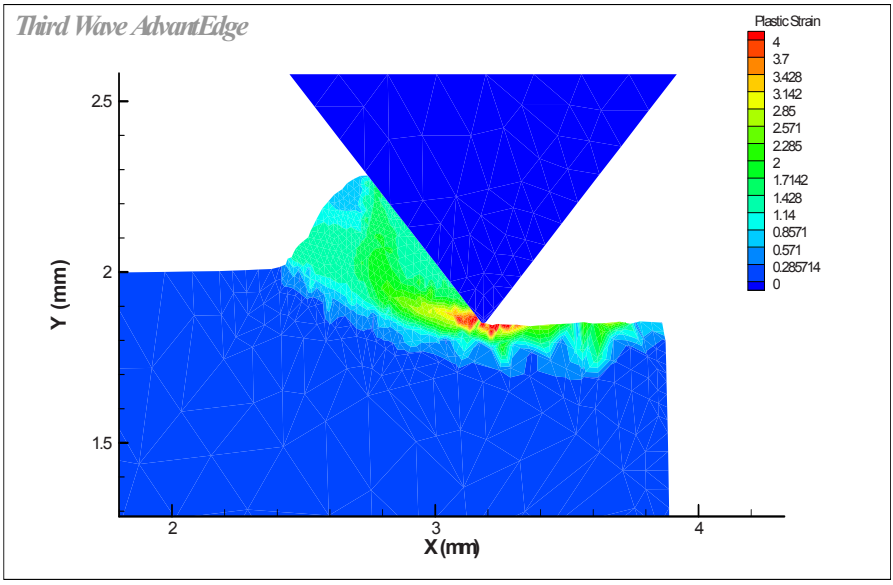

Figure 9.9. Magnitude of plastic shear strain during the formation of the initial chip showing intense shear strain at the root of the chip

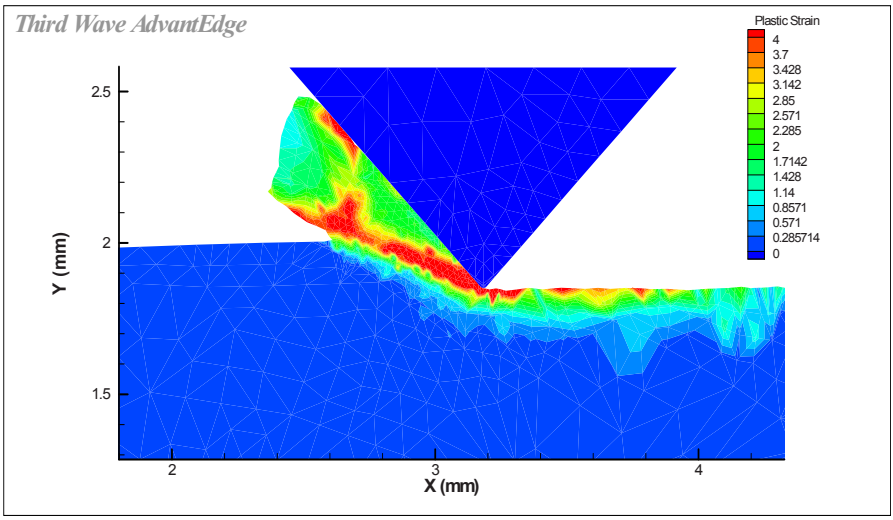

Figure 9.10. Magnitude of plastic shear strain during the formation of the initial chip showing intense shear strain at the root of the chip and developing along the primary shear plane

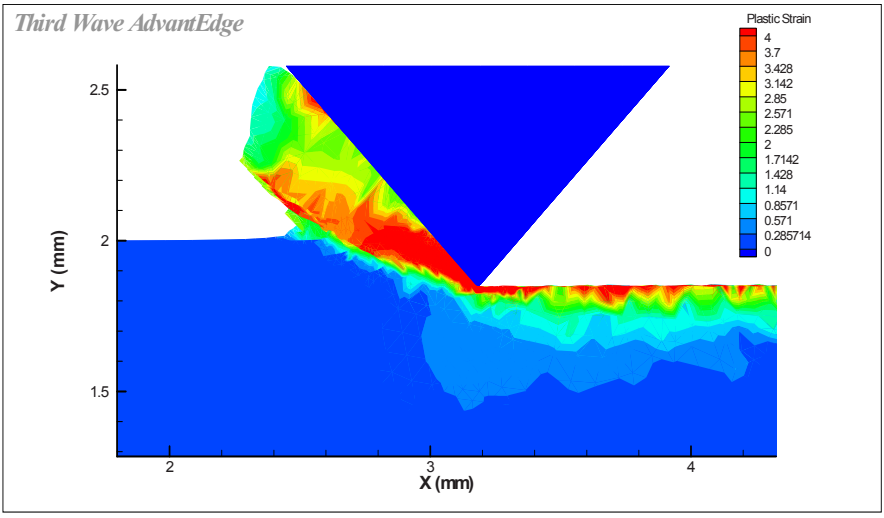

Figure 9.11. Magnitude of plastic shear strain during the formation of the initial chip showing intense shear strain at the root of the chip, developing along the primary shear plane, and beginning to form along the rake face known as the secondary shear plane

Figure 9.11 shows the magnitude of plastic shear strain during the formation of the initial chip showing intense shear strain at the root of the chip, developing along the primary shear plane, and beginning to form along the rake face known as the secondary shear plane. This amount of intense shear along the rake face actually allows a thin layer of the workpiece to protect the cutting tool wedge from being worn away.

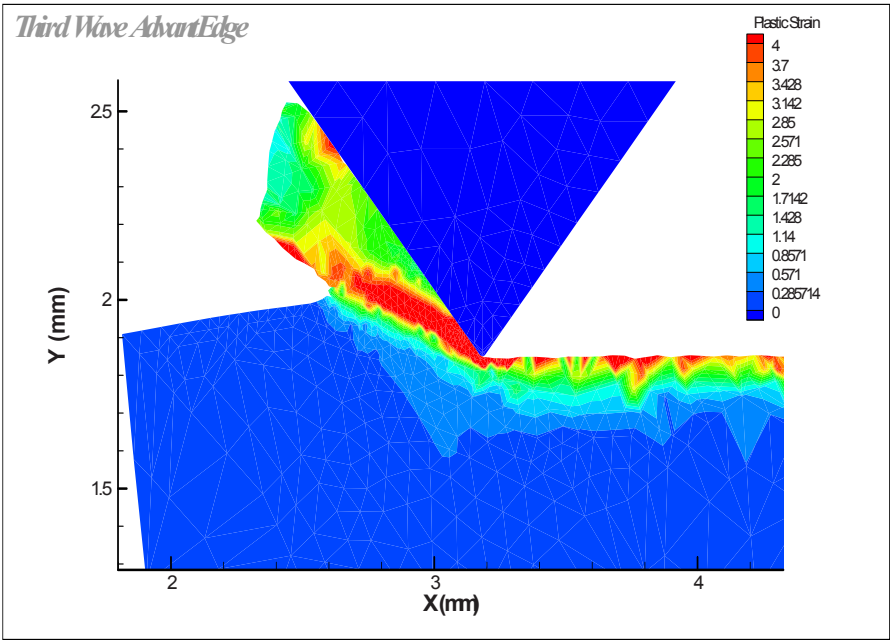

Figure 9.12. Magnitude of plastic shear strain during the formation of the initial chip showing intense shear strain at the root of the chip and rake face, and along the surface of the machined surface

Figure 9.12 shows the development of intense shear at the root of the chip and rake face as machining progresses. The surface of the workpiece is also subjected to intense shear. Figure 9.13 shows the magnitude of plastic shear strain toward the end of the formation of the initial chip. Figure 9.13 shows how the shear stain has projected to the free surface of the chip at the end of the machined workpiece.

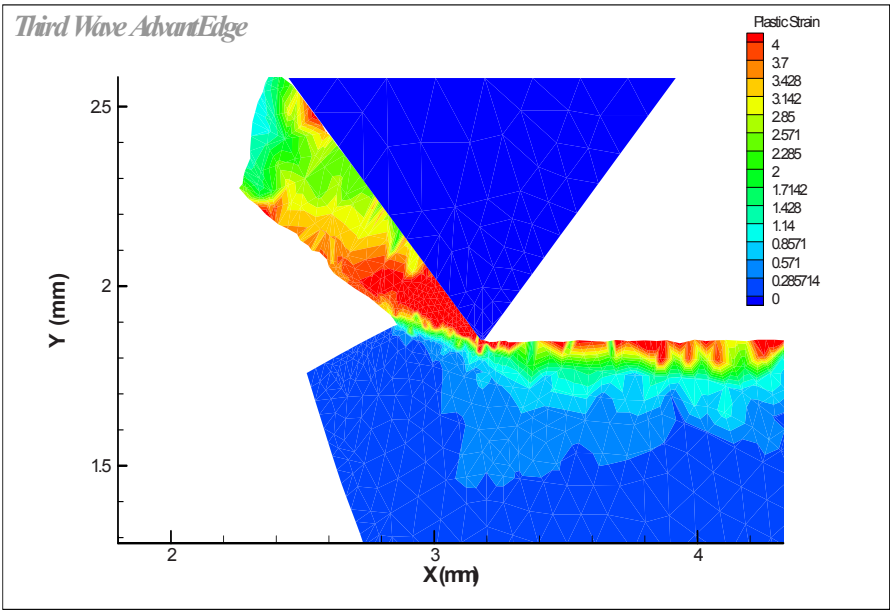

Figure 9.13. Magnitude of plastic shear strain during the formation of the initial chip showing intense shear strain at the root of the chip and along the free surface of the chip at the end of the machining stroke

9.4.2 Microgrinding Experiments

The results of machining pure metals at the microscale are compared to the model described for primary chip curl during the primary stages of metal cutting. It should be noted that all results presented in Table 9.1 are for metals machined in an oxidizing environment. Table 9.1 shows the results for micromachining using a variety of negative rake angles. It should be noted that bending of the cutting tool produces a less acute rake angle when machining takes place. However, when the shear plane angle is increased larger chips are produced and the magnitude of shear strains is highly variable.

Type of Metal	Rake Angle (^{O})	Shear Plane Angle (^{O})	Mean lamellar spacing (μm)	Observed chip curl (mm)	Calculated chip curl (mm)
Pure Tin	-25°	27°	1.3	20.4	18.7
Pure Tin	-5°	17°	2.5	12.4	13.7
Pure Tin	-23^{o}	37^{o}	1	17.6	18.05
Pure Lead	-16^{o}	26^{o}	1.6	14.4	14.8
Pure Lead	-8^{o}	18^{o}	1.9	16.6	17.2
Pure Lead	-3^{o}	12^{o}	3	15.8	16.0

Table 9.1. Experimental data comparing chip curl during micromachining and chip curl predicted by the model. The depth of cut is 200μm

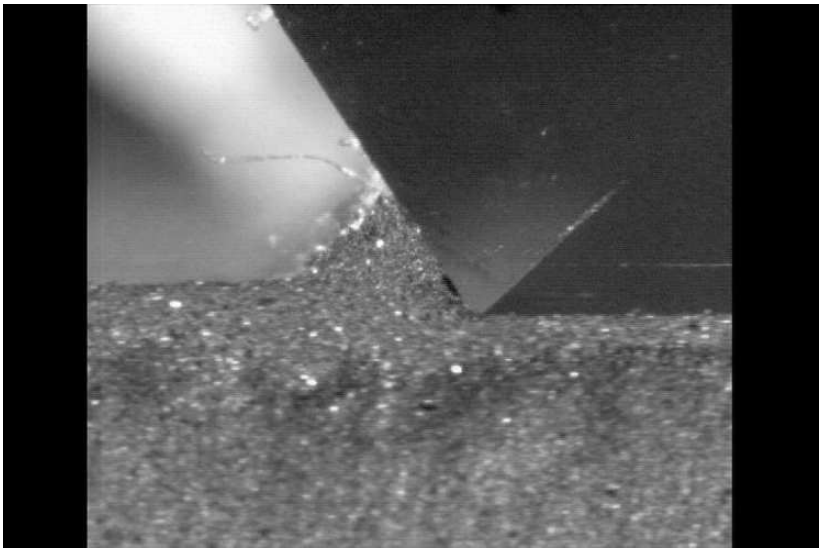

Figure 9.14. High-speed image of the initial formation of the chip. Image taken after 1.5 seconds of machining

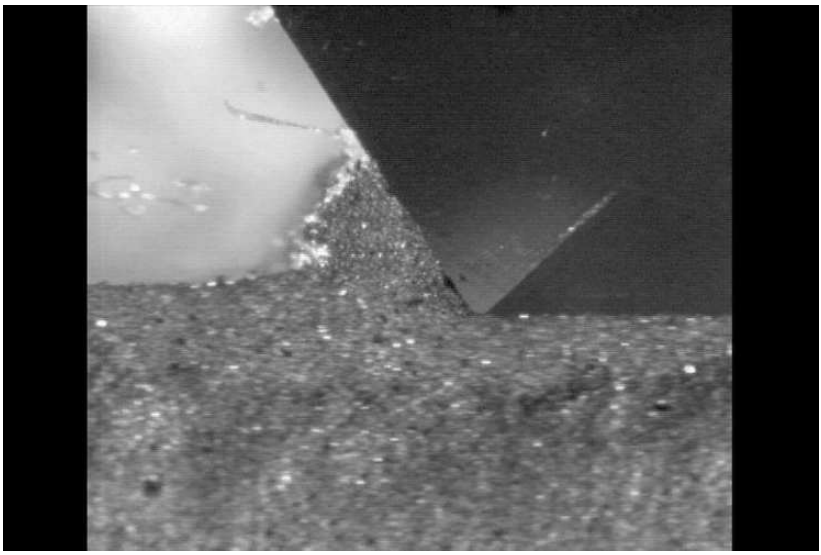

Figure 9.15. High-speed image of the initial formation of the chip. Image taken after 2 seconds of machining

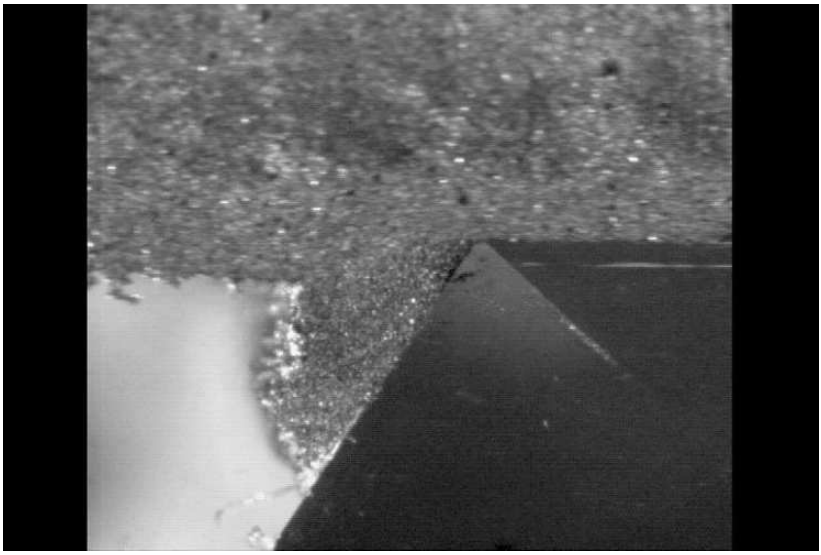

Figure 9.16. High-speed image of the initial formation of the chip. Image taken after 3 seconds of machining

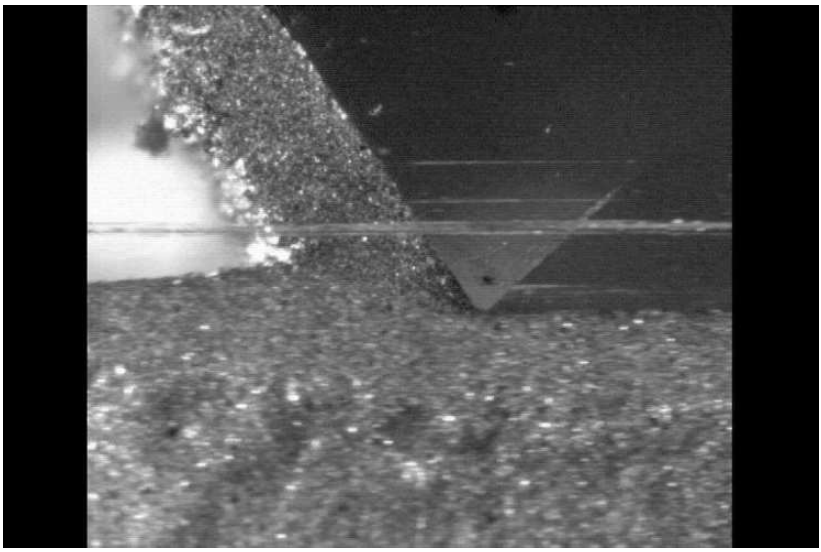

Figure 9.17. High-speed image of the initial formation of the chip. Image taken after 7 seconds of machining

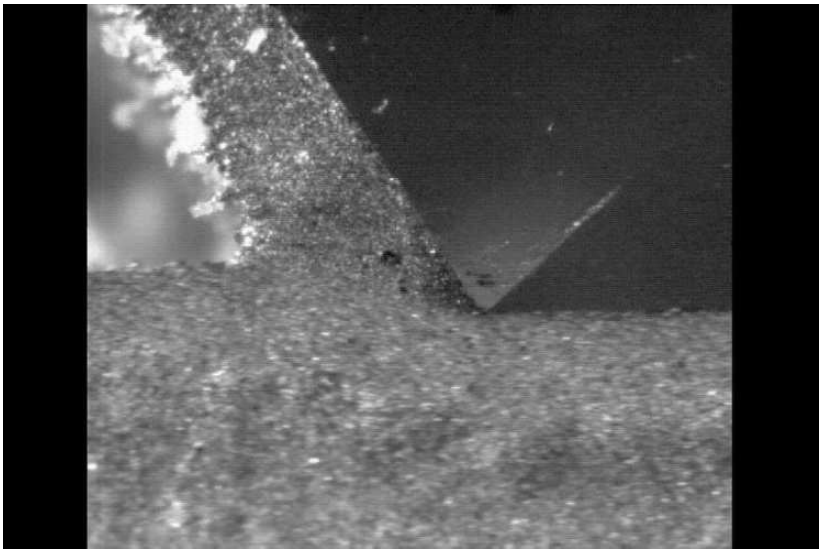

Figure 9.18. High-speed image of the initial formation of the chip. Image taken after 15 seconds of machining

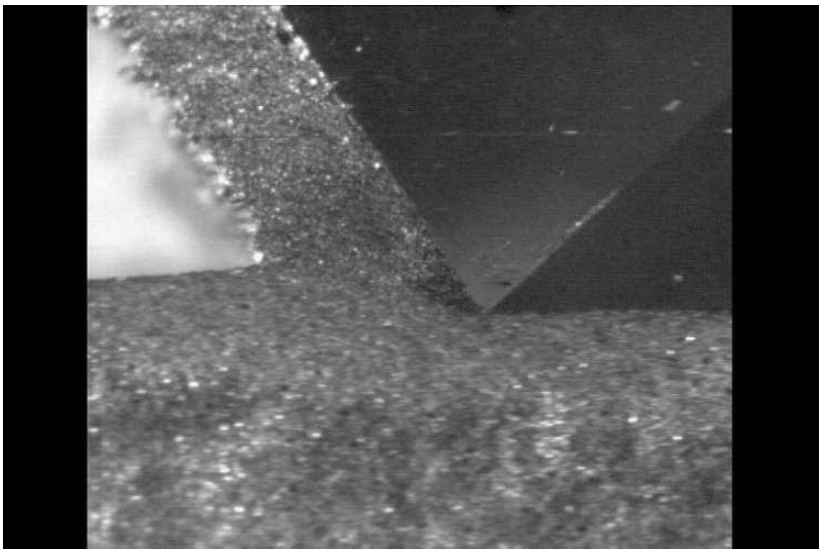

Figure 9.19. High-speed image of the initial formation of the chip. Image taken after 20 seconds of machining

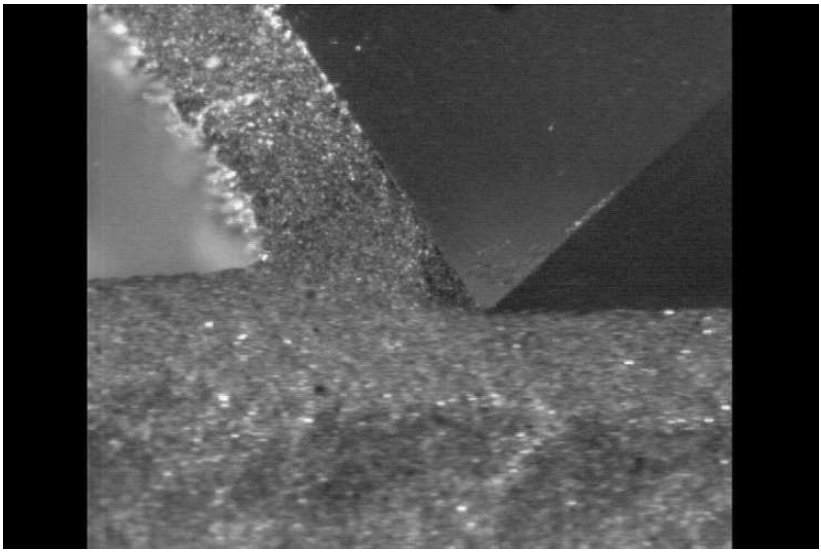

Figure 9.20. High-speed image of the initial formation of the chip. Image taken after 23 seconds of machining

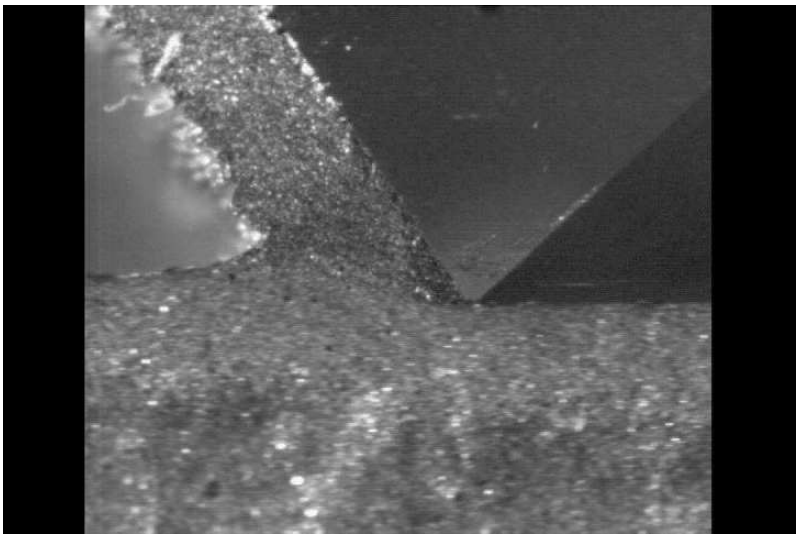

Figure 9.21. High-speed image of the initial formation of the chip. Image taken after 24 seconds of machining

Figures 9.14 – 9.21 shows the results of high speed imaging of the initial chip formation process using a negative rake angle cutting tool. The figures clearly show how the primary shear plane changes shape between concave, convex, and linear depending upon the loading conditions that are placed on the freshly cut chip by the rake face of the cutting tool. When comparing chip forms, significant differences in chip shape are observed. It was observed that many of the particles generated are in fact chunks of material rather than nicely formed chips. It is possible that the chunks were formerly parts of larger chips that have since broken down and that chip thickness values should be re-calculated based on the larger chip size. It can also be seen that the high-speed machined chips are more consistent in terms of length, width, and depth. Their lamellar spacing is regular in period, which would indicate that cutting conditions at high speed are highly stable. The chip length of high-speed machined chips is much shorter than low-speed chips. This could be because at low speed the chip has a greater time in contact with the workpiece thereby removing more material, which is reflected in the increased chip length. One of the major differences

observed between low- and high-speed chips is in the spacing of the lamellae. In low-speed machining, the chip spacing varies by a significant amount. However, at high machining speeds the spacing is regular in period. Part of the mechanism of chip removal is the forced alignment of dislocations resulting from the impact of the cutting tool against the workpiece. At high speeds this process is accelerated to an extremely high level as the strain rate calculations have shown. In fact, experiments show that chip types are similar in other pure metals such as copper and aluminum. This suggests that high strain rates induce a material removal mechanism independent of the material itself.

9.5. Discussion

9.5.1 Chip Curl Modeling

The experimental results and observations provide an interesting view of machining a variety of metals at the microscale. When one considers the approximations made in the derivation of the chip curl model, the experimentally measured results compare well with the calculated chip curl. This indicates that cutting tool motion contributes significantly to initial chip curl prior to any significant frictional interactions on the rake face of the cutting tool. The proposed model describes the initial stages of chip curl accurately. If the description of chip curl is accurate, then continuous chip formation at the microscale needs to be re-investigated. If one considers the movement of the cutting tool (Figure 9.1), from point A towards point D, we expect the shear plane to oscillate between AC and HC depending on the amount of energy required to move the built-up edge into the segment of the subsequent chip. The cycle begins again when accumulated metals are deposited on to the edge of the cutting tool then on to the subsequent segment of the chip produced during machining.

9.5.2 Finite Element Modeling

Finite element analysis of chip formation by the action of a perfectly sharp wedge shows that initial chip formation begins with the workpiece material subjected to shear strains between 1 and 4. Frictional interactions between the workpiece and the tool ensures intimate contact between chip and cutting tool and the shear strains between to increase after approximately 300ms. Plastic shear strains develop ahead of the tool and are shown in the experimental observations. Friction coefficient decreases as the speed of machining increases and as the chip passes over the rake face. Further movement of the tool subjects the freshly machined workpiece to further levels of plastic shear strain. The chip then begins to curl in the form of a radius that is dependent on the bending moment that is applied about the shear plane.

9.5.3 Microgrinding Observations

In observing the micrographs showing machining with negative rake angles, the plane of shear appears to be curved with a tendency to become convex and concave depending on the loading conditions exerted by the cutting tool. During initial contact conditions, the shear plane appears to be concave and progressively becomes convex as machining continues. The shear plane appears to be linear under steady-state conditions. Curvature of the shear plane produces a change in the shear plane angle that is outward along the plane of shear with a consequent change in the cutting ratio towards the free surface. In this case, the chip in contact with the tool will be elongated (if the shear plane is concave) as compared to the outer edge of the chip. This will cause the chip to curl away from the cutting tool. The apparent area of contact between chip and tool will be a function of the amount of chip curl. If the shear plane becomes convex then the chip tends to curl towards the cutting tool and there will be an increase in the apparent area of contact. This increases the concentration of load on the outer edge of the shear plane and will cause it to become concave. In addition to the change in curvature of the shear plane, there will be an accompanying change in the average value of shear plane angle. This will create a

variation in the chip thickness ratio, variation in plastic shear strains, and the magnitude of chip curl. From the experimental evidence and finite element calculations, it appears that modulating the formation of metal chips may produce large variations in plastic shear strain in the cut chip. This will inevitably lead to variations in the aspect ratios of the grains within the chips, and will also lead to variations in the grain size within the cut chip.

9.6 Conclusions

A model of chip curl at the microscale has been developed and agrees well with experimental data. It appears that the motion of the cutting tool contributes significantly to the primary chip prior to significant frictional interactions on the rake face of the cutting tool. It is shown that primary chip curl is initiated by the amount of material deposited onto the cutting tool that manifests itself as a wedge angle that controls the amount of material pushed into the base of the segment of the chip between oscillations of the primary shear plane. Finite element calculations confirm that frictional interactions between chip and wedge tool dominate the magnitude of plastic shear strain and also controls the shape of the shear plane. This was also confirmed by observing a series of still images taken from high-speed video montage of the machining process. Modulation of the chip formation process tends to produce highly variable shear strains and grain sizes within a freshly cut chip.

Acknowledgements

The chapter contributors wish to thank Inderscience publishers for granting permissions to reproduce work presented in this chapter.

References

[1] Askatov, V. P., On The Inadequacy of the Single-Shear Plane Model of Chip Formation, International Journal of Mechanical Sciences, 2005, **47**, 1649-1672.
[2] Timme, I.I., On the Resistance of Metals and Wood in Cutting, Dermacov, St. Petersburg, 1880 (In Russian).
[3] Lee, E.H., and Shafer, B. W., The Theory of Plasticity Applied to a Problem of Machining, Journal of Applied Mechanics, 1951, **18**, 405-413.
[4] Shaw M. C., Cook N. H., and Finnie, I., The Shear Angle Relationship in Metal Cutting, Trans. ASME, Journal of Engineering for Industry, 1953, **75**, 273-288.

[5] Zorev, N.N., Metal Cutting Mechanics, Pergamon Press, Oxford, England, 1966.
[6] Doyle, E. D., Horne, J. G., and Tabor, D., Frictional Interactions Between Chip and Rake Face in Continuous Chip Formation, Proc. Roy. Soc., of London, 1979, **A366**, 173 – 183.
[7] Jackson, M. J., Primary Chip Formation During the Micromachining of Engineering Materials, Proceedings of the Institution of Mechanical Engineers (London): Part B – Journal of Engineering Manufacture, 2005, **219** (3), 245-254.
[8] Jackson, M. J., and Robinson, G. M., High Strain Rate Induced Initial Chip Formation of Certain Metals During Micromachining Processes, Journal of the Institute of Materials, Minerals, and Mining – Materials Science and Technology, 2005, **21** (3), 281-288.
[9] Bowden, F. P., and Tabor, D., The Friction and Lubrication of Solids, Oxford Science Publications, Clarendon Press, University of Oxford, 2001, p.p. 168, 327.
[10] Brown, T. L., Swaminathan, S., Chandrasekar, S., Compton, W. D., King, A. H., and Trumble, K. P., Low-cost Manufacturing Process for Nanostructured Metals and Alloys, Journal of Materials Research, 2002, **17** (10), 2484-2488.
[11] Luo, X., Cheng, K., Guo, X., and Holt. R., An Investigation into the Mechanics of Nanometric Cutting and the Development of its Test Bed, Int. J. Prod. Res., **41**, 2003, 1449-1465.
[12] Jackson, M. J., Robinson, G.M., Sein, H., Ahmed, W., and Woodwards, R., Machining of Cancellous Bone Prior to Prosthetic Implantation, Journal of Materials Engineering and Performance, 2005, **14** (3), 293-301.
[13] Jackson, M. J., Microgrinding Electronic and Optical Materials Using Diamond Coated Piezoelectric Materials, International Journal of Manufacturing Technology and Management, 2006**, 9** (1/2), 1-17.
[14] Komanduri, R., Chandrasekaran, N., and Raff, L. M., Molecular Dynamics Simulation of the Nanometric Cutting of Silicon, Philosophical Magazine, **B81**, 2001, 1989-2019.

Chapter 10

Manufacture and Development of Nanostructured Diamond Tools

M. J. Jackson, W. Ahmed and J. S. Morrell

10.1 Introduction

Chemical vapor deposited diamond films have many industrial applications but are assuming increasing importance in the area of microfabrication, most notably in the development of diamond-coated micro-tools. For these applications the control of structure and morphology is of critical importance. The crystallite size, orientation, surface roughness, and the degree of sp^3 character have a profound effect on the machining properties of the films deposited. In this paper experimental results are presented on the effects of nitrogen doping on the surface morphology, crystallite size, and wear of micro-tools. The sp^3 character optimises at 200 ppm of nitrogen and above this value the surface becomes much smoother and crystal sizes decrease considerably.

Fracture induced wear of the diamond grain is the most important mechanism of material removal from a micro-grinding tool during the grinding process. Fracture occurs as a consequence of tensile stresses induced into diamond grains by grinding forces to which they are subjected. The relationship between the wear of diamond coated grinding tools, component grinding forces, and induced stresses in the model diamond grains is described in detail. A significant correlation is found between the maximum value of tensile stress induced in the diamond grain and the appropriate wheel-wear parameter (grinding ratio) machining a selection of engineering steels and cast iron materials. It is concluded that the

magnitude of tensile stresses induced in the diamond grain by grinding forces at the rake face is the best indicator of tool wear during the grinding process. Diamond has a unique combination of excellent physical and chemical properties, which makes it ideal for numerous applications [1-3]. It can be used in biomedical components, cutting tools, optical components, microelectronic circuits and thermal management systems. A number of methods have been investigated in order to deposit diamond in thin form to various substrates, the most common being silicon and tungsten carbide cemented with a small amount of cobalt metal [4-6]. Arguably, the most successful method of depositing polycrystalline films of diamond is chemical vapor deposition (CVD). In this paper we investigate a variant of the basic CVD process known as hot filament CVD for the deposition of diamond. It is generally agreed that the properties of the films, such as morphology, quality, and adhesion that determine the suitability for use in a particular application [7]. In the case of micro-tools, extremely small particles of diamond are required that are blocky in form so that cutting of metals and other materials can be performed with relative ease. Both the diamond nucleation stage and the CVD process conditions critically affect the structure and morphology of diamonds. Abrasion of the substrate material with diamond powder prior to deposition is commonly used to enhance the diamond nucleation density [8-10]. However, such abrasion methods damage the surface in a poorly defined manner. Thus, more controlled methods of nucleation such as biasing prior to CVD are becoming increasingly common [11,12] and can even enable heteroepitaxial growth of diamond films [13,14]. The gas-phase environment during deposition also affects the quality and morphology of the resulting diamond films. The addition of nitrogen [15,16], boron [17] and phosphorus [18] containing gases to the standard methane/hydrogen gas mixtures can change crystal size and its faceting. The effect of changing the stoichiometric balance of the mixture of gases has a significant effect on the development of wear in micro-tools. Wear mechanisms in micro-tools appear to be similar to that of single-point cutting tools, the only difference being the size and nature of swarf generated. Micro-tools contain very small sharp abrasive grains with blunted cutting edges (known as wear flats), and

diamond grains with sharp cutting edges that are released from the grinding tool before they had a chance to remove material from the workpiece. The general form of the wear curve is similar to that of a single-point cutting tool. The wear behavior observed is similar to that found in other wear processes; high initial wear followed by steady-state wear. A third accelerating wear regime usually indicates the occurrence of catastrophic wear of the tool. This type of wear is usually accompanied by thermal damage to the surface of the machined workpiece, which reduces fatigue strength and the life of the component. The performance index used to characterise wear resistance is the grinding ratio, or G-ratio, and is expressed as the ratio of the change in volume of the workpiece ground, Δv_w, to the change in the volume of the surface of the tool removed, Δv_s, and is shown in Eq. (10.1),

$$G = \Delta v_w / \Delta v_s \tag{10.1}$$

Grinding ratios cover a wide range of values ranging from less than one for high speed steels [19] to over 60,000 when internally grinding bearing races using cubic boron nitride abrasive wheels [20]. Attempts have been made to address the problems related to the wear of abrasive grains in terms of the theory of brittle fracture [21]. The conclusions of various researchers lead us to believe that the variety of different and interacting wear mechanisms involved, namely, plastic flow of abrasive, crumbling of the abrasive, chemical wear, etc., makes grinding tool wear too complicated to be explained using a single theoretical model [22]. The following analysis of diamond grains represented by single-point loaded wedges assumes that diamond grain fracture is the dominant wear mechanism in a set of grinding tools operating under various grinding conditions. In this paper it is shown that the addition of nitrogen to methane and hydrogen process gases may be used to influence the surface morphology and structure of the films such that they become suitable for use on micro-tools. The effects of substrate biasing and abrasion on the nucleation and growth of N-doped diamond films, and their influence on the wear of micro-tools is discussed.

10.2. Analysis of Stress in a Loaded Wedge

Diamond grains are angular in habit and possess sharp cutting points prior to grinding workpiece materials. When deposited on a tool substrate, these grains can be considered to be representative infinite wedges. An infinite wedge represents the cutting point of a diamond grain in contact with the workpiece material (Figure 10.1).

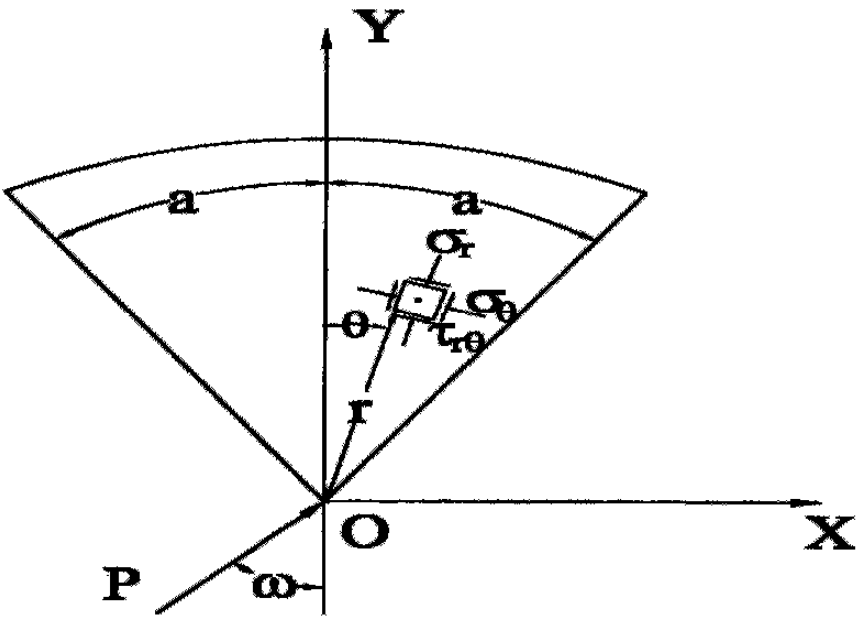

Figure 10.1. The single-point, loaded infinite wedge

The wedge is loaded at the apex by a load P in an arbitrary direction at angle ω to the axis of symmetry of the wedge. Resolving the force into components P.cosω in the direction of the axis, and P.sinω perpendicular to that the stresses due to each of these forces can be evaluated from two-dimensional elastic theory [23]. The state of stress in the wedge, due to force P.cos ω, can be obtained from the stress function,

$$\phi = C.r.\theta.\sin\theta \tag{10.2}$$

Where r and θ are polar coordinates at the point N in Figure 10.2, and C is a constant. The stress function yields the following radial, tangential, and shear stress components,

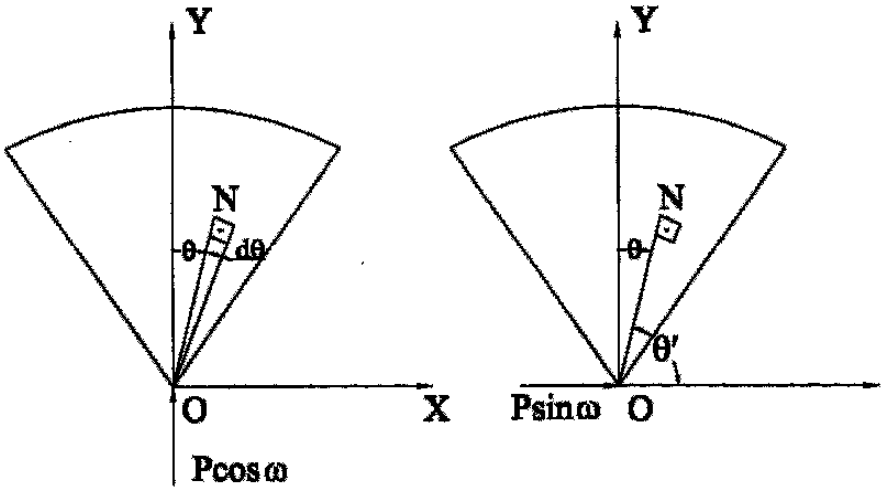

Figure 10.2. The single-point, loaded infinite wedge showing force components, and the point N within the wedge at polar co-ordinates, r and θ

$$\sigma_r = -2C\frac{\cos\theta}{r} \tag{10.3}$$

$$\sigma_\theta = 0 \tag{10.4}$$

$$\tau_{r\theta} = 0 \tag{10.5}$$

To determine the constant, C, the equilibrium of forces along the Y-axis is,

$$P\cos\omega - \int_{-a}^{a} \sigma_{r.} \cos\theta dA = 0 \tag{10.6}$$

Where dA is an element of cross sectional area within the wedge. If, t, is the thickness of wedge, then,

$$\cos\omega P = \int_{-a}^{a} 2C\frac{\cos\theta}{r}.t.r.\cos\theta d\theta \quad = 2Ct\int_{-a}^{a}\cos^2\theta d\theta \quad = \text{Ct (2a + sin 2a)} \tag{10.7}$$

Therefore, $$C = \frac{P\cos\omega}{t(2a+\sin 2a)} \tag{10.8}$$

And $$\sigma_r = -\frac{2P\cos\theta.\cos\omega}{r.t(2a+\sin 2a)} \tag{10.9}$$

Note that the negative sign denotes that the stress is compressive in this region. The state of stress in the point-loaded wedge, due to force P.sin ω, can be obtained from the following stress function,

$$\phi = C'.r.\theta'.\sin\theta' \tag{10.10}$$

Therefore,

$$\sigma_r = -2C\frac{\cos\theta'}{r} \tag{10.11}$$

And, $$\sigma_\theta = 0 \tag{10.12}$$

$$\tau_{r\theta} = 0 \tag{10.13}$$

Equilibrium of forces along the X-axis (Figure 10.2) yields the following solution for the constant, C,

$$P\sin\omega - \int_{\pi/2-a}^{\pi/2+a} \sigma_r .t.r.\cos\theta' d\theta' = 0 \tag{10.14}$$

$$P\sin\omega = -\int_{\pi/2-a}^{\pi/2+a} 2C\frac{\cos\theta'}{r}.t.r.\cos\theta' d\theta' \; = 2Ct.\int_{\pi/2-a}^{\pi/2+a} \cos^2\theta' d\theta' \; = \text{- C.t}$$

(2a – sin2a)

(10.15)

$$C = \frac{P\sin\omega}{t(2a - \sin 2a)} \tag{10.16}$$

Thus,

$$\sigma_r = -\frac{2P\cos\theta'.\sin\omega}{r.t(2a - \sin 2a)} \tag{10.17}$$

Expressing in terms of the angle θ (where θ' is negative), yields,

$$\sigma_r = -\frac{2P\cos\theta.\sin\omega}{r.t(2a - \sin 2a)} \tag{10.18}$$

Therefore, the combined stresses are,

$$\sigma_r = -\frac{2P}{r.t}\left[\frac{\cos\omega\cos\theta}{2a + \sin 2a} + \frac{\sin\omega\cos\theta}{2a - \sin 2a}\right] \tag{10.19}$$

It follows that the radial stress, σ_r, vanishes for angle θ_o defined using the expression,

$$\tan\theta_o = \frac{1}{\tan\omega}.\frac{2a - \sin 2a}{2a + \sin 2a} \tag{10.20}$$

This equation corresponds to a straight line through the apex as shown in Figure 10.3. This natural axis separates the regions of compressive and tensile stresses in the wedge. It can be seen that for values of angle ω which gives, $|\theta_o| > |a|$, provides a neutral axis that lies outside the included angle of the wedge. This means that the whole area of the wedge will be under stresses of uniform sign. Expressing equation (10.19) in terms of the rake angle of the diamond grain, β, and force components F_t and nF_t (Figure 10.3), yields,

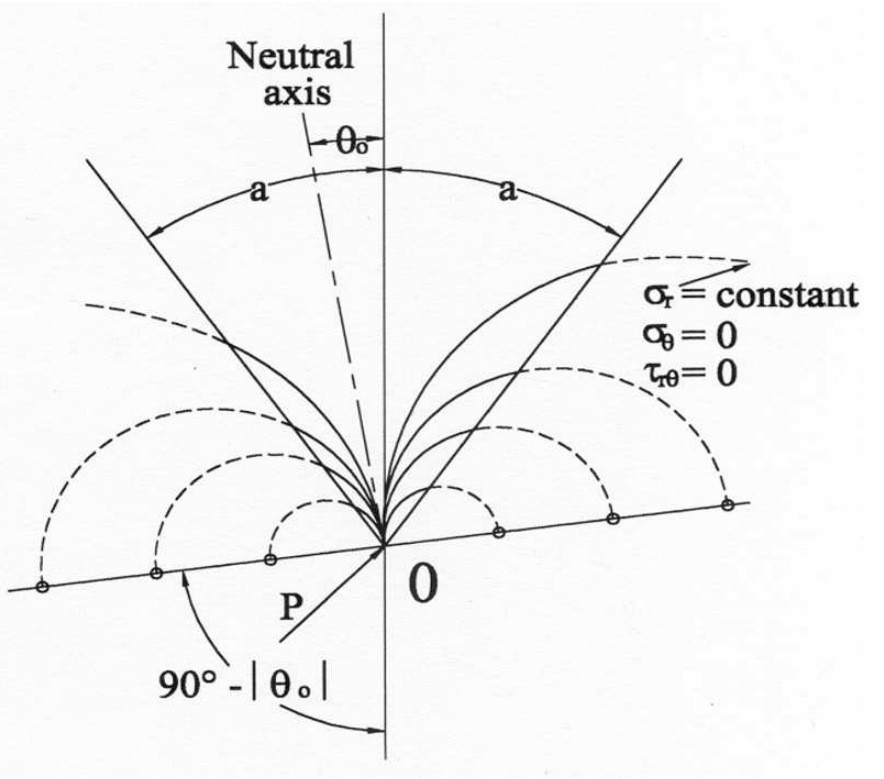

Figure 10.3. Stress analysis of a single-point loaded wedge

$$\sigma_r = -\frac{2F_t}{r.t}\left\{\frac{[n.\cos(a-\beta)+\sin(a-\beta)]\cos\theta}{2a+\sin 2a}+\frac{[\{\cos(a-\beta)-n.\sin(a-\beta)\}\cos\theta]}{2a-\sin 2a}\right\} \quad (10.21)$$

It is observed that,

$$\tan\omega = \frac{\cos(a-\beta)-n.\sin(a-\beta)}{n.\cos(a-\beta)+\sin(a-\beta)} \quad (10.22)$$

In the simple case of a wedge with the normal force nF_t along the wedge axis, a is equal to β, hence,

$$\tan\omega = 1/n \quad (10.23)$$

It is interesting to examine the radial stresses on the left-hand face of the wedge, which corresponds to the leading face of idealised wedge. Thus, for the left-hand face, θ is equal to –a, and from equation (10.19),

$$\sigma_r = -\frac{2P}{r.t}\left[\frac{\cos\omega\cos a}{2a+\sin 2a}+\frac{-\cos a.\sin\omega}{2a-\sin 2a}\right] \quad (10.24)$$

This stress is zero, i.e., the neutral axis coincides with the left-hand limit of the wedge, when,

$$\frac{1}{\tan\omega} = \frac{\sin a(2a+\sin 2a)}{\cos a(2a-\sin 2a)} \quad (10.25)$$

Thus if,

(a) a = β, then,

$$n = \frac{\sin a}{\cos a} . \frac{2a + \sin 2a}{2a - \sin 2a} \tag{10.26}$$

(b) $a - \beta = \frac{\pi}{2} - a$ (as is the case when F_t is parallel to the right-hand face of the wedge).

From equation (10.23),

$$\tan \omega = \frac{\sin a - n.\cos a}{n.\sin a + \cos a} = \frac{\sin a - n\cos a}{n.\sin a + \cos a} \tag{10.27}$$

And substituting in (10.25), yields,

$$\frac{n\sin a + \cos a}{\sin a - n\cos a} = \frac{\sin a}{\cos a} . \frac{2a + \sin 2a}{2a - \sin 2a} \tag{10.28}$$

Therefore,
$$\frac{\frac{1}{2}.n\sin 2a + \cos^2 a}{\sin^2 a - \frac{1}{2}.n.\sin 2a} = \frac{2a + \sin 2a}{2a - \sin 2a} \tag{10.29}$$

$$\frac{1}{2}.n.\sin 2a(2a - \sin 2a) + 2a\cos^2 a - \cos^2 a.\sin 2a =$$

$$= 2a.\sin^2 a + \sin^2 a.\sin 2a - \frac{1}{2}.n.\sin 2a(2a + \sin 2a)$$

$$\frac{1}{2}.n.\sin 2a(2a - \sin 2a + 2a\sin 2a) = 2a(\sin^2 a - \cos^2 a) + \sin 2a$$

$$n.2a.\sin 2a = -2a.\cos 2a + \sin 2a$$

Hence,

$$n = \frac{1}{2a} - \cot 2a \tag{10.30}$$

Equation (0.25) expresses the condition for the whole of the wedge's cross sectional area to be under the influence of a compressive stress. It can be seen that this depends not only upon the rake angle, β, but also upon the force ratio, n. In general the relative size of the region of compressive stresses to the region of tensile stresses depends upon β and n, as equation (10.20) and (10.22) indicate. Also, from equation (10.21), the magnitude of the stress on the left-hand face of the wedge is found to be dependent upon the tangential force component, F_t, and the force component ratio, n. Referring to equation (10.19), it can be seen that for constant stress, σ_r = constant,

$$r.\ C_1 = C_2.\cos\theta + C_3.\sin\theta \tag{10.31}$$

Where C_1, C_2, C_3 are constants. Equation (10.31) represents, in polar co-ordinates, the circumference of a circle tangent to the line. Therefore,

$$C_2.\cos\theta + C_3.\sin\theta = 0 \tag{10.32}$$

i.e., to the neutral axis at the point when r = 0. However, the point r = 0 must be considered separately because the stress at that point approaches infinity, since by definition P is a point load. The central point of these circles are of constant radial stress, and so the point of constant maximum shear stress must lie on a line perpendicular to the neutral axis at the point where r is equal to zero. The radius of each of those circles depends upon the magnitude of the radial stress, σ_r. Maximum values of stress were computed for a variety of point loads and then correlated to the relevant wear parameter, grinding ratio, for a variety of micro-tools. However, this may not represent the real situation where loads may be distributed along the rake face. Further analysis is required that consider point loads distributed along the rake face.

10.3 Stress Analysis in a Wedge with a Distributed Load

Consider an infinite wedge of included angle, 2a, loaded on one face with a linearly distributed normal and shear load as demonstrated in Figure 10.4. Within the loaded region of the wedge, the two-dimensional stress components in the wedge can be found using the plane stress function quoted by Timoshenko and Goodier [23] for wedges under polynomial distributed load. In polar co-ordinates, the stress function is,

$$\phi = a_0 \log r + b.r^2.\log r + c_0 r^2.\log r + d_0.r^2\theta + a_0'\theta + \frac{a_1}{2} r\theta \sin\theta$$

$$+ (b_1.r^3 + a_1'r^{-1} + b_1'r\log r)\cos\theta - \frac{c_1}{2} r\theta\cos\theta$$

$$+ (d_1 r^3 + c_1'r^{-1} + d_1'r\log r)\sin\theta + \sum_{n=2}^{\infty}(a_n r^n + b_n.r^{n+2} + a'r^{-n} + b_n'r^{-n+2}\cos n\theta$$

$$+ \sum_{n=2}^{\infty}(c_n r^n + d_n r^{n+2} + c_{n'}.r^{-n} + d_n'r^{-n+2})\sin n\theta$$

(10.33)

The stress components in the radial, circumferential, and shear directions are,

$$\sigma_r = \frac{1}{r}\frac{\partial\phi}{\partial r} + \frac{1}{r^2}\frac{\partial^2\phi}{\partial\theta^2}, \qquad \sigma_\theta = \frac{\partial^2\phi}{\partial r^2},$$

$$\tau_{r\theta} = \frac{1}{r^2}\frac{\partial\phi}{\partial\theta} - \frac{1}{r}\frac{\partial^2\phi}{\partial r\partial\theta}$$

Considering the terms containing, r^n, and assuming that $n \geq 0$, the radial stress in the wedge is,

$$\sigma_r = 2b_0 + 2d_0 - 2a_2 \cos 2\theta - 2c_2 \sin 2\theta$$
$$+ r(2b_1 \cos\theta + 2d_1 \sin\theta - 6a_3 \cos 3\theta - 6c_3 \sin 3\theta$$
$$- 12r^2(a_4 \cos 4\theta + c_4 \sin 4\theta) - r^n\{(n^2 - n - 2)(b_n \cos n\theta + d_n \sin n\theta$$
$$+ (n+1)(n+2)[a_{n+2} \cos(n+2)\theta + c_{n2} \sin(n+2)\theta]\}$$

(10.34)

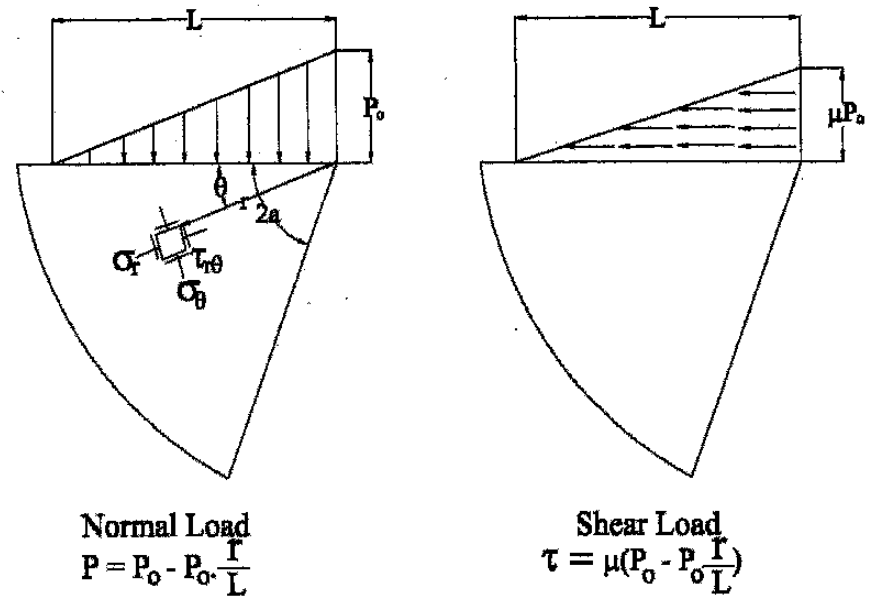

Figure 10.4. Single-point infinite wedge with a linearly distributed normal and shear load

Similarly, the circumferential stress in the wedge is,

$$\sigma_\theta = 2b_0 + 2d_0\theta + 2a_2 \cos 2\theta + 2c_2 \sin 2\theta$$
$$+ 6r(b_1 \cos\theta + d_1 \sin\theta + a_3 \cos 3\theta + c_3 \sin 3\theta)$$

$$+12r^2(b_2\cos 2\theta + d_2\sin 2\theta + a_4\cos 4\theta + c_4\sin 4\theta$$
$$+(n+1)(n+2)r^n[b_n\cos n\theta + d_n\sin n\theta$$
$$+a_{n+2}\cos(n+2)\theta + c_{n+2}\sin(n+2)\theta \tag{10.35}$$

And, the shear stress component in the wedge is,

$$\tau_{r\theta} = -d_0 + 2a_2\sin 2\theta - 2c_2\cos 2\theta$$
$$+r(2b_1\sin\theta - 2d_1\cos\theta + 6a_3\sin 3\theta - 6c_3\cos 3\theta)$$
$$+r^2(6b_2\sin 2\theta - 6d_2\cos 2\theta + 12a_4\sin 4\theta - 12d_4\cos 4\theta)$$
$$+r^n[n(n+1)b_n\sin n\theta - n(n+1)d_n\cos n\theta$$
$$+(n+1)(n+2)a_{n+2}\sin(n+2)\theta - (n+1)(n+2)d_{n+2}\cos(n+2)\theta] \tag{10.36}$$

The boundary conditions to be satisfied in the model are,

$$\sigma_\theta]_{\theta=0} = -(P_0 - P_0\frac{r}{L}), \sigma_\theta]_{\theta=2a} = 0 \tag{10.37}$$

$$\tau_{r\theta}]_{\theta=0} = -\mu(P_0 - P_0.\frac{r}{L}), \tau_{r\theta}]_{\theta=2a} = 0 \tag{10.38}$$

Applying the boundary conditions to equations (10.35) and (10.36) yields the following two sets of simultaneous equations,

$$\left.\begin{aligned} &2b_0 + 2a_2 = -P_0 \\ &2b_0 + 2d_0.2a + 2a_2\cos 2(2a) + 2c_2\sin 2(2a) = 0 \\ &-d_0 - 2c_2 = -\mu P_0 \\ &-d_0 + 2a_2\sin 2(2a) - 2c_2\cos 2(2a) = 0 \end{aligned}\right\}$$

And,

$$\left.\begin{aligned}
&6(b_1 + a_3) = \frac{P_0}{L} \\
&b_1 \cos(2a) + d_1 .\sin(2a) + a_3 \cos 3(2a) + c_3 \sin 3(2a) = 0 \\
&-2d_1 - 6c_3 = \mu \frac{P_0}{L} \\
&2b_1 \sin(2a) - 2d_1 \cos(2a) + 6a_3 \sin 3(2a) - 6c_3 \cos 3(2a) = 0
\end{aligned}\right\}$$

The simultaneous equations yield the following values for the unknowns,

$$a_2 = \frac{P_0}{4}\left[\frac{(\mu(2a)-1)\tan^2(2a) + \mu(\tan(2a) - 2a)}{(\tan(2a) - 2a)\tan(2a)}\right]$$

$$b_0 = -\frac{P_0}{2}\left\{1 + \frac{1}{2}\left[\frac{(\mu(2a)-1)\tan^2(2a) + \mu(\tan(2a) - 2a)}{(\tan 2a) - 2a)\tan(2a)}\right]\right\}$$

$$c_2 = \frac{P_0}{4}\left[\frac{1 - 2\mu(2a) + \mu\tan(2a)}{\tan(2a) - 2a}\right]$$

$$d_0 = \frac{P_0}{2}\left[\frac{\mu\tan(2a) - 1}{\tan(2a) - 2a}\right]$$

$$a_3 = \frac{P_0}{24L}\left[\frac{\tan^2(2a) + 3 - 6\mu\tan(2a)}{\tan^2(2a)}\right]$$

$$c_3 = -\frac{P_0}{24L}\left[\frac{3\mu\tan(2a)(\tan^2(2a)-1)+2}{\tan^3(2a)}\right]$$

$$b_1 = \frac{P_0}{8L}\left[\frac{\tan^2(2a)-1+2\mu\tan(2a)}{\tan^2(2a)}\right]$$

$$d_1 = \frac{P_0}{8L}\left[\frac{2-\mu(\tan^2(2a)+3)\tan(2a)}{\tan^3 2a}\right]$$

The stresses can now be computed anywhere in the loaded region of the wedge. For the point, r = 0, the angle, θ, is equal to zero, i.e., at the apex of the wedge an arbitrary choice of shear loading on the two faces of the wedge will not produce equilibrium conditions. This is observed if the edge is taken as a 90° corner, and shear loading is considered on one face only. The clearance face is free from shear stress and the corner element is not in equilibrium. Assuming that the error is small, the radial stress, σ_r, at the apex (from equation (10.34) and for r = 0, then θ = 0), is,

$$\sigma_r]_{\substack{r=0\\ \theta=0}} = 2(b_0 - a_2)$$
$$= -P_0\left[\frac{2a\tan(2a)(\mu\tan 2a)-1)+\mu(\tan(2a)-2a)}{(\tan(2a)-2a)\tan(2a)}\right] \quad (10.39)$$

The analysis shown can be applied to any type of polynomial distribution of the load over the rake face of the wedge-shaped abrasive grain. If the force distribution is not polynomial, an approximate solution can be obtained by considering a linearly

distributed load that is equivalent to the original one. Maximum values of stress were computed for a variety of distributed loads and then correlated to the relevant wheel wear parameter, grinding ratio, for a variety of micro-tools.

10.3.1 Development of Wear Model

Brittle materials exhibit high strength properties when loaded in compression than in tension. The ratio of rupture strengths is usually between 3:1 and 10:1 [24]. The existence of relatively low tensile stresses in the diamond grains, may cause failure by fracture to occur. To alleviate fracture, it is possible to use larger grains that reduce the stress levels in the grain when subjected to grinding forces. The effects of changing the amount of nitrogen in the gaseous mixture when creating diamond grains has the effect of changing morphology and the sizes of grains. Therefore, special attention must be paid to deposition conditions that will optimise the size and shape of diamond grains that will resist negative tensile stresses established in the grains when grinding takes place. Therefore, processing conditions determine the life of diamond grains when subjected to large grinding forces. To measure the effectiveness of the deposition process, it is required to model the effects of tensile stresses on the fracture properties of diamond grains deposited in various gaseous environments in order to quantify the effects of nitrogen on the life of micro-tools.

To model the action of the micro-tool, we must consider a single active cutting point to be classed as a wedge of constant width loaded at its inverted apex with point loads, F, and, nF, which represent the radial and tangential force components with reference to the micro-tool in which the grain is supported, and P is the resultant force (Figure 10.5). The stress distributions within point-loaded wedges can be determined analytically, and the results of such an analysis indicate that if tensile stresses exist within the wedge then it will occur at its maximum along the rake face. The existence of a tensile stress depends on the magnitude of the force ratio, n. If the ratio is especially small that a tensile stress exists in the wedge, then for a specific force ratio the tensile stress is

proportional to the tangential grinding force, F. Stresses of this nature would extend to and beyond the diamond grain-substrate interface. The fracture of diamond grain and the interface between the substrate depends on the particular micro-tool used and the magnitude of the tensile stress induced during grinding. Grains of diamond are typically seven-to-ten times stronger in compression than in tension, and therefore the probability of grain fracture is likely to increase with an increase in tensile stress exerted in the grain although the magnitude of the stress may be slightly higher than one-fifth the magnitude of the maximum compressive stress in the grain. A significant barrier to the acceptance of stress patterns evaluated for such situations arises because point loads applied to perfectly sharp wedges produce infinitely high stresses at, and about, the point of contact. Therefore, the loads must be applied over a finite area. This implies that compressive stresses dominate over the finite area. Experimental results [24] show that rake face stresses are compressive over the entire length of chip-tool contact but are tensile outside of this region. The zone of fracture initiation points were located in the tensile zone at about two to two-and-a-half times the chip-tool contact length.

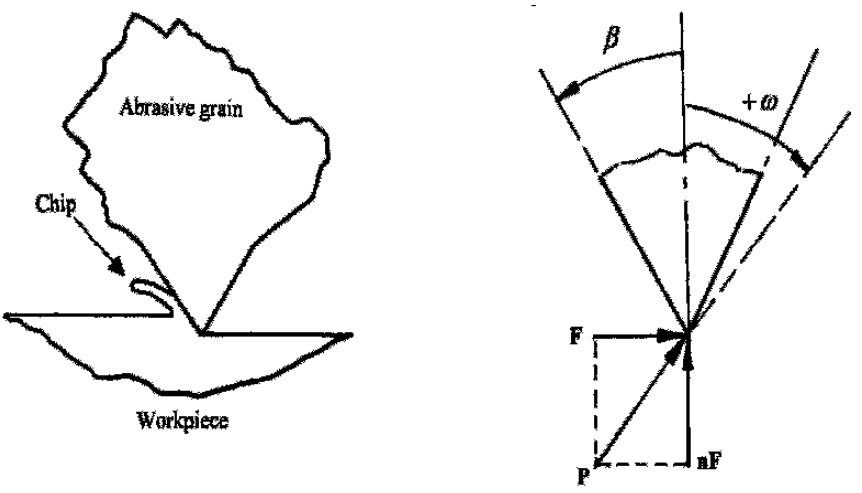

Figure 10.5. Ideal wedge-shaped cutting point and grinding force diagram

It seems likely that higher tensile stresses are associated with higher grain fracture probability resulting in rapid loss of diamond grains and, consequently, lower grinding ratios. The wear model should incorporate the fact that the loads are spread over a finite area. This implies that single-point loads are resolved into multiple point loads along the rake face, or are indeed, applied directly along the rake face of the cutting tool. The model should allow the relationship between the wear of a micro-tool and the general nature of stresses established in active diamond grains subjected to grinding forces to be examined. However, the development of a wear model that represents the effects of induced stress in the material is required. The analytical models developed here describe well the initial stages of grinding. However, as the grains are worn by a mechanism of abrasive wear rather than fracture wear, then a computational model must be considered.

10.3.2 Computational Stress Analysis of Single Diamond Grains

The assumed geometry of an ideal grain in the vicinity of its cutting edge is a simple symmetrical wedge of constant width with an included angle of 70^{O} that results in a rake angle of -35^{O}. There is no wear flat on the model cutting grain. In order that a finite element method is used to evaluate stresses in the wedge, the wedge was subdivided into 210 diamond-shaped elements with a total of 251 nodes. Forty-one nodes were constrained at the boundary of the wedge and the leading five nodes on the rake face were loaded (Figure 10.6). The tangential and normal grinding point loads were replaced by a series of multiple loads (F_Y and F_Z) acting perpendicular to (normal load) and along (shear load) the rake face of the wedge.

The loads at the five nodes are representative of the distributed and normal loads acting on the rake face over the diamond grain-chip contact length. The normal force distribution on the rake face was taken as being a maximum value at the cutting edge and decreases linearly to zero at the end of the diamond grain-chip contact length. The shear force was taken to be constant over the

first half of the contact length, decreasing linearly to zero over the contact length. Grinding loads were also applied directly to the rake face and at the tip of the diamond without applying multiple loads along the rake face. This was performed in order to compare and contrast the effect of different force distributions on the stresses generated within the diamond wedge.

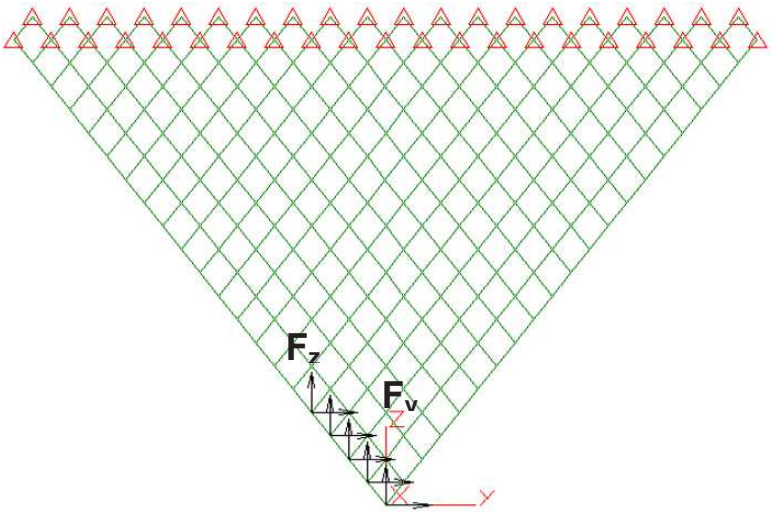

Figure 10.6. Finite element assemblage with grinding loads applied at the rake face nodes

To measure the value of using the maximum tensile stress as a way to estimate grain fracture tendency, the correlation between the two sets of data were calculated for each set of data. The region of fracture initiation was also located using Griffith's criterion of fracture [26], which is applicable to the fracture of brittle materials. For,

$$\frac{\sigma_c}{\sigma_t}.\sigma_1 + \sigma_3 > 0 \qquad (10.33)$$

Then,

$$\sigma_1 = \sigma_t \tag{10.34}$$

But for,

$$\frac{\sigma_c}{\sigma_t}.\sigma_1 + \sigma_3 < 0 \tag{10.35}$$

Then,

$$\left(|\sigma_1| - |\sigma_3|\right)^2 + 8\sigma_t\left(|\sigma_1| - |\sigma_3|\right) = 0 \tag{10.36}$$

Where σ_1 and σ_3 are the principal stresses, assuming that $\sigma_1 > \sigma_3$, σ_t is the ultimate tensile strength of the abrasive grain, and σ_c is the ultimate compressive strength. For diamond, the ratio of σ_t and σ_c is approximately 0.1.

10.4 Experimental Methods

10.4.1 Hot filament chemical vapor deposition

The hot filament CVD system is composed of a water-cooled stainless-steel vessel, which is connected to a rotary pump enabling a vacuum to be produced. The hot filament CVD apparatus is shown in Figure 10.7. Gas flow rates are controlled using MKS mass flow controllers to accurately control the amounts of gases flowing into the reactor. The system allows independent bias to be applied between the substrate and filament. The filament consisted of a coiled tantalum wire of diameter 0.5 mm to activate the reaction mixture. The filament temperature was measured using an optical pyrometer with values between 2200 and 2500K. Substrate temperatures were measured using a K-type thermocouple in direct thermal contact with the substrate. After abrasion, the samples were

ultrasonically cleaned with acetone prior to deposition. The diamond films were grown on pre-abraded WC-Co substrates for 4 h under standard deposition conditions [4]. To investigate the effects of changing the gas-phase environment different concentrations of nitrogen, from 50 to 100,000 ppm, were added to the standard 1% methane in hydrogen gas mixture. This is equivalent to varying the N/C ratio from 0.01 to 20. The film morphology, growth rate, and quality were characterised using Raman spectroscopy (Kaiser Holo Probe: 532 nm, Nd : YAG laser), and scanning electron microscopy (SEM).

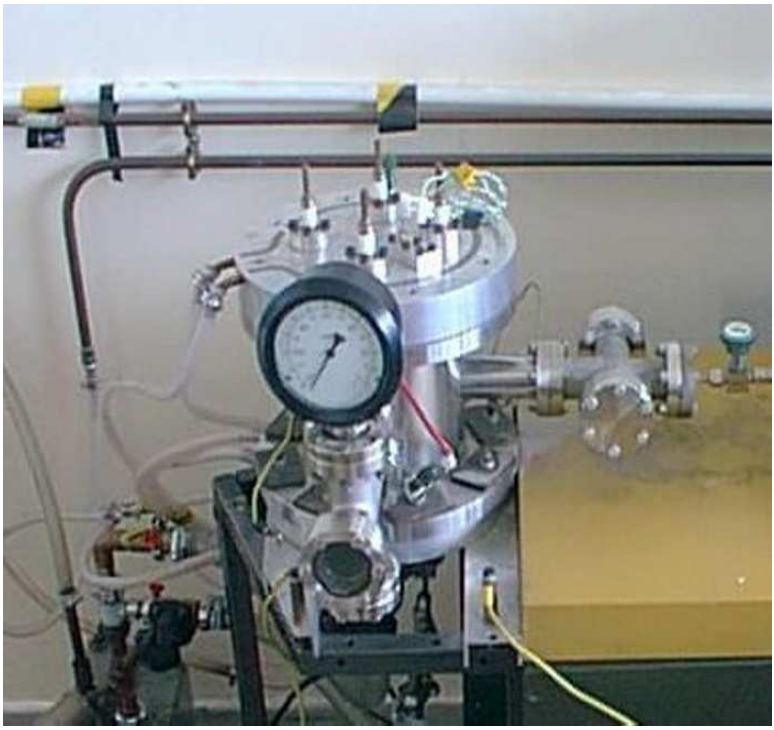

Figure 10.7. Hot filament CVD apparatus

10.4.2 Measurement of wear of diamond tools

The measurement of the wear of diamonds on a single layer deposited to the grinding tool requires grinding various workpiece materials on a specially constructed machine tool. The machine tool

was constructed using a tetrahedral space frame design that attenuates vibrations generated during grinding. The grinding tool is held in an air turbine spindle capable of rotating the grinding tool in excess of speeds of 350,000 revolutions per minute. Figure 10.8 shows the machine tool complete with three axes of motion in the x, y, and z-directions. A fourth axis capable of rotary motion can also be used on the machine tool. The machine tool was used to measure the performance of the grinding tools machining materials such as medium carbon steels (hypoeutectoid), high carbon tool steels (hypereutectoid), and cast iron. Grinding experiments were conducted using a number of micro-tools coated with diamonds that were produced in a hot filament CVD reactor containing gases with varying amounts of nitrogen in a methane/hydrogen mixture. The grinding ratio was measured in accordance with that stated in section 1. However, in order to correlate the magnitude of tensile stress in the diamond grains to the grinding ratio, it is required to know the number of active cutting grains on the surface of the micro-tool.

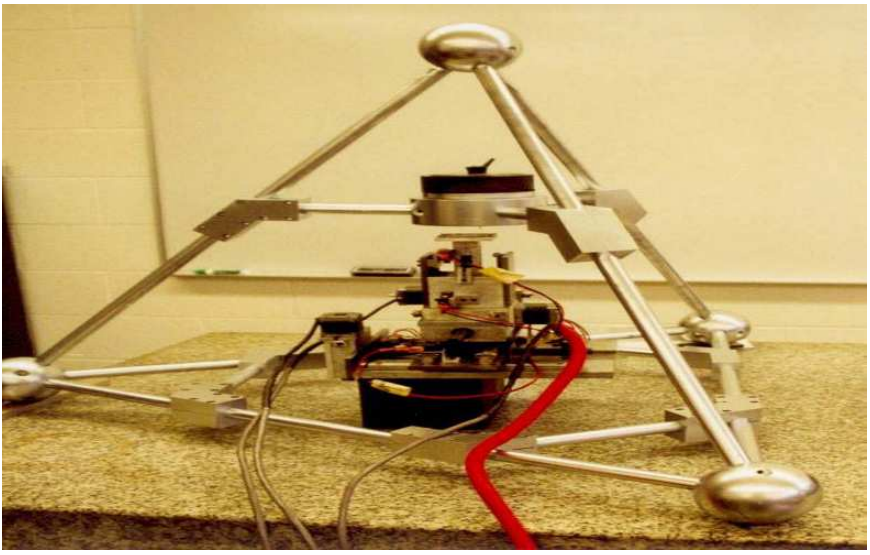

Figure 10.8. Micro-machine tool showing tetrahedral spaceframe surrounding the precision x-y-z table and the extremely high-speed air-turbine spindle

The number of active cutting grains on the micro-tool surface is found quite simply by driving a grinding tool into a piece of soft metal that has a length equal to the grinding tool's circumferential length. The depth to which the grinding tool is driven into the length of soft metal is equal to the depth of cut. The impression that the grinding tool produces in the length of soft metal is equal to the number of cutting points that are active during the grinding stroke at that particular rate of cut. However, the micro-tool must be prepared by simulating the grinding conditions used during the experimental conditions. Once the micro-tool has stabilized at its optimum grinding condition, then the tool is removed from the machine tool and driven into the soft metal that simulates one grinding revolution into the workpiece material. The force components are then applied to a 'model' diamond grain by dividing the grinding force data generated using a dynamometer into the number of active cutting grains over an area that simulates the diamond grain-workpiece contact area over one revolution. Stresses established in this area are calculated using finite elements. The wear of the micro-tool, expressed in terms of a grinding ratio, and its relationship to the stresses set up in the model grain is compared.

10.5 Discussion

10.5.1 Diamond deposition

Figure 10.9 shows CVD diamond growth on unabraded WC-Co substrate for six hours: A striking increase in diamond nucleation density is observed with the presence of nitrogen in the process gas. It is evident that nitrogen enhances the nucleation of diamond. However, even after 6 hours it not sufficient on its own to cause the growth of a continuous diamond film. Hence, surface abrasion or another form of substrate preparation is a necessary in the creation of nucleation sites for the growth of diamond films. Figure 10.10 shows CVD diamond growth with and without surface abrasion. It is clearly evident that without abrasion even after 4 hours of deposition only isolated crystals of diamond appear on the surface of the substrate. However, surface abrasion results in a continuous film of

diamond with the nucleation density of about 9 x 10^8 /cm^2. Mixed crystals of <111> and <100> orientation are formed, which are typically 1-3 μm in diameter. The film is continuous with no evidence of pin-holes, or cracks. For micro-tools, a highly controlled method of surface treatment is desirable. Even though surface abrasion is very effective in creating nucleation sites it does not allow a high degree of precision and control of surface preparation and therefore bias enhanced nucleation has been investigated as an alternative.

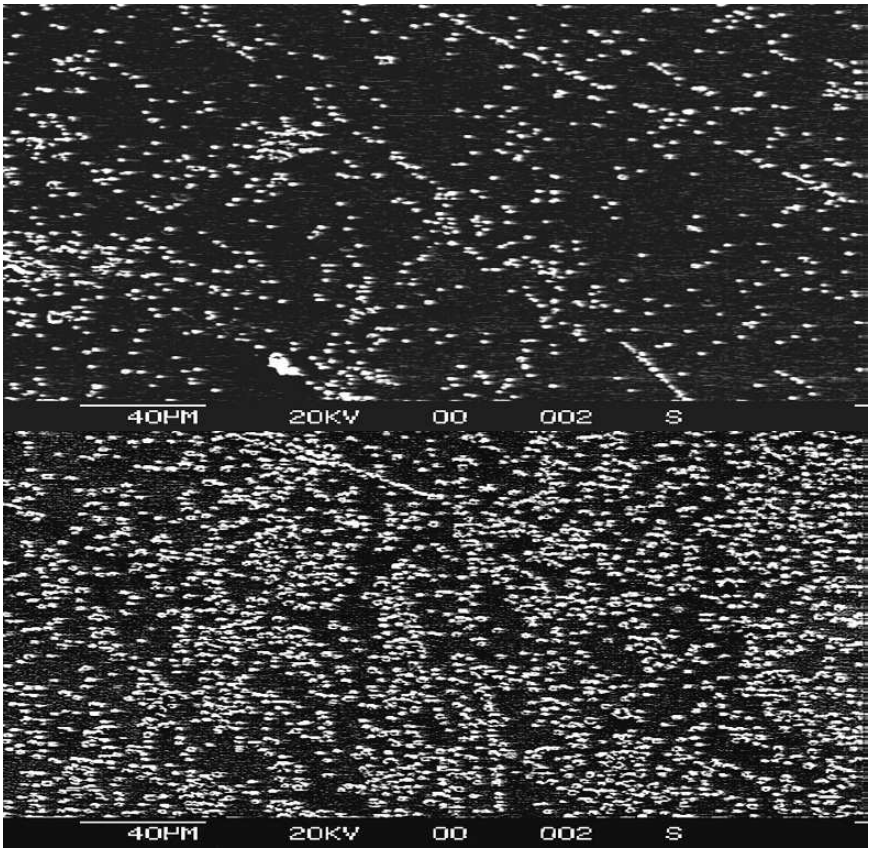

Figure 10.9. Diamond nucleation on the unabraded surface prior to deposition for 6 hour at 0 and 200ppm nitrogen addition

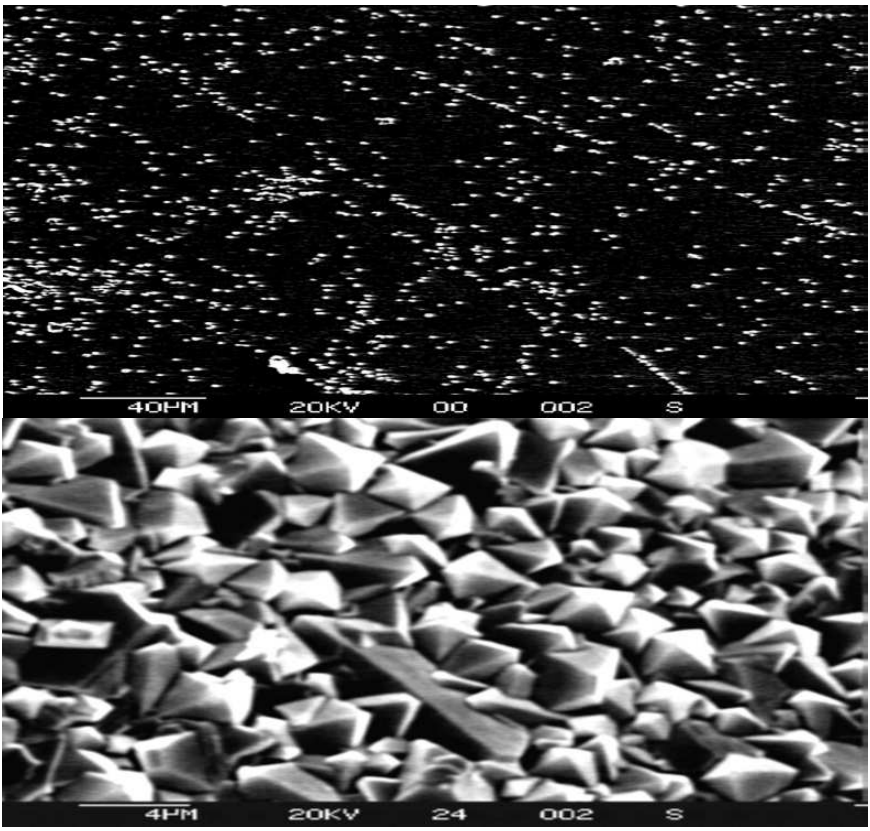

Figure 10.10. Diamond growth: (a) without surface abrasion; and (b) with surface abrasion with a diamond powder

Application of a negative bias of –300V to the substrate for 30 minutes prior to the deposition stage gives a measurable increase in the nucleation density with a continuous film forming (Figure 10.11). The increase in nucleation is due to the creation of nucleation sites arising from ion bombardment of the substrate. However, at the pressures utilised in this study of 2660 Pa the mean free path is relatively small and ion acceleration appears unlikely and an alternative explanation may be more likely. Biasing the substrate changes the composition of the plasma creating a higher concentration of hydrogen radicals near to the substrate and therefore the changes in the morphology could be due to a chemical etching effect rather than an ion bombardment effect. It is evident

from Figure 10.12 that as the amount of nitrogen is increased from 0 to 200ppm the size of diamond crystals also increases. The addition of nitrogen is thus enhancing the growth of the diamond crystals. However, the precise reasons for this growth enhancement are still unclear and are being investigated. Figure 10.13 illustrates that further additions of nitrogen degrade the crystal structure considerably but improves the surface roughness of the films.

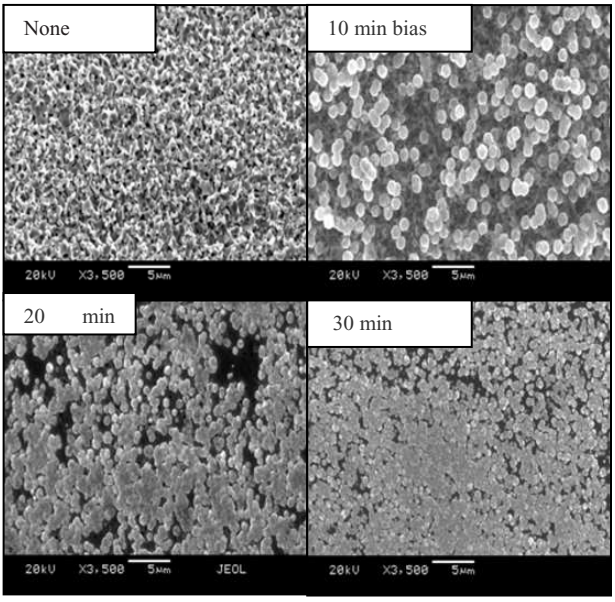

Figure 10.11. Scanning electron micrograph showing the effects of biasing time on the nucleation density

These films were grown under the same conditions but in separate studies. The different grain densities indicate the difficulty in obtaining absolute reproducibility, though the relative density measurements are significant. Raman analysis confirms this trend. For relatively small amounts of nitrogen in the gas phase the FWHM of the 1332 cm^{-1} absorption characteristic of diamond is reduced indicating an increase in the diamond phase purity. For higher levels of nitrogen the diamond peak broadens and disappears altogether with N_2 levels above 50,000 ppm in the gas mixture (Figure 10.14). This data is consistent with films produced from microwave

diamond CVD studies [8]. The changes in the surface morphology and structure are related to the carbon supersaturation, which is controlled by the supply of carbon and the creation of growth sites at the surface [8]. Small amounts of nitrogen are able to reduce carbon supersaturation, which leads to an improvement in crystal quality. At higher levels of nitrogen the carbon supersaturation increases and the morphology changes from blocky to spherical, which is accompanied by deterioration of the diamond phase purity.

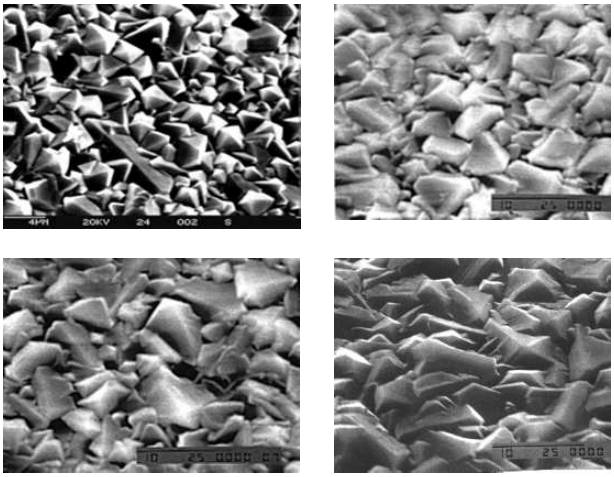

Figure 10.12. N-doped CVD diamond growth at 0, 50, 100 and 200 ppm of nitrogen

10.5.2 Wear of diamonds

The wear of micro-tools coated with diamonds deposited from various gaseous environments doped with nitrogen appears in Table 10.1. Here, it is shown that the nature of the diamond is optimised at 200 parts-per-million of nitrogen in methane/hydrogen mixture. Beyond this value, the grinding ratio decreases because the diamonds are becoming smaller in size and the surface is becoming smoother.

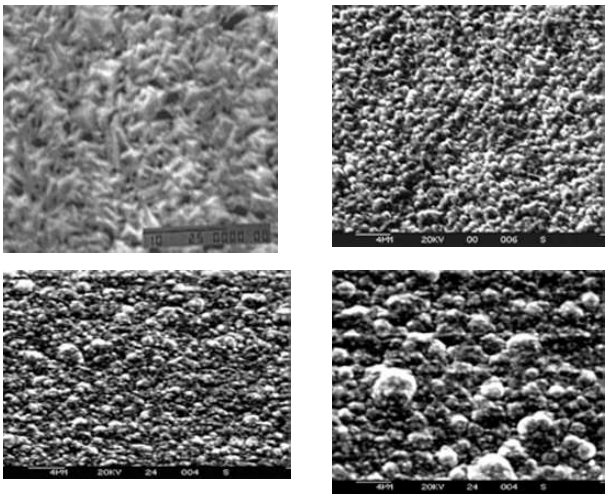

Figure 10.13. N-doped diamond at 5000, 10000, 50000 and 100000 ppm of nitrogen

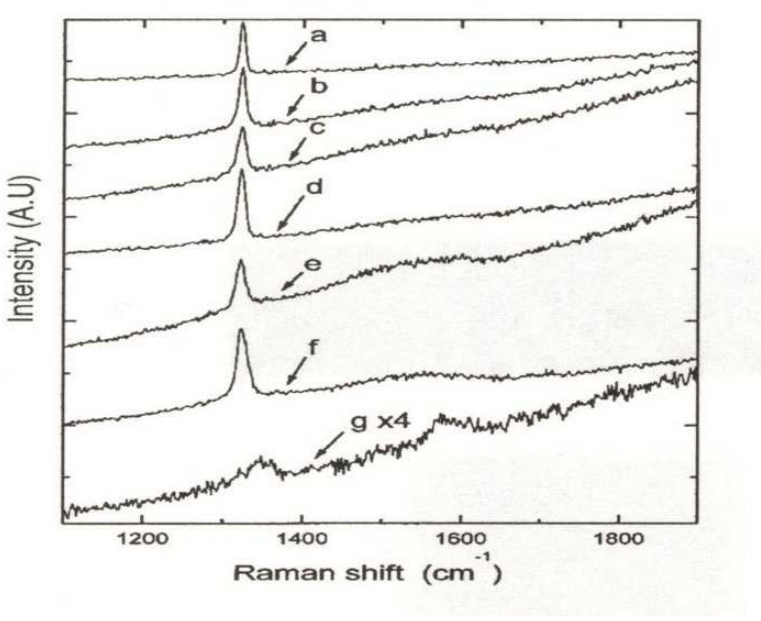

Figure 10.14. Raman spectra of n-doped diamond coatings: (a) 200 ppm; (b) 100 ppm; (c) 5000 ppm; (d) 50 ppm; (e) 10000 ppm; (f) 50000 ppm; and (g) 0 ppm

Below 200 ppm, the diamonds are scattered in random formation producing a discontinuous film of diamonds leaving large areas of the tool unable to grind the surface of the workpiece material. The results of the two-dimensional stress analyses were consistent with the experimentally determined stress distribution obtained by Loladze [25] when cutting soft metal with photoelastic tools. The maximum tensile stress always occurs at the rake face at a distance from the cutting edge ranging from 1.5 – 4 times the abrasive grain-chip contact length, the exact magnitude of the coefficient depends on the loading conditions for a particular grinding event. For a given value of the tangential force component, F, the higher the force ratio, F/nF, the greater the distance the maximum tensile stress is away from the cutting edge. These results indicate that mechanically induced fracture occurs at a finite distance away from the cutting edge. When using Griffith's criterion, the influence of mechanically induced stresses indicate that fracture initiation zones are established. Figure 10.15 shows the occurrence of such zones in an idealized wedge. The first zone is located around the point of maximum tensile stress and is always at the rake face.

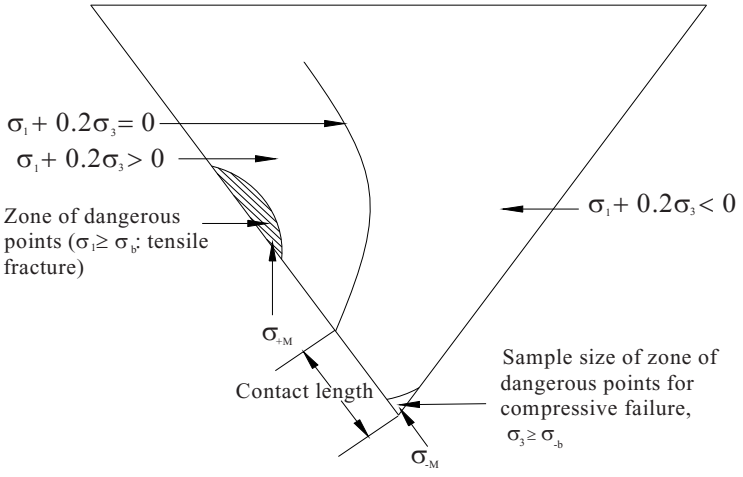

Figure 10.15. Griffith's criterion applied to the idealized wedge showing tensile and compressive fracture initiation zones

Failure in this zone is tensile and would initiate fracture at a point on the rake face of the order of two-to-three times the diamond grain-chip contact length away from the cutting edge. This type of fracture is consistent with fracture on a scale comparable with the chip thickness and tends to produce the so-called 'self-sharpening action'. The second much smaller zone is located at the immediate vicinity of the cutting edge. Failure is compressive in this region and results in 'crumbling' of the cutting edge leading to the formation of a wear flat on the diamond grain.

Nitrogen (ppm in methane/hydrogen mixture)	**Grinding ratio**
0	50
50	110
100	200
200	300
5000	175
10000	85
50000	60
100000	20

Table 10.1. Performance data for grinding normalized M2 tool steel. Grinding conditions: tool diameter: 750μm; spindle speed: 350,000rpm; depth of cut: 10μm; feed rate: 10μm/min

The correlation between the magnitude of the maximum tensile stress in the model diamond grains and the grinding ratio (Table 10.2) is high and is dependent on the way the forces are applied to the grains. It would be expected that the higher the tensile stress, the greater is the rate of grinding wheel wear and consequently the corresponding grinding ratio. Perfect linear correlation in accordance with this would result in a correlation coefficient of –1. The correlation coefficient between the maximum tensile stress and the grinding ratio is significant. This is to be expected as the force ratio may vary slightly. However, if the tangential component of the grinding force changes significantly without a change in force ratio, then it is expected that the maximum tensile stress will change significantly and consequently reduce the grinding ratio.

Workpiece material	Grinding Ratio	Exact wedge model with point loads applied to apex of the wedge	Approximate finite element model: multiple grinding loads applied to rake face of wedge	Approximate finite element model: grinding forces applied directly to the rake face of the wedge
En2 steel (hypoeutectoid)	500	-0.7	-0.82	-0.99
Normalized M2 tool steel	300	-0.54	-0.68	-0.98
En8 steel (hypoeutectoid)	250	-0.15	-0.25	-0.6
AISI 52100 (hypereutectoid)	350	-0.76	-0.86	-0.98
Annealed M2 tool steel	250	-0.8	-0.9	-0.99
Chilled Grey Cast Iron (Flake Graphite)	650	-0.83	-0.85	-0.91
Spheroidal Graphite Cast Iron	580	-0.9	-0.95	-0.99
Austempered Ductile Iron (Bainitic Structure)	525	-0.92	-0.95	-0.99

Table 10.2. Correlation coefficient between maximum tensile stress and grinding ratio for an idealized wedge that simulates a grinding tool that has an optimum diamond coverage using a controlled gas atmosphere of 200ppm of nitrogen in methane/hydrogen mixture. Comparison is also made between the methods of applying loads to the idealized wedge models

The calculation and application of multiple grinding loads along the rake face produces a lower correlation coefficient compared to directly applied grinding loads. This implies that grinding loads are simply not point loads acting act the tip of the inverted apex and along the abrasive grain-chip contact length of the grinding grain. In

fact, directly applied grinding forces produce better correlation coefficients. This means that for perfectly micro-tools, one must apply the component grinding loads directly to the rake face.

10.6 Conclusions

We have shown that the surface morphology of the diamond films can be controlled by employing surface abrasion, substrate biasing, or nitrogen addition to the gas mixture. The application of a bias voltage during normal diamond growth enables re-nucleation of the diamond film. Thus, the crystal size and surface roughness may be controlled with no reduction in the diamond phase purity. Addition of nitrogen to the gas phase during diamond CVD can also be used to control the surface morphology. For diamond-coated microtools, grain fracture appears to be the dominant cause of diamond loss during a grinding operation. Grain fracture is much more likely to be caused by mechanically induced tensile stresses within diamond grains than by mechanically induced compressive stresses. The best indicator of microtool performance during a grinding operation under different operating conditions is the level of tensile stress established in diamond grains. High tensile stresses are associated with grain fracture and low grinding ratios in perfectly sharp micro-tools. Finite element models of sharp diamond grains can be applied to micro-tools where the dominant wear mechanism is grain fracture.

References

[1] Fan Q H, Periera E, Gracio J., Time modulated CVD diamond processing of diamond, J. Mater. Res., 1998, **13**(10), 2787-2794.
[2] May P, Rego C A, Thomas R M, Ashfold M N R, Rosser K N, Everitt N M., CVD diamond wires and tubes, Diamond Related Mater., 1994, **3**, 810-813.
[3] Kostadinov L, Dobrev D, Okano K, Kurosu T, Iida M., Nuclear and growth of diamond from the vapor phase, Diamond Related Mater., 1992, **1**, 157-160.
[4] Ali N, Ahmed W, Hassan IU, Rego CA., Surface engineering of diamond coated tools, Surf. Eng., 1998, **14**(4), 292.
[5] Beckmann R, Kulisch W, Frenck H J, Kassing R., Influence of gas phase parameters on diamond kinematics of thin diamond films deposited by MWCVD and HFCVD techniques, Diamond Related Mater., 1992, **1**, 164-167.

[6] Ojika SI, Yamoshita S, Ishikura T., Diamond growth on copper substrate, Japanese J. Appl. Phys., 1998, **32**(2), L1681-L1683.
[7] Muller-Serbert W, Worner E, Fuchs F, Wild C, Koidl P., Nitrogen induced increase in growth rate in CVD diamond, Appl. Phys. Lett., 1996**,** **68**(6), 759-760.
[8] Bohr B, Haubner R, Lux B., Influence of nitrogen additions on HFCVD diamond, Appl. Phys. Lett., 1996, **68**(8), 1075-1077.
[9] Yarbrough W A, Messier R., Diamond deposition to silicon, Science, 1988, **247**, 688.
[10] Kanetkar S M, Metera G, Chen X, Pramanick S, Tiwari P, Narayan J, Pfei!er G, Paesler M., Growth of diamond on silicon substrates, J. Elect. Mater., 1991;**20**:4.
[11] Wolter S D, Stoner B R, Glass J T, Ellis P J, Jenkins D S, Southworth P., Textured growth of diamond on silicon via in situ carburisation and bias enhanced nucleation, Appl. Phys. Lett., 1993, **62**, 1215-1217.
[12] Jiang X, Klages C P, Zachia R, Hartureg M, Fuser H J., Epitaxial diamond films on (001) silicon substrates, Appl. Phys. Lett., 1993, **62**, 3438-3440.
[13] Stubhan F, Ferguson M, Fusser H J, Behom R J., Heteroepitaxial nucleation of diamond on Si (001) in HFCVD, Appl. Phys. Lett., 1995, **66**, 1900-1902.
[14] Li X, Hayashi Y, Nishino S., Analysis of oriented diamond nucleation processes on silicon substrates by HFCVD, Japanese J. Phys., 1997, **36**, 5197-5201.
[15] Locher R, Wild C, Herres N, Behr D, Koidl P., Nitrogen stabilized <100> texture in CVD diamond films, Appl. Phys. Lett., 1994, **65,** 34-36.
[16] Jin S, Moustakas T D., Effect of nitrogen on the growth of diamond films, Appl. Phys. Lett., 1994, **65**, 403-405.
[17] Borst T H, Munzinger P C, Weiss O., Characterization of undoped and doped homoepitaxial diamond layers produced by microwave plasma CVD, Diamond Related Mater., 1994, **3**, 515-519.
[18] Koizumi S, Kamo M, Sato Y, Mita S, Sauabe A, Reznik C, Growth and characterization of phosphorous doped n-type diamond films, Diamond Related Mater., 1998, **7**, 540-544.
[19] L. P. Tarasov, Grindability of Tool Steels, American Society of Metals, 1951, **43**, 1144 – 1151.
[20] H.K. Tonshoff and T. Grabner, Cylindrical and profile grinding with boron nitride wheels, Proceedings of the 5th International Conference on Production Engineering, Japanese Society of Precision Engineers, p.326, 1984.
[21] S. Malkin and N. H. Cook, The wear of grinding wheels – Part 1: attritious wear, Trans. A.S.M.E. – Journal of Engineering for Industry, 1971, **93**, 1120 – 1128.
[22] M. J. Jackson, Vitrification heat treatment during the manufacture of corundum grinding wheels, Journal of Manufacturing Processes, 2001, **3**, 17-28.
[23] S. P. Timoshenko and J. N. Goodier, Theory of Elasticity, 3rd Edition – International Student Edition, McGraw-Hill Kogakusha Ltd., p.p. 109-113, and p.p. 139-144, 1970.

[24] A. G. King and W. M. Wheildon, Ceramics in Machining Processes, (Academic Press, New York, 1966).
[25] T. N. Loladze, Requirements of tool materials, Proceedings of the 8th International Machine Tool Design and Research Conference, Pergamon Press, 821-842, 1967.
[26] A. A. Griffith, The phenomena of rupture and flow in solids, Philosophical Transactions of the Royal Society of London, 1921, **A221**, 163-198.

Subject Index

D

Dr. Mark J. Jackson

Professor of Mechanical Engineering and
University Faculty Scholar
Purdue University
United States of America

C. Eng., Engineering Council of London, U.K., 1998
M. A. Status, Natural Sciences, University of Cambridge, U.K., 1998
Ph. D., Mechanical Engineering, Liverpool, U.K., 1995
M. Eng., Mechanical & Manufacturing Engineering, Liverpool, U.K., 1991
O.N.D., Mechanical Engineering, Halton College, U.K., 1986
O.N.C. Part I, Mechanical Engineering, Halton College, U.K., 1984

Doctor Jackson began his engineering career in 1983 when he studied for his O.N.C. part I examinations and his first-year apprenticeship-training course in mechanical engineering. After gaining his Ordinary National Diploma in Engineering with distinctions and I.C.I. prize for achievement, he read for a degree in mechanical and manufacturing engineering at Liverpool Polytechnic and spent periods in industry working for I.C.I. Pharmaceuticals, Unilever Industries, and Anglo Blackwells. After graduating with a Master of Engineering (M. Eng.) degree with Distinction under the supervision of Professor Jack Schofield, M.B.E., Doctor Jackson subsequently read for a Doctor of Philosophy (Ph. D.) degree at Liverpool in the field of materials engineering focusing primarily on microstructure-property relationships in vitreous-bonded abrasive materials under the supervision of Professor Benjamin Mills. He was subsequently employed by Unicorn Abrasives' Central Research & Development Laboratory (Saint-Gobain Abrasives' Group) as materials technologist, then technical manager, responsible for product and new business development in Europe, and university liaison projects concerned with abrasive process development. Doctor Jackson then became a research fellow at the Cavendish Laboratory, University of Cambridge, working with Professor John Field, O.B.E., F.R.S., on impact fracture and friction of diamond before becoming a lecturer in engineering at the University of Liverpool in 1998. At

Liverpool, Dr. Jackson established research in the field of micromachining using mechanical tools, laser beams, and abrasive particles. At Liverpool, he attracted a number of research grants concerned with developing innovative manufacturing processes for which he was jointly awarded an Innovative Manufacturing Technology Center from the Engineering and Physical Sciences Research Council in November 2001. In 2002, he became associate professor of mechanical engineering and faculty associate in the Center for Manufacturing Research, and Center for Electric Power at Tennessee Technological University (an associated university of Oak Ridge National Laboratory), and a faculty associate at Oak Ridge National Laboratory. Dr. Jackson was the academic adviser to the Formula SAE Team at Tennessee Technological University. In 2004 he moved to Purdue University as Professor of Mechanical Engineering in the College of Technology.

Doctor Jackson is active in research work concerned with understanding the properties of materials in the field of microscale metal cutting, micro- and nanoabrasive machining, and laser micro machining. He is also involved in developing next generation manufacturing processes. Doctor Jackson has directed, co-directed, and managed research grants funded by the Medical Research Council, Engineering and Physical Sciences Research Council, The Royal Society of London, The Royal Academy of Engineering (London), European Union, Ministry of Defense (London), Atomic Weapons Research Establishment, National Science Foundation, N.A.S.A., U. S. Department of Energy (through Oak Ridge National Laboratory), Y12 National Security Complex at Oak Ridge, Tennessee, and Industrial Companies, which has generated research income in excess of $15 million. Dr. Jackson has organized many conferences and served as General Chairman of the International Surface Engineering Congress and is Deputy President of the World Academy of Materials and Manufacturing Engineering. He has authored and co-authored over 250 publications in archived journals and refereed conference proceedings, has written a book on "micro and nanomanufacturing", is guest editor to a number of refereed journals, and has edited a book on "commercializing micro- and nanotechnology products". He is the editor of the "*International Journal of Nanomanufacturing*", "*International Journal of Nano and Biomaterials*", "*Journal of Manufacturing Technology Research",* associate editor of the "*International Journal of Molecular* Engineering", and is on the editorial board of the "*International Journal of Machining and Machinability of Materials*", "*International Journal of Computational Materials Science and Surface Engineering",* and the "*International Journal of Manufacturing Research*".

Dr. Jonathan S. Morrell

Senior Development Chemist and
Technical Manager of Compatibility
and Surveillance Section
Y-12 National Security Complex
Oak Ridge, Tennessee
United States of America

Ph.D., Inorganic Chemistry, University of Tennessee, U.S.A., 2000
B.S., Chemistry, King College, U.S.A., 1996
B.S., Biology, King College, U.S.A., 1996

Dr. Morrell is a senior chemist and technical manager at the Y-12 National Security Complex in Oak Ridge, Tennessee, and has led the Compatibility and Surveillance section of the Applied Technologies Division since 2005. As a technical manager, Dr. Morrell oversees work related to fundamental understanding of materials properties and performance for national security applications. He also serves as an adjunct faculty professor in the College of Technology at Purdue University, West Lafayette, Indiana, and in the Natural and Behavioral Science Department at Pellissippi State Technical Community College, Knoxville, Tennessee. His research at Purdue involves development of the next generation of coated cutting tools and characterization of their materials properties. At Pellissippi he teaches general chemistry and is the adjunct representative for the Faculty Senate. Dr. Morrell has three issued patents, authored and co-authored more than 20 publications in archived journals and refereed conference proceedings as well as authoring 40 formal reports. He is currently a member of the editorial boards of the *International Journal of Molecular Engineering*, *International Journal of Nano and Biomaterials*, and *International Journal of Nanoparticles*.

Dr. Morrell received his bachelors' degrees with honors from King College in chemistry and in biology. His honors research was conducted at the J. H. Quillen College of Medicine on the campus of East Tennessee

State University, Johnson City, Tennessee, and was funded under a grant from the Department of Biochemistry and Molecular Biology at John Hopkins Medical Institute. The topic of this research was the antibiotic inhibition of ribosomal subunit formation in *Escherichia coli* cells. His doctor of philosophy in inorganic chemistry was obtained in 2000 from the University of Tennessee in Knoxville under the guidance of Professors David B. Beach and Ziling B. Xue. For his doctoral dissertation, Dr. Morrell studied the heteroepitaxial growth of complex oxide thin films via solution chemical techniques using novel alkoxide precursors. This research involved both the synthesis of precursor solutions and the processing and characterization of epitaxial thin films for ferroelectric and superconductor applications. The research was conducted at the Oak Ridge National Laboratory (ORNL), Oak Ridge, Tennessee, under a grant from the Office of Basic Energy Sciences, United States Department of Energy. Dr. Morrell, briefly employed by ORNL as a post-doctoral fellow, joined the Y-12 National Security Complex, Oak Ridge, Tennessee, in the summer of 2000. As a principal investigator in the Applied Technologies Division, he was initially involved in experimental testing and small-scale verification of operating conditions associated with industrial production issues related to national defense. Dr. Morrell later initiated research and development programs in pyrochemistry, materials processing, forensic analysis, machining, and environmental aging studies. Dr. Morrell, a native of Bristol, Tennessee, resides in Farragut, Tennessee, with his wife, Holly, and twin sons, Graham and Parker.